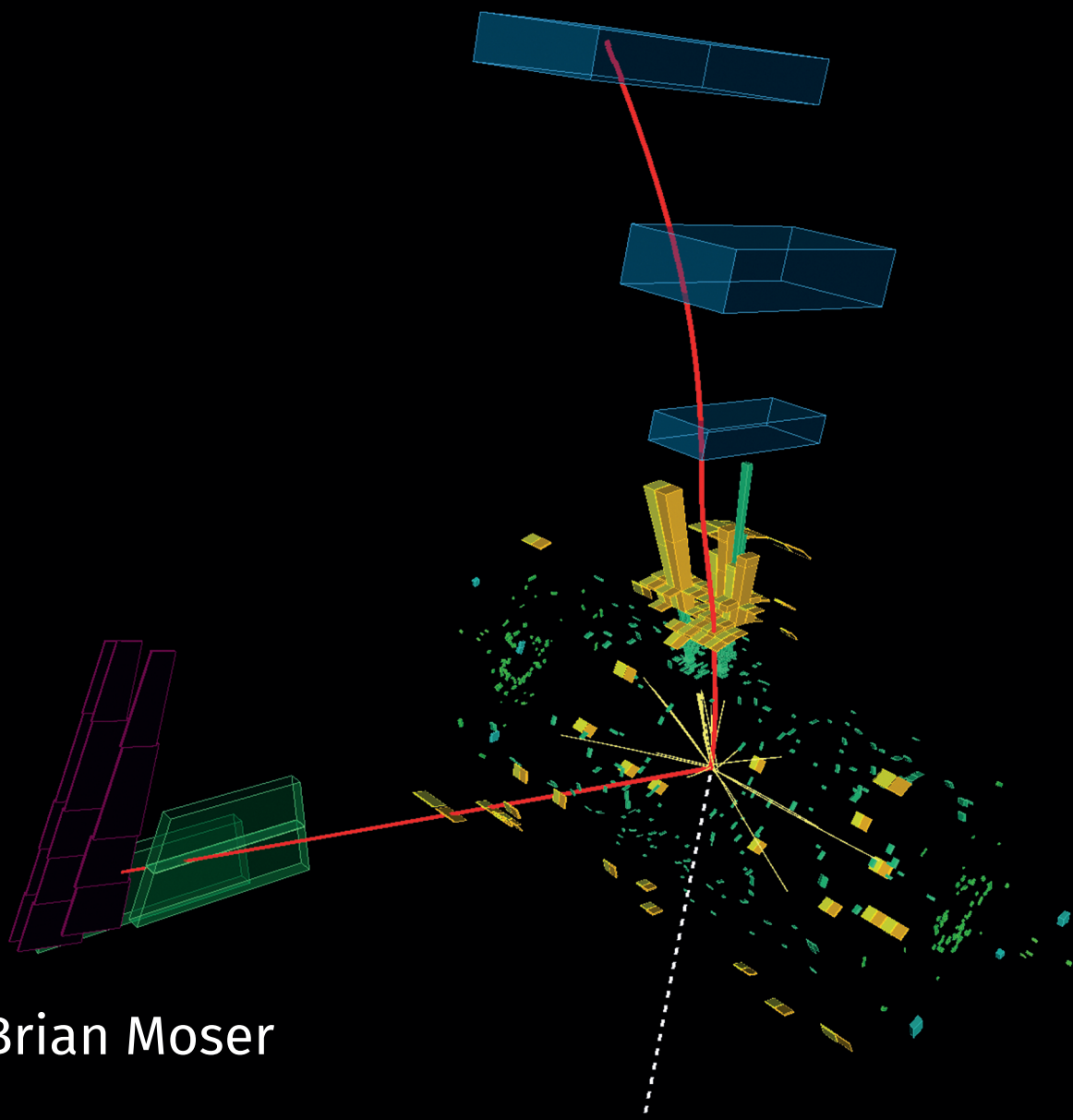


# The Beauty and the Boost: a Higgs Boson Tale

Measurements of Higgs Boson Production at High Energy  
in Decays to Bottom Quarks and Their Interpretations  
with the ATLAS Experiment at the LHC

CERN-THESIS-2021-298



Brian Moser



# **The Beauty and the Boost: a Higgs Boson Tale**

Measurements of Higgs Boson Production at High Energy in Decays  
to Bottom Quarks and Their Interpretations with the ATLAS  
Experiment at the LHC

Brian Moser

Copyright © 2022 by Brian Moser  
ISBN: 978-94-6421-637-0

**The Beauty and the Boost: a Higgs Boson Tale** - Measurements of Higgs Boson Production at High Energy in Decays to Bottom Quarks and Their Interpretations with the ATLAS Experiment at the LHC

Thesis, Universiteit van Amsterdam (UvA), Amsterdam

Printed in the Netherlands by Ipskamp printing



This work originates as part of the research programme of the Foundation for Fundamental Research on Matter (FOM), and falls as of April 1, 2017 under the responsibility of Foundation for Nederlandse Wetenschappelijk Onderzoek Instituten (NWO-I), which is part of the Dutch Research Council (NWO). The work has been performed at the National Institute for Subatomic Physics (Nikhef).



# **The Beauty and the Boost: a Higgs Boson Tale**

Measurements of Higgs Boson Production at High Energy in Decays  
to Bottom Quarks and Their Interpretations with the ATLAS  
Experiment at the LHC

## **ACADEMISCH PROEFSCHRIFT**

ter verkrijging van de graad van doctor

aan de Universiteit van Amsterdam

op gezag van de Rector Magnificus

prof. dr. ir. K.I.J. Maex

ten overstaan van een door het College voor Promoties ingestelde commissie,

in het openbaar te verdedigen in de Agnietenkapel

op vrijdag 4 maart 2022, te 13.00 uur

door

**Brian Moser**

geboren te Freiburg im Breisgau, Duitsland

PROMOTIECOMMISSIE:

PROMOTOR:	prof. dr. W. Verkerke	Universiteit van Amsterdam
COPROMOTOR:	dr. T.A. du Pree	Nikhef
OVERIGE LEDEN:	prof. dr. R. Fleischer	Vrije Universiteit Amsterdam
	prof. dr. M.P. Decowski	Universiteit van Amsterdam
	prof. dr. M. Vreeswijk	Universiteit van Amsterdam
	dr. M.M. Kado	Sapienza Università di Roma
	dr. J. de Vries	Universiteit van Amsterdam

Faculteit der Natuurwetenschappen, Wiskunde en Informatica

# Contents

<b>1</b>	<b>Introduction</b>	<b>1</b>
<b>2</b>	<b>Theoretical foundations</b>	<b>5</b>
2.1	The Standard Model of particle physics . . . . .	5
2.1.1	Particles and forces . . . . .	5
2.1.2	Quantum electrodynamics . . . . .	8
2.1.3	Quantum chromodynamics . . . . .	8
2.1.4	Electroweak unification . . . . .	9
2.1.5	Particle masses and the Higgs boson . . . . .	10
2.1.6	The full SM Lagrangian . . . . .	13
2.1.7	Renormalisation and constraints on the particle content . .	13
2.1.8	Free parameters of the SM . . . . .	14
2.2	Breaking the Standard Model . . . . .	16
2.2.1	Theoretical issues . . . . .	16
2.2.2	Inexplicable observations . . . . .	17
2.3	Effective Field Theories . . . . .	18
2.3.1	The Standard Model EFT . . . . .	19
2.3.2	Operator bases . . . . .	19
2.3.3	Operator selection . . . . .	20
2.3.4	The Warsaw basis . . . . .	21
2.3.5	Advantages and limitations of the SMEFT approach . . . .	21
2.4	Phenomenology of proton-proton collisions . . . . .	22
2.4.1	Parton-density functions and factorisation . . . . .	23
2.4.2	Event generation . . . . .	24
2.4.3	Cross-sections and luminosity . . . . .	25
<b>3</b>	<b>Higgs boson physics</b>	<b>27</b>
3.1	The importance of the Higgs boson . . . . .	27
3.2	Production modes and decay channels at the LHC . . . . .	28
3.3	Simplified Higgs Template Cross-Sections (STXS) . . . . .	32
3.4	Effective Higgs boson coupling modifiers . . . . .	35
3.5	Experimental status of Higgs boson physics . . . . .	38
<b>4</b>	<b>The ATLAS experiment at the Large Hadron Collider</b>	<b>43</b>
4.1	The Large Hadron Collider . . . . .	43
4.2	The ATLAS experiment . . . . .	45
4.2.1	The ATLAS coordinate system . . . . .	46
4.2.2	Particle identification with the ATLAS detector . . . . .	47
4.2.3	The Inner Detector . . . . .	48

4.2.4	The Calorimeters . . . . .	50
4.2.5	The Muon Spectrometer . . . . .	53
4.2.6	Luminosity measurements . . . . .	55
4.2.7	Triggering and data acquisition . . . . .	55
<b>5</b>	<b>Reconstruction of physics objects</b>	<b>59</b>
5.1	Tracks and vertices . . . . .	59
5.2	Topological calorimeter clusters . . . . .	60
5.3	Electrons . . . . .	61
5.4	Photons . . . . .	63
5.5	Muons . . . . .	63
5.6	Jets . . . . .	65
5.6.1	Jet algorithms . . . . .	65
5.6.2	Small- $R$ jets . . . . .	66
5.6.3	Large- $R$ jets . . . . .	67
5.6.4	Variable- $R$ jets . . . . .	71
5.7	$\tau$ leptons . . . . .	72
5.8	Missing transverse energy . . . . .	72
<b>6</b>	<b>Flavour tagging</b>	<b>75</b>
6.1	Properties of jets originating from heavy-flavour quarks . . . . .	75
6.2	Flavour-tagging algorithms . . . . .	77
6.3	Measurement of the $b$ -tagging efficiency in dense jet-environments . . . . .	81
6.3.1	Simulated samples . . . . .	82
6.3.2	Object and event selection . . . . .	82
6.3.3	Dense jet-environments . . . . .	84
6.3.4	The efficiency measurement . . . . .	84
6.3.5	Results and outlook . . . . .	85
<b>7</b>	<b>Measurement of Higgs boson production at high transverse momentum in the <math>VH, H \rightarrow b\bar{b}</math> channel</b>	<b>89</b>
7.1	Motivation . . . . .	89
7.2	Analysis overview . . . . .	91
7.2.1	The Higgs boson reconstruction . . . . .	91
7.2.2	The vector boson reconstruction . . . . .	92
7.2.3	The main backgrounds . . . . .	95
7.2.4	Goal of the measurement . . . . .	95
7.2.5	A sketch of the event selection and categorisation . . . . .	97
7.2.6	The signal extraction . . . . .	99
7.3	Data and simulated samples . . . . .	100
7.3.1	The data sample . . . . .	100
7.3.2	The simulated signal and background samples . . . . .	100
7.4	Event reconstruction and selection . . . . .	109
7.4.1	Object definitions . . . . .	109
7.4.2	Event reconstruction . . . . .	113
7.4.3	Event selection and categorisation . . . . .	117

7.5	Background composition and estimation . . . . .	125
7.5.1	Top quark pair production . . . . .	125
7.5.2	Single top production . . . . .	128
7.5.3	V+jets production . . . . .	129
7.5.4	Diboson production . . . . .	129
7.5.5	QCD multijet production . . . . .	130
7.5.6	Contamination from other Higgs boson processes . . . . .	131
7.6	Systematic uncertainties . . . . .	131
7.6.1	Experimental uncertainties . . . . .	132
7.6.2	Luminosity and pile-up modelling . . . . .	132
7.6.3	Electrons . . . . .	132
7.6.4	Muons . . . . .	132
7.6.5	Small- $R$ jets . . . . .	133
7.6.6	Large- $R$ jets . . . . .	133
7.6.7	Flavour tagging . . . . .	134
7.6.8	Missing transverse energy . . . . .	134
7.6.9	$\tau$ leptons . . . . .	134
7.6.10	Principle component analysis of uncertainties . . . . .	135
7.6.11	Modelling uncertainties . . . . .	135
7.7	Statistical treatment and inference . . . . .	141
7.7.1	The likelihood function definition . . . . .	141
7.7.2	The fit model . . . . .	143
7.8	Results . . . . .	145
7.8.1	Validation of the maximum likelihood fit . . . . .	146
7.9	Simplified Template Cross-Section measurement . . . . .	159
<b>8</b>	<b>(SM) EFT interpretation</b>	<b>169</b>
8.1	Simulation of the SMEFT impact . . . . .	169
8.1.1	Parameterising the STXS cross-sections . . . . .	170
8.1.2	Selection of effective operators . . . . .	172
8.1.3	Technical setup . . . . .	173
8.2	1D and 2D limits . . . . .	175
8.3	Effect of the STXS split at 400 GeV . . . . .	176
8.4	EFT limits in the analysis eigenspace . . . . .	179
8.5	Miscellaneous considerations . . . . .	182
8.5.1	SMEFT effects on experimental acceptance . . . . .	184
8.5.2	SMEFT effects on background processes . . . . .	184
8.5.3	Validity of the SMEFT . . . . .	185
<b>9</b>	<b>Combination of measurements of Higgs boson decays to heavy-flavour quarks</b>	<b>187</b>
9.1	Combination of resolved and boosted $VH, H \rightarrow b\bar{b}$ . . . . .	187
9.1.1	The resolved $VH, H \rightarrow b\bar{b}$ analysis . . . . .	189
9.1.2	The modifications to the input analyses and the combination strategy . . . . .	191
9.1.3	Statistical treatment and inference . . . . .	191

9.1.4	$VZ$ cross-check measurement . . . . .	196
9.1.5	Measurement results . . . . .	196
9.1.6	Constraints on effective interactions . . . . .	204
9.1.7	Inclusion in the ATLAS-wide combination of Higgs boson measurements . . . . .	211
9.2	Combination of $VH, H \rightarrow b\bar{b}$ and $VH, H \rightarrow c\bar{c}$ . . . . .	214
9.2.1	The $VH, H \rightarrow c\bar{c}$ analysis . . . . .	214
9.2.2	The signal cross-contamination . . . . .	216
9.2.3	The combination procedure . . . . .	219
9.2.4	Results and interpretation . . . . .	219
9.2.5	Inclusion in the ATLAS-wide combination of Higgs boson measurements . . . . .	222
<b>10</b>	<b>Conclusion and outlook</b>	<b>227</b>
	<b>Summary</b>	<b>231</b>
	<b>Samenvatting</b>	<b>239</b>
	<b>Bibliography</b>	<b>246</b>
<b>A</b>	<b>Supplementary information to the SMEFT interpretation</b>	<b>269</b>
	<b>Acknowledgements</b>	<b>271</b>

# 1 Introduction

The Standard Model of Particle Physics (SM) accurately describes the dynamics of the subatomic particles and unifies three out of the four fundamental forces of nature in a common framework. Not only did the SM withstand various experimental tests in the past, it also made precise predictions that were later confirmed by experiments. The discovery of the Higgs boson by the ATLAS [1] and CMS [2] collaborations at the Large Hadron Collider (LHC) in 2012 marked the most recent milestone in the road of success of this theory.

Yet, both theoretical considerations and experimental observations suggest that the SM is merely an approximation to a more fundamental theory of nature. Finding this theory is the goal of high energy physics. In the absence of any direct discoveries of new matter particles or new force carriers, a detailed test of the SM predictions is one of the most important tasks for experimental particle physics.

The Higgs boson is a prime candidate to test the predictions of the SM. It sits at the heart of the theory and is connected to 15 out of the 19 free parameters. At the same time, the Higgs boson is deeply connected to the underlying theoretical issues with the SM and many attempts to extend the SM in order to explain observations like dark matter result in significant changes of the Higgs boson's properties with respect to the SM predictions [3]. For this reason, a precise determination of all of the Higgs boson's properties is indispensable and might prove to be a portal to the discovery of new physics.

While the coupling strengths of the Higgs boson to the other elementary particles are uniquely predicted by the SM, only a subset of them has experimentally been observed to date. In particular, it is not known if the Higgs boson couples to fermions of the second and first generation. The Higgs boson couplings to fermions of the third generation have been shown to agree with the predictions of the SM within relative uncertainties of about 20% [4]. Similarly, the couplings to vector bosons are measured in agreement with the SM within relative uncertainties of about 10% [4].

In addition to the measurements of inclusive coupling strengths, the study of differential quantities such as the transverse momentum distribution of the Higgs boson,  $d\sigma/dp_T^H$ , is of interest. Even if the collision energy of the LHC is too low to directly probe new physics, modifications to the SM can manifest themselves

as more or less subtle deviations at high  $p_T^H$ . Due to the low cross-section in this extreme phase space, even relatively large deviations would not conflict with the existing inclusive coupling measurements.

Experimentally, the only collider with sufficient luminosity and high enough centre-of-mass energy  $\sqrt{s}$  to produce enough Higgs bosons for these measurements is the LHC, colliding protons on protons at  $\sqrt{s} = 13 \text{ TeV}$ . The large collision data set of  $139 \text{ fb}^{-1}$ , which has been collected by the ATLAS experiment during the second operational run of the LHC, is an unprecedented opportunity to perform measurements in such extreme regions with low cross-sections.

This thesis presents a novel measurement in this interesting phase space at high  $p_T^H$  using Higgs boson production in association with a heavy vector boson. Due to its large branching fraction, the Higgs boson decay into a pair of bottom quarks ( $H \rightarrow b\bar{b}$ ) is targeted and newly developed techniques are applied to reconstruct the decay products of Higgs bosons with such high Lorentz boosts. To provide a consistent differential cross-section measurement over the largest  $p_T$  range possible, the dedicated high- $p_T^H$  analysis is combined with a measurement of  $VH, H \rightarrow b\bar{b}$  at low and intermediate  $p_T^H$ . Finally, the  $VH, H \rightarrow b\bar{b}$  analysis is combined with a direct search for  $H \rightarrow c\bar{c}$  to constrain the ratio of the Higgs boson coupling to  $b$ -quarks and  $c$ -quarks. Since this ratio is independent of assumptions on the total width of the Higgs boson, it provides an important model-independent insight into the structure of the Higgs boson coupling strength to second and third generation quarks.

The  $VH, H \rightarrow b\bar{b}$  measurements are further used to constrain the coupling strengths of potential interactions that originate from new physics scenarios. For this interpretation, a generic expansion of the SM with higher dimensional effective operators, the framework of SM Effective Field Theory (SMEFT), is used. The SMEFT approach allows for the most general parameterisation of deviations from the SM. In particular for this thesis, effective interactions that lead to cross-section modifications with respect to the SM that increase with  $p_T^H$  are constrained from the measurements.

## Outline of the thesis and personal contributions

The research that is presented in this thesis has been conducted within the ATLAS collaboration. For the corresponding chapters, the level of detail reflects my personal contribution to the analyses. My contributions are furthermore summarised in this section. The thesis is structured as follows:

Chapter 2 sets the theoretical foundation of the thesis. The SM and its limitations are briefly introduced, followed by a description of Effective Field Theories and the



phenomenology of proton-proton collisions.

Chapter 3 presents an overview of Higgs boson physics. After stressing the importance of the Higgs boson, its phenomenology is introduced. The chapter closes with the current status of Higgs boson measurements.

Chapter 4 introduces the LHC and the ATLAS experiment.

Chapter 5 describes the algorithms used by the ATLAS collaboration to reconstruct physics objects from the raw detector information. These objects, together with the corresponding calibrations and uncertainties, are distributed centrally within the collaboration. As developer of one of the common analysis frameworks, I was responsible to implement the calibrations and uncertainties for large- $R$  jets.

Chapter 6 presents the principles and algorithms that are used for the identification of jets originating from heavy-flavour quarks, the so-called flavour tagging. Furthermore, a measurement of the  $b$ -tagging efficiency in dense jet-environments is presented. I improved the design of previous measurements in this regime and was the main analyser of the full data set collected during Run 2 of the LHC. To perform the measurement, I developed an analysis framework that is now also used to perform other performance measurements in similar topologies.

Chapter 7 constitutes the main part of the thesis. In this chapter, a novel measurement of Higgs boson production at high transverse momentum in the  $VH, H \rightarrow b\bar{b}$  channel is presented. I made leading contributions in all steps of the analysis, from the development of the analysis strategy and its technical implementation to the measurement and interpretation. I was the principle analyser of the  $WH$  channel and furthermore contributed to all three channels, e.g. through flavour-tagging studies and the modelling of the  $VH$  signal. I performed the statistical inference and the cross-section measurement within the STXS framework. I was editor of the ATLAS-internal documentation of the analysis. The measurement that is presented in this chapter is published in Ref. [5].

In Chapter 8, the  $VH, H \rightarrow b\bar{b}$  measurement at high  $p_T^H$  is interpreted as limits on the coupling strengths of effective SMEFT operators. I developed and performed this first SMEFT interpretation of a  $VH$  measurement using the Warsaw basis, which is published together with the measurement in Ref. [5].

Chapter 9 presents two combinations of measurements that target Higgs boson decays to heavy-flavour quarks. First, the  $VH, H \rightarrow b\bar{b}$  measurement at high  $p_T^H$  is combined with a  $H \rightarrow b\bar{b}$  measurement that targets the low and intermediate  $p_T^H$  regime [6], to provide the most precise  $VH$  differential cross-section measurement to date. I was one of three principle analysers of this combination and coordinated the

analysis team as the ATLAS analysis contact. Additionally, I performed the SMEFT interpretation to benchmark the improvement from the combination in terms of sensitivity to new physics. I was editor of the ATLAS-internal documentation. The results are published in Ref. [7]. For the ATLAS-wide combination of Higgs boson measurements that are shown at the end of this section, I provided support for the integration of the  $H \rightarrow b\bar{b}$  measurements.

The second combination that is presented in this chapter combines the  $H \rightarrow b\bar{b}$  measurement with a direct search for  $H \rightarrow c\bar{c}$  [8] to constrain the ratio of the Higgs boson coupling to  $b$ - and  $c$ -quarks. I implemented the effective Higgs boson coupling interpretation of the  $H \rightarrow c\bar{c}$  search and was the main analyser of the combination with the  $H \rightarrow b\bar{b}$  measurement.

Chapter 10 concludes the thesis and provides an outlook.

## 2 Theoretical foundations

The theoretical framework that forms the foundation of nearly all modern particle physics is referred to as the Standard Model (SM). It has been put together over the course of many decades by an interplay of theoretical predictions on one side and experimental observations on the other side. This chapter provides an overview of the SM in Section 2.1, with a particular focus on the role of the Higgs boson, to form the theoretical basis of the measurements presented in this thesis. Furthermore, the known shortcomings of the SM are discussed in Section 2.2, followed by an introduction to Effective Field Theories in Section 2.3, as a systematic tool to look for deviations from the predictions of the SM. Finally, the phenomenology of proton-proton collisions, such as the ones that are analysed in this work, is introduced in Section 2.4.

### 2.1 The Standard Model of particle physics

The SM is a Lorentz invariant, relativistic quantum field theory. It categorises the known matter particles according to quantum numbers (charges), and predicts the dynamics of their interactions by requiring local gauge invariance with respect to the non-Abelian gauge group

$$\mathrm{SU}(3)_C \times \mathrm{SU}(2)_L \times \mathrm{U}(1)_Y \quad , \quad (2.1)$$

which is explained in more detail later in this section. The section follows to large extent Ref.s [9–11] and, together with the rest of the thesis, makes use of the Einstein summation convention, as well as Lorentz-Heaviside units, where  $\hbar = c = 1$ .

#### 2.1.1 Particles and forces

The particles of the SM are grouped according to their spin into fermions with half-integer spin and bosons with integer spin. A summary of all SM particles is given in Figure 2.1. Fermions, which obey the Pauli exclusion principle, are the matter particles of the SM and have a spin of  $1/2$ . They are grouped further into quarks, which carry the quantum numbers of the strong interaction, and leptons which do not. The bosons can be grouped into the force carrier particles with spin 1 and the Higgs boson with spin 0.

The SM describes three out of the four known fundamental forces on a quantum-

mechanical level: electromagnetism, the strong and the weak nuclear force. On a macroscopic level, gravity is described by Einstein's theory of general relativity. A quantum theory of gravity that works with a positive cosmological constant for all energies up to the Planck scale is yet to be found.

**Fermions** Quarks and leptons exist in three generations or families. The stable matter that we observe around us is entirely built from the charged fermions of the first generation. The fermions of the subsequent two generations differ from the first generation only in their mass, all other quantum numbers are identical. They are unstable, which means they decay into fermions of lower generations after a typical life time, and therefore need to be produced in particle collisions in order to be studied. An exception to this pattern of increasing masses are the neutrinos, which are assumed to be massless in the SM. To each fermion type, there is a corresponding anti-fermion with the same properties, but opposite additive quantum numbers.

**Gauge bosons** Gauge bosons are the mediators of the three forces that are described by the SM. They arise from symmetry requirements, when requiring the equations to be invariant under local, i.e. spacetime-dependent, gauge transformations of the SM symmetry groups. Eight massless gluons couple to colour charge and mediate the interaction between quarks, which carry this quantum number. One photon mediates the electromagnetic force between electrically charged fermions. The weak force is mediated via two charged  $W$  bosons and a neutral  $Z$  boson. The three mediators of the weak force are originally massless but acquire mass via electroweak symmetry breaking (EWSB).

**The Higgs boson** The Higgs boson arises as a consequence of EWSB. It is the only scalar boson of the theory, which means it carries no spin. The Higgs boson is also the only boson which is not connected to the SM symmetry groups but instead arises from the need to generate mass terms without violating local gauge invariance.

**The relation between particles and fields** The SM, being a QFT, uses quantum fields as the fundamental objects to describe reality. Particles emerge as excitations of these quantum fields, that will be introduced in this section. As a direct consequence, all electrons, for example, have identical properties, because they all are excitations of the same underlying electron field.

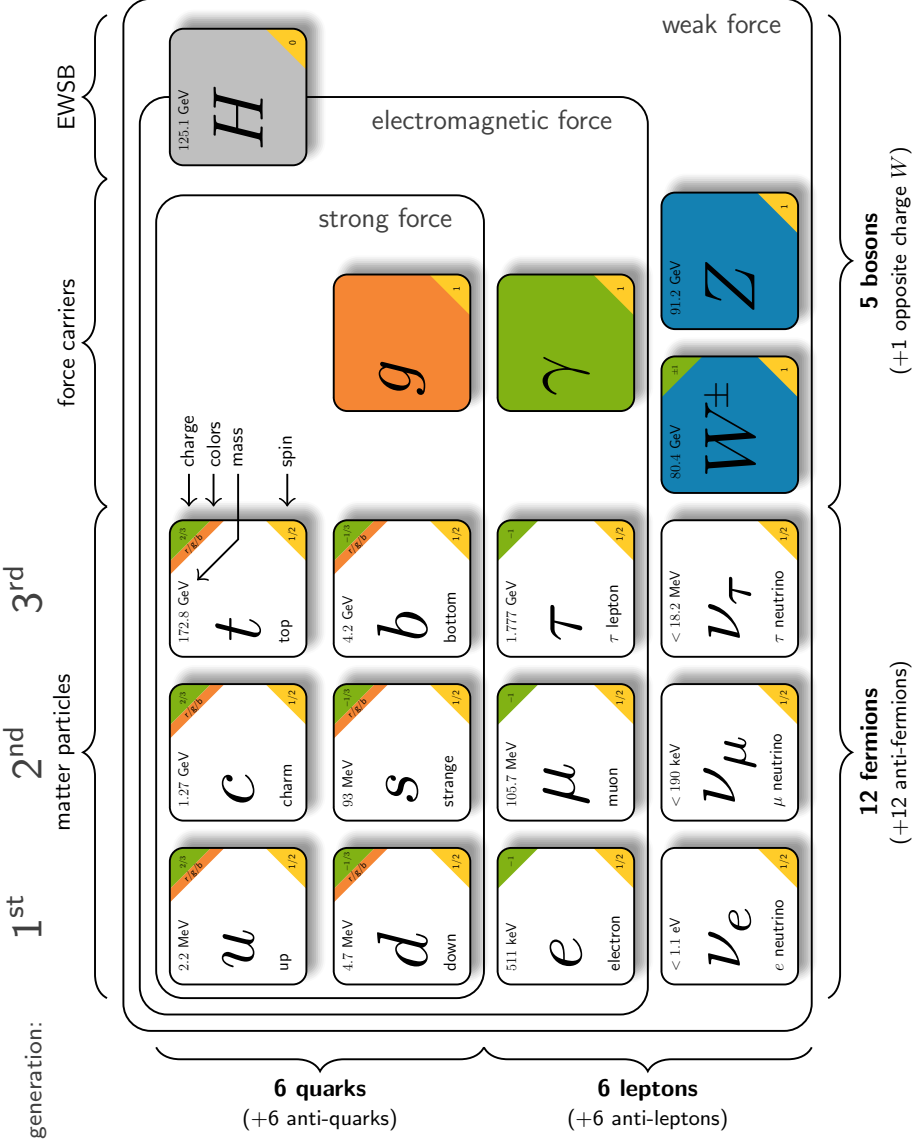


Figure 2.1: Overview of the SM particle content, divided into matter particles and force carriers. Adapted from Ref. [12]. Values taken from Ref. [13].

### 2.1.2 Quantum electrodynamics

Quantum electrodynamics (QED) is the quantum theory that describes electromagnetic interactions. It incorporates Maxwell's equations in a 'kinematic term', and additionally features a 'Dirac term' to describe the equations of motion of free fermions. Consequentially, the Lagrangian of QED reads

$$\mathcal{L}_{\text{QED}} = \mathcal{L}_{\text{Dirac}} + \mathcal{L}_{\text{kin.}} = \sum_f \bar{\psi}_f (i\gamma_\mu D^\mu - m_f) \psi_f - \frac{1}{4} F_{\mu\nu} F^{\mu\nu} \quad , \quad (2.2)$$

where the sum  $f$  runs over all electrically charged fermions with mass  $m_f$ ,  $\psi_f$  denotes their Dirac spinor,  $D_\mu = \partial_\mu + ieA_\mu$  is the covariant derivative and  $F_{\mu\nu} = \partial_\mu A_\nu - \partial_\nu A_\mu$  is the field strength tensor of electrodynamics, where  $A_\mu$  denotes the photon field. Under local  $U(1)_{\text{QED}}$  phase transformations, the photon field behaves as  $A_\mu \rightarrow A_\mu - 1/e \partial_\mu \alpha$ , where  $\alpha$  is the (space-time dependent) phase. The Lagrangian is constructed to be invariant under local gauge transformations of the  $U(1)_{\text{QED}}$  group, with the electric charge as the associated quantum number. The  $U(1)_{\text{QED}}$  symmetry is not initially part of the  $SU(3)_C \times SU(2)_L \times U(1)_Y$  symmetry of the SM. Instead, during EWSB the  $SU(2)_L \times U(1)_Y$  symmetry gets broken into the  $U(1)_{\text{QED}}$  subgroup.

### 2.1.3 Quantum chromodynamics

The theory of strong interactions, quantum chromodynamics (QCD) [14–16], describes the interactions between quarks and gluons and is therefore of particular relevance for the phenomenology at hadron colliders. Quarks carry a quantum number called colour charge and each quark flavour can carry either a red (r), a green (g) or a blue (b) charge. Anti-quarks consequently carry anti-colours and any bound state of quarks is required to be colour neutral, which is achieved by either combining a colour and the corresponding anti-colour or an equal amount of r, g and b. Due to the nature of the strong interaction, quarks hadronise and are therefore only observed confined in colourless bound states.

QCD is a non-Abelian gauge theory with the gauge group  $SU(3)_C$ , whose 8 generators are the Gell-Mann matrices  $\lambda^a$ . The fermion spinors are triplets under  $SU(3)_C$ . The QCD Lagrangian is given by a Dirac- and a kinematic term as

$$\mathcal{L}_{\text{QCD}} = \sum_f \bar{\psi}_f (i\gamma_\mu D^\mu - m_f) \psi_f - \frac{1}{4} G_{\mu\nu}^a G_a^{\mu\nu} \quad . \quad (2.3)$$

The sum  $f$  includes all quark fields and  $\psi_f$  indicates a spinor triplet. The covariant derivative  $D_\mu$  is given by

$$D_\mu = \partial_\mu + ig_s \frac{\lambda^a}{2} G_\mu^a \quad , \quad (2.4)$$

where  $g_s$  is the  $SU(3)_C$  coupling constant and  $G_\mu^a$  are the eight gluon fields. The

field strength tensors  $G_{\mu\nu}^a$  are given as

$$G_{\mu\nu}^a = \partial_\mu G_\nu^a - \partial_\nu G_\mu^a - g_s f^{abc} G_\mu^b G_\nu^c, \quad (2.5)$$

where  $f^{abc}$  are the  $SU(3)_C$  structure constants. The non-Abelian nature of  $SU(3)_C$ , i.e. the non-zero values of  $f^{abc}$  lead to triple or quartic self-interactions between gluons. In contrast to QED, the gluons carry themselves a combination of colour and anti-colour, which explains why they can interact with each other.

### 2.1.4 Electroweak unification

Weak interactions, which are observed e.g. in radioactive  $\beta$  decay, are described jointly with the electromagnetic interactions within the Glashow-Salam-Weinberg (GSW) model [17–19]. This model describes interactions by requiring local gauge-invariance under the symmetry group

$$SU(2)_L \times U(1)_Y. \quad (2.6)$$

Experimentally, it was observed that weak interactions, that change the fermion charge, show a V-A structure, which means they only couple to left-handed fermions. Therefore, the fields of the interacting particles are split into their left- and right-handed projections using the projection operators

$$\psi = P_L \psi + P_R \psi = \frac{1 - \gamma^5}{2} \psi + \frac{1 + \gamma^5}{2} \psi = \psi_L + \psi_R. \quad (2.7)$$

The charge associated with weak interactions is the weak isospin  $I$ . Its component along an arbitrary third axis  $I_3$  is conserved in weak interactions. Left-handed fields transform as doublets with  $I_3 = \pm 1/2$  under  $SU(2)_L$ , whereas right-handed fields are singlets with  $I_3 = 0$ .

To incorporate the electromagnetic interactions, the group  $U(1)_Y$  is added. Its generator, the hypercharge  $Y$ , however, cannot be directly associated with the electromagnetic charge. The generators of  $U(1)_{\text{QED}}$  and  $U(1)_Y$  are related via the Gell-Mann-Nishijima relation

$$Q = I_3 + \frac{Y}{2}. \quad (2.8)$$

During EWSB, the  $SU(2)_L \times U(1)_Y$  group is spontaneously broken into  $U(1)_{\text{QED}}$ .

Two electrically charged and one neutral  $W_\mu$  field are introduced to ensure local gauge invariance of the weak Dirac terms under  $SU(2)_L$  transformations. Their coupling to particles with weak isospin is parameterised with a coupling strength  $g$ . Similarly, one  $B_\mu$  field is associated to the  $U(1)_Y$  group and its coupling to hypercharged particles is parameterised with a coupling strength  $g'$ . As both the  $W_\mu^3$  field and the  $B_\mu$  field carry the same quantum numbers, quantum mechanical mixing between them occurs. The degree of mixing into the physically observable

$Z$  boson and photon fields is parameterised via the weak mixing angle  $\theta_W$ . Since  $SU(2)_L \times U(1)_Y$  is non-Abelian, similarly to QCD, triple and quartic self-couplings of the gauge bosons arise.

## 2.1.5 Particle masses and the Higgs boson

The introduction of mass terms to the SM Lagrangian violates local gauge invariance, both for the fermion masses and for the masses of the  $W$ - and  $Z$  boson. In the 1960s, P. Higgs [20, 21], R. Brout and F. Englert [22], as well as T. Kibble, C. Hagan and G. Guralnik [23, 24], realised that a mechanism that was known from solid state physics could be used to dynamically generate the needed mass terms for the heavy vector bosons, while at the same time preserving local gauge invariance. This mechanism, applied to the SM, is known as electroweak symmetry breaking (EWSB) or the Brout-Englert-Higgs (BEH) mechanism.

### 2.1.5.1 The BEH mechanism

The SM Lagrangian is extended by

$$\mathcal{L}_{\text{Higgs}} = (D_\mu \phi)^\dagger (D^\mu \phi) - V(\phi) = (D_\mu \phi)^\dagger (D^\mu \phi) - \mu^2 (\phi^\dagger \phi) - \lambda (\phi^\dagger \phi)^2 \quad , \quad (2.9)$$

where  $\phi$  is a  $SU(2)_L$  doublet of complex scalar fields with hypercharge  $Y = 1$ :

$$\phi = \begin{pmatrix} \phi^+ \\ \phi^0 \end{pmatrix} = \frac{1}{\sqrt{2}} \begin{pmatrix} \phi_1 + i\phi_2 \\ \phi_3 + i\phi_4 \end{pmatrix} \quad . \quad (2.10)$$

The potential  $V(\phi)$  has two free parameters,  $\mu$  and  $\lambda$ , that are chosen such that  $\mu^2 < 0$  and  $\lambda > 0$ , which yields the Mexican-hat shaped potential that is displayed in Figure 2.2. The minimum of  $V(\phi)$  is at non-zero values of  $\phi$  that fulfil

$$\phi^\dagger \phi = \frac{1}{2} (\phi_1^2 + \phi_2^2 + \phi_3^2 + \phi_4^2) = -\frac{\mu^2}{\lambda} \quad . \quad (2.11)$$

Without loss of generality, the field is assumed to be in the minimum at  $\phi_1 = \phi_2 = \phi_4 = 0$  and  $\phi_3 = v$ , where  $v = \sqrt{-2\mu^2/\lambda}$  is the vacuum expectation value of the Higgs field. An expansion of the field for small deviations  $\{H, \theta_1, \theta_2, \theta_3\}$  around this minimum yields

$$\phi(x) = \frac{1}{\sqrt{2}} \begin{pmatrix} \theta_1(x) + i\theta_2(x) \\ v + H(x) + i\theta_4(x) \end{pmatrix} \approx \frac{1}{\sqrt{2}} \begin{pmatrix} 0 \\ v + H(x) \end{pmatrix} e^{i\frac{\sigma^j}{2} \frac{\theta_j(x)}{v}} \quad . \quad (2.12)$$

In the last step, the Goldstone fields  $\theta_j$  are absorbed into an overall phase factor, that can be gauged away by choosing the transformation behaviour of the vector



fields appropriately. Inserting the expression back into the Higgs Lagrangian yields

$$\begin{aligned} \mathcal{L}_{\text{Higgs}} = & \frac{1}{2}(\partial_\mu H)(\partial^\mu H) + \frac{g^2}{4}(v + H)^2 W_\mu^+ W^{-\mu} + \frac{1}{8} \frac{g^2}{\cos(\theta_W)^2} (v + H)^2 Z_\mu Z^\mu \\ & + 0 A_\mu A^\mu + \frac{\mu^2}{2}(v + H)^2 - \frac{\lambda}{4}(v + H)^4 \quad . \end{aligned} \quad (2.13)$$

Through the transition into the minimum at  $\phi \neq 0$ , mass terms for the physical fields  $W_\mu^\pm$ ,  $Z_\mu$ , as well as for the newly introduced expansion  $H$ , are generated. The physical fields  $W_\mu^\pm$ ,  $Z_\mu$ , together with the photon field  $A_\mu$ , are obtained from the fundamental fields via

$$\begin{aligned} W_\mu^\pm &= \frac{1}{\sqrt{2}}(W_\mu^1 \mp iW_\mu^2) \quad , \text{ and} \\ \begin{pmatrix} Z_\mu \\ A_\mu \end{pmatrix} &= \begin{pmatrix} \cos(\theta_W) & -\sin(\theta_W) \\ \sin(\theta_W) & \cos(\theta_W) \end{pmatrix} \begin{pmatrix} W_\mu^3 \\ B_\mu \end{pmatrix} \quad . \end{aligned} \quad (2.14)$$

The masses of  $W^\pm$ ,  $Z$ ,  $\gamma$  and  $H$  are given as

$$m_W = \frac{vg}{2}, \quad m_Z = \frac{m_W}{\cos(\theta_W)}, \quad m_\gamma = 0, \quad m_H = \sqrt{-2\mu^2}. \quad (2.15)$$

The excitation of the physical Higgs field  $H$  is called the Higgs boson and has a mass that depends on  $\mu$ . The BEH mechanism has two free parameters  $\mu$  and  $\lambda$ , that define the Higgs potential. These two degrees of freedom are conventionally re-expressed as the Higgs boson mass  $m_H$  and the vacuum expectation value  $v$ , which both need to be determined from experiment.

The electroweak SM Lagrangian at  $\phi = 0$  is invariant under  $\text{SU}(2)_L \times \text{U}(1)_Y$ , but when the Higgs field acquires a non-zero vacuum expectation value, this symmetry gets broken and the mass terms for the heavy vector bosons are generated. The vacuum expectation value  $\phi_0 = 1/\sqrt{2} (0, v)^T$  is chosen to be electrically neutral ( $Q = 0$ ), which leaves the  $\text{U}(1)_{\text{QED}}$  symmetry unbroken and therefore the photon remains massless.

### 2.1.5.2 Fermion masses

The complex doublet field  $\phi$ , that is introduced in the BEH mechanism, is used together with its charge conjugation  $\phi^C$  to generate mass terms of the form

$$\bar{\psi} m \psi = m(\bar{\psi}_L \psi_R + \bar{\psi}_R \psi_L) \quad (2.16)$$

for the fermions. After EWSB, these fields take the form

$$\phi(x) = \frac{1}{\sqrt{2}} \begin{pmatrix} 0 \\ v + H(x) \end{pmatrix}, \quad \phi^C(x) = \frac{1}{\sqrt{2}} \begin{pmatrix} v + H(x) \\ 0 \end{pmatrix} \quad . \quad (2.17)$$

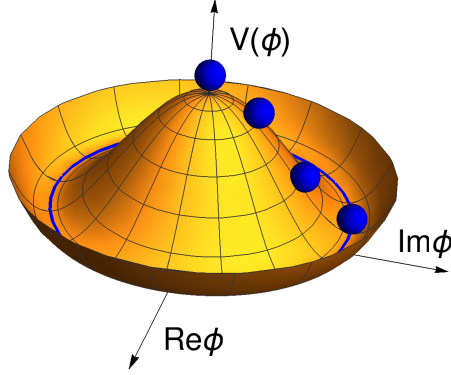


Figure 2.2: Illustration of the Higgs potential  $V(\phi)$  as a function of the real and imaginary parts of a complex singlet field  $\phi$ . A blue line indicates the minimum of the potential.

An additional Yukawa term is added to the SM Lagrangian, in which the fermion fields are coupled to  $\phi$  and  $\phi^C$  like

$$\mathcal{L}_{\text{Yukawa}} = - \underbrace{\sum_i Y_1^i \bar{L}^i \phi \ell_R^i}_{\text{leptons}} - \underbrace{\sum_{i,j} \left( Y_u^{ij} \bar{Q}^i \phi u_R^j + Y_d^{ij} \bar{Q}^i \phi^C d_R^j \right)}_{\text{quarks}} + \text{h.c.} \quad . \quad (2.18)$$

The sums over  $i$  and  $j$  include all lepton and quark fields. The upper case  $L$  and  $Q$  denote the left-handed lepton and quark doublets, whereas the lowercase  $\ell$ ,  $u$  and  $d$  denote the right-handed charge leptons, up-type and down-type quarks. The coupling constants  $Y_1^i$ ,  $Y_u^{ij}$  and  $Y_d^{ij}$  to the fermions are referred to as Yukawa couplings and are free parameters of the theory.  $Y_u^{ij}$  and  $Y_d^{ij}$  are  $3 \times 3$  matrices whose off-diagonal elements allow for a mismatch between the weak eigenstates and the mass eigenstates of quarks and consequentially lead to quark mixing across generations. These matrices can be diagonalised via unitary transformations to obtain the Yukawa couplings with respect to the physically observable mass eigenstates of the fermions. The Cabibbo-Kobayashi-Maskawa (CKM) [25, 26] matrix is built from these unitary transformations and describes the quark mixing empirically. This complex unitary matrix is conventionally parameterised with 3 mixing angles and one CP violating phase.

Finally, the (diagonalised) Yukawa coupling strengths  $y_f$  are related to the fermion

masses via

$$y_f = \sqrt{2} \frac{m_f}{v} \quad . \quad (2.19)$$

This mechanism removes the need to introduce the Fermion masses ad-hoc into the Lagrangian, which would violate local gauge invariance.

## 2.1.6 The full SM Lagrangian

The full SM Lagrangian before EWSB is written as

$$\begin{aligned} \mathcal{L}_{\text{SM}} = & \mathcal{L}_{\text{QCD}} + \mathcal{L}_{\text{EW}} + \mathcal{L}_{\text{Higgs}} + \mathcal{L}_{\text{Yukawa}} \\ \sim & -\frac{1}{4} W_{\mu\nu}^j W_j^{\mu\nu} - \frac{1}{4} B_{\mu\nu} B^{\mu\nu} - \frac{1}{4} G_{\mu\nu}^a G_a^{\mu\nu} \\ & + \sum_f i \bar{\psi}_f \gamma^\mu D_\mu \psi_f \\ & + (D_\mu \phi)^\dagger (D^\mu \phi) - \mu^2 (\phi^\dagger \phi) - \lambda (\phi^\dagger \phi)^2 \\ & - \sum_i Y_1^i \bar{L}^i \phi \ell_R^i - \sum_{i,j} \left( Y_u^{ij} \bar{Q}^i \phi u_R^j + Y_d^{ij} \bar{Q}^i \phi^C d_R^j \right) + \text{h.c.} \end{aligned} \quad (2.20)$$

The field strength tensors are defined as:

$$\begin{aligned} W_{\mu\nu}^j &= \partial_\mu W_\nu^j - \partial_\nu W_\mu^j - g \epsilon^{jkl} W_\mu^k W_\nu^l \quad , \text{ with } \quad j, k, l \in \{1, 2, 3\}, \\ B_{\mu\nu} &= \partial_\mu B_\nu - \partial_\nu B_\mu \quad , \text{ and } \\ G_{\mu\nu}^a &= \partial_\mu G_\nu^a - \partial_\nu G_\mu^a - g_s f^{abc} G_\mu^b G_\nu^c \quad , \text{ with } \quad a, b, c \in \{1, \dots, 8\}. \end{aligned} \quad (2.21)$$

The terms involving  $\epsilon^{jkl}$  and  $f^{abc}$  contain implicit sums over similar indices, where  $\epsilon$  and  $f$  are the structure constants of  $\text{SU}(2)_L$  and  $\text{U}(1)_Y$ , respectively. The sum over  $f$  in the Dirac term contains all fermion spinors  $\psi_f \in \{Q, L, u_R, d_R, \ell_R\}$ . The covariant derivative  $D_\mu$  takes the form

$$D_\mu = \partial_\mu + ig I_W^j W_\mu^j + ig' \frac{Y}{2} B_\mu + ig_s T_C^a G_\mu^a \quad . \quad (2.22)$$

The term  $I_W^j$  denotes the generators of  $\text{SU}(2)_L$ , i.e. the Pauli matrices  $\sigma_j/2$ , for weak isospin doublets and is 0 for the singlets. Similarly,  $T_C^a = \lambda^a/2$  for the  $\text{SU}(3)_C$  triplets and  $T_C^a = 0$  for the singlets. A summary of the SM fields, their quantum numbers and their associated physical particles, i.e. the quarks, leptons, gauge bosons and the Higgs boson, is given in Table 2.1.

## 2.1.7 Renormalisation and constraints on the particle content

It is generally not possible to find exact solutions for the SM equations of motions that include interactions. Instead, such calculations are performed within the

framework of perturbation theory, making use of Feynman diagrams.

At leading order (LO) in perturbation theory, the SM gives finite predictions. At higher orders, however, predictions for physical observables diverge. These infinities can be regularised, which makes the predictions of the theory again finite, but at the same time dependent on an arbitrary scale parameter. In a procedure called renormalisation, this is bypassed by re-expressing the bare quantities of the theory, such as couplings and masses, in terms of measured finite quantities at an arbitrary renormalisation scale  $\mu_R$ . The renormalised couplings and masses are now considered to be running, which means they change their value as  $\mu_R$  changes. Including all perturbative orders in the calculation would exactly cancel this  $\mu_R$  dependence, however, a truncated series would retain some dependence on the unphysical parameter  $\mu_R$ . The more orders are included in the calculation, the smaller this  $\mu_R$  dependence becomes.

The SM is shown to be a renormalisable theory [27, 28], but the requirement of renormalisability imposes conditions on the matter content for which the SM describes the dynamics. To be free of anomalies that spoil renormalisability, the number of lepton doublets needs to be equal to the number of quark doublets [29].

The determination of the invisible partial decay width of the  $Z$  boson at the LEP collider constrained the number of light neutrino generations with  $m_\nu < m_Z/2$  to be exactly three [30, 31]. Together with the anomaly cancellation requirements, this rules out a fourth generation, unless a fourth generation neutrino does not couple to the  $Z$  boson or has a mass that is more than half that of the  $Z$  boson. Measurements of the Higgs cross-sections at the LHC pose severe constraints on heavy particles of a fourth generation that would couple to the SM Higgs boson.

### 2.1.8 Free parameters of the SM

The SM relies on a total of 19 parameters, that have to be experimentally determined and can not be calculated from first principles. One possible representation of the 19 parameters is:

- The 3 coupling constants of  $SU(3)_C$ ,  $SU(2)_L$  and  $U(1)_Y$ :  $g_s$ ,  $g$  and  $g'$
- 9 Yukawa couplings of the Higgs boson to the fermion mass eigenstates
- 3 mixing angles and 1 CP violating phase of the CKM matrix
- The 2 free parameters of the Higgs potential  $\mu$  and  $\lambda$
- The QCD vacuum angle  $\theta_{\text{QCD}}$

There is no unique basis of input parameters, however, and often, e.g. instead of the 9 Yukawa couplings, the masses of the fermions are used to express the results of calculations, as they are experimentally better measured. Similarly, the three coupling constants can be re-expressed as the  $U(1)_{\text{QED}}$  coupling  $e = g \sin(\theta)$ , the fine structure constant  $\alpha = e^2/(4\pi)$  and  $\alpha_s = g_s^2/(4\pi)$ . Instead of the two Higgs parameters of the Higgs potential, the Higgs boson mass and the vacuum expectation value of the ground state of the Higgs field can be used.

Spin	Field	1 <sup>st</sup>	2 <sup>nd</sup>	3 <sup>rd</sup>	SU(3) <sub>C</sub> rep.	SU(2) <sub>L</sub> $I_3$	U(1) <sub>Y</sub> $Y$	$Q$
Fermions	Quarks	$Q$	$\begin{pmatrix} u \\ d \end{pmatrix}_L$	$\begin{pmatrix} c \\ s \end{pmatrix}_L$	$\begin{pmatrix} t \\ b \end{pmatrix}_L$	$+1/2$	$+1/3$	$+2/3$
		$u_R$	$u_R$	$c_R$	$t_R$	$-1/2$	$+1/3$	$-1/3$
		$d_R$	$d_R$	$s_R$	$b_R$	$0$	$+4/3$	$+2/3$
	Leptons	$L$	$\begin{pmatrix} \nu_e \\ e \end{pmatrix}_L$	$\begin{pmatrix} \nu_\mu \\ \mu \end{pmatrix}_L$	$\begin{pmatrix} \nu_\tau \\ \tau \end{pmatrix}_L$	$+1/2$	$-1$	$0$
		$\nu_R$	do not exist in the SM			$-1/2$	$-1$	$-1$
		$\ell_R$	$e_R$	$\mu_R$	$\tau_R$	$0$	$-2$	$1$
		$G_\mu^a$	$g$			$8$	$0$	$0$
	Bosons	$W_\mu^1$	$\xrightarrow{\text{EWSB}}$	$W^+$		$+1$	$0$	$+1$
		$W_\mu^2$	$\xrightarrow{\text{EWSB}}$	$W^-$		$-1$	$0$	$-1$
		$W_\mu^3$	$\xrightarrow{\text{EWSB}}$	$Z^0$		$0$	$0$	$0$
		$B_\mu$	$\xrightarrow{\text{EWSB}}$	$\gamma$		$0$	$0$	$0$
0	Higgs	$\begin{pmatrix} \phi^+ \\ \phi^0 \end{pmatrix}$	$\xrightarrow{\text{EWSB}}$	$H$		$+1/2$	$+1$	$+1$
					$1$	$-1/2$	$+1$	$0$

Table 2.1: Summary of the SM fields and associated particles. The column with the 'SU(3)<sub>C</sub> rep.' indicates the QCD symmetry representations, i.e. singlet (1), triplet (3) or octet (8).  $I_3$  denotes the third component of the weak isospin,  $Y$  the hypercharge and  $Q$  the electrical charge.

## 2.2 Breaking the Standard Model

The SM is an incredibly successful theory. Not only allows it to calculate the behaviour of subatomic particles to unprecedented precision, during development of the SM, precise predictions about the particle content could be made, that were later experimentally verified.

Examples of such predictions include the weak neutral current, which was observed in 1973 with the Gargamelle bubble chamber at CERN [32] and the subsequent discovery of the  $W$  and  $Z$  bosons with the UA1 and UA2 experiments at mass values inside of the predicted ranges [33]. More recently, the top quark discovery in 1995 [34, 35], the observation of the  $\tau$ -neutrino [36] and ultimately the discovery of the Higgs boson in 2012 [1, 2] conclude this successful synergy between theory and experiment.

Nevertheless, the SM has substantial shortcomings that suggest that it is not the final theory of nature. These shortcomings can be grouped into theoretical issues with the SM itself and into observations that the SM is not able to explain. Examples for arguments that belong to the two categories are given in this section.

### 2.2.1 Theoretical issues

**The Higgs boson** The SM does not provide an explanation for the shape of the Higgs potential. Any even polynomial in  $(\phi^\dagger\phi)$  fulfils the symmetry requirements. The value of  $\mu$  is arbitrary and the value of  $\lambda$  is only restricted to be  $> 0$  by requirements on the stability of the vacuum. The Higgs boson is the only scalar of the theory and a singlet under all gauge symmetries. Therefore, its mass gets corrections from closed fermion loops like  $\Delta m_H \propto m_f^2$ , which would break the notion of separation of scales if the Higgs boson couples to heavy BSM fermions. The separation of scales refers to the principle that the physics at a given energy scale should not depend on the detailed structure of phenomena that become important only at much higher energies.

**Quantum theory of gravity** The SM does not provide a UV complete description for gravitation at the quantum level. The space-time structure of the macroscopic theory of general relativity suggests that its force carrier, the graviton, must be a spin 2 particle. However, attempts to quantise the theory lead to issues with renormalisability since an infinite number of counterterms would be needed to renormalise the theory to all orders. Practically, this issue only becomes relevant at very high energies. Below the Planck scale, general relativity works as an effective theory and for particle collisions at the currently available energies gravity can even safely be neglected, due to the weakness of the force. Only at energies near the Planck scale, gravity becomes important and breaks the predictions of the SM.

**Charge quantisation** The SM does not provide an explanation why electric charge only appears in multiples of  $1/3$ . Anomaly cancellation poses a requirement on the total summed charge of all fermions to be 0, but not on the individual values.

**Origin of the SM flavour structure** The SM provides no explanation for its fermion structure. No reason for the three generations is given, the vastly different fermion masses are unexplained, as are the CKM quark mixing angles and the CP violating phase.

**The strong CP problem** It is possible to add a term to the QCD part of the SM Lagrangian that reads

$$\mathcal{L}_\theta = \frac{\theta_{\text{QCD}} g^2}{2 \cdot 32\pi^2} \epsilon^{\mu\nu\alpha\beta} G_{\alpha\beta,a} G_{\mu\nu}^a, \quad (2.23)$$

where  $\epsilon^{\mu\nu\alpha\beta}$  is the totally antisymmetric tensor of rank 4. This  $\theta$  term is usually added to the SM to explain the high mass of the  $\eta$  meson [37] and receives contributions from the QCD vacuum and potential CP-violating terms in the Yukawa couplings. The  $\theta$  term leads to an electric dipole moment of the neutron that is dependent on the value of the angle  $\theta$ , which is theoretically not constrained. Experimentally,  $\theta$  is constrained to be smaller than  $\mathcal{O}(10^{-10})$ , which renders this parameter to be fine-tuned. Although a solution to the strong CP problem exists in the form of the Peccei-Quinn theory [38], the Axion particle, that is predicted by this theory, has not been observed to date.

## 2.2.2 Inexplicable observations

**Neutrino masses** Right handed neutrinos are not part of the SM, it therefore has no mechanism to generate neutrino masses. It is known from oscillation experiments, however, that neutrinos do have small masses [39–41]. Direct measurements constrain the absolute mass scale of neutrinos to be  $< 1.1 \text{ eV}$  at 90% CL [42]. Mass terms for neutrinos can be added if the SM is treated as an effective field theory. However, since it is not clear whether neutrinos are Majorana or Dirac particles, it is not clear which type of terms to add.

**Dark matter** About 85% of the matter content of the universe that is subject to gravitation is made out of dark matter [43]. So far, dark matter has only been observed via its gravitational impact. The SM does not contain any viable dark matter candidate.

**Dark energy** Cosmological observations suggest that the acceleration of the universe is expanding [44, 45]. The measured energy density causing the expansion is many orders of magnitude smaller than what back-of-the-envelope calculations from

SM vacuum fluctuations would suggest. The SM does not provide an explanation of what causes this small value [46].

**Matter-antimatter asymmetry** The amount of CP violation that is present in the SM is unlikely to explain the observed matter-antimatter asymmetry in the universe [47].

## 2.3 Effective Field Theories

Many UV complete theories have been constructed over the years to solve the shortcomings of the SM. With no direct evidence for new physics in the form of a resonance observed at colliders, many of these theories cannot be judged against each other because they all contain the SM as a low energy limit, due to the decoupling theorem [48].

The fundamental statement of the decoupling theorem is that physics at some energy scale  $E_0$  does not depend on the microscopic structures of some (more complete) theory at scales  $E_1 \gg E_0$ . To make calculations at  $E_0$ , it is therefore sufficient to use an effective field theory (EFT) that does not contain all the degrees of freedom of the full theory. The most prominent example in particle physics is the Fermi theory of the weak interaction, where instead of considering a  $W$ -boson propagator, charged current weak interactions are modelled via effective four-fermion vertices with a coupling strength that is proportional to the Fermi constant  $G_F$ . This approach works well at energies much below  $m_W$ .

EFTs are tools that make use of existing hierarchies to determine the necessary features to describe a system at a given scale and identify the pieces that can be neglected, because they are irrelevant at this particular scale. In this thesis, the hierarchy that is used will be the energy scale of the scatter processes that are studied.

There are two approaches to EFTs:

1. **Top-down:** Starting from a known theory at high energies, an effective theory at low energies is constructed by integrating out the heavy degrees of freedom.
2. **Bottom-up:** Starting from a known theory at low energies, an EFT expansion allows to systematically classify all possible effects from nearly decoupled theories without any a priori assumption on their actual structure.

Given the current experimental situation at the LHC, i.e. the fact that no particles outside of the SM have been observed, the bottom-up approach is used in this thesis to interpret experimental data.



### 2.3.1 The Standard Model EFT

Assuming that new physics at a scale  $\Lambda$  well above the electroweak scale is nearly decoupled, and that at the energy scale  $E \ll \Lambda$  that is currently accessible by the LHC, only the SM fields and symmetries contribute, the SM Lagrangian can be augmented by an expansion in dimensions of  $(v, E)/\Lambda$ :

$$\mathcal{L}_{\text{SMEFT}} = \mathcal{L}_{\text{SM}} + \sum_i \frac{c_i^{(5)}}{\Lambda} \mathcal{Q}_i^{(5)} + \sum_i \frac{c_i^{(6)}}{\Lambda^2} \mathcal{Q}_i^{(6)} + \sum_i \frac{c_i^{(7)}}{\Lambda^3} \mathcal{Q}_i^{(7)} + \sum_i \frac{c_i^{(8)}}{\Lambda^4} \mathcal{Q}_i^{(8)} + \dots \quad (2.24)$$

$\mathcal{L}_{\text{SM}}$  is the SM Lagrangian, which has a mass dimension of 4. The effective operators  $\mathcal{Q}_i^{\text{dim}=d}$  are built from the SM fields, including the Higgs field, and required to be invariant under local gauge transformations of the SM symmetry group. This approach is therefore also referred to as SMEFT. To make the overall Lagrangian have mass dimension 4, the higher dimensional operators are suppressed by  $d - 4$  powers of  $\Lambda$ . The Wilson coefficients  $c_i^{(d)}$  are the effective coupling strengths corresponding to each operator. Since both  $c_i$  and  $\Lambda$  are a priori unknown, the Wilson coefficients  $c_i$  have to be determined from experimental data for a specific choice of  $\Lambda$ . A matching with a UV-complete theory later allows to identify the measurement of  $c_i$  for an arbitrary choice of scale  $\Lambda$  with the coupling strength and mass scale of the theory.

### 2.3.2 Operator bases

The augmented SM Lagrangian of Equation 2.24 can be used to calculate the effect that the effective operators have on a given process. The power of this bottom-up SMEFT approach lies in the fact that this expansion is able to account for all possible effects from any theory at higher energy, without having to know exactly how the theory looks like, other than that it reduces to the SM at low energies. The set of operators is furthermore overcomplete, which means, that the effect of some operators can be expressed as a linear combination of the effects of other operators.

Via the equations of motion and integration by parts, the number of operators can be reduced to a minimal set, that still allows for the most general description of all potential BSM effects. This set is referred to as an operator basis. Since there is no unique choice of basis, the basis which is best suited for an interpretation of experimental data depends on the type of measurement that is performed. Also, the interpretation of a measurement in terms of anomalous couplings is strongly basis dependent. However, the physics that is described by the various bases is basis independent, and tools exist to transform one basis into another [49].

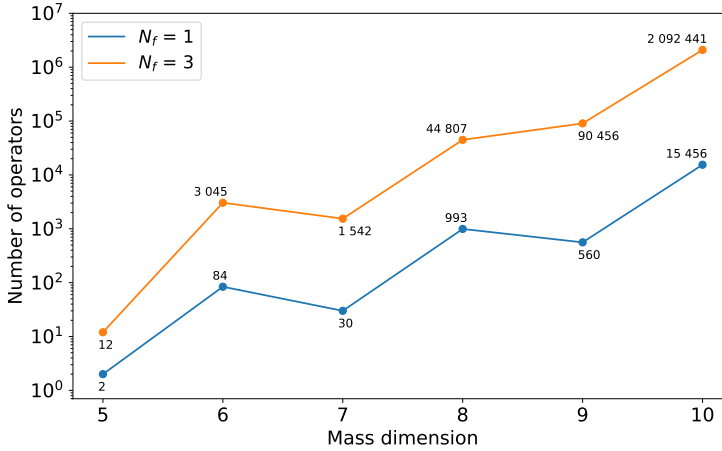


Figure 2.3: Number of operators in the SMEFT for a given mass dimension assuming one (blue line) or three (orange line) generations of fermions. Values taken from Ref. [50].

### 2.3.3 Operator selection

The minimal number of operators increases drastically when the mass dimension that is considered in the EFT expansion increases. This is shown in Figure 2.3 and poses a technical difficulty if all terms needed to be considered. Fortunately, since these operators are suppressed by increasing powers of  $\Lambda$ , the general size of their effect at a fixed energy scale becomes smaller the higher the considered mass dimension.

It is important to note that different operator-types do not necessarily have to be generated from the same BSM mechanism and can therefore originate from vastly different energy scales. Since here  $\Lambda$  is an assumed scale, however, and only ratios of  $c$  and  $\Lambda$  enter the calculations, it is sufficient to start with a common suppression scale, as long as  $(v, E)/\Lambda \ll 1$ .

The terms corresponding to different mass dimensions are discussed briefly in the following:

- **dim = 5:** At mass dimension 5, only one type of operator contributes. This operator is called the Weinberg operator [51, 52] and leads to Majorana neutrino masses, which violates lepton number conservation. As neutrino masses are measured to be small, the suppression scale for this type of operator is expected to be larger than the accessible scales for LHC physics. Therefore, dimension 5 operators are usually neglected for the interpretation of collider data.
- **dim = 6:** At mass dimension 6 [53, 54], there are  $\mathcal{O}(3000)$  operators

that contribute. The operators that violate lepton and baryon number by  $\Delta B = \Delta L = 1$  lead to proton decay. Limits on proton decay are very stringent, which suggests that the suppression scale for these operators is sufficiently large to be neglected at the LHC. This reduces the set of operators to the ones with  $\Delta B = \Delta L = 0$  of which 2499 exist. Assuming that BSM physics does not distinguish between flavour, the number of operators is reduced to 76 assuming a global  $U(3)^5$  flavour symmetry. This symmetry thus assumes that an effective operator acts similarly on all three generations, for each of the five fundamental SM fields.

- **dim = 7:** Dimension 7 operators [55] violate lepton number conservation. Some violate in addition baryon number conservation. As such violations are not observed at the LHC, these terms are expected to be sufficiently well suppressed to be neglected at LHC energies.
- **dim = 8:** The  $\sim 45$  thousand operators at dimension 8 [56] are suppressed by an additional  $\Lambda^2$  with respect to the dimension 6 terms, and are therefore generically considered as sub-leading, but not necessarily negligible in all cases.

This thesis focuses on the effective operators with mass dimension 6 for the interpretation of the measurements.

### 2.3.4 The Warsaw basis

A common basis choice for the dimension 6 operators is the Warsaw basis [54], for which technical implementations in Monte Carlo event generators exist, that can be used to make predictions for physical observables [57].

### 2.3.5 Advantages and limitations of the SMEFT approach

The advantage of the SMEFT approach is that deviations originating from the same effective operator can be correlated across a multitude of measurements. Therefore, SMEFT is a global scheme that unfolds its full potential when many measurements of different processes are combined. This is illustrated in Figure 2.4, where some of the Wilson coefficients of the Warsaw basis are grouped according to the type of measurements that they influence.

Furthermore, because SMEFT is a QFT, the theoretical predictions for the experimental observables that are used in the measurements can be improved as the experimental precision increases. Starting from LO predictions, one can systematically increase the perturbative order wherever more precision is needed. SMEFT also allows for a consistent treatment of the operator effects on the calculations. Some operators will e.g. also lead to a redefinition of the Higgs field, or to a change of the input parameter values that are used in the calculation, such as the Fermi constant. All these effects can be calculated and considered in the SMEFT approach.

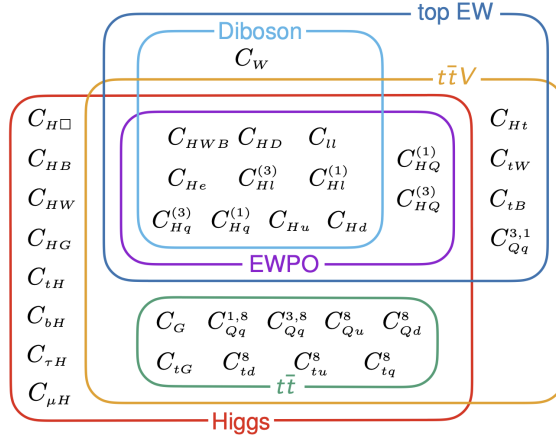


Figure 2.4: Illustration of how different Wilson coefficients impact different measurements of the SM. The abbreviation EWPO refers to electroweak precision observables, such as e.g.  $\Gamma_Z$  and  $m_W$ . Taken from Ref. [58].

Once the Wilson coefficients are estimated from experimental data, their measured values and uncertainties can be mapped onto the parameters of various UV-complete models. SMEFT therefore provides an additional level of abstraction between the actual measurement and the interpretation in terms of concrete UV models, which simplifies the process of constraining these individual models.

$$\text{Measurements} \xrightarrow{\text{constrain}} \text{SMEFT interpretations} \xrightarrow{\text{constrain}} \begin{cases} \text{BSM Model 1} \\ \text{BSM Model 2} \\ \dots \end{cases} \quad (2.25)$$

Due to the assumptions made in its construction, SMEFT does not encompass all possibilities for new physics. Firstly, only heavy new physics can be described. Secondly, the SM Higgs structure is assumed. However, different EFTs are available for extended Higgs sectors of the SM, broadly known as HEFTs. While any SMEFT can be rewritten as a HEFT, the reverse is not true.

## 2.4 Phenomenology of proton-proton collisions

This thesis studies high energetic particle collisions to test the predictions of the SM. The collisions are provided by the LHC, which collides protons with protons at  $\sqrt{s} = 13 \text{ TeV}$ . To be able to compare the SM predictions to LHC data requires a detailed understanding of the proton itself, of the scatter of constituents with

large momentum transfer, as well as the behaviour of the proton remnants. This section introduces the phenomenology of proton-proton ( $pp$ ) collisions.

Protons are compound objects: bound states with three valence quarks ( $u, u, d$ ) and a sea of other virtual particles, like quarks and gluons, that exist through vacuum fluctuations. The valence quarks make up most of the proton's properties, like its charge and its colour neutrality. They only contribute marginally to the proton's mass, however, with the majority being attributed to the energy of the QCD interactions inside of the proton. Due to the strong coupling strength being large at low energies, the description of the proton itself is dominated by non-perturbative effects. For high energetic  $pp$  collisions with large momentum transfer, asymptotic freedom provides the possibility to perform perturbative calculations, at least for the partons that are involved in the hard scatter.

### 2.4.1 Parton-density functions and factorisation

The factorisation theorem states that the calculation of the cross-section of a high energetic  $pp$  collision to a final state  $f$  can be broken down into [59]

$$d\sigma_{pp \rightarrow f}(s, \mu_R^2, \mu_F^2) = \sum_{i,j} \int_0^1 dx_1 \int_0^1 dx_2 f_i(x_1, \mu_F^2) f_j(x_2, \mu_F^2) d\hat{\sigma}_{ij \rightarrow f}(\hat{s}, \mu_F^2, \mu_R^2) \quad . \quad (2.26)$$

In this equation, the non-perturbative low energy part of the process is parameterised using parton distribution functions  $f_i$  and  $f_j$  (PDFs). At LO, the PDFs quantify the probability to find a parton inside the proton that carries a momentum fraction  $x_{i/j}$  of the proton's total  $z$ -momentum. The second part of the equation is the hard scatter, i.e. the partonic cross section  $d\hat{\sigma}$  for the process  $i j \rightarrow f$ , which is perturbatively calculated using Feynman diagrams. The sum including  $i$  and  $j$  runs over all partons in the two incoming protons. The variable  $s$  denotes the squared centre of mass energy of the collision,  $\hat{s}$  is the fraction of it that is used in the hard scatter.

The PDFs can not be calculated from first principles within perturbation theory, but have to be extracted from measurements, mostly from deep inelastic scattering. Example PDFs are shown in Figure 2.5. The scale at which the PDFs are evaluated is known as the factorisation scale  $\mu_F$  and marks the boundary between soft physics and the hard scatter. The PDFs are assumed to be universal; once determined, they can be applied to any process.

The partonic cross-section depends on the choice of the renormalisation scale  $\mu_R$  and on  $\mu_F$  due to QCD corrections to the parton model. The more perturbative orders are included in the calculation, the smaller the dependence of the prediction on the choices of  $\mu_R$  and  $\mu_F$ .

The dependence of other input parameters, such as the value of  $\alpha_S$  or the PDF

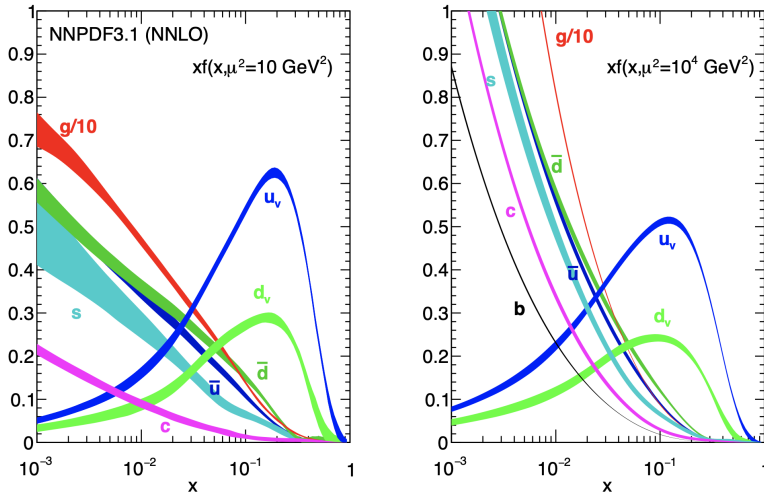


Figure 2.5: Parton distribution functions provided by the NNPDF collaboration and shown as a function of  $x$  for two different scales  $\mu^2$ . The  $x$ -dependence is obtained from a combined fit to data, the scale dependence is calculated using DGLAP evolution. Taken from Ref. [60]

values on the choice of  $\mu_R$  and  $\mu_F$  can be calculated. For the  $\mu_R$  dependence, this is performed using renormalisation group equations (RGEs). For the  $\mu_F$  dependence of the PDFs, DGLAP evolution can be used.

### 2.4.2 Event generation

Figure 2.6 sketches a typical  $pp$  collision. Two partons of the proton undergo a hard scatter with high momentum transfer. These incoming partons, as well as the outgoing partons in the final state can undergo a series of subsequent parton emissions or splittings. Emissions from the initial state partons are referred to as initial state radiation (ISR), emissions from the outgoing partons are referred to as final state radiation (FSR). Depending on the perturbative order of the available matrix element calculation, some of these real emissions, together with virtual contributions are calculated in perturbation theory.

The remaining real emissions are afterwards modelled approximately by a parton shower algorithm that relies on unitarity arguments. The showering is controlled to happen in an ordered way, with the emission that carries the most energy transfer happening at the beginning. The shower evolution of the outgoing partons continues until  $\alpha_S$  grows too large, after which fragmentation converts the partons non-perturbatively into colour neutral hadrons. The process of hadronisation is parameterised by universal fragmentation functions that encode the probability that a certain parton  $i$  hadronises into a hadron  $h_i$  carrying a momentum fraction

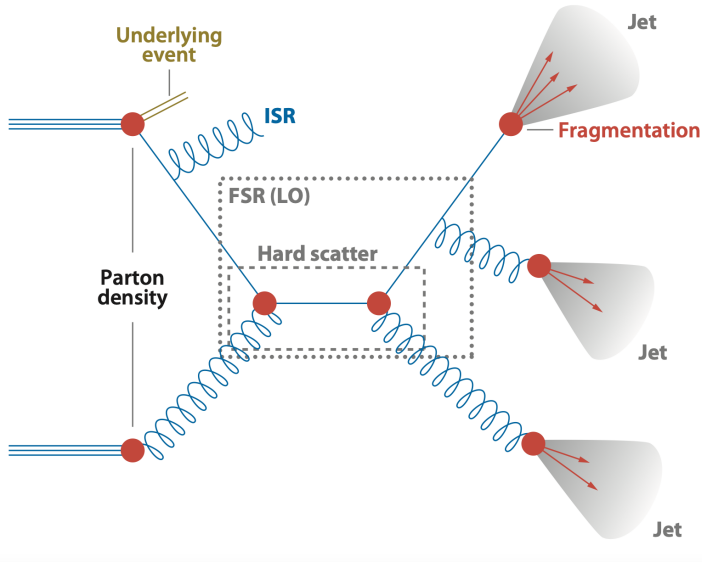


Figure 2.6: Illustration of a proton-proton collision. Taken from Ref. [61]

$x_i$  of the initial parton. In this way, the outgoing partons are converted into collimated sprays of particles, referred to as jets.

The proton remnants undergo QCD interactions, too. This process is usually referred to as the underlying event.

Monte Carlo techniques are used to simulate every step in the event generation chain from the hard scatter to the hadronisation. Various multipurpose generators exist that differ in the way the matrix element calculation is combined with the parton shower, in the variable which is used to order the parton shower emissions, or in the hadronisation modelling.

### 2.4.3 Cross-sections and luminosity

At hadron colliders such as the LHC, bunches of protons are passed through each other, which leads to individual  $pp$  collisions. The resulting collisions from one such bunch-crossing is referred to as an event. Additional interactions in the same bunch crossing, that happen with a momentum that is lower than that of the hardest collision, are referred to as pile-up. These additional interactions are usually simulated by overlaying inclusively generated  $pp$  collisions, which have no pre-selection on the physics process of interest, with the hard scatter process that one is interested in.

The number of events of a certain process that is produced in  $pp$  collisions per unit

time, the event rate  $R$ , is calculated as

$$R = \frac{dN}{dt} = \sigma \times \mathcal{L} \quad , \quad (2.27)$$

where  $\sigma$  is the cross-section for the process and  $\mathcal{L}$  is the instantaneous luminosity. The total number of events can be calculated by integrating the instantaneous luminosity over time to obtain the integrated luminosity  $L_{\text{int}}$ .

The instantaneous luminosity is a property of the collider, and for circular machines it can be calculated as

$$\mathcal{L} = \frac{N_1 N_2 f_{\text{rev}} n_b}{2\pi \sqrt{\sigma_{1,x}^2 + \sigma_{2,x}^2} \sqrt{\sigma_{1,y}^2 + \sigma_{2,y}^2}} \cdot F \cdot W \quad . \quad (2.28)$$

$N_1$  and  $N_2$  quantify the number of protons per bunch. The revolution frequency of the bunches is denoted as  $f_{\text{rev}}$  and the total number of bunches is referred to as  $n_b$ . The beam size is assumed to be Gaussian in the transverse plane with widths  $\sigma_{1/2,x/y}$ . The factors  $F$  and  $W$  quantify the luminosity reduction due to a finite crossing angle of the bunches and their transverse displacement.



## 3 Higgs boson physics

This chapter provides an overview of the current theoretical and experimental knowledge on the Higgs boson. After motivating the importance of the Higgs boson in Section 3.1, its main production modes and decay channels at the LHC are introduced in Section 3.2. Furthermore, the framework of simplified template cross-sections, which is used in this thesis for all cross-section measurements, is introduced in Section 3.3, followed by an introduction to effective Higgs boson coupling modifiers as a tool to interpret Higgs boson measurements. The chapter closes with a summary of the experimental status of Higgs boson physics in Section 3.5.

### 3.1 The importance of the Higgs boson

The SM Higgs boson is a unique particle. It is the only fundamental scalar of the theory, which means it carries no spin. Furthermore, it is the only boson that does not arise from the requirement of local gauge invariance with respect to a SM symmetry group. Instead, it originates from an ad-hoc solution to explain boson and fermion masses in the SM without violating local gauge invariance.

The Higgs boson is connected to various big questions of contemporary high energy physics [3] that impact our understanding of the universe.

- In the SM, the Higgs field acquires a non-zero vacuum expectation value by transitioning into a stable minimum of the Mexican-hat shaped potential. The Higgs boson mass, together with the mass of the top quark, strongly affects the shape of the Higgs potential at high field values via loop-corrections to the Higgs boson self coupling. At very high energies, a second minimum appears whose depth is dependent on the two mass values. If the minimum is lower than the current minimum, there is a non-zero probability to transition into it, which would render our universe unstable [62]. The Higgs boson mass is therefore directly linked to the stability of our universe.
- As explained in Section 2.2.1, the lightness of the Higgs boson mass seems to violate the separation of scales in the SM, which constitutes the so-called hierarchy problem and challenges our understanding of the decoupling theorem.
- The vacuum expectation value of the Higgs field also contributes to the vacuum energy density of the universe, which links the Higgs sector of the SM to the cosmological constant problem [63].

- The Higgs field is an inflaton candidate in cosmological models of inflation in the early universe [64]. While the SM seems to not be a sufficient model of the particle physics of inflation, modifications such as introducing an extra coupling between the Higgs boson and gravity seem promising.
- If the Higgs condensation happened as a first order phase transition, the Higgs boson is linked to baryogenesis. In the SM, the phase transition is of second order but enhanced Higgs boson self couplings change it into a first order transition [65].
- In Higgs portal models, the Higgs part of the SM Lagrangian connects to a new dark sector that contains the dark matter content of the universe [66].
- Although not predicted by the SM, the Yukawa part of the SM Lagrangian leaves room for additional CP violation, which is needed to understand the matter-antimatter asymmetry in the universe.

With the discovery of the Higgs boson in 2012, a whole new part of the SM is now experimentally accessible. Due to its unique features and its close links to many of the open questions, the Higgs boson is a prime study candidate in the quest for physics beyond the SM. Only through a thorough and complete experimental study of the Higgs boson can its role in our universe be understood.

## 3.2 Production modes and decay channels at the LHC

The Higgs boson couples directly to all massive particles of the SM. The possible vertices and coupling strengths can be derived from the SM Lagrangian, as shown in Figure 3.1 for the allowed three-point vertices that involve a Higgs boson. Most notably, the coupling to fermions (green), to massive vector bosons (orange) and the self-couplings (blue) originate each from separate parts of the SM Lagrangian.

Since the Higgs boson mass  $m_H$  is measured, it is possible to calculate cross-sections for processes that involve Higgs bosons. The total decay width of the SM Higgs boson at  $m_H = 125 \text{ GeV}$  is calculated to be  $\Gamma_H^{\text{total}} = 4.09 \pm 0.06 \text{ MeV}$  [67], which is more than 30 thousand times smaller than the Higgs boson mass itself. Therefore, the Narrow Width Approximation holds and the cross-section for any process like  $pp \rightarrow H \rightarrow X$  can be factorised into a production cross-section  $\sigma(pp \rightarrow H)$  and a decay branching ratio  $\text{BR}(H \rightarrow X)$  as

$$\sigma(pp \rightarrow H \rightarrow X) = \sigma(pp \rightarrow H) \times \text{BR}(H \rightarrow X) = \sigma(pp \rightarrow H) \times \frac{\Gamma_H^X}{\Gamma_H^{\text{total}}} \quad . \quad (3.1)$$

The partial width for the  $H \rightarrow X$  decay is denoted  $\Gamma_H^X$ . Therefore, the main Higgs boson production modes at the LHC are presented in the following separately from the possible decay channels.

Example Feynman diagrams of the main Higgs boson production modes at the

$$\begin{aligned}
\mathcal{L}_{\text{SM}} \sim & -\frac{1}{4}W_{\mu\nu}^j W_j^{\mu\nu} - \frac{1}{4}B_{\mu\nu}B^{\mu\nu} - \frac{1}{4}G_{\mu\nu}^a G_a^{\mu\nu} \\
& + \sum_f i\bar{\psi}_f \gamma^\mu D_\mu \psi_f \\
& + (D_\mu \phi)^\dagger (D^\mu \phi) \quad \text{BEH mechanism} \\
& - \mu^2(\phi^\dagger \phi) - \lambda(\phi^\dagger \phi)^2 \\
& - \sum_i Y_1^i \bar{L}^i \phi \ell_R^i - \sum_{i,j} \left( Y_u^{ij} \bar{Q}^i \phi u_R^j + Y_d^{ij} \bar{Q}^i \phi^C d_R^j \right) + \text{h.c.} \quad \text{Yukawa sector}
\end{aligned}$$

Figure 3.1: SM three-point vertices involving a Higgs boson and their origin in the SM Lagrangian.

LHC are shown in Figure 3.2. The corresponding cross-sections for each mode are shown in Figure 3.4. At the LHC, the main production mode of Higgs bosons is gluon fusion (ggF), where two initial state gluons ‘fuse’ via an internal quark loop to an outgoing Higgs boson. The production of a single Higgs boson is most likely to happen at  $\sqrt{s} \sim m_H$ , which occurs at the LHC at low Bjorken  $x$ , where the gluon PDF is enhanced. This contributes to the relatively large cross-section of ggF production with respect to production mechanisms that are initiated by quarks. The main contribution to the loop stems from the top quark because its Yukawa coupling is the largest with  $Y_t \sim 1$ . The second largest production mode is vector-boson fusion (VBF), where two incoming quarks radiate off massive vector bosons, either two  $W$ - or two  $Z$ -bosons, that fuse to an outgoing Higgs boson. The third largest production mode is the associated production with a heavy vector boson ( $VH$ ). In the main Feynman diagram for this production mode, the heavy vector boson radiates off a Higgs boson, which is why this mode is also referred to as Higgs-strahlung. The associated production of a Higgs boson with a pair of top or  $b$ -quarks ( $t\bar{t}H/b\bar{b}H$ ) or with a single top quark ( $tH$ ) are the production modes with the smallest cross-section.

The coupling of the Higgs boson to an other particle is dependent on that particle’s mass. For fermions, the coupling strength is linearly proportional to the mass of the involved fermion. For bosons, the coupling strength is proportional to the mass of the boson squared. Because the Higgs boson is lighter than any vector boson pair, the decays into such a pair of vector bosons only happens if one of the two bosons is off-shell, which lowers the branching ratios of  $H \rightarrow WW^*$  and

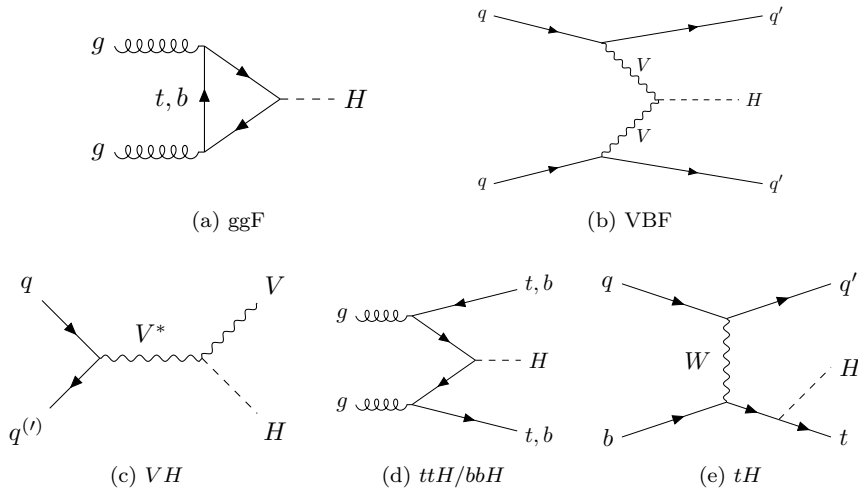


Figure 3.2: Feynman diagrams for the main Higgs production mechanisms at the LHC.

$H \rightarrow ZZ^*$ . With a mass of  $m_H \sim 125$  GeV, the heaviest pair of particles that the Higgs boson is able to decay into at rest is a pair of  $b$ -quarks. Consequently, this decay occurs most prominently, with a branching ratio of  $\sim 58\%$ . For all decays that are kinematically allowed, the BR is proportional to the squared Yukawa coupling and therefore proportional to the mass of the involved fermion squared. Therefore, the lighter the fermion, the smaller the branching ratio. For example, with  $\sim 3\%$ , the branching ratio for  $H \rightarrow c\bar{c}$  is roughly 20 times smaller than the one for  $H \rightarrow b\bar{b}$ . The Higgs boson can also decay indirectly into massless gauge bosons, such as a pair of gluons or photons, e.g. via loops involving heavy quarks or  $W$  bosons. Example Feynman diagrams for Higgs boson decays are shown in Figure 3.3. The corresponding branching ratios are shown in Figure 3.4.

The combinations of production process and decay mode that have the highest overall cross-section, are not necessarily the channels with the most experimental sensitivity. Instead, the inimitability of the experimental signature plays a crucial role, too. For example, the Higgs boson process that is most likely to happen is  $pp \rightarrow H \rightarrow b\bar{b}$ , which leads to an all-hadronic di- $b$ -jet final state. At a hadron collider such as the LHC, this signal faces a QCD multi-jet background that is more than seven orders of magnitude larger.

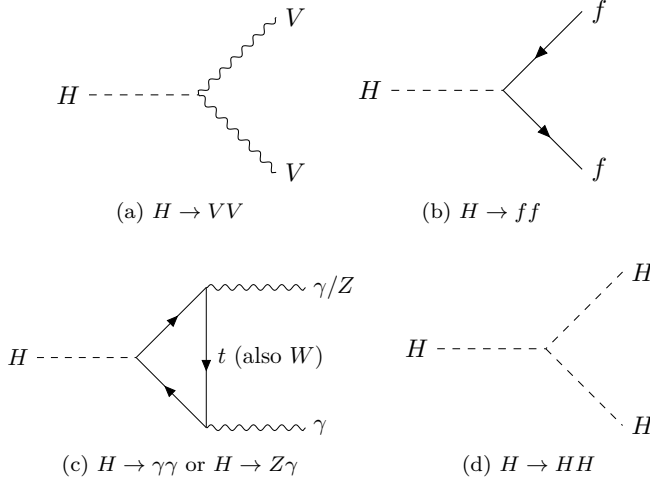
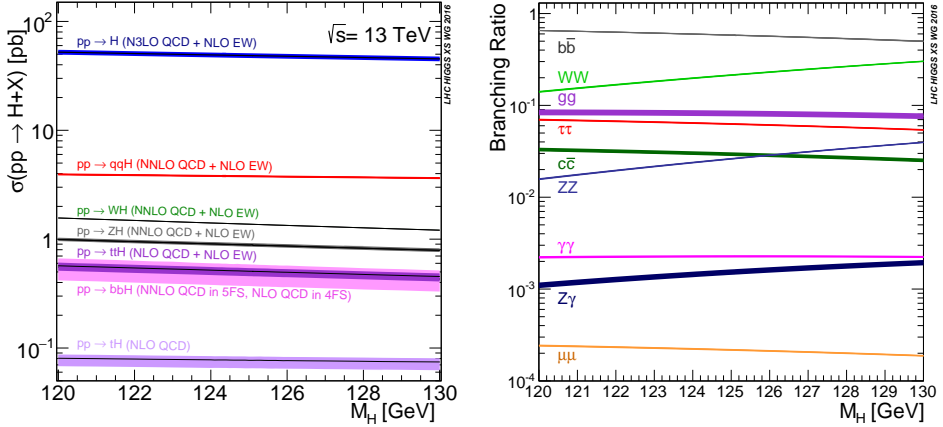


Figure 3.3: Example Feynman diagrams for Higgs boson decays.

Figure 3.4: Left: Production cross-section for various Higgs boson production mechanism at  $\sqrt{s} = 13$  TeV as a function of the Higgs boson mass. Right: Higgs boson decay branching ratios as a function of the Higgs boson mass. Taken from Ref. [67].

### 3.3 Simplified Higgs Template Cross-Sections (STXS)

The increasing data set collected by the ATLAS experiment allows to measure the Higgs boson properties with unprecedented precision. While for the first Higgs boson measurements, a maximal sensitivity to the Higgs boson signal was the only objective, with increasing data, differential measurements of Higgs boson cross-sections are possible. For these differential measurements, a compromise between experimental sensitivity and independence from theoretical assumptions needs to be found. The framework of simplified Higgs template cross-sections (STXS) [67] represents such a compromise. The STXS measurements are physical cross-section measurements in exclusive, abstract regions of phase space, that are agreed upon commonly across experiments. This section motivates the necessity by comparing the framework to signal strength and fully fiducial measurements before explaining in more details its technical realisation.

**Signal strength measurements** During the first stages of a Higgs boson measurement, it is important to maximise the overall sensitivity to the Higgs boson signal. For this reason, during Run 1 of the LHC, the ATLAS experiment provided measurements of inclusive signal strengths  $\mu$ . For a given process  $pp \rightarrow H(+X) \rightarrow \text{FS}$ , the signal strength is defined as

$$\mu(pp \rightarrow H(+X) \rightarrow \text{FS}) = \frac{[\sigma(pp \rightarrow H + (X)) \times \text{BR}(H \rightarrow \text{FS})]_{\text{measured}}}{[\sigma(pp \rightarrow H + (X)) \times \text{BR}(H \rightarrow \text{FS})]_{\text{predicted}}} , \quad (3.2)$$

where the total signal yield that is extracted from the measurement is compared to the SM prediction. This approach allows the usage of multivariate analysis techniques to maximise the signal sensitivity. At the same time,  $\mu$  measurements are inclusive, which means that even large deviations from the SM prediction will not alter  $\mu$  significantly, if they happen in regions where there are relatively little signal events compared to the total signal yield. In addition, these measurements are fully dependent on the underlying theory predictions. This dependence manifests itself in two ways. First, in order to determine how many signal events are expected in a certain analysis region, the kinematics of the SM Higgs boson processes is assumed. Second, the uncertainty of the measurement is fully dependent on the theoretical uncertainty associated with the signal simulation. As a consequence of these two dependencies, any non-trivial change in the assumed theory requires the measurement to be redone.

**Fully fiducial cross-section measurements** The standard of measurements that are minimally theory dependent are fully fiducial cross-section measurements. The fiducial region of phase space that is measured has to be as close as possible to the experimental selection, which disqualifies the usage of complex MVAs in the definition of the selection. Furthermore, the definition of the fiducial volume needs to be as production mode agnostic as possible, in order to not make the measurement

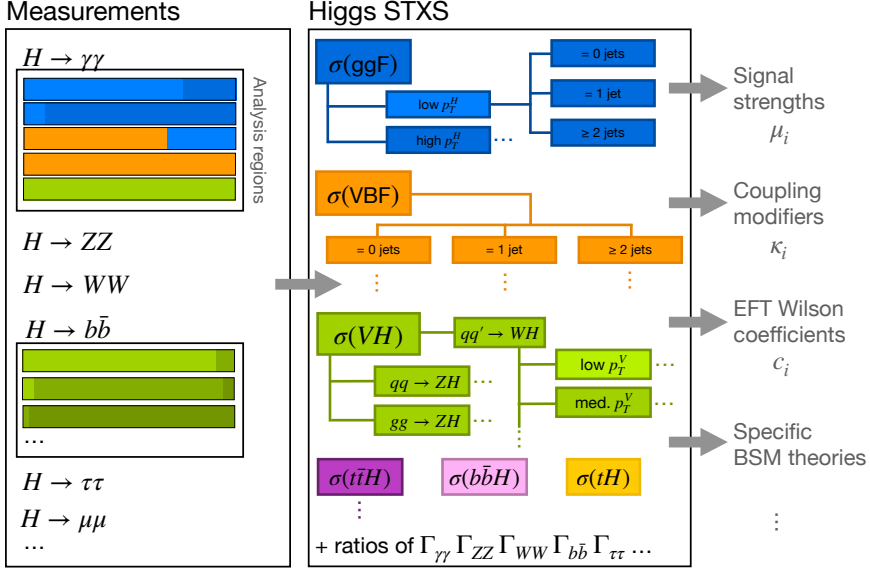


Figure 3.5: Illustration of the Higgs STXS framework. Graphic adapted from Ref. [67].

dependent on the SM prediction of the production mode mixture. For these reasons, with the Run 1 data, fiducial (differential) cross-section measurements have only been performed in the clean  $H \rightarrow \gamma\gamma$ ,  $H \rightarrow ZZ^* \rightarrow 4\ell$  and  $H \rightarrow WW^*$  channels. The resulting measurements rely minimally on underlying theory assumptions and extrapolations, with the majority of remaining assumptions being linked to the unfolding of detector effects. In complex Higgs boson decay channels, such as for  $H \rightarrow b\bar{b}$ , the signal sensitivity is not yet good enough to perform such measurements.

**STXS** For the  $139\text{ fb}^{-1}$  of data collected during the second operational run of the LHC (Run 2), the STXS framework is used to perform differential measurements that balance experimental precision on one hand and theoretical independence on the other hand. While not being as theory independent as fully fiducial measurements, STXS measurements can also be performed in the less clean channels like  $H \rightarrow \tau\tau$  or  $H \rightarrow b\bar{b}$ , where MVAs are heavily utilised. In contrast to signal strength measurements, STXS measurements provide differential information and allow to isolate regions with high BSM sensitivity.

An illustration of the STXS framework is shown in Figure 3.5. Within the STXS framework, the Higgs boson signal is split according to the production mode into

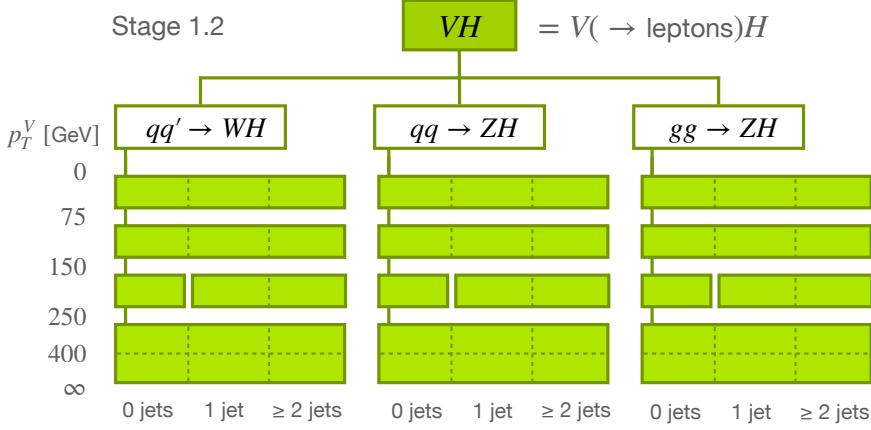


Figure 3.6: Stage 1.2 split of the  $V(\rightarrow \text{leptons})H$  STXS. Graphic adapted from Ref. [67]

$ggF$ ,  $VBF$ ,  $V(\rightarrow \text{quarks})H$ ,  $V(\rightarrow \text{leptons})H$ ,  $t\bar{t}H$ ,  $b\bar{b}H$  and  $tH$  production. No splitting is performed on the Higgs boson decay side, which allows to combine STXS measurements across analyses. Partial decay widths are fitted for the various Higgs boson decays. In the absence of total Higgs width measurements, only ratios of STXS cross-sections and ratios of decays widths can be measured without assumptions on  $\Gamma_H$ . To match the detector acceptance, only Higgs bosons with a rapidity of  $y_H < 2.5$  are considered. The different production modes are further split into exclusive regions of phase spaces, so called STXS 'bins'. The bins are defined to reduce the theory dependence, because the STXS measurement is only dependent on the kinematic predictions of the SM within a given bin. Furthermore, the bin widths are chosen to have a flat experimental acceptance within each bin, where possible. The binning itself is done in a variety of variables, such as the number of additional anti- $k_t$   $R = 0.4$  jets with  $p_T > 30$  GeV, the  $p_T$  of the Higgs boson, the  $p_T$  of the vector boson for  $V(\rightarrow \text{leptons})H$  production, or the invariant dijet mass for VBF topologies. These variables are defined on generator level, and the STXS fit itself is used to perform the unfolding from the reconstruction level. Regions with particular sensitivity to potential BSM physics are isolated, too, with one example being the high  $p_T^V$  region in  $V(\rightarrow \text{leptons})H$  production. Once measured, the STXS bins can serve as inputs to perform signal strength measurement or to constrain effective coupling modifiers, Wilson coefficients of a SMEFT or specific BSM models, as shown in Figure 3.5. As long as the BSM model under consideration has an experimental acceptance that is, as for the SM Higgs boson, roughly flat within the STXS bins, the STXS measurement does not need to be redone to perform the interpretations, which makes the STXS measurements advantageous to the  $\mu$  measurements. Because regions with high BSM sensitivity are explicitly isolated, BSM re-interpretations of STXS measurements are often



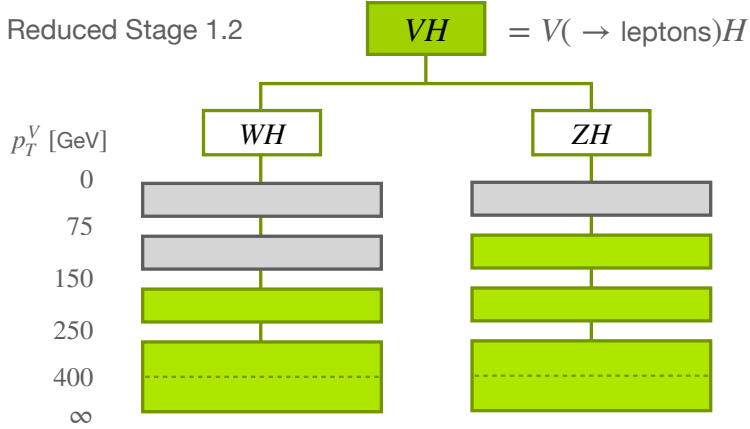


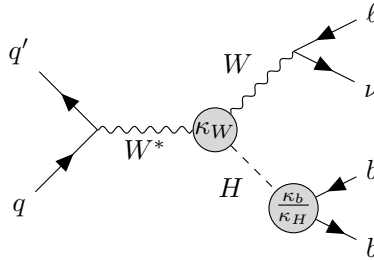
Figure 3.7: Reduced stage 1.2 split of the  $V(\rightarrow \text{leptons})H$  STXS. The green partitions indicate the bins that are currently measured by  $VH, H \rightarrow b\bar{b}$  analyses.

more powerful than BSM re-interpretations of  $\mu$  measurements.

The bin definitions of the STXS framework are not fixed but evolve with time in stages. The general mantra is that the more precise the measurements become, the finer the possible STXS binning. For  $V(\rightarrow \text{leptons})H$  production, which is the production mode that is targeted in the measurements presented in this thesis, the most recent stage 1.2 splitting is shown in Figure 3.6. The production cross-section is split into contributions from  $qq \rightarrow WH$ ,  $qq \rightarrow ZH$  and  $gg \rightarrow ZH$ . Further splittings are introduced as a function of the vector boson  $p_T$ , with bin boundaries at 75, 150 and 250 GeV, and the number of additional jets in the event. The dashed lines represent optional splits that can be introduced as the sensitivity of the measurements increase. The experimental sensitivity at the time of writing is not good enough yet to measure all bins of the full stage 1.2 split. Most notably, the current measurements can not separate the  $qq$ -initiated from the  $gg$ -initiated  $ZH$  production. Therefore, a reduced splitting is used, which is summarised in Figure 3.7.

### 3.4 Effective Higgs boson coupling modifiers

The STXS framework discussed in the previous section allows to combine multiple Higgs boson measurements according to their production mode in a decay-agnostic way. A study of the Higgs boson couplings, however, needs to take into account both the Higgs boson production and its decay at the same time. A framework of leading-order coupling modifiers, the so-called  $\kappa$  framework, has been developed



$$\begin{aligned}
 (\sigma \times \text{BR})(pp \rightarrow WH \rightarrow \ell\nu b\bar{b}) &= \sigma_{\text{SM}}(pp \rightarrow WH) \times \text{BR}_{\text{SM}}(H \rightarrow b\bar{b}) \\
 &\times \frac{\kappa_W^2 \kappa_b^2}{\kappa_H^2}
 \end{aligned}$$

Figure 3.8: Leading order Feynman diagram for  $pp \rightarrow WH \rightarrow \ell\nu b\bar{b}$  and corresponding  $\kappa$  parameterisation of the cross-section times branching ratio.

for such a treatment of both production and decay vertices in the analysis of the Run-1 LHC data [68].

Based on leading-order amplitudes, coupling modifiers  $\kappa$  are introduced that modify the SM Higgs boson couplings  $g$  multiplicatively as  $g \rightarrow \kappa g$ . The signal strength of Equation 3.2 can then be reparameterised as a function of these coupling modifiers. An example of this parameterisation is shown for the  $qq \rightarrow WH \rightarrow \ell\nu b\bar{b}$  process in Figure 3.8.

In the SM, all coupling modifiers  $\kappa_i$  are unity. The  $\kappa$  framework allows to combine the same couplings across analyses, both in the production and decay and is therefore a valuable benchmark tool for experimental sensitivities to different Higgs boson couplings. Nevertheless, it is based on assumptions that strongly limit its generality and especially its interpretability if non-SM values were to be observed. The main assumptions of the  $\kappa$  framework are:

- The observed signal in all measurements originates from a single, CP-even scalar resonance with  $m_H \sim 125$  GeV.
- The width of the resonance is small enough such that the narrow-width approximation holds and the cross-section factorises into a production cross-section and a decay branching ratio.
- The production and decay kinematics for all channels agree with the expectations from a SM Higgs boson.
- The coupling modifiers are real numbers, i.e. they leave the tensor structure of each coupling untouched as predicted for the SM Higgs boson.
- The coupling strength modifications are not dependent on the width of the

resonance, i.e. they are similar for the on-shell and off-shell regions. This assumption is of particular importance for indirect Higgs-width measurements.

Specific care needs to be taken in the treatment of the total width scale factor  $\kappa_H$ , that enters via the branching ratio in all signal strength parameterisations. The most generic way to parameterise the total width is

$$\Gamma_H = \frac{\kappa_H^2}{1 - \text{BR}_{\text{inv.}} - \text{BR}_{\text{undet.}}} \times \Gamma_H^{\text{SM}}, \quad \text{with} \quad (3.3)$$

$$\kappa_H^2 = \sum_{i \in \text{SM}} \text{BR}(H \rightarrow ii) \times \kappa_i^2 \quad . \quad (3.4)$$

The branching ratios  $\text{BR}_{\text{inv.}}$  and  $\text{BR}_{\text{undet.}}$  parameterise possible invisible and undetected Higgs boson decays beyond the SM contributions of 0.1% and 11%, respectively [4]. Invisible refers to the fact that the decay is not seen as any signal in the detector but can be inferred via momentum imbalance measurements. In contrast, undetected refers to BSM Higgs boson decays that currently cannot be distinguished from background processes. In the SM,  $\text{BR}_{\text{inv.}} = \text{BR}_{\text{undet.}} = 0$ . The loop over  $i$  in the expression for  $\kappa_H^2$  includes all SM particles that the Higgs boson couples to.

Loop-induced processes, such as ggF production or  $H \rightarrow \gamma\gamma$  decays, are either parameterised via an effective Higgs boson coupling modifier  $\kappa_g$  or  $\kappa_\gamma$  or re-expressed assuming SM-like contributions to the loop. The latter method maximises the combination power between analyses but also introduces additional model dependence.

For the  $VH, H \rightarrow b\bar{b}$  process, the necessary  $\kappa$  parameterisations are [69]:

- $\sigma(pp \rightarrow WH) = \sigma(pp \rightarrow WH)_{\text{SM}} \times \kappa_W^2$
- $\sigma(qq \rightarrow ZH) = \sigma(qq \rightarrow ZH)_{\text{SM}} \times \kappa_Z^2$
- $\sigma(gg \rightarrow ZH) = \sigma(gg \rightarrow ZH)_{\text{SM}} \times (2.456\kappa_Z^2 + 0.456\kappa_t^2 - 1.903\kappa_Z\kappa_t - 0.011\kappa_Z\kappa_b + 0.003\kappa_t\kappa_b) \quad .$

While the  $\kappa$  framework was a suitable choice for interpretations of the first Higgs boson measurements, the increased precision of the Run 2 Higgs boson measurements asks for a more refined interpretation framework. In particular, the assumption of SM kinematics in both production and decay, limits the class of new physics models that can be mapped. The SMEFT framework introduced in Chapter 2 does not require this assumption. An example of the advantages of the SMEFT approach is illustrated in Figure 3.9, where the impact of non-SM  $\kappa$ - and Wilson coefficient values on the Higgs  $p_T$  spectrum in  $WH$  production are shown. While non-SM values of  $\kappa_W$  only induce modifications of the total rate, the effective operators, in this case  $\mathcal{Q}_{Hq}^{(3)}$ , can additionally modify the shape of the Higgs  $p_T$  spectrum itself.

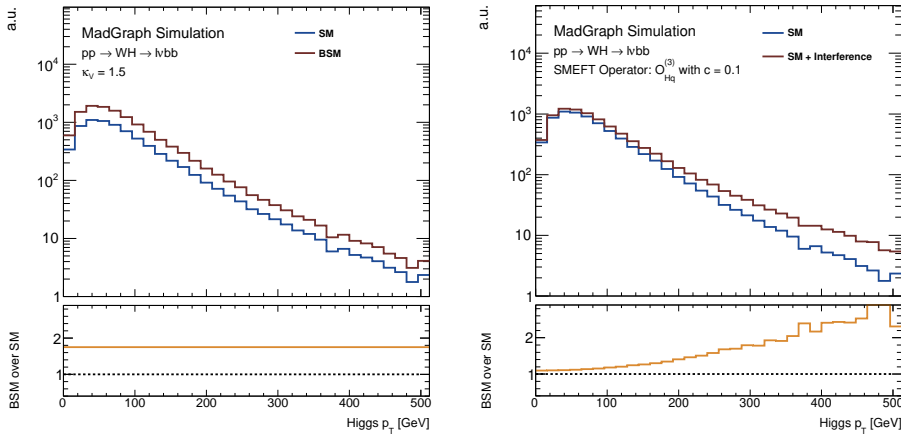


Figure 3.9: Simulated modifications of the Higgs  $p_T$  spectrum in  $WH$  production due to non-SM values of  $\kappa_W$  (left) and  $c_{Hq}^{(3)}$  (right).

### 3.5 Experimental status of Higgs boson physics

The discovery of a narrow resonance at  $\sim 125$  GeV by the ATLAS and CMS collaborations [1, 70] marked the starting point of an extensive research programme into the detailed properties of the new particle. Ever since then, a detailed comparison of the particle's measured properties with the predictions from the Higgs boson of the SM is of paramount interest. This section provides an overview of the experimental status of Higgs boson physics at the time of writing, which allows to place the measurements that are presented in this thesis into a wider context. The experimental results focus on measurements performed by the ATLAS collaboration. So far, no significant deviations from the predictions of a SM Higgs boson are observed.

**Spin and CP structure** Analyses of the spin parity nature of the new particle exclude hypotheses other than the SM one of a scalar CP-even boson beyond 99.9% CL [71], leading to the particle being commonly referred to as the Higgs boson. Although a pure CP-odd eigenstate has been ruled out, pseudo-scalar admixtures of CP-even and CP-odd eigenstates are still within experimental bounds [72–74]. So far, no sign of CP violation in the Higgs sector has been found.

**Decay to bosons** The two decay channels,  $H \rightarrow \gamma\gamma$  and  $H \rightarrow ZZ^* \rightarrow 4\ell$ , have driven the sensitivity for the Higgs boson discovery. Electrons, muons and photons are precisely reconstructed by the ATLAS detector, which makes these two measurement channels powerful tools to investigate Higgs boson properties, despite the relatively low final state branching ratios of 0.23% and 0.013%, respectively. The Higgs boson signal in both channels has been observed without any reasonable

doubt and the most recent measurements using the full Run 2 data set allow to measure finely granular STXS bins, fully fiducial cross-sections as well as unfolded single and double differential distributions [75–78]. The  $H \rightarrow WW^*$  decay is observed in both the ggF and VBF production modes, for both of which a variety of STXS bins is measured [79].

**Mass and width** The most precise Higgs boson mass measurement by the ATLAS collaboration to date is performed in the  $H \rightarrow ZZ^* \rightarrow 4\ell$  channel and amounts to [80]

$$m_H = 124.92 \pm 0.19 \text{ (stat.)}_{-0.06}^{+0.09} \text{ (syst.) GeV} \quad , \quad (3.5)$$

corresponding to a relative uncertainty of less than two permille. Direct measurements of the Higgs boson width are limited by the experimental resolution of the detector to a couple of GeV. Indirect measurements relying on the ratio of off-shell to on-shell Higgs boson production in the  $H \rightarrow ZZ^*$  decay places an upper limit on the width of 14.4 MeV at 95% CL [81].

**Decay to fermions** The Higgs boson has been observed to decay into fermions of the third generation, namely to  $\tau$ -leptons and  $b$ -quarks with rates as predicted by the SM. In both channels, the  $139 \text{ fb}^{-1}$  of data are used to measure STXS cross-sections coarsely binned in e.g.  $p_T^H$  and  $p_T^V$ , respectively [6, 82]. Furthermore the coupling to top quarks has been observed [83], rendering the massive fermions of the third generation complete. In the search for the Higgs boson decaying into leptons of the second generation, a  $H \rightarrow \mu\mu$  search by the ATLAS collaboration observed an excess with a significance of 2.0 standard deviations, where 1.7 were expected [84]. A search for the direct Higgs boson decay into a pair of charm quarks resulted in an upper limit on the signal strength of less than 26 times the SM prediction [8].

**Self-coupling** Measurements of di-Higgs production are used to provide limits on enhanced Higgs boson self-couplings. The most stringent limits set by the ATLAS collaboration involve searches for  $HH \rightarrow b\bar{b}\gamma\gamma$  and  $HH \rightarrow b\bar{b}\tau\tau$ , where limits of 4.1 and 4.7 times the SM prediction are set at the 95% CL [85, 86].

**Summary of couplings** A self consistency test of the SM is shown in Figure 3.10, where the measured reduced  $\kappa$  modifiers are shown as a function of each particle’s mass, testing the proportionality predicted by the SM. For the massive gauge bosons, which couple to the Higgs boson proportional to their mass squared, the square-root of the coupling modifier is drawn to change the SM prediction to be a straight line. These results are obtained by assuming SM contributions to the loop-processed, by fixing  $\text{BR}_{\text{inv.}} = \text{BR}_{\text{undet.}} = 0$  and furthermore assuming that all unmeasured couplings behave as predicted by the SM. Given these assumptions,

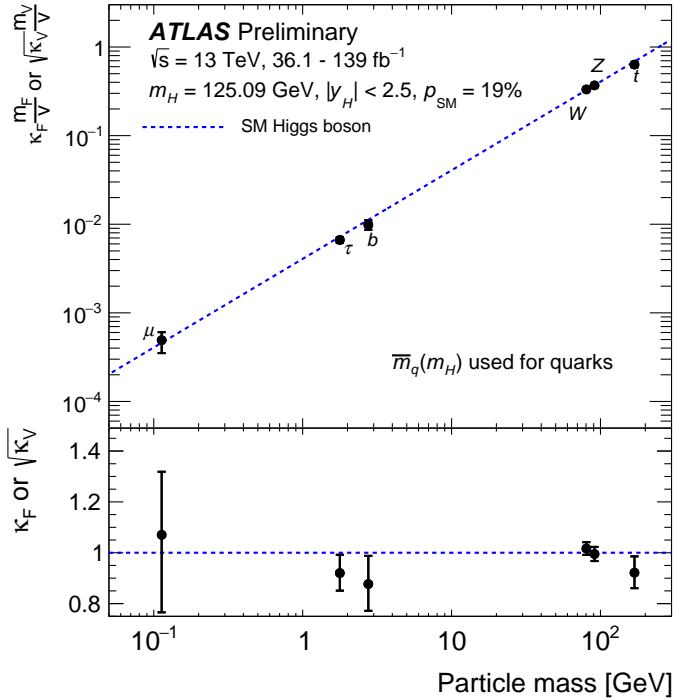


Figure 3.10: Measurement of reduced  $\kappa$  modifiers,  $\kappa_f m_f/v$  for fermions and  $\sqrt{\kappa_V} m_V/v$  for the massive gauge bosons and their uncertainties at 68% CL versus their mass. Loop contributions are assumed to follow their SM structure. The values are obtained from a fit with  $\text{BR}_{\text{inv.}} = \text{BR}_{\text{undet.}} = 0$ . Taken from Ref. [4].

this test reflects nicely the self consistency of the SM, but does not give a just representation of the certainty to which the Higgs sector has been measured.

**Precision development** Figure 3.11 shows the  $1\sigma$  uncertainties on LO Higgs boson coupling modifiers  $\kappa$  obtained by a combination of Higgs boson measurements. The green line, which corresponds to the precision achieved after the LHC’s Run 1 [87], is compared with the red line from a recent Run 2 combination [69] and a projection for the end of the High Luminosity LHC, depicted in blue [88]. As can be seen, the Higgs boson coupling strength to bosons is currently measured with a precision better than 10%, whereas the uncertainty on the coupling strength to fermions ranges around 10% to 15%. In the future, these uncertainties are expected to shrink further to a few %.

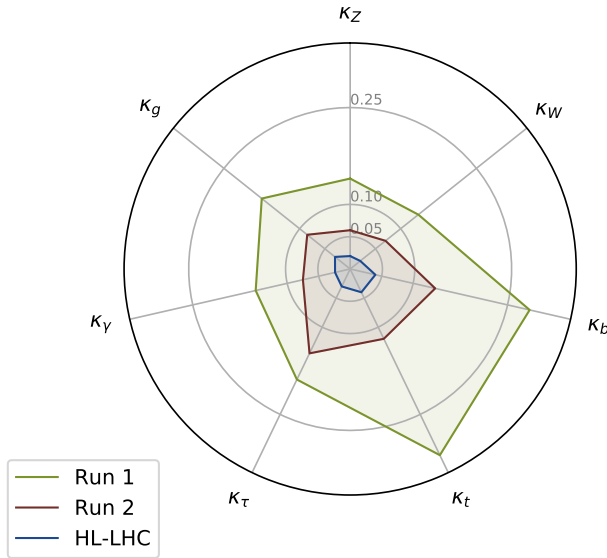


Figure 3.11: Observed (Run 1 and Run 2) and expected (HL-LHC) precision ( $1\sigma$ ) with which the Higgs boson coupling modifiers  $\kappa_i$  can be constrained by the ATLAS experiment. The Run 1 numbers are extracted from Ref. [87], the Run 2 numbers from Ref. [69] and the HL-LHC extrapolation from Ref. [88]. Indirect couplings via loops are parameterised using the effective coupling modifiers  $\kappa_\gamma$  and  $\kappa_g$ . The values are obtained from a fit with  $\text{BR}_{\text{inv.}} = \text{BR}_{\text{undet.}} = 0$ .





# 4 The ATLAS experiment at the Large Hadron Collider

To test the Higgs sector of the Standard Model Lagrangian in a model independent way requires the direct production of Higgs bosons in a controlled environment at a particle collider. Currently, the only operating machine that reaches high enough energies to produce a sufficient amount of Higgs bosons to study them experimentally is the Large Hadron Collider (LHC). The proton-proton collisions that are analysed in this thesis have been recorded by the ATLAS experiment, one of the two general-purpose detectors at the LHC. This chapter introduces the LHC and gives an overview of the technical design of the ATLAS experiment.

## 4.1 The Large Hadron Collider

The LHC [89] is a particle accelerator and collider installed at the CERN laboratory, near Geneva in Switzerland. Located in the 26.7 km long tunnel of the former LEP collider [90], between 45 and 170 m under the ground, the LHC is designed to collide protons on protons ( $pp$ ) at a peak centre-of-mass energy of 14 TeV. In addition, lead ions can be accelerated and brought to collision either with protons or other lead ions, too. The design of the LHC is driven by two main goals:

1. Operate at the highest centre-of-mass energy that is technically possible, to be able to produce particles with masses up to the TeV-scale. For this reason, protons are chosen over electrons because they loose less energy due to synchrotron radiation during circulation due to their higher mass. Given the fixed tunnel size, this allows to reach higher energies.
2. Operate at a sufficient instantaneous luminosity to be able to observe rare processes within an affordable runtime. For this reason, protons are collided with protons rather than anti-protons, because of the difficulties associated with the creation of a high-intensity anti-proton beam.

In the LHC, two beams of protons circulate in opposite directions through evacuated beam pipes. Following the LEP tunnel geometry, the LHC consists of eight arc sectors and eight straight sections. In the arc sectors of the machine, a total of about 1200 dipole magnets bend the protons on a closed path. To be able to sufficiently deflect the protons at collision energy, magnetic field strengths of up to 8.3 T are required. Consequentially, the magnets are made out of niobium-titanium coils, which are brought to superconductivity by cooling them down with superfluid

Helium to 1.9 K. Four of the eight straight sections feature interaction points at which the protons are brought into collisions. The other four sections house utilities for beam cleaning, beam dumping and the superconducting radio frequency cavities that accelerate the beams. Additional beam optics are installed, e.g. to focus the beam before a collision point and to deflect it for collision with the other beam.

Before the protons are injected into the LHC, they pass through a sequence of pre-accelerators, making use of the existing infrastructure at CERN. To make use of a sequence of different accelerators eases the engineering effort, because every machine in the chain is specifically optimised for a certain range of magnetic bending field-strengths. The injector chain that is used to fill the LHC with protons is illustrated in Figure 4.1. In a first step, hydrogen gas is ionised in a duoplasmatron to obtain a continuous proton beam. A radio frequency quadrupole focuses, bunches and accelerates the protons before they enter a linear accelerator (LINAC 2) followed by a sequence of synchrotrons with increasing size: the Booster, the Proton Synchrotron (PS) and the Super Proton Synchrotron (SPS). In the PS, the bunches are grouped together to a bunch train with a spacing of 25 ns between each bunch. When the proton bunch trains leave the SPS and are injected into the LHC, they have an energy of 450 GeV. A variety of filling schemes is used to target various instantaneous luminosity values. At its design luminosity of  $\mathcal{L} = 10^{34} \text{ cm}^{-2} \text{ s}^{-1}$ , each proton beam consists of up to 2808 bunches with around  $10^{11}$  protons each.

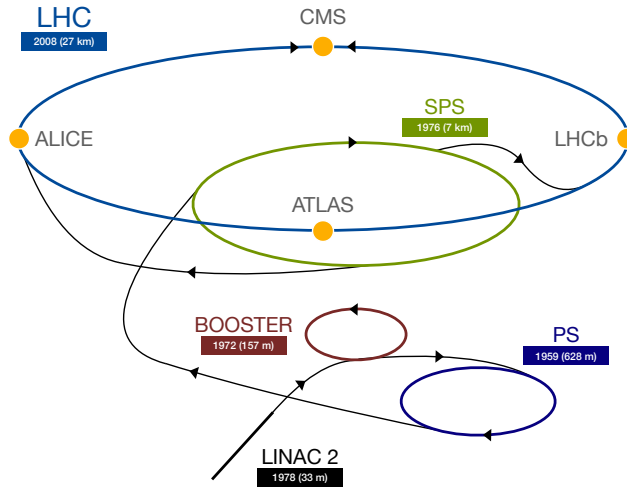


Figure 4.1: Illustration of the LHC injector chain. Graphic adapted from Ref. [91].

At each of the four interaction points, a particle detector records the collision debris. Two general-purpose detectors, ATLAS and CMS [92], record the collisions at peak instantaneous luminosity on opposite sides of the ring. They are designed independently from each other, which allows for a cross-confirmation of the measurements

between the two experiments. The LHCb detector [93] is a forward spectrometer with excellent vertex resolution to measure heavy-flavour hadron decay-chains. The ALICE detector [94] is optimised to study heavy ion collisions and explore states with very high energy density, in particular the quark-gluon plasma. In addition to the four main detectors, several smaller experiments are installed around the LHC, studying e.g. the forward physics close to the beam pipe or searching for exotic particles.

## 4.2 The ATLAS experiment

The ATLAS (**A Toroidal LHC ApparatuS**) [95] detector is a general-purpose detector that records the LHC collisions. It consists of a cylindrical barrel region in which sub-detectors are placed in layers around the interaction point to measure the particles that are created in the collisions. At both ends of the barrel, there are layered end-cap structures of sub-detectors that close the detector to the sides. In this way, a nearly  $4\pi$  coverage in solid angle is reached, which maximises the detector acceptance and allows to reconstruct the scatter final states as complete as possible. A cutaway illustration of the ATLAS detector with its various sub-detectors is shown in Figure 4.2.

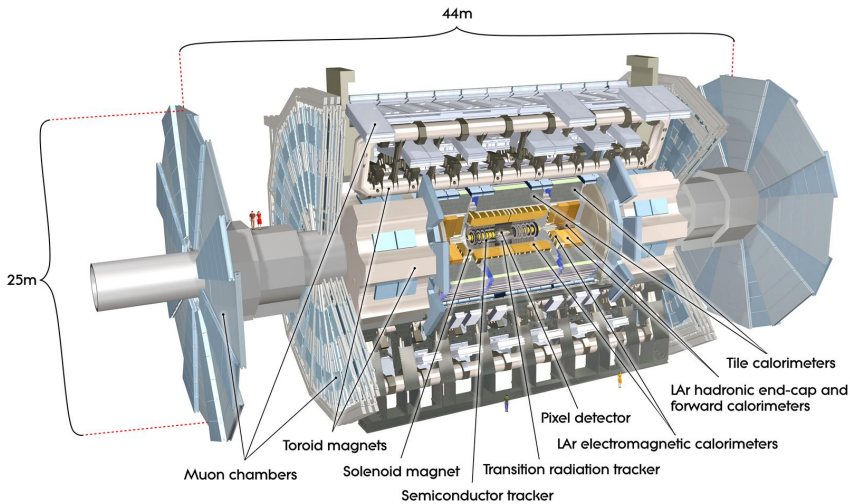


Figure 4.2: Cutaway illustration of the ATLAS detector [95].

In the region closest to the interaction point, the Inner Detector (ID) measures the tracks of charged particles that are bent in the 2 T magnetic field of a superconducting solenoid that surrounds the ID. This configuration is surrounded by an electromagnetic and a hadronic calorimeter, that provide energy measurements for particles showering either via the electromagnetic or strong force, respectively. The

outermost part of the ATLAS detector consists of the Muon Spectrometer (MS), a dedicated tracker for muons, that are bent using a toroid magnet system.

In order to be able to perform the  $VH, H \rightarrow b\bar{b}$  measurements that are presented in this thesis, the detector needs to match the following design criteria:

- Excellent spatial resolution close to the beam-pipe, to be able to reliably identify the primary interaction vertex and well as secondary (or tertiary) vertices from  $b$ -hadron decay-chains.
- Excellent electromagnetic calorimeters with fine transverse segmentation for electron measurements.
- A good hadronic calorimeter for jet measurements that has full azimuthal coverage in order to infer information about neutrinos via energy-imbalance in the transverse plane.
- Precise muon measurements through a combination of the ID and the MS.
- Trigger systems that can efficiently cope with the high instantaneous luminosity provided by the LHC.

All sub-detectors of the ATLAS experiment are needed in order to reach the above stated criteria, and therefore the following section introduces them briefly one-by-one. A more complete description can be found e.g. in Ref. [95].

### 4.2.1 The ATLAS coordinate system

The ATLAS collaboration uses a right-handed Cartesian coordinate system in which the  $x$ -axis points from the interaction point towards the centre of the LHC, the  $y$ -axis points upwards and the  $z$ -axis points along the beam pipe. Given that the detector is approximately rotational symmetric around the beam axis, cylindrical coordinates  $(r, \phi)$  are often used when describing particle properties in the transverse  $(xy)$  plane. The azimuthal angle  $\phi$  is hereby defined as the angle with respect to the  $x$ -axis in the transverse plane. Transverse quantities are denoted with a subscript T in this thesis. Instead of the polar angle  $\theta$ , often the rapidity  $y = \frac{1}{2} \left( \frac{E+p_z}{E-p_z} \right)$  of a particle is used, where  $E$  is the particle's energy and  $p_z$  its momentum fraction along the beam axis. Using the rapidity has the advantage that differences in rapidity are invariant under Lorentz boosts along the beam axis. For  $pp$ -collisions, where partons with unknown momentum fraction collide, and the boost along the  $z$ -axis is a priori unknown, the rapidity provides a physically more suited description. In the ultra-relativistic limit, when  $m \approx 0$ , the rapidity can be approximated by the pseudo-rapidity  $\eta$ , which is calculated from the polar angle  $\theta$  as  $\eta = -\ln(\theta/2)$ . The geometric distance between two particles,  $\Delta R$ , is defined as  $\Delta R = \sqrt{(\Delta\phi)^2 + (\Delta\eta)^2}$ .

### 4.2.2 Particle identification with the ATLAS detector

Figure 4.3 illustrates the signatures that particles leave when they traverse the ATLAS detector and how they are used to identify them. Electrons are electrically charged and therefore leave energy deposits (hits) in the ID from which their momentum and charge sign can be inferred. Once they reach the electromagnetic calorimeter, they initiate a shower which induces a signal that is proportional to their total energy. The electron is completely stopped within the volume of the electromagnetic calorimeter, therefore no traces are left in the hadronic calorimeter and the MS. Photons have similar calorimeter signatures to electrons, but because they are not electrically charged, they pass the ID without leaving hits and being bent. Protons, being positively charged, leave like electrons a bent track in the ID. Because they are hadrons, however, their calorimeter shower starts on average later and protons therefore deposit most of their energy in the hadronic calorimeter. Neutrons show similar calorimetric signatures to protons, but since neutrons don't carry electrical charge, they do not leave hits in the ID. Muons leave hits in the ID and, because they are minimally ionising most of the time, also traverse the calorimeters with only minimal energy deposits and without initiating a shower. As a consequence, they are the only particles that will also leave hits in the Muon Spectrometer. Neutrinos leave the ATLAS detector without any trace. Their presence can only be inferred indirectly via momentum imbalance in the transverse plane.

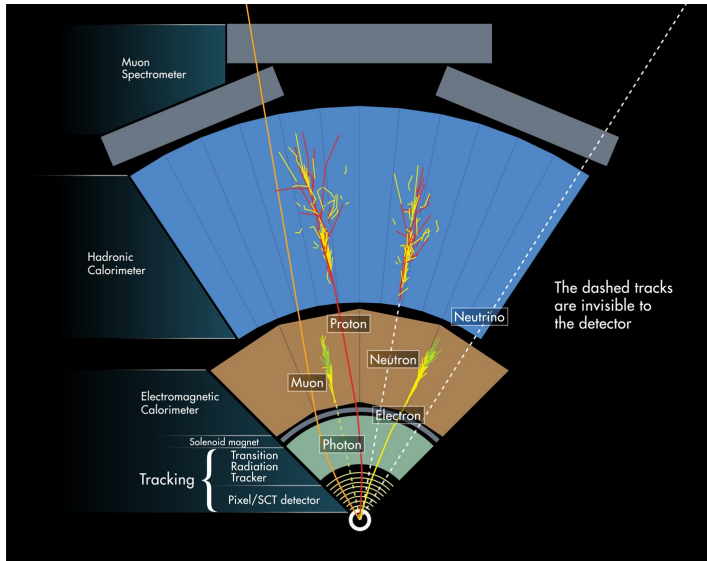


Figure 4.3: Illustration of the signatures that various particles leave in the ATLAS detector [96]. Shown is part of a cut through the transverse plane.

### 4.2.3 The Inner Detector

The ATLAS ID is a precise tracking detector that surrounds the beam pipe and is immersed in a 2 T axial magnetic field that is generated by a superconducting solenoid. With its three sub-detectors, the pixel detector, the semiconductor tracker and the transition radiation tracker, it measures localised energy deposits (hits) of charged particles that are used to reconstruct their bent trajectories (tracks). The track information is in turn used to infer the sign of the electrical charge of particles, as well as their momentum. Additionally, the tracks are used to identify the primary interaction vertex and secondary, as well as tertiary vertices that originate from heavy-flavour hadron decay-chains. Figure 4.4 shows a cutaway illustration of the ID, which consists of a barrel region, where the detector modules are arranged on concentric cylinders around the beam axis, and two end-caps where the detector modules form discs perpendicular to the beam pipe. A transverse cut through the barrel structure is illustrated in Figure 4.5. With all three sub-detectors combined, the ID has a length of approximately 6.2 m and a diameter of about 2.1 m, covering a pseudo-rapidity range of  $|\eta| < 2.5$ . Charged particle tracks with a  $p_T$  larger than about 0.5 GeV can be reconstructed using the hit measurements. The ID is designed to match transverse momentum resolutions for the reconstructed tracks of  $\sigma_{p_T}/p_T = 0.05\% p_T [\text{GeV}] \oplus 1\%$ .

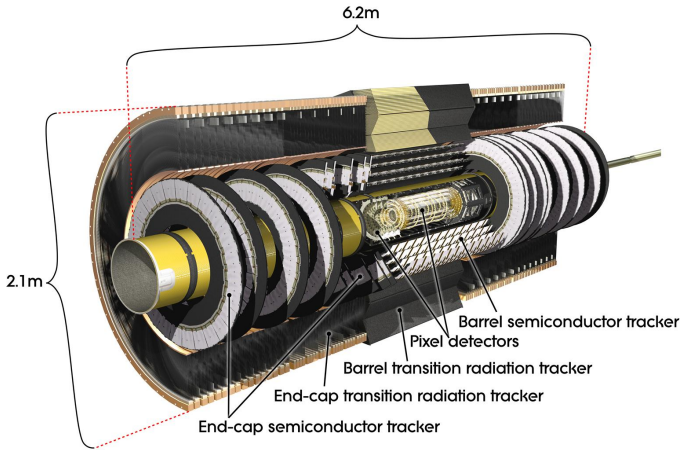


Figure 4.4: Cutaway illustration of the ATLAS Inner Detector [95].

**The Pixel Detector with the Insertable B-Layer** The pixel detector is the innermost sub-detector of the ATLAS ID. It consists of four layers of modules in the barrel region and 3 disks in each of the two end-cap structures. The innermost layer of the barrel, which is referred to as the Insertable B-Layer [98, 99], is positioned at a distance of  $r = 33 \text{ mm}$  from the centre of the beam-pipe and consists of modules with a pixel size of  $50 \times 250 \mu\text{m}^2$  in  $r - \phi$  and  $z$  direction, respectively. In addition to

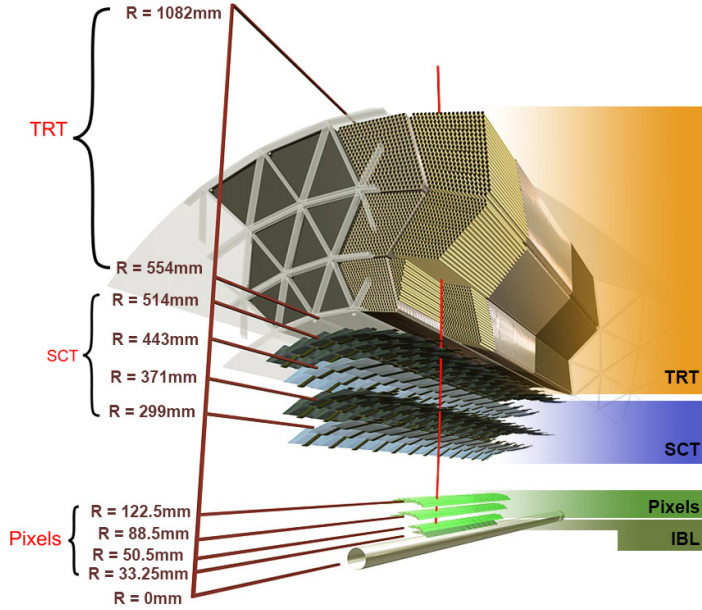


Figure 4.5: Illustration of the barrel structure of the ATLAS Inner Detector with the IBL [97].

planar pixel sensors, it also features 3D pixel sensors. The remaining pixel modules are made of planar sensors with a nominal pixel size of  $50 \times 400 \mu\text{m}^2$ . Without the IBL, the intrinsic hit accuracy of the pixel detector is approximately  $10 \times 115 \mu\text{m}^2$  in  $r - \phi \times z$  for the barrel region and  $115 \times 10 \mu\text{m}^2$  in  $r - \phi \times z$  for the end-caps. The addition of the IBL improves significantly the impact parameter resolution in  $r - \phi$  direction for low  $p_T$  particles due to providing an additional hit point close to the beam and in  $z$  direction due to the smaller pixel size. This benefits the secondary vertex reconstruction that is important for  $b$ -hadron identification. On average, a charged particle leaves 4 hits in the pixel detector.

**The Semiconductor Tracker** The semiconductor tracker (SCT) consists of silicon microstrip modules with a mean strip pitch of  $80 \mu\text{m}$ . Each module features two sensor layers which are tilted with respect to each other by a small stereo angle of  $40 \text{ mrad}$  to allow a 2D hit reconstruction in the module plane. The barrel region consists of four cylindrical layers of strip modules and each end-cap is made of nine discs of modules. The intrinsic accuracy of the SCT is  $17 \times 580 \mu\text{m}^2$  in  $r - \phi \times z$  for the barrel region and  $580 \times 17 \mu\text{m}^2$  in  $r - \phi \times z$  for the end-caps. Charged particles leave on average 8 hits in the SCT.

**The Transition Radiation Tracker** The outermost part of the ATLAS ID is the transition radiation tracker (TRT). The TRT is a straw tube tracker featuring

gas-filled tubes with a diameter of 4 mm and an anode wire in the centre. In the barrel region the tubes have a length of 144 cm and are assembled in 72 layers parallel to the beam pipe. In the two end-caps the tubes are 37 cm long and assembled perpendicular to the beam pipe in 160 planes. This allows charged particle tracking up to  $|\eta| < 2.0$ . The TRT provides  $r - \phi$  hit information in the barrel region and  $z - \phi$  information in the end-caps with an intrinsic accuracy of 130  $\mu\text{m}$  per straw via drift time measurements. Although this intrinsic accuracy is lower than for the pixel detector and the SCT, the TRT compensates to some extent by providing a large number of hit measurements of a long distance. On average, a charged particle leaves 36 hits in the TRT. In the barrel region, the straw tubes are embedded in a matrix of polypropylene fibres, which create transition radiation for traversing relativistic particles. This effect helps to distinguish electrons from pions. In the end-cap regions, foils are interlayered with the tube planes to create the transition radiation. During Run 1, the TRT was exclusively operated with a Xenon-based gas mixture. Due to the occurrence of irreparable gas leaks, parts of the TRT were operated with a cheaper Argon-based gas mixture in Run 2 at the cost of loosing the particle identification feature because the Argon does not provide a sufficient absorption of the transition radiation photons [100].

## 4.2.4 The Calorimeters

The ATLAS calorimeter system, illustrated in Figure 4.6, consists of an electromagnetic calorimeter (ECAL) and a hadronic calorimeter (HCAL) to measure the energy of particles that shower either predominantly via the electromagnetic or the strong force, respectively. The calorimeters are rotational symmetric around the beam axis and cover a region up to  $|\eta| < 4.9$ . Furthermore, they are segmented to provide directional information for the reconstruction of electrons, photons, jets and the missing transverse energy. Both the ECAL and the HCAL are sampling calorimeters, which means that they consist of multiple alternating layers of active detection and passive high-density absorption material. The total energy of the particles is then extrapolated from the signal measured in the active detection layers. The combination of the two calorimeters provides enough stopping power to contain the entire particle shower and prevent leakage of particles into the Muon Spectrometer.

### 4.2.4.1 The electromagnetic calorimeter

The ECAL is a sampling calorimeter that uses liquid Argon (LAr) together with kapton electrodes as active material and lead plates as absorber. In the barrel region, it is situated behind the superconducting solenoid and consists of two coaxial cylinders that are separated by a small gap at  $z = 0$ . Each cylinder is about 3.2 m long and has an inner radius of 1.4 m and an outer radius of 2 m. Together, they cover the region up to  $|\eta| < 1.475$ . The electrodes and absorber plates are shaped following an accordion geometry which allows to provide full azimuthal symmetry and crack-less coverage. A high voltage is applied between



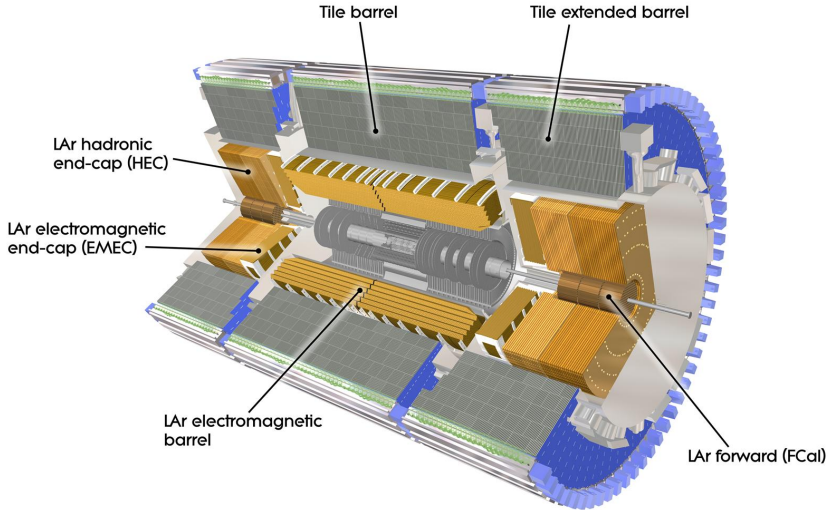


Figure 4.6: Cutaway illustration of the ATLAS calorimeter system [95].

the electrodes to collect ionisation charges produced in the interaction of particles with the LAr. The barrel ECAL readout is separated into three radial layers with varying depth that are each segmented in both  $\phi$  and  $\eta$  to provide shape information about the particle showers. The first layer is about four radiation lengths  $X_0$  deep and segmented into thin strips of  $\Delta\phi \times \Delta\eta \approx 0.01 \times 0.003$ , which are especially useful to identify  $\pi^0 \rightarrow \gamma\gamma$  decays. The second layer is about 16  $X_0$  deep and comprised of cells with a size of  $\Delta\phi \times \Delta\eta \approx 0.025 \times 0.025$ . In it, the largest part of electromagnetic showers is contained. Together with the first layer, the second layer provides excellent directional information for both photons and electrons. Finally, a third layer with a width of about 2  $X_0$  and coarser  $\eta$  segmentation is used to estimate the energy leakage into the hadronic calorimeter and to distinguish electromagnetic from hadronic showers.

In each end-cap region, two ECAL wheels are installed. An outer wheel covers the region with  $1.375 < |\eta| < 2.5$  and an inner wheel covers the region with  $2.5 < |\eta| < 3.2$ . The end-cap modules follow the same geometry as the barrel modules. The outer wheel is mostly segmented into three layers, like the barrel, featuring also a strip layer. The inner wheel and the outer parts of the outer wheel only consist of two layers with reduced granularity.

Thin pre-sampler layers with fine resolution are installed before the ECAL in various regions of the barrel and end-cap to provide an additional energy measurement that is used to correct for energy losses in the material before the ECAL.

The designed relative energy resolution of the ECAL is  $\sigma_E/E = 10\%/\sqrt{E[\text{GeV}]} \oplus 0.7\%$ . With a depth of more than 22  $X_0$ , most of the electromagnetic showers from

electrons and photons with an energy of up a few TeV are contained within the ECAL volume. At the same time, the ECAL material only amounts to about 1.5 nuclear interaction lengths  $\lambda$ . Therefore, particles interacting predominantly via the strong interaction likely initiate showers in the ECAL that are not contained by it and continue far into the HCAL.

#### 4.2.4.2 The hadronic calorimeter

The ATLAS HCAL is positioned behind the ECAL and is of particular importance for energy measurements of hadronic cascades. It consists of three sampling calorimeters that use different choices of active and passive materials depending on requirements on the performance and radiation hardness. The designed relative energy resolution of the hadronic calorimeter is  $\sigma_E/E = 50\%/\sqrt{E[\text{GeV}]} \oplus 3\%$  for the barrel and end-cap, worsening to  $\sigma_E/E = 100\%/\sqrt{E[\text{GeV}]} \oplus 10\%$  for the forward calorimeter.

**The tile calorimeter** The tile calorimeter consists of a 5.8 m long barrel and two 2.6 m long extended barrels on each side, all with an inner radius of  $\sim 2.3$  m and an outer radius of  $\sim 4.3$  m. They provide coverage in the regions with  $|\eta| < 1.0$  and  $0.8 < |\eta| < 1.7$ , respectively. The individual modules consist of layers of scintillating tiles as active material, sandwiched with steel plates as absorber. Similar to the ECAL, the tile calorimeter is segmented in depth into three layers with decreasing granularity. In the barrel region, the individual layers have nuclear interaction lengths of 1.5, 4.1 and 1.8  $\lambda$ , whereas the extended-barrel parts are segmented into layers with 1.5, 2.6 and 3.3  $\lambda$ . The individual cells in each layer are significantly larger than the ECAL cells, with typical sizes of  $\Delta\phi \times \Delta\eta \approx 0.1 \times 0.1$ . This reduced granularity is partly compensated by the fact that hadronic showers are less localised than electromagnetic ones.

**The LAr hadronic end-cap calorimeter** The LAr hadronic end-cap calorimeter (HEC) is located directly behind the end-cap of the ECAL, sharing the same cryostats. Each end-cap consists of a front and a rear wheel that are made of planar modules using LAr as active medium and copper as an absorber. Together they cover the pseudo-rapidity range of  $1.5 < |\eta| < 3.2$ . In the central region, similar to the tile calorimeter, readout cells with a size of  $\Delta\phi \times \Delta\eta \approx 0.1 \times 0.1$  are used. Further away from the IP, the granularity is reduced. In the forward regions of the detector, where particle fluxes are high, the usage of LAr as an active material is beneficial because of its resistance to radiation and the possibility to replace the liquid in case of serious performance degradation.

**The LAr forward calorimeter** In the very forward region with pseudo-rapidities of  $3.1 < |\eta| < 4.9$ , the LAr forward calorimeter is positioned. It consists of three modules on each side. Each module consists of a metal base with holes parallel to the beam-pipe. In each of these holes, metal rods are put leaving a small gap that is

filled with LAr. The small gap ensures a fast signal to be able to deal with the high particle fluxes in this forward region. The first module provides electromagnetic energy measurements and uses copper as passive material in addition to the active LAr. The consecutive two modules use tungsten and provide hadronic energy measurements.

Radially outward from the interaction point at  $\eta = 0$ , the HCAL material corresponds to  $\sim 7.4$  nuclear radiation lengths. Together with the  $1.5\lambda$  of the ECAL, this provides enough material to ensure hermetic closure to enable energy balance measurements in the transverse plane and shield the Muon Spectrometer from punch-through of particles other than muons (and neutrinos).

### 4.2.5 The Muon Spectrometer

Situated on the outermost part of the ATLAS detector is the Muon Spectrometer (MS), a tracking detector that aims to provide precise momentum measurements for muons up to an energy of a few TeV. A cutaway illustration of the MS is shown in Figure 4.7. In the energy range from  $\mathcal{O}(\text{GeV}) - \mathcal{O}(\text{TeV})$ , muons only lose relatively little energy via ionisation and are not stopped by the calorimeters. With a mean lifetime of  $\tau \approx 2.2\mu\text{s}$ , almost all muons leave the ATLAS detector before they decay. Since all other SM particles, apart from the neutrino, don't pass the calorimeter, a track in the MS is indicative of a muon<sup>1</sup>.

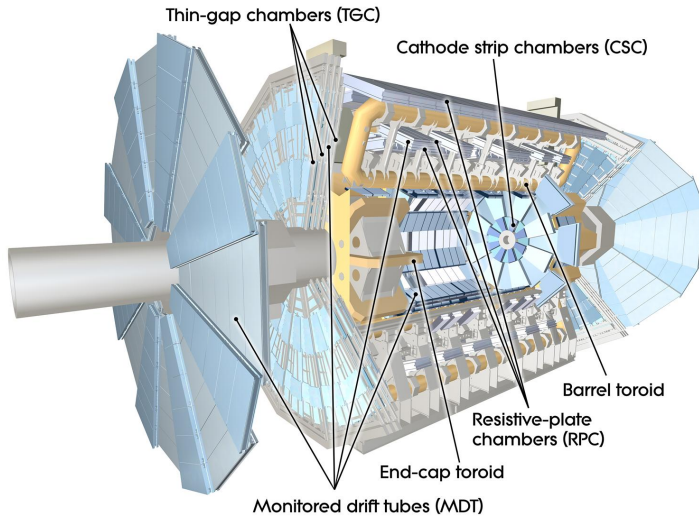


Figure 4.7: Cutaway illustration of the ATLAS Muon Spectrometer [95].

<sup>1</sup>High energetic hadronic showers can be very elongated, such that shower particles may leak from the HCAL into the MS. This effect is usually referred to as punch-through and forms a background to tracks from hard scatter muons in the MS.

A separate toroid magnet-system creates the field in which the muons are bent. In the barrel region, eight superconducting coils create a 4 T magnetic field to deflect muons in the  $\eta$  direction for  $|\eta| < 1.4$ . At the end-caps, two separate smaller toroid magnets create a 4 T magnetic field for the region  $1.6 < |\eta| < 2.7$ . In the transition region, a combination of both magnetic fields bends the muons. The installation of separate magnet fields allows to maximise the bending volume to increase the momentum resolution. At the same time, the magnets have an air core which reduces the amount of multiple scattering.

In the air volume around the toroids, tracking chambers are placed to record the muon trajectories. Different technologies are used to fulfil different purposes. Generally speaking, the chambers can be divided into tracking and triggering chambers:

**Tracking chambers** The main technology used for precision tracking are monitored drift tubes (MDTs). The basic unit consists of gas-filled aluminium drift-tubes of  $\sim 3$  cm diameter with an anode wire in the centre. The tubes are arranged in layers and each chamber has either one or two layers consisting of three or four rows of tubes. Three layers of MDT chambers are installed at increasing radius from the centre both in the barrel and end-cap regions. In the barrel region, the tubes are positioned in the  $\phi$  direction since the muon bending occurs in the  $\eta$  direction at radii of 5, 7.5 and 10 m, respectively. In the end-caps the chambers are mounted on large wheels that are perpendicular to the beam pipe at distances of 7.4, 10.8, 14 and 21.5 m from the nominal interaction point and cover a region up to  $|\eta| < 2.7$ . To reach the design resolution of  $35 \mu\text{m}$  per chamber, a dedicated optical alignment system monitors the position of the chambers. The maximum drift time of the ionisation charges in each tube is about 700 ns, therefore MDTs are rather slow compared to the collision rate of 25 ns.

In the forward region, the particle flux is particularly high and detectors with a smaller drift time and good radiation hardness are needed. Therefore, in the range of  $2.0 < |\eta| < 2.7$ , cathode strip chambers (CSC) are used. CSCs are multiwire proportional chambers with wires orthogonal to the beam pipe and two cathode planes that are segmented in strips of orthogonal orientation to allow for 2D position measurements. The maximum drift time is 20 ns, significantly smaller than for MDTs. The position accuracy per chamber is  $40 \mu\text{m}$  in the bending plane and 5 mm in the transverse direction.

**Triggering chambers** To provide fast signals that can be used for triggering and to complete the MDT position measurement, special triggering chambers are installed around the precision tracking chambers. In the barrel region, resistive plate chambers (RPCs) are installed around the middle MDT layer and behind the third layer. They consist of two electrode plates with a thin, gas-filled gap between them and high voltage applied. Both electrodes are orthogonally segmented to provide coarse spatial information with a resolution of  $\sim 10$  mm in both directions. In the forward region, thin gap chambers (TGCs), multi-wire proportional chambers with

small distance between the wire and the cathode, are used to provide fast signals for triggering and spatial measurements with mm precision. Both technologies achieve nanosecond time resolution.

The standalone MS is designed to reach relative momentum resolutions of  $\sigma_{p_T}/p_T = 10\%$  for 1 TeV muons within  $|\eta| < 2.7$ . Usually, the MS information is combined with tracking information from the ID, which significantly improves the momentum resolution for low  $p_T$  muons.

### 4.2.6 Luminosity measurements

The correct determination of the luminosity is vital to estimate the expected number of events from a given process when analysing the collision data. Multiple detectors provide information that is proportional to the instantaneous luminosity, the most important of which is the LUCID-2 detector [101]. It consists of multiple PMTs in the forward arms of the ATLAS detector, around 17 m from the IP, and measures the Cherenkov light produced by particles from the collision in the quartz windows of the PMTs. The LUCID-2 measurements are calibrated in dedicated van-der-Meer scans, where special low-luminosity beams are passed through each other in both  $x$ - and  $y$ -direction. The calibration is then extrapolated to physics data taking conditions at higher instantaneous luminosity by using luminosity-sensitive quantities such as the number of tracks or the calorimeter current [102].

### 4.2.7 Triggering and data acquisition

During the physics data taking of the LHC Run 2, bunches of protons collide every 25 ns corresponding to a collision frequency of 40 MHz. This amount of data cannot be stored on tape and therefore a multi-layered trigger and data acquisition system is in place to select and subsequently store events that are of particular interest. An illustration of the system and the corresponding data rates is shown in Figure 4.8.

The main components of the trigger system are the level one trigger (L1) and the high level trigger (HLT) [104]. The L1 trigger is a custom hardware trigger that uses among other things information from the Muon Spectrometer and reduced calorimeter information to look for signs of high  $p_T$  objects such as muons, electrons, jets or missing transverse energy. It reduces the peak event rate to about 100 kHz and defines crude regions of interest in the detector that are further passed to the HLT. In the time it takes the L1 trigger to make a decision, the event information is stored on custom front-end (FE) buffers on the detector before being passed to read-out-drivers (ROD) outside of the detector. The software-based HLT runs on a dedicated computing farm and has access to the whole detector information in addition to the specific regions of interest from the L1 trigger. The HLT reduces the event rate further down to about 1.5 kHz at peak times that are afterwards permanently stored and sent to the CERN T0 computing site for offline

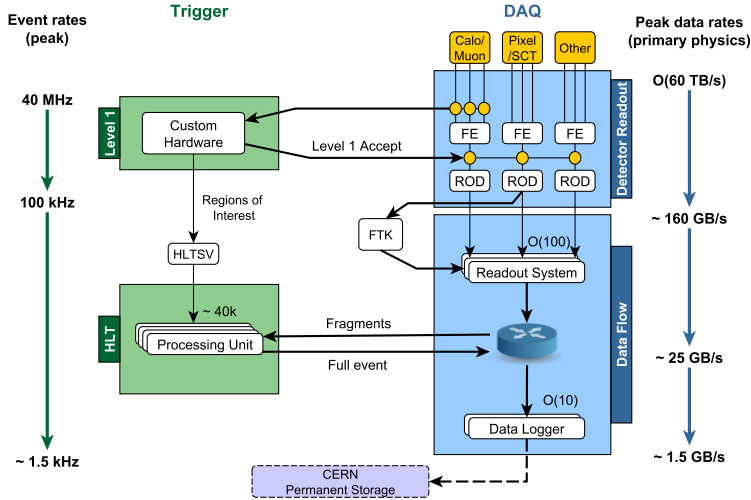


Figure 4.8: Illustration of the ATLAS trigger and data acquisition chain [103].

reconstruction. In the time that it takes the HLT to make a decision, the event information is retained in the read-out-system buffer.

The datasets that are analysed in this thesis were collected during Run 2 of the LHC from 2015 to 2018 at a centre-of-mass energy of  $\sqrt{s} = 13 \text{ TeV}$ . During this time, a total integrated luminosity of  $159 \text{ fb}^{-1}$  was delivered to ATLAS by the LHC, of which  $147 \text{ fb}^{-1}$  were recorded and  $139 \text{ fb}^{-1}$  of good enough quality to be used in physics analyses as illustrated in Figure 4.9. During the four years of Run 2, different settings of the LHC, such as for example the bunch filling scheme, were used. Therefore, the distribution of the mean number of interactions per bunch-crossing changed throughout the years as illustrated in Figure 4.9. These measured pile-up distributions are later used to apply a per-year correction on the simulation to agree with data.

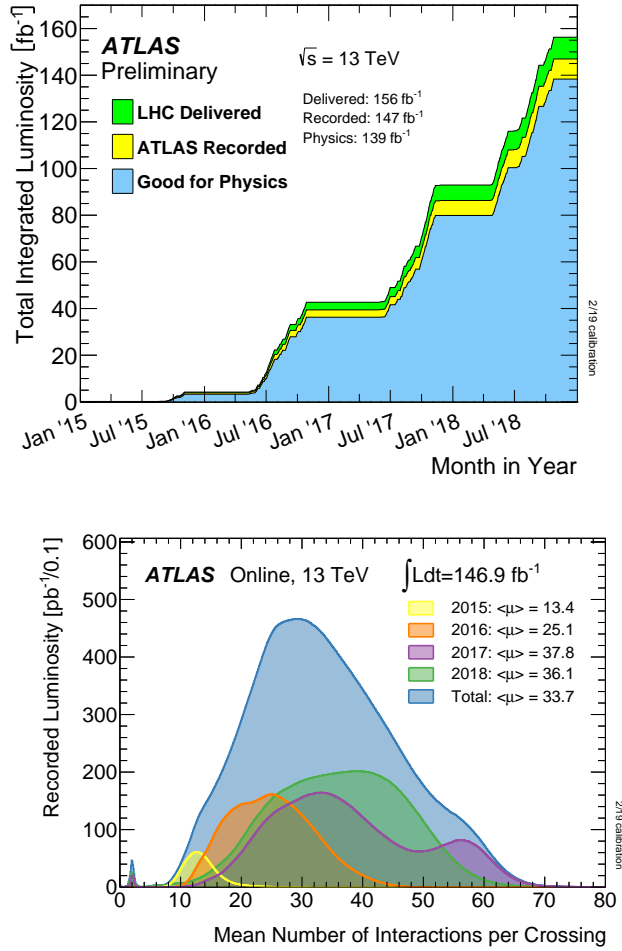


Figure 4.9: Top: Cumulative luminosity versus time, delivered to ATLAS (green), recorded by ATLAS (yellow) and certified to match the quality criteria (blue). Bottom: Luminosity-weighted distribution of the mean number of interactions per bunch crossing. Both taken from Ref. [105].





# 5 Reconstruction of physics objects

To convert the raw detector information into physics objects that can be used in an analysis, dedicated reconstruction and identification algorithms are developed. The ATLAS collaboration implements these algorithms centrally in the ATHENA framework [106], which processes the data that has been stored offline. The reconstructed objects, like electrons, muons, or jets, are subsequently calibrated to correct for detector-specific effects. This chapter presents a brief overview of the reconstruction algorithms that are used, with particular focus on the objects that are used in the analyses presented in this thesis. An exception is flavour tagging, which is discussed in Chapter 6. Furthermore, the calibration procedures are summarised and an overview of the related uncertainties is given.

The reconstruction of physics objects starts with basic high-level detector information, namely tracks and vertices in the ID, tracks in the MS and topological calorimeter clusters. From these quantities, physics objects are built based on their expected detector signature. Since detector signatures are never unique, and the targeted objects therefore face backgrounds from other objects with similar signatures, dedicated identification algorithms exist that combine a multitude of detector information to select a pure collection of object candidates. Different identification working points exist that compromise between signal efficiency and background rejection. Furthermore, objects can be required to be isolated, which means that object candidates are rejected if there is significant additional detector activity in the vicinity of the object. These isolation requirements, typically applied for leptons, help to further suppress background contamination.

## 5.1 Tracks and vertices

The trajectories of charged particles (tracks) are reconstructed from the energy deposits that the particles leave in the ATLAS tracking detectors, the ID and the MS. This section focuses on the track reconstruction in the ID [107]. During Run 2 data taking, about 600 charged particles were produced in each bunch-crossing and their precise reconstruction is of vital importance also to the reconstruction of other objects: reconstructed tracks serve as inputs e.g. for lepton reconstruction, the primary vertex finding, pile-up removal and flavour tagging.

Input to the track reconstruction are three-dimensional space points, constructed from clusters in the Pixel and SCT detectors and drift circles in the TRT. Two algorithms are used:

- An inside-out algorithm starts from the pixel layers and builds the tracks outwards, with the aim of efficiently reconstructing charged particles from the hard-scatter or from the decay of very short-lived particles. The algorithm is seeded using a triplet of hits in the Pixel and SCT detectors. Given the known material and magnetic field configuration, the track is then extrapolated from the seeds to the end of the SCT using a combinatorial Kalman filter [108]. If ambiguities arise, multiple track candidates are considered. An ambiguity solver applies quality requirements to the track candidates and ranks them e.g. according to the fit quality, or applies penalties for missing hits. In a final step, the surviving tracks are extended to the TRT and combined with its hit measurements.
- A complementary outside-in algorithm targets the tracks of charged particles that are produced in decay chains of long-lived particles such as  $b$ - or  $c$ -hadrons, photon conversions or hadronic interactions that don't have sufficient hits in the innermost layers. The algorithm starts from the TRT measurements and consecutively adds silicon hits.

The tracks that are used for physics analyses are required to be within the acceptance of the ID ( $|\eta| < 2.5$ ), have a  $p_T > 0.5$  GeV and pass additional quality criteria such as the number of silicon detector hits and the association to the primary vertex.

Vertices are reconstructed from intersections of tracks. The primary vertex, i.e. the position of the primary  $pp$  interaction per bunch-crossing, is reconstructed using an iterative vertex finding and fitting procedure [109, 110]. The most important quantities that enter the algorithms are the longitudinal and transverse impact parameter of each track,  $z_0$  and  $d_0$ , respectively. Starting from a vertex seed, tracks are added if they are compatible with the vertex position, which is iteratively updated by weighting the candidate tracks according to their compatibility with the vertex position. All tracks that are associated to a given vertex are refit under the assumption that they originate from this vertex. Tracks that are not compatible with the identified vertex serve as seed for an other vertex. This procedure is repeated until no further vertices can be built anymore. Vertices with at least two associated tracks with  $p_T > 0.5$  GeV are valid primary vertex candidates and among them, the one with the largest sum of the squared  $p_T$  of the associated tracks is chosen as the primary vertex.

## 5.2 Topological calorimeter clusters

The main input to many object reconstruction algorithms using calorimeter information, such as electron or jet reconstruction, are so-called topological clusters (topo-clusters) [111]. Topo-clusters are grouped energy deposits in calorimeter cells that are estimated to have originated from the same single particle shower. The algorithm used to perform the topo-cluster grouping is based on the signal significance of adjacent calorimeter cells. Each cell is calibrated to the EM scale using calibration constants from testbeam measurements. The signal significance

used in the clustering is calculated as

$$Z = \left| \frac{E_{\text{cell}}^{\text{EM}}}{\sigma_{\text{noise, cell}}^{\text{EM}}} \right|, \quad (5.1)$$

where  $E_{\text{cell}}^{\text{EM}}$  is the cell energy and  $\sigma_{\text{noise, cell}}^{\text{EM}}$  is the expected cell noise. Seeds are formed by considering cells starting from the second calorimeter layer outwards that have  $Z \geq 4$ . Sequentially, adjacent cells are added if they fulfil  $Z \geq 2$ . If two clusters contain the same cells with  $Z \geq 2$ , the clusters are merged into one cluster. After all cells with  $Z \geq 2$  have been added, a final round of neighbouring cells with  $Z \geq 0$  is added to the cluster. The resulting cluster is afterwards checked for local maxima that exceed an energy of 500 MeV. If more than one such maximum is found, the cluster is split further, sharing the energy of the initial proto-clusters using dedicated weighting techniques.

While the regular topo-clusters are calibrated at the EM scale, an alternative algorithm attempts to calibrate the clusters based on a weighting procedure using cluster properties such as the energy density or the shower width and depth. This Local Cell Weighting (LCW) [111], applies cell weights to account for the fact that the calorimeter has a different energy response for EM and hadronic interactions, for signal losses due to the applied energy thresholds in clustering or signal losses in inactive calorimeter material. Each cluster is then calibrated individually by a product of these different weights. Both cluster types are used in the analyses that are presented in this thesis.

## 5.3 Electrons

Electrons that emerge from the  $pp$  collisions will leave tracks in the ID and deposit all of their energy in the ECAL. In the central region with  $|\eta| < 2.47$ , electrons are therefore reconstructed by combining the tracker and calorimeter information in a dedicated reconstruction algorithm [112, 113]. The electron energy is estimated from the calorimeter, whereas the directional information is taken from the tracker. The path that an electron takes through the subsystems of the ATLAS detector is sketched in Figure 5.1. Electrons that leave the ATLAS detector in the forward regions without tracker coverage are not used in this thesis.

The electron reconstruction chain starts with topo-clusters calibrated at the EM scale. Tracks that are loosely matched to a topo-cluster are refit using a Gaussian Sum Filter [114], that has been optimised for electron track-fitting and allows for non-linear Bremsstrahlung effects. The track-matched topo-clusters are seeds for the creation of a variable-sized super-cluster [115]. This super-cluster can also take into account satellite photon clusters that arise from Bremsstrahlung of the initial electron.

Jets with a high EM fraction, electrons from photon conversions and electrons from semi-leptonic heavy-flavour hadron decays are potential backgrounds in the

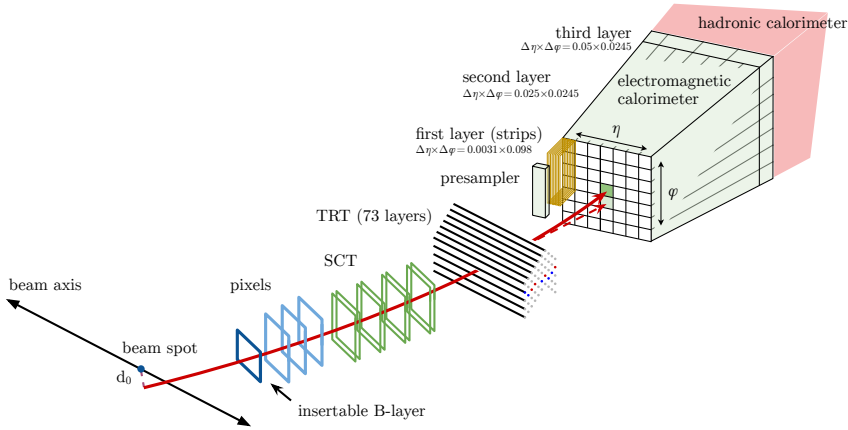


Figure 5.1: Illustration of an electron passing the sub-systems of the ATLAS detector until showering in the ECAL. The electron path is shown using a solid red line, whereas the dashed red line corresponds to a Bremsstrahlung photon which causes an adjacent energy deposit in the ECAL. Figure taken from Ref. [112].

reconstruction of electrons. While conversion electrons and electrons from heavy-flavour hadron decays are real electrons, they are nevertheless regarded as a background for electrons created in the hard scatter. A dedicated identification algorithm is used to reject these backgrounds as much as possible, while at the same time keeping a high efficiency for hard scatter electrons. This algorithm combines multiple variables in a likelihood-based discriminant, using  $Z \rightarrow ee$  and  $J/\Psi \rightarrow ee$  as signal processes and dijet events as background. Three working points (Loose, Medium and Tight) are defined, corresponding to different levels of reduced signal efficiency vs. increased background rejection.

An additional measure that is used to reject electron backgrounds is to require the electron candidate to be isolated from other tracks or energy deposits. Several isolation working points are available, rejecting candidates for which the energy deposits in a cone around the actual electron candidate exceeds a certain (sometimes electron  $p_T$  dependent) threshold.

The energy of the reconstructed electrons is initially determined from the energy deposits inside the super-clusters, that are calibrated to the EM scale using testbeam measurements. Residual corrections are applied to compensate for non-uniformities between the different calorimeter layers, before MC-based correction factors are applied to calibrate the overall energy scale. Remaining differences between data and simulation are corrected by using dedicated energy scale and resolution measurements of standard-candle processes, especially the invariant mass  $m_{ee}$  in  $Z \rightarrow ee$  decays. The total electron efficiency, i.e. the product of the reconstruction, identification and isolation efficiency, is measured in data using a tag-and-probe approach on  $Z \rightarrow ee$  events. Furthermore,  $E_T$  and  $|\eta|$  dependent correction factors

ranging from 1% to 5% are applied to the simulation to match the efficiencies measured in data. Uncertainties related to electrons are mostly at the sub-% level and do not impact the measurements presented in this thesis significantly.

## 5.4 Photons

Photons shower in the ECAL, leaving an energy deposit that is similar to electrons. Due to the fact that they are not electrically charged, however, they do not have a track pointing from the primary vertex to the energy deposits. Given the similarity with electrons, the photon reconstruction is performed in parallel with the electron reconstruction [112, 113]. Two cases of photons are distinguished: converted photons create an  $e^+e^-$  pair inside of the tracker volume that then showers in the ECAL and can be identified by looking for a conversion vertex arising from a pair of tracks with opposite charge. Unconverted photons, on the other hand, leave no track in the ID. An ambiguity solver distinguishes electrons from converted and unconverted photons. Photons are not explicitly used by the measurements that are presented in this thesis.

## 5.5 Muons

At typical LHC energies, muons produced in the hard-scatter are minimum ionising particles. Consequently, they leave a track in the ID, deposit only little energy in the calorimeters (which they traverse) and subsequently create hits in the MS. Given the variety of signatures, multiple ways to reconstruct muons exist, depending on the used subdetector information [116, 117]. Primarily, muon reconstruction algorithms are based on track information from the ID and the MS. Muon tracks are reconstructed in the ID as described in Section 5.1. In the MS, track-candidates are initially formed per station using straight lines. The candidates are subsequently extrapolated across stations assuming parabolic muon trajectories and taking into account spatial information out of the bending plane from the trigger chambers to form three-dimensional track prototypes. These track prototypes are afterwards refit, taking into account the actual magnetic field configuration and also accounting for possible energy losses in the material of the MS. After an ambiguity solving step, the final set of tracks are refit, requiring that the track is loosely compatible with the IP and correcting for energy losses in the calorimeter.

Five different types of reconstructed muons are considered:

- *Combined muons* join the fitted muon tracks from the ID and the MS together. If two individual tracks from ID and MS match, their combined hits are refit as one single track, taking into account the energy loss in the calorimeter. The fit is performed from the outside inwards. Combined muons are the purest and therefore the most commonly used type of reconstructed muons.
- *Inside-out* muons do not rely on a separate track in the MS. Instead, given

a track candidate in the ID, only a couple of loosely aligned MS hits are required. This increases the reconstruction efficiency in regions of poor MS coverage or for low- $p_T$  muons.

- *Muon-spectrometer extrapolated* muons are reconstructed from MS tracks that cannot be matched to an ID track. They have an increased efficiency outside of the ID coverage for  $2.5 < |\eta| < 2.7$ .
- For *segment-tagged muons*, an ID track has to be associated with at least one track segment in the MS, posing more stringent criteria than inside-out muons. No refit is performed, instead the properties of the ID track are used to define the muon.
- *Calorimeter-tagged* muons are reconstructed by extrapolating ID tracks into the calorimeter and searching for energy deposits that are in agreement with expectations from a minimum ionising particle. If such energy deposits are found, the properties of the ID track are used to define the muon.

Most of the muons that are considered in the analyses presented in this thesis are combined muons. Considering also other muon types increases the reconstruction efficiency in poorly instrumented regions of the MS, especially for  $|\eta| < 0.1$ .

Similar to the situation for electron identification, so-called non-prompt muons are a background to muons that originate from the final state of hard scatters. These non-prompt muons are muons that e.g. originate from heavy-flavour hadron decays or additionally from the decays of kaons or pions. Muons from heavy-flavour decays can be differentiated from prompt muons because their track is compatible with the primary vertex position and less isolated. In addition, dedicated identification working points exist to discriminate against muons from kaon or pion decays. Since these decays happen inside of the detector volume, such muon tracks are of worse quality, featuring a 'kink' at the decay vertex. Five working points (Low- $p_T$ , Loose, Medium, Tight and High- $p_T$ ) are defined, corresponding to different levels of reduced signal efficiency vs. increased background rejection. The definition of the working points is based on the type of the reconstructed muon and variables that quantify both the quality of the muon track and its compatibility between ID and MS, if applicable. Different isolation working points, based on calorimeter or tracker information, are available to further reject backgrounds.

The two processes  $Z \rightarrow \mu\mu$  and  $J/\psi \rightarrow \mu\mu$  are used to calibrate the muon energy scale to the permille and the energy resolution to the percent level. Furthermore, the same processes are used in a tag-and-probe approach to measure the reconstruction, identification and isolation efficiencies and apply residual corrections to the simulation to match the efficiencies measured in data. Uncertainties related to muons are small w.r.t. the jet-related uncertainties and do not impact the measurements presented in this thesis significantly.

## 5.6 Jets

Final state quarks and gluons that are produced in  $pp$  collisions fragment and hadronise into colour-neutral particles like pions or kaons. If the quarks and gluons are sufficiently Lorentz boosted, this leads to a collimated spray of these particles, visible in the ATLAS detector through tracks in the ID and energy deposits in the calorimeter. On the experimental side, a jet is defined as a grouping of 4-vectors that represent either calorimeter clusters (calorimeter jet) or tracks in the ID (track jet). Dedicated algorithms exist to perform this grouping and the same algorithms can also be run on the 4-vectors of simulated stable particles in the final state. If the algorithm to perform the jet building is chosen well, a reconstructed jet provides information about the underlying partons that initiated the jet [118]. To optimise this correspondence, a jet algorithm needs to be infrared and collinear safe, which means that the jet definition is not altered by very low energy and very collinear radiation off the initial parton.

### 5.6.1 Jet algorithms

The jets used in this thesis are clustered using the anti- $k_t$  algorithm [119] implemented in the FASTJET package [120]. Inputs to the clustering algorithm are individual 4-vectors of objects that represent calorimeter clusters or tracks. For each pair of objects  $i$  and  $j$ , their relative distance measure  $d_{ij}$  is defined as

$$d_{ij} = \min \left( \frac{1}{p_{T,i}^2}, \frac{1}{p_{T,j}^2} \right) \times \frac{\Delta y_{ij}^2 + \Delta \phi_{ij}^2}{R^2} \quad , \quad (5.2)$$

where  $\Delta y_{ij}$  is the rapidity difference between the particles  $i$  and  $j$ ,  $\Delta \phi_{ij}$  is the difference in azimuthal angle and  $p_{T,i(j)}$  is their transverse momentum. The radius parameter  $R$  is a free parameter of the algorithm. A minimal distance is calculated for each object  $i$  as

$$d_{\min} = \min(d_{iB}, d_{ij}) \quad \text{with} \quad d_{iB} = \frac{1}{p_{T,i}^2} \quad . \quad (5.3)$$

If  $d_{\min} = d_{ij}$ , the two objects  $i$  and  $j$  are clustered together and the distances are recalculated. If  $d_{\min} = d_{iB}$ , the object  $i$  is called a jet. If the jets of an event are sufficiently isolated, the anti- $k_t$  algorithm leads to round jets in  $y - \phi$  space with a radius determined by the free parameter  $R$ . An example of anti- $k_t$  jets in the  $y - \phi$  plane is shown in Figure 5.2.

An other sequential cluster algorithm that is used in this thesis is the  $k_t$  algorithm [121, 122]. The algorithm works similar to the anti- $k_t$  algorithm, but the distance measures are defined as

$$d_{ij} = \min(p_{T,i}^2, p_{T,j}^2) \times \frac{\Delta y_{ij}^2 + \Delta \phi_{ij}^2}{R^2} \quad , \quad \text{and} \quad d_{iB} = p_{T,i}^2 \quad . \quad (5.4)$$

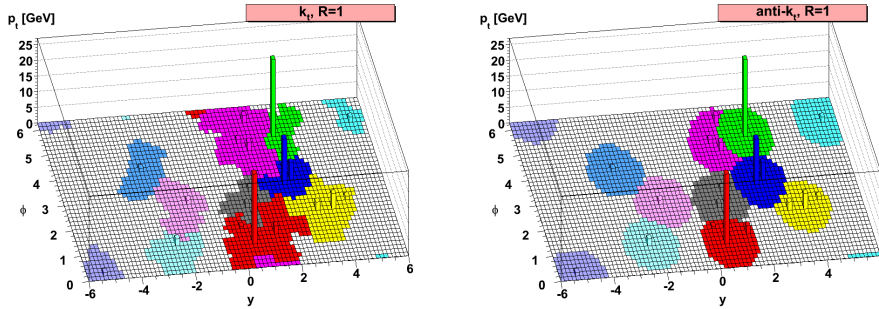


Figure 5.2: Illustration of  $k_t$  (left) and anti- $k_t$  (right) jet reconstruction in the  $y-\phi$  plane on an example event. Taken from Ref. [119].

The jet shapes produced by the  $k_t$  algorithm are less regular than for anti- $k_t$ , as shown in Figure 5.2. In this thesis, the  $k_t$  algorithm is used when attempting to cluster sub-jets because the energy sharing between close-by jets is done more accurately than for anti- $k_t$  jets [118].

The measurements presented in this thesis use three different types of jets that are referred to as small- $R$ , large- $R$  and jets with variable radius (VR).

### 5.6.2 Small- $R$ jets

Small- $R$  jets are anti- $k_t$  jets built from calorimeter clusters using a radius parameter of  $R = 0.4$ . Topo-clusters calibrated at the EM scale are used as inputs to form the 4-vectors used in the clustering. The direction of these 4-vectors is determined by the primary vertex and the barycentre of the topo-cluster and furthermore the clusters are each assumed to be massless.

A dedicated calibration chain [123], illustrated in Figure 5.3, is applied to the small- $R$  jets. This calibration corrects for experimental effects such as pile-up contamination, different calorimeter responses for electromagnetic and hadronic interactions and energy leakage. It assures that the measured jet energy scale (JES) is as close as possible to the particle-level scale. The main steps of the calibration chain are:

- *Pile-up corrections:* The jet  $p_T$  is corrected for contamination from pile-up via a correction that is applied proportional to the jet area. The value of the correction is dependent on the median  $p_T$ -density of all jets in the event. Residual corrections based on the number of primary vertices and the mean interactions per bunch-crossing are applied.
- *MC-based calibration:* Using energy- and  $\eta$ -dependent scale-factors that are derived from inclusive dijet simulations, the jet energy  $E$  is corrected to match the energy for simulated particle-level jets.



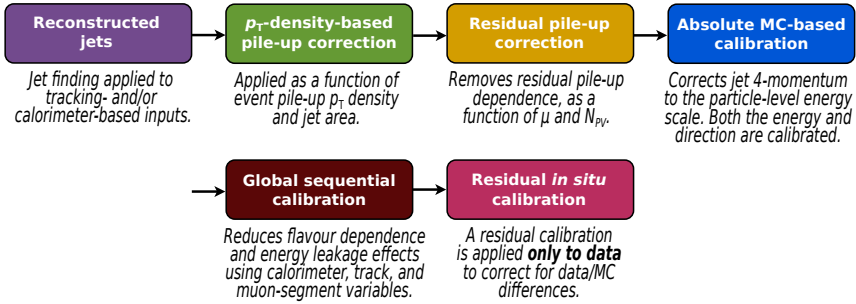


Figure 5.3: Illustration of the jet energy scale calibration chain for small- $R$  jets. Taken from Ref. [123].

- *Global sequential calibration (GSC)*: A series of multiplicative correction factors is applied to correct e.g. for residual jet response differences between quark-initiated and gluon-initiated jets.
- *In-situ calibration*: In a final step, the JES is measured in data and correction factors are applied to correct for residual differences between data and simulation. Such differences can arise e.g. from imperfect descriptions of the detector or the physics processes involved such as the description of the jet formation, pile-up or the underlying event. The measurement is performed by looking at well-measured reference objects balancing in the transverse plane against jets. Such reference objects include photons or leptonically decaying  $Z$  bosons. Additionally, multijet events can be used. The result of such balance measurements of the JES response is shown in Figure 5.4. This correction is applied only to data.

After the JES calibration, the jet energy resolution (JER) is measured in data using dijet balance measurements. The JER noise term is constrained using a measurement that applies the random cones method [123]. The measured and simulated relative JER,  $\sigma(p_T)/p_T$ , is shown in Figure 5.4, as a function of the jet  $p_T$ . As can be seen in the figure, the simulated JER is better than the measured JER. To match the values measured in data, a residual jet energy smearing is therefore applied to the simulation. A dedicated jet vertex tagger (JVT) combines multiple track, jet and vertex variables per event into an output score that is used to differentiate between hard-scatter jets and jets from pile-up [124]. Jets with  $p_T < 120$  GeV and  $|\eta| < 2.5$  are removed if the tagger does not associate them with the primary vertex of the collision.

### 5.6.3 Large- $R$ jets

Large- $R$  jets are anti- $k_t$  jets built from LCW topo-clusters using a radius parameter of  $R = 1.0$ . An overview of the reconstruction and calibration chain for large- $R$

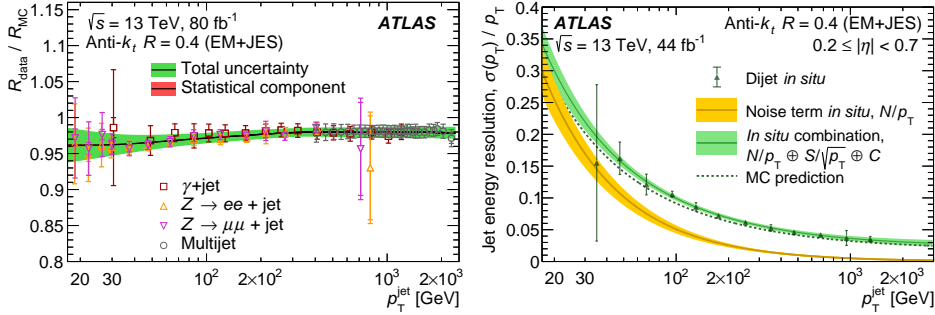


Figure 5.4: Left: Data to simulation ratio of the jet energy response before correction as a function of the jet  $p_T$ , obtained from balance measurements. Right: Relative jet energy resolution as a function of the jet  $p_T$ . Figures taken from Ref. [123].

jets is shown in Figure 5.5. Similar to small- $R$  jets, its topo-clusters are assumed to be massless and the input 4-vectors are built by pointing the barycentre of each cluster to the primary vertex.

Due to their large size, large- $R$  jets are particularly sensitive to contamination from pile-up and the underlying event. Dedicated grooming techniques, that aim at resolving the underlying large- $R$  jet substructure, are used to remove such contamination. The grooming procedure used for the large- $R$  jets considered in this thesis is referred to as trimming [126] and illustrated in Figure 5.6. The implementation used for the large- $R$  jets of this thesis works as follows [127]:

- The initial constituents of the large- $R$  jet are reclustered into sub-jets using the  $k_t$  algorithm with a radius parameter of  $R = 0.2$ . The  $k_t$  algorithm is chosen due to its ability to better describe the energy sharing between close-by jets.
- If a sub-jet carries less of 5% of the energy of the total large- $R$  jet, it is removed.
- The constituents that survive the trimming procedure make up the groomed large- $R$  jet.

In contrast to small- $R$  jets, large- $R$  jets are often used to reconstruct hadronically decaying resonances like top-quarks,  $W$ -,  $Z$ - or Higgs bosons within one single object. A precise determination of the large- $R$  jet mass is therefore very important. Since the large- $R$  jet is calculated from calorimeter information, initially its mass is estimated from the 4-vector sum of all topo-clusters. This mass is referred to as the calorimeter mass  $m_{\text{calo}}$ . For highly boosted objects however, the granularity of the calorimeter is too coarse and the opening angle between individual particles, that enters the mass estimation, can not be calculated reliably. In such cases, it is advantageous to make use of tracker information, which has excellent spatial resolution and can resolve very close-by tracks. The track-assisted mass  $m_{\text{TA}}$  [129]

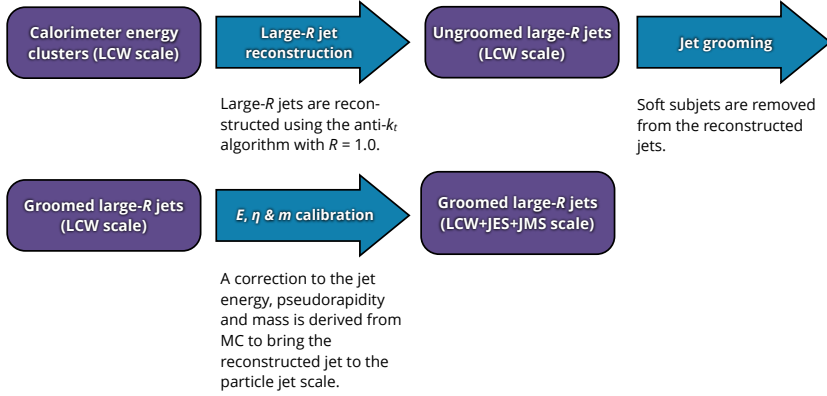


Figure 5.5: Illustration of the large- $R$  jet reconstruction and calibration procedure. Adapted from Ref. [125].

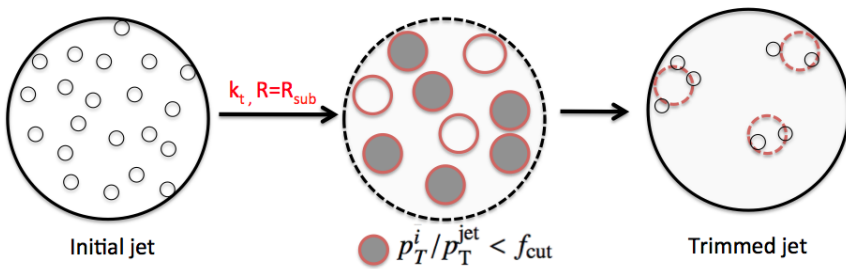


Figure 5.6: Illustration of the trimming procedure for large- $R$  jets. Taken from Ref. [128].

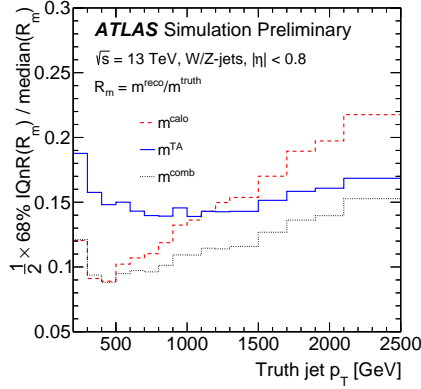


Figure 5.7: Fractional large- $R$  jet mass resolution for the calorimeter, the track-assisted and the combined jet mass as a function of the simulated jet  $p_T$ . Taken from Ref. [129].

is calculated from the 4-vectors of all tracks that are associated to the large- $R$  jet [130, 131]. A residual correction factor proportional to  $p_T^{\text{calo}}/p_T^{\text{tracker}}$  is applied because the neutral particles of the jet do not leave tracks in the ID. Figure 5.7 shows the jet mass resolutions for both  $m_{\text{calo}}$  and  $m_{\text{TA}}$  as a function of the large- $R$  jet  $p_T$  for simulated  $W/Z \rightarrow qq$  jets. This thesis uses a weighted average of both masses to maximise performance over the whole jet  $p_T$  range:

$$m_{\text{comb}} = w_{\text{calo}} \times m_{\text{calo}} + w_{\text{TA}} \times m_{\text{tracker}} \times \frac{p_T^{\text{calo}}}{p_T^{\text{tracker}}} \quad . \quad (5.5)$$

The weights  $w_{\text{calo}}$  and  $w_{\text{TA}}$  are chosen such that they minimise the overall variance of  $m_{\text{comb}}$ . An imposed constraint of  $w_{\text{calo}} + w_{\text{TA}} = 1$  ensures that the combined mass is calibrated automatically once the two individual masses are calibrated.

Similar to small- $R$  jets, the trimmed large- $R$  jets are calibrated for their properties to match particle-level jets. In addition to the jet energy, it is also of importance to calibrate the large- $R$  jet mass. Using correction factors obtained from simulation, the large- $R$  jet  $\eta$ , its energy and its mass are calibrated sequentially. The validity of the MC-based calibrations is checked in dedicated  $R_{\text{trk}}$  measurements that look at the ratio of different jet properties estimated both from calorimeter and tracker information. For the large- $R$  jet  $p_T$  and mass, these ratios are constructed as

$$R_{\text{trk}}^{p_T} = \left\langle \frac{p_T^{\text{calo}}}{p_T^{\text{track}}} \right\rangle \quad \text{and} \quad R_{\text{trk}}^m = \left\langle \frac{m^{\text{calo}}}{m^{\text{track}}} \right\rangle \quad . \quad (5.6)$$

The advantage of using the  $R_{\text{trk}}$  ratio instead of bare quantities is that the ratios are

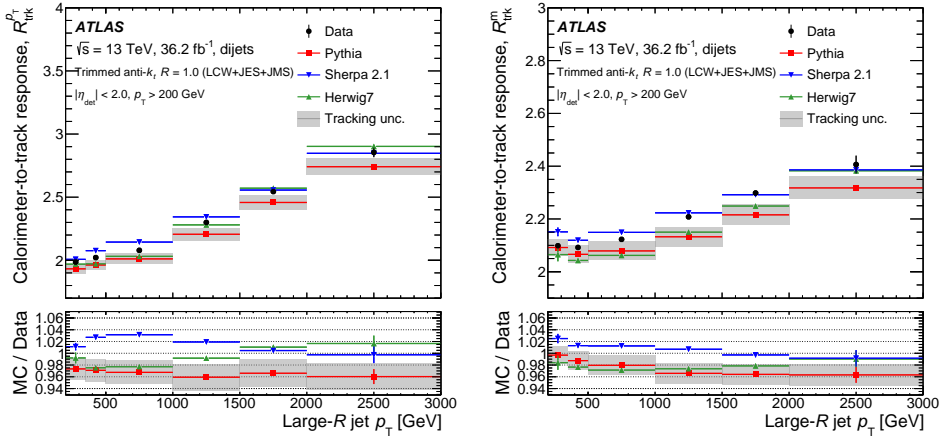


Figure 5.8:  $R_{\text{trk}}$  measurements for the large- $R$  jet  $p_T$  (left) and mass (right) as a function of large- $R$  jet  $p_T$  for large- $R$  jets with a mass to  $p_T$  ratio of 0.2. Taken from Ref. [125].

independent of any physics process mismodelling as long as it affects both the track and the calorimeter estimate in the same way. A comparison of  $R_{\text{trk}}$  in simulation and data is used to validate the MC-based calibrations for the large- $R$  JES and the jet mass scale (JMS). The results of this comparison are shown in Figure 5.8. The observed differences are not corrected in simulation, but uncertainties are estimated to cover both the difference between data and simulation and the difference between the various MC generators. These uncertainties are between 5% and 10%.

The large- $R$  jet energy resolution (JER) and the jet mass resolution (JMR) are not calibrated, i.e. no residual smearing is applied to make simulation in agreement with data. Dedicated uncertainties are applied in the analyses, however, that cover the observed differences. For the large- $R$  JER uncertainty, a 2% absolute smearing is applied to the simulated jets, whereas the JMR is smeared in a way that the relative jet resolution increases by 20% in order to estimate the JMR uncertainty. Dedicated resolution maps are estimated from simulation to perform this uncertainty calculation and depend on the jet type and its kinematic properties.

### 5.6.4 Variable- $R$ jets

Variable- $R$  jets are reconstructed using the anti- $k_t$  algorithm with a radius parameter  $R$  that depends on the jet  $p_T$  itself [132]. In this case, tracks are used as input 4-vectors and  $R(p_T)$  is chosen such that the radius shrinks as the jet  $p_T$  increases:

$$R(p_T) = \frac{\rho}{p_T} \quad . \quad (5.7)$$

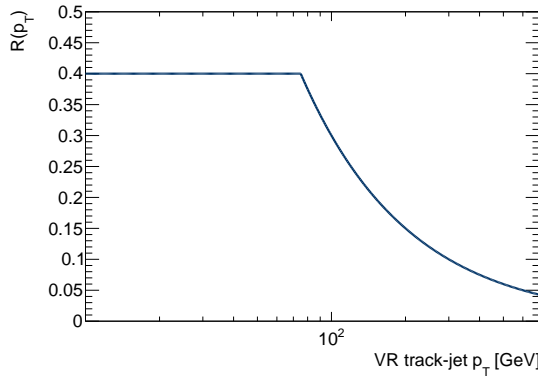


Figure 5.9: Effective radius  $R$  of VR track-jets as a function of the jet  $p_T$ .

The parameter  $\rho$  can be freely chosen and is adjusted depending on the physics goal. In this thesis, VR track-jets are used to perform  $b$ -tagging in boosted environments, where jets have a high Lorentz boost and get very close to each other. The shrinking size, in combination with the good spatial resolution of the tracker, makes VR track-jets ideal for such environments. The radius parameter  $R(p_T)$  is bound to be in the range  $[0.02, 0.4]$ , and a value of  $\rho = 30$  GeV is used. These values are optimised for double  $b$ -labelling efficiency in boosted  $H \rightarrow b\bar{b}$  decays [133]. Figure 5.9 shows the effective cone size of the VR track-jets as a function of their  $p_T$ .

As the tracks entering the VR track-jets are calibrated, no residual jet calibration is applied. Due to the missing information from neutral jet constituents, however, the energy scale of track-jets is on average off by a factor of  $1/3$  with respect to calorimeter jets.

## 5.7 $\tau$ leptons

With a lifetime of  $\sim 290$  fs [13],  $\tau$  leptons decay after only travelling a mean path of  $\sim 85 \mu m$ . In 35% of cases, they decay leptonically into either an electron or a muon and two neutrinos  $\tau \rightarrow \ell \nu_\ell \nu_\tau$ . In the remaining 65% of cases, they decay hadronically, yielding narrow jets that can be identified using dedicated multivariate algorithms [134]. Hadronically decaying  $\tau$  leptons are not explicitly targeted by the analyses presented in this thesis. They are considered in the overlap removal algorithms between different objects, however.

## 5.8 Missing transverse energy

The only SM particles that cannot be detected with the ATLAS detector are neutrinos, since they interact only weakly and interaction cross-sections with

matter are extremely small. Information about the presence of neutrinos can nevertheless be inferred indirectly, making use of energy/momentum conservation in the transverse plane. To good approximation, the incoming partons do not carry any initial transverse momentum, therefore the vector sum of all particles should sum up to zero in the transverse plane. The missing transverse energy is defined as the absolute value of this momentum imbalance, calculated from its components along the  $x$ - and  $y$ -axes as

$$E_T^{\text{miss}} = \sqrt{(E_x^{\text{miss}})^2 + (E_y^{\text{miss}})^2} \quad . \quad (5.8)$$

The individual components  $E_x^{\text{miss}}$  and  $E_y^{\text{miss}}$  are calculated by summing over all contributions from the calibrated final state objects and taking into account an additional track-based soft-term that quantifies tracks that are not associated to any object but compatible with the primary vertex:

$$E_{x/y}^{\text{miss}} = -E_{x/y}^{\text{miss,soft, trk}} - \sum_{i \in \text{objects}} E_{x/y}^{\text{miss},i} \quad . \quad (5.9)$$

A dedicated overlap removal is applied to avoid double counting of signatures that can be identified as multiple object types. Because  $E_T^{\text{miss}}$  is dependent on the entire event activity, it is one of the most imprecise objects. Systematic uncertainties on all objects that enter the  $E_T^{\text{miss}}$  calculation are propagated by recalculating  $E_T^{\text{miss}}$  for each uncertainty. In addition, uncertainties related to the track-based soft term are estimated from processes where no  $E_T^{\text{miss}}$  is expected, such as  $Z \rightarrow \ell\ell$  with no jets in the event. The scale of the  $E_T^{\text{miss}}$  soft term is estimated in topologies where  $E_T^{\text{miss}}$  recoils against the reconstructed  $Z$ -boson in the transverse plane. The  $E_{x/y}^{\text{miss}}$  resolution is measured to be about 10 GeV for low pile-up values of  $\mu \sim 5$  to about 20 GeV for  $\mu \sim 40$  [135].

While in the SM only neutrinos generate true  $E_T^{\text{miss}}$ , any particle-type that is produced in the  $pp$  collision and has an extremely weak interaction cross-section with the detector material will act as a source of  $E_T^{\text{miss}}$ . Therefore  $E_T^{\text{miss}}$  is also a powerful observable to search for weakly interacting dark matter candidates or supersymmetric particles.





# 6 Flavour tagging

The identification of jets that originate from heavy-flavour quarks, referred to as flavour tagging, is a vital tool for many measurements and searches for BSM physics. If the aim is to identify jets that originate from the hadronisation of a  $b$ -quark, the procedure is referred to as  $b$ -tagging. Consequently, the identifications of jets that originate from the hadronisation of a  $c$ -quark is known as  $c$ -tagging. The analyses presented in this thesis, for example, make use of  $b$ -tagging to identify  $H \rightarrow b\bar{b}$  decays. Furthermore, as the top quark decays nearly exclusively as  $t \rightarrow Wb$ ,  $b$ -tagging also plays a crucial role in  $t\bar{t}H$  measurements or in top-quark physics in general.

This chapter introduces the basic properties that are used to identify jets originating from heavy-flavour quarks and discusses the tagging algorithms that are deployed within the ATLAS collaboration. The chapter concludes with a measurement of the  $b$ -tagging efficiency in dense jet-environments, which are created e.g. in hadronic decays of boosted objects.

In the remainder of the thesis, jets are labelled depending on the flavour of the particle that initiated them, i.e.  $b$ -jets,  $c$ -jets,  $\tau$ -jets or light-flavour jets ( $u, d, s$  quarks or gluons). In simulated jets, this labelling is performed by looking subsequently for  $b$  quarks,  $c$  quarks or  $\tau$  leptons with  $p_T > 5$  GeV within a cone of  $\Delta R = 0.3$  around the jet axis. Searching in the listed order, if a corresponding particle is found, the jet is labelled accordingly. Otherwise the jet is labelled a light-flavour jet. In contrast, if any jet, simulated or data, passes the operating point of a tagging algorithm, it is labelled as *tagged*, e.g.  $b$ -tagged,  $c$ -tagged or untagged.

## 6.1 Properties of jets originating from heavy-flavour quarks

Jets that originate from the hadronisation of heavy-flavour quarks have specific properties that are used to identify them. This section gives a brief overview of these properties, focusing mainly on  $b$ -jets.

A  $b$ -quark hadronises into a  $b$ -flavoured hadron. This process happens at energies at which the strong coupling constant  $\alpha_s$  is large and consequently cannot be calculated using perturbation theory. Instead, so-called fragmentation functions are used to encode the probability for a certain  $b$ -hadron to be produced from an outgoing  $b$ -quark. The fragmentation functions are not universal, they e.g. show a

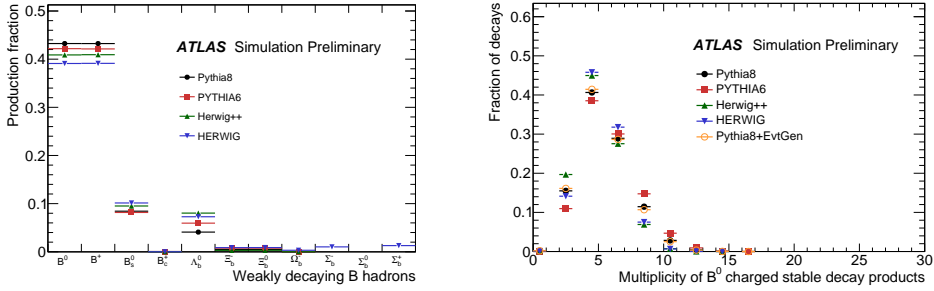


Figure 6.1: Left: Production fraction of weakly decaying  $B$  hadrons as predicted by various MC generators. Right: Multiplicity of charged stable particles from a  $B^0$  decay as predicted by various MC generators. Both distributions are extracted from simulated  $t\bar{t}$  events produced from  $pp$  collisions at  $\sqrt{s} = 8$  TeV. Taken from Ref. [137].

dependence on the  $p_T$  spectrum of the produced  $b$ -hadron [136]. Figure 6.1 shows the production fractions for various weakly decaying  $b$ -hadrons in a sample of simulated  $t\bar{t}$  events produced from  $pp$  collisions at  $\sqrt{s} = 8$  TeV.

For 90% of  $b$ -quarks, the produced hadron is a meson, that most of the time contains a light quark of the first generation in addition. Whereas the fraction of produced ( $bs$ ) mesons is about 10%, the probabilities for a ( $bc$ )- or ( $bb$ ) bound-state are negligibly small. Often, excited states are produced, that then deexcite to the ground state via the electromagnetic or the strong interaction. As these deexcitations happen sufficiently quick, for the purpose of this thesis it is enough to directly consider the production of a ground-state hadron, which is compatible with the primary collision vertex. Most of the produced  $b$  hadrons have an invariant mass of about 5 GeV [13], which is larger than for  $c$ - or light-flavour hadrons and is used to distinguish them.

The  $b$  hadrons subsequently decay via the weak interaction. As off-diagonal CKM elements are small,  $b$  hadrons have a relatively large lifetime  $\tau$  of about 1.5-1.6 ps [136] for the most abundant species. A  $b$  hadron with a momentum of 50 GeV therefore flies 4-5 mm, before decaying, which leads to a displaced secondary vertex inside of the jet.

Because in the CKM matrix,  $|V_{cb}|^2$  is more than 100 times larger than  $|V_{ub}|^2$ , most of the  $b$  hadrons decay into  $c$  hadrons. These  $c$ -hadrons will decay further, with a smaller lifetime, which leads to a tertiary vertex in the jet, that is displaced both with respect to the primary and the secondary vertex. A typical  $b$ -hadron decay chain with secondary and tertiary vertex inside of a jet is illustrated in Figure 6.2. Finding such a topology of displaced secondary and tertiary vertices is indicative of the presence of a  $b$ -hadron and is consequently used for  $b$ -tagging. As shown in Figure 6.1 for  $B^0$  decays, on average, about 5 stable charged particles are produced in the decay of  $b$  hadrons. This is an other quantity that is used to discriminate

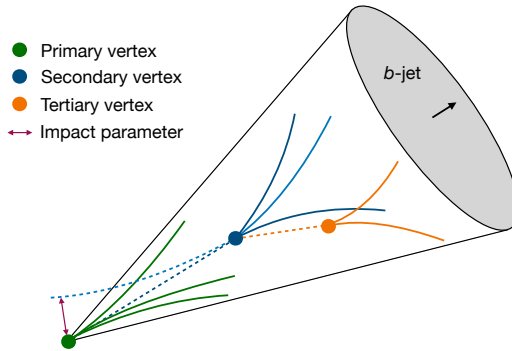


Figure 6.2: Illustration of a  $b$ -jet with tracks originating from the fragmentation at the primary vertex and the tracks from the  $b$ - and  $c$ -hadron decay at the secondary and tertiary vertex, respectively.

against  $c$ -jets and light-jets, where this number is smaller on average. Moreover,  $b$ -hadron decay chains have more weak decays and therefore the fraction of  $b$ -jets containing electrons or muons from leptonic decays is enhanced to  $\sim 40\%$ .

The fragmentation functions for  $b$ -hadrons are significantly harder than for  $c$ - or light-flavour hadrons. As a result, in  $b$ -jets, the  $b$  hadron carries on average about 80% of the jet's momentum as is shown in Figure 6.3. This property is used to discriminate  $b$ -jets against  $c$ -jets and light-jets, where this fraction is on average significantly smaller.

Similar to  $b$ -jets,  $c$ -jets also feature secondary vertices that are displaced with respect to the primary vertex. The lifetime of  $c$  hadrons is on average smaller than for  $b$  hadrons but shows a large variety among the most produced species. This makes it difficult to distinguish  $b$ -jets and  $c$ -jets.

For light-flavour jets, most of the tracks are produced in the fragmentation process and are compatible with the primary vertex. Displaced tracks can nevertheless arise due to poor track reconstruction or interactions with the detector material.

## 6.2 Flavour-tagging algorithms

To perform flavour tagging, multiple algorithms are used that each target different properties to separate  $b$ -jets,  $c$ -jets and light-flavour jets. The output of these baseline taggers is further combined into a high-level multivariate classifier, that forms a final discriminant whose value is used to perform the tagging of each jet. This section focuses on the  $b$ -tagging algorithms that are used in this thesis.

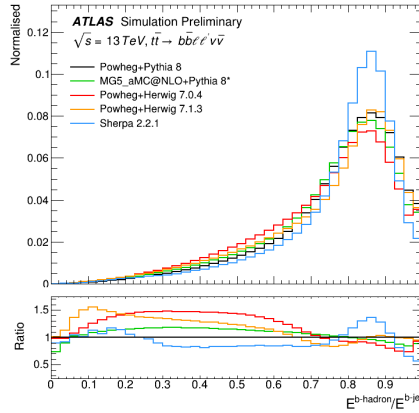


Figure 6.3: Fraction of the  $b$ -jet energy that is carried by the  $b$  hadron as predicted by various MC generators. The jets are clustered using the anti- $k_t$  algorithm with a radius parameter of  $R = 0.4$  and all stable hadrons, leptons and photons enter the jet energy calculation. Taken from Ref. [138].

**Inputs to the algorithms** The most important input for  $b$ -tagging algorithms are tracks. To determine if a certain jet is  $b$ -tagged, the jet-axis is used as reference around which tracks are geometrically matched to the jet. The  $\Delta R$  requirement to match a track to a jet varies with the jet  $p_T$ , taking into account that the decay products of high- $p_T$   $b$  hadrons are more collimated than the ones from low- $p_T$   $b$  hadrons. Ambiguities between close-by jets are resolved by matching the tracks uniquely to the closest jet axis. The signed impact parameters of the tracks are then calculated with respect to the jet axis that they are matched to.

**Algorithms based on impact parameters** As sketched in Figure 6.2, tracks originating from a  $b$ -hadron decay are not compatible with the PV. Two algorithms make use of the signed impact-parameter significances to construct a likelihood-based discriminant that is used for tagging. The IP2D algorithm uses the transverse impact-parameter significance, whereas the IP3D algorithm uses both the transverse and the longitudinal impact parameter significances [139]. Per-track likelihood-ratios are defined to separate  $b$ -jets from  $c$ -jets,  $b$ -jets from light-flavour jets and  $c$ -jets from light-flavour jets. The PDFs that enter the likelihood ratios are obtained from simulation.

**Secondary vertex finders** The SV1 algorithm [140] reconstructs a single secondary vertex inside a jet. Starting from tracks within a  $\Delta R$  cone around the jets axis, two-track vertex candidates are formed. Tracks that are compatible with photon conversions, interactions with the hadronic material or the decay of long-lived

particles like  $K_S$  and  $\Lambda$  are rejected. The two-track vertices are iteratively combined until a single vertex is found. From this vertex, properties like the invariant vertex mass, the number of tracks associated to it, or the distance between the primary and the secondary vertex are calculated and later used as inputs for the high-level taggers.

**Decay-chain multivertex algorithm** The JETFITTER algorithm [141] reconstructs full  $b$ - and  $c$ -hadron decay chains using a Kalman filter. Assuming that the secondary and tertiary vertex lie on a single line that approximates the  $b$ -hadron flight path, vertices are reconstructed, even if they have only one associated track. From the reconstructed vertices, topological variables similar to the ones for SV1 are calculated and used as inputs for the high-level taggers.

**High-level algorithms** The information that is provided by the individual tagging algorithms is used as input to multivariate classifiers in order to form a final tagging discriminant. Two algorithms are used in this thesis. The first one, MV2 [139], is a boosted decision tree, that is trained to discriminate  $b$ -jets from a background of 7%  $c$ -jets and 93% light-flavour jets from simulated  $t\bar{t}$  and  $Z'$  events. In addition to the tagger-related input variables, the  $p_T$  and  $|\eta|$  of each jet is also used to exploit possible correlations with other input variables. In order not to train the tagger to use differences in the distributions of  $p_T$  and  $|\eta|$  to discriminate  $b$ -jets from  $c$ -jets and light-flavour jets, and thereby bias the tagger on the kinematics of the training samples, the distributions are reweighted for  $b$ -jets and  $c$ -jets to match the ones of light-flavour jets before training. A second algorithm, DL1 [139], consists of a feed-forward neural network with three output nodes, corresponding to the probabilities that a jet is a  $b$ -jet,  $c$ -jet or a light-flavour jet. The DL1 tagger uses the same inputs as MV2 and considers in addition variables that are tailored for  $c$ -tagging. Since the training happens with multiple output nodes, the final  $b$ -tagging discriminant is a Neyman-Pearson ratio of the output probabilities. The background in this ratio is a combination of  $c$ -jets and light-flavour jets and the admixture of  $c$ -jets is a tuneable parameter. It is set to 8%, which is found to be a suitable compromise between  $c$ -jet and light-flavour jet rejection.

Different tagger working points, that correspond to different levels of  $b$ -jet efficiency vs.  $c$ -jet and light-flavour jet rejection rate are maintained. The rejection rate is defined as the inverse mistagging efficiency. The working points that are used in this thesis are single-cut working points, where a fixed threshold on the discriminant variable is used. A jet that has a score above the threshold is labelled as  $b$ -tagged, a jet with a score below is labelled as untagged. An example plot of the MV2 score, together with the indicated single cut working points at 85%, 77%, 70% and 60%  $b$ -jet efficiency, is shown in Figure 6.4. The efficiencies are determined from a simulated sample of 1-lepton  $t\bar{t}$  events.

The efficiency for each working point is measured in data in order to calibrate the performance on simulation. The calibrations of both the  $b$ -tagging efficiency as well as the  $c$ -jet and light-flavour jet mistagging efficiency are performed by selecting

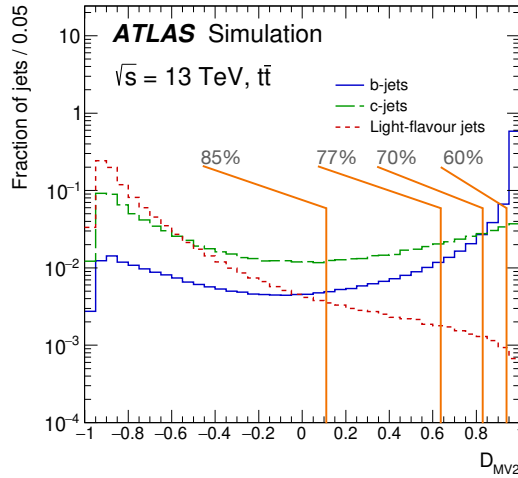


Figure 6.4: Output score distribution of the MV2 tagger for simulated small- $R$  jets from  $t\bar{t}$  events. The various single-cut working points are indicated. Adapted from Ref. [142].

events with enriched  $b$ -jet,  $c$ -jet or light-flavour jet content, respectively [142–144]. The calibrations result in jet- $p_T$  dependent simulation scale factors, that correct for the observed efficiency differences. The uncertainties from the efficiency measurements are translated into uncertainties on the scale factors and are considered by the individual analyses that make use of  $b$ -tagging.

The fragmentation and hadronisation of heavy-flavour hadrons happens at energies for which the strong coupling constant is large and perturbation theory does not apply. Consequently, these processes are modelled using parametric models that are implemented in the parton shower generator. This modelling directly influences the simulated  $b$ -tagging efficiency. Since the approaches differ from MC generator to MC generator, it is important that the correct reference is used when applying the simulation scale factors to correct the simulated  $b$ -tagging efficiency to the one measured in data. The scale factors are conventionally provided with respect to a reference generator, in this case PYTHIA. Dedicated 'MC-to-MC' scale factors exist to convert the scale factors to be applicable to other MC parton shower generators like SHERPA or HERWIG.

A simulation-based procedure extrapolates the calibrations towards high jet  $p_T$  of  $\mathcal{O}(\text{TeV})$ , where the data-driven calibration methods do not have enough events to work reliably [145]. The procedure estimates an uncertainty that is added when calibration scale factors are used for jets with higher  $p_T$  than the ones for which the  $b$ -tagging calibration measurement has been performed.

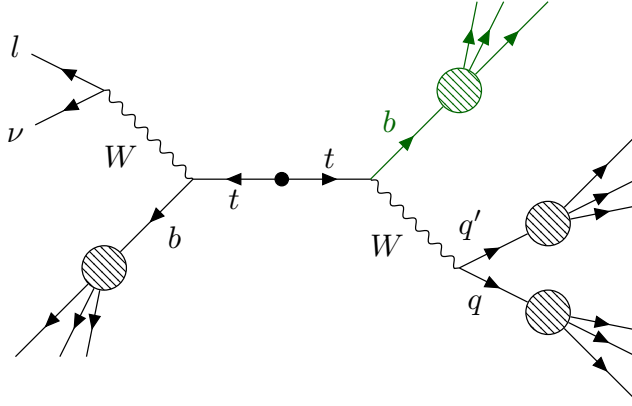


Figure 6.5: Sketch of a leading order 1-lepton  $t\bar{t}$  event in the transverse plane. The central dot marks the interaction point from which the two top quarks emerge and subsequently decay. The  $b$ -jet from the  $t \rightarrow Wb \rightarrow qq'b$  decay (green) is used as a probe to measure the  $b$ -tagging efficiency in dense jet-environments.

### 6.3 Measurement of the $b$ -tagging efficiency in dense jet-environments

The  $b$ -tagging efficiency for  $b$ -jets is conventionally measured using geometrically well isolated jets in dilepton  $t\bar{t}$  events [142]. The measurement shows good agreement between the efficiency from data and from simulation with uncertainties ranging from 1% to 8%, depending on the jet  $p_T$ . For measurements of boosted objects that involve  $b$ -tagging of the decay products, however, it is important to verify that the efficiencies in data and simulation also agree in events where many jets are geometrically close to each other. In such events, additional activity in the calorimeter from close-by jets can cause the jet axis to shift with respect to the  $b$ -hadron flight directions, which leads to a reduction of the  $b$ -tagging efficiency.

This section presents a measurement of the  $b$ -tagging efficiency as a function of variables that are sensitive to such dense jet-environments. For this purpose, 1-lepton  $t\bar{t}$  event candidates are selected in data. Figure 6.5 shows a sketch of the leading order event topology of such 1-lepton  $t\bar{t}$  events. If the top quark is sufficiently boosted, the  $b$ -jet from the  $t \rightarrow Wb \rightarrow qq'b$  decay gets geometrically close to the two jets from the hadronic  $W$ -boson decay to create dense jet-environments. For this reason, this  $b$ -jet is used as a probe to measure the  $b$ -tagging efficiency in dense jet-environments. The measurement that is presented in this section improves upon the methodology developed in Ref.s [146, 147], and is the first measurement of its kind using the full Run 2 data set collected by the ATLAS experiment.

### 6.3.1 Simulated samples

As shown in Figure 6.5, the 1-lepton  $t\bar{t}$  decay leads to final states with at least four jets, exactly one charged lepton and missing transverse energy from the neutrino. On the leptonic side, only  $W \rightarrow e\nu$  or  $W \rightarrow \mu\nu$  decays are explicitly targeted by the measurement. A variety of other processes form a background to the  $t\bar{t}$  signal. The main backgrounds are single top and  $W$ +jets production, but also  $Z$ +jets, diboson and  $t\bar{t} + V$  production are considered. The individual contributions of the signal and the backgrounds are estimated from MC simulations. The used generators are similar to what is described in more detail in Chapter 7.

### 6.3.2 Object and event selection

To record the events of interest, a set of unprescaled single electron or single muon triggers, that target the leptons from the  $W \rightarrow \ell\nu$  decay, is used. The specific lepton selection is similar to what is described in more detail in Chapter 7. The jets used for this measurement are small- $R$  jets with a radius parameter of  $R = 0.4$ . In contrast to the jets used for the other analyses presented in this thesis, they are not only built from topological calorimeter clusters, but instead a combination of calorimeter and tracker information is used to form them. These *particle flow* jets [148] show an improved resolution and pile-up stability and are the new default jet collection for the ATLAS collaboration<sup>1</sup>. Only central jets with  $|\eta| < 2.5$  and  $p_T > 20$  GeV, that are compatible with the hard-scatter vertex, are considered.

To select a pure  $t\bar{t}$  sample, events are required to have at least four jets and exactly one electron or muon that fired the event trigger. To suppress the contamination from QCD multijet events to a negligible minimum, the lepton needs to have  $p_T > 40$  GeV, and in addition it is required that  $E_T^{\text{miss}} > 30$  GeV and  $E_T^{\text{miss}} + m_T^W > 60$  GeV. The transverse mass of the  $W$ -boson candidate  $m_T^W$  is defined as

$$m_T^W = \sqrt{2p_T^\ell E_T^{\text{miss}}(1 - \cos(\phi_{\ell, E_T^{\text{miss}}}))} \quad . \quad (6.1)$$

The single most important task of the analysis is to select the probe jets, i.e. the  $b$ -jets from the (hadronic)  $t \rightarrow Wb \rightarrow qq'b$  decay in each event, as accurately as possible, without checking beforehand whether the probe jet is  $b$ -tagged or not. This is done in three steps:

1. The jets in the event are assigned to the leading order  $t\bar{t}$  decay products by minimising a  $\chi^2$  function that uses invariant mass constraints.
2.  $b$ -tagging requirements are applied on the jets that are not assigned to be the probe jet.
3. The output score of a boosted decision tree, which is trained to discriminate events with correct probe jet assignment from events with wrong assignment,

---

<sup>1</sup>For the  $VH, H \rightarrow b\bar{b}$  analyses presented in this thesis, no significant improvement from using particle flow jets is expected, based on preliminary comparison studies.



is used to further purify the probe jet collection.

The  $\chi^2$  function, which is minimised in order to assign the reconstructed jets to the  $t\bar{t}$  decay products, is defined as

$$\chi^2 = \underbrace{\left[ \frac{m_{jj} - m_W}{\sigma_W} \right]^2}_{\text{hadronic } W \text{ candidate}} + \underbrace{\left[ \frac{m_{jjj} - m_{jj} - m_{th-W}}{\sigma_{th-W}} \right]^2}_{\text{hadronic top candidate}} + \underbrace{\left[ \frac{m_{j\ell\nu} - m_{tl}}{\sigma_{tl}} \right]^2}_{\text{leptonic top candidate}}, \quad (6.2)$$

where  $m_{jj}$  is the invariant dijet mass for the jets that are assigned to have originated from the hadronically decaying  $W$ -boson,  $m_{jjj}$  the invariant mass of the hadronically decaying top-quark candidate and  $m_{j\ell\nu}$  the invariant mass of the lepton, the neutrino and the jet that is assigned to have originated from the leptonically decaying top-quark candidate. To calculate this invariant mass  $m_{j\ell\nu}$ , the complete neutrino momentum is needed. For the  $x$ - and  $y$ -direction, the  $E_T^{\text{miss}}$  components are taken. The neutrino  $z$ -momentum  $p_z^\nu$  is reconstructed by using a  $W$ -boson mass constraint. In case two solutions for  $p_z^\nu$  exist, both of them are used in the  $\chi^2$  minimisation. If no solution exists, the  $E_T^{\text{miss}}$  vector is rotated in the transverse plane until the equation has a solution.

The central values and uncertainties for the  $\chi^2$  function, which are marked blue in the equation, are derived from a  $t\bar{t}$  simulation by matching the outgoing final state quarks geometrically to the reconstructed jets. On the hadronic top-quark decay side, the difference between the reconstructed top-quark mass  $m_{jjj}$  and the reconstructed  $W$ -boson mass  $m_{jj}$  is used instead of  $m_{jjj}$  as a second term in the equation, because  $m_{jj}$  and  $m_{jjj}$  are correlated. This  $\chi^2$  score is calculated for each possible jet assignment and the pairing with the lowest  $\chi^2$  is chosen.

To increase the purity of selected events,  $b$ -tagging requirements are placed on the jet assignment with the minimal  $\chi^2$  score. The jet that is identified as the  $b$ -jet on the leptonic decay side (the tag jet) has to be  $b$ -tagged, whereas the two jets that are associated with the hadronically decaying  $W$  boson have to be untagged. For this tagging, an improved version of the DL1 tagger, called DL1r, is used at the 77% efficiency single-cut working point. Even though this selection leads to a pure region of  $t\bar{t}$  events, the jet that is assigned as the  $b$ -jet from the hadronically decaying top-quark (the probe jet), and that is later used to calculate the  $b$ -tagging efficiency, is only in 60% of the cases a true  $b$ -jet.

To further purify the selection of probe jets, a BDT is trained on simulated  $t\bar{t}$  events to separate cases where the probe jet is correctly assigned from events where it is not. The BDT uses event information like the geometrical distance between objects or the number of jets in addition to the individual terms from the  $\chi^2$  score as inputs. Through a cut on the BDT output score, the probe-jet purity is increased to an average of about 80%.

### 6.3.3 Dense jet-environments

Two variables are used to investigate the effect of dense jet-environments on the  $b$ -tagging efficiency. The first variable is the minimal geometrical distance between the probe jet and the closest jet nearby, denoted  $\Delta R_{\min}$ . The second variable is the geometrical distance between a line connecting the primary and the secondary vertex and the jet axis. This variable is denoted  $\Delta R(\text{vertex}, \text{jet})$  and is only well defined in cases where either the iterative vertex finder or JETFITTER are able to reconstruct secondary vertices within the jet. Under the assumption that the direction between the two vertices approximates the  $b$ -hadron flight direction, this variable allows to quantify the difference in jet- and  $b$ -hadron flight direction. Since it doesn't rely on generator information it is calculable both for simulation and data.

Figure 6.6 shows the  $\Delta R_{\min}$  and  $\Delta R(\text{vertex}, \text{jet})$  distributions for both the simulation and the data. The  $t\bar{t}$  contribution is split according to the flavour label of the probe jet into  $t\bar{t}$  ( $b$ ),  $t\bar{t}$  ( $c$ ) and  $t\bar{t}$  (light). The  $\Delta R_{\min}$  distribution is limited from below by radius parameter that is used in the jet algorithm. Since this measurement uses anti- $k_t$  jets with  $R = 0.4$ , the distribution starts from this value. The  $\Delta R(\text{vertex}, \text{jet})$  distribution is obtained by using the  $b$ -hadron flight direction as estimated by JETFITTER. It peaks at low values of  $\Delta R(\text{vertex}, \text{jet})$ , which means that for the majority events the estimated  $b$ -hadron flight direction and the jet axis are well aligned. A small slope is observed in the data-to-prediction ratio, where at low values of either distribution more events are predicted than observed. This slope is fully covered by the systematic uncertainties, which range between 10% and 15%.

### 6.3.4 The efficiency measurement

The data  $b$ -tagging efficiency is extracted from the fraction of  $b$ -tagged probe jets  $f_{b\text{-tags}}$ . Separating the  $t\bar{t}$  signal from the non- $t\bar{t}$  backgrounds,  $f_{b\text{-tags}}$  can be written as

$$f_{b\text{-tags}} = \varepsilon_b^{t\bar{t}} f_{b\text{-jets}}^{t\bar{t}} + \varepsilon_c^{t\bar{t}} f_{c\text{-jets}}^{t\bar{t}} + \varepsilon_l^{t\bar{t}} f_{l\text{-jets}}^{t\bar{t}} + \varepsilon_{\text{bkg}} f_{\text{bkg}} \quad , \text{ with} \quad (6.3)$$

$$\varepsilon_{\text{bkg}} f_{\text{bkg}} = \varepsilon_b^{\text{bkg}} f_{b\text{-jets}}^{\text{bkg}} + \varepsilon_c^{\text{bkg}} f_{c\text{-jets}}^{\text{bkg}} + \varepsilon_l^{\text{bkg}} f_{l\text{-jets}}^{\text{bkg}} \quad . \quad (6.4)$$

The equation can be rearranged to yield an expression for the  $b$ -tagging efficiency in data as

$$\varepsilon_b^{\text{data}} = \frac{1}{f_{b\text{-jets}}^{t\bar{t}}} \times (f_{\text{tag}}^{\text{data}} - \varepsilon_c f_{c\text{-jets}}^{t\bar{t}} - \varepsilon_l f_{l\text{-jets}}^{t\bar{t}} - \varepsilon_{\text{bkg}} f_{\text{bkg}}) \quad . \quad (6.5)$$

Here,  $f_{b\text{-tags}}$  is taken as the fraction of  $b$ -tagged probe jets in data  $f_{\text{tag}}^{\text{data}}$ . Since the fraction of  $b$ -,  $c$ -, light-flavour and background jets is not known for the data, this measurement uses the expected flavour fractions from simulation. The fraction of  $\tau$  jets is not included in the formula as the contamination is expected to be negligible.

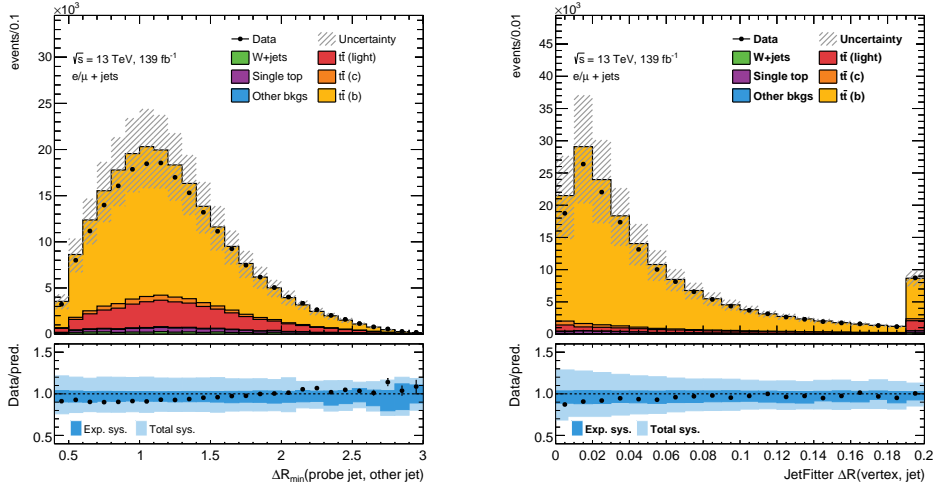


Figure 6.6: Distributions of  $\Delta R_{\min}$  (left) and  $\Delta R(\text{vertex, jet})$  (right) for the probe jet after the event selection. The  $t\bar{t}$  contribution is split according to the flavour label of the probe jet into  $b$ -jets,  $c$ -jets and light-flavour jets.

The flavour fractions for  $b$ -,  $c$ -, light-flavour jets are shown in Figure 6.7 both as a function of  $\Delta R_{\min}$  and  $\Delta R(\text{vertex, jet})$ . The efficiencies  $\varepsilon_c$ ,  $\varepsilon_l$  and  $\varepsilon_{\text{bkg}}$  in Formula 6.5 are also taken from simulation, but corrected to the efficiencies obtained from dedicated calibration measurements via data-to-simulation scale factors.

With the use of Equation 6.5, the data  $b$ -tagging efficiency is extracted as a function of both  $\Delta R_{\min}$  and  $\Delta R(\text{vertex, jet})$ . The effect of systematic uncertainties is taken into account by considering the effect of each source of uncertainty at their  $\pm 1\sigma$  value and recalculating  $\varepsilon_b$ . Systematic uncertainties on the detector performance, e.g. the reconstruction, identification and calibration of the objects used in the analysis, are considered as well, in addition to uncertainties on the modelling of both the  $t\bar{t}$  signal and all background processes.

### 6.3.5 Results and outlook

Figures 6.8 and 6.9 show a comparison of the measured and expected  $b$ -tagging efficiency as a function of  $\Delta R_{\min}$  and  $\Delta R(\text{vertex, jet})$ , respectively. The efficiency that is shown in the plots of this thesis corresponds to the 77% single-cut working point of the DL1r tagger, although similar conclusions can be drawn for the other single-cut working points, too. In both cases, an average signal purity  $f_{b\text{-jets}}$  of roughly 80% or higher is expected, thanks to the usage of the purification BDT. For  $\Delta R(\text{vertex, jet})$ , this fraction is higher because only events with at least one secondary vertex are considered. The measured  $b$ -tagging efficiency is roughly flat as a function of  $\Delta R_{\min}$ . In the immediate proximity of close-by jets, at the lowest

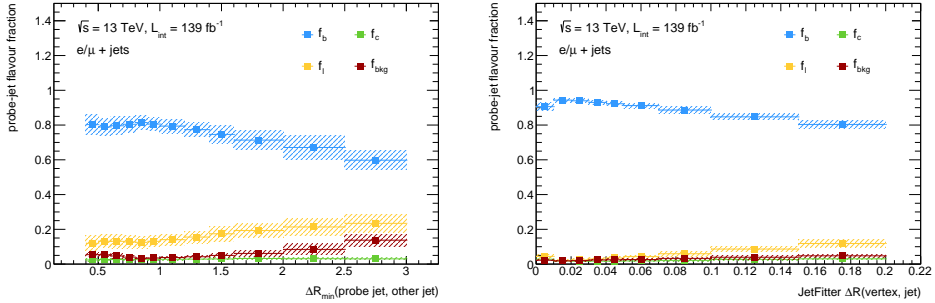


Figure 6.7: Expected probe-jet flavour fractions before  $b$ -tagging as a function of the geometrical distance between the probe-jet and the closest jet,  $\Delta R_{\min}$  (left) and as a function of the geometrical distance between the probe-jet axis and the estimated  $b$ -hadron flight direction,  $\Delta R(\text{vertex}, \text{jet})$  (right).

values of  $\Delta R(\text{vertex}, \text{jet})$ , the observed and expected efficiencies differ the most, but still agree within uncertainties. The measured  $b$ -tagging efficiency as a function of  $\Delta R(\text{vertex}, \text{jet})$  decreases the higher the separation between the jet axis and the estimated  $b$ -hadron flight direction, i.e. the larger the value of  $\Delta R(\text{vertex}, \text{jet})$ . An exception is the first bin, which has a slightly lower efficiency due to the fact that JETFITTER allows also for single-track vertices. The measured  $b$ -tagging efficiency agrees well with the expectation. The observed characteristics of the  $b$ -tagging efficiency as a function of the dense jet-environment variables agree well with earlier measurements performed during Run 1 of the LHC at  $\sqrt{s} = 7$  TeV and  $\sqrt{s} = 8$  TeV [146, 149]. For both variables, the effect of dense jet-environments on the  $b$ -tagging efficiency agrees between data and simulation. Some trends are visible for  $\Delta R_{\min}$ , they are however covered by the large systematic uncertainties.

The dominant source of uncertainty on the measured values of  $\varepsilon_b$  is related to differences in the prediction of  $f_{b\text{-jets}}$ . These differences arise when changing parameters in the  $t\bar{t}$  simulation, such as the amount of ISR and FSR, the parton-shower and hadronisation modelling or the NLO+PS matching. Currently, the  $t\bar{t}$  modelling uncertainties are limiting this efficiency measurement. Future measurements could therefore benefit from extracting the flavour-fractions directly from a fit to data in suitable signal regions.

In light of the measurements that are presented in this thesis, it would further be interesting to extend this efficiency measurement to VR track-jets. However, this requires non-trivial modifications to the analysis strategy. For example, the  $\chi^2$  minimisation that is performed to find the correct probe jet, relies on mass constraints from the  $W$  boson and the top quark. Since VR track-jets do not contain information about neutral particles that are created in the hadronisation, the measurement strategy is not directly transferable to VR track-jets.

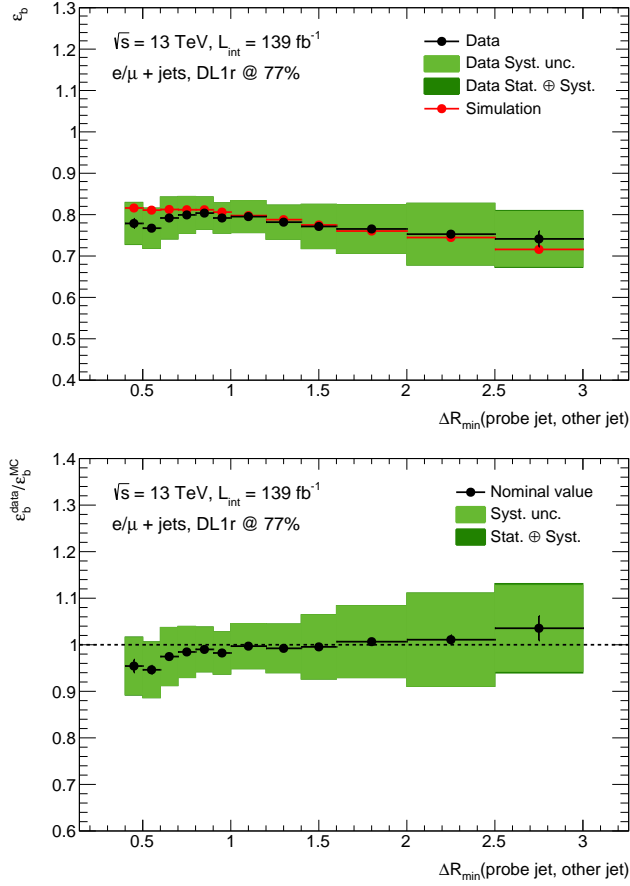


Figure 6.8: Comparison of measured and expected  $b$ -tagging efficiency (top) and data-to-simulation ratio of the  $b$ -tagging efficiency (bottom) as a function of the geometrical distance between the probe-jet and the closest jet,  $\Delta R_{\min}$ .

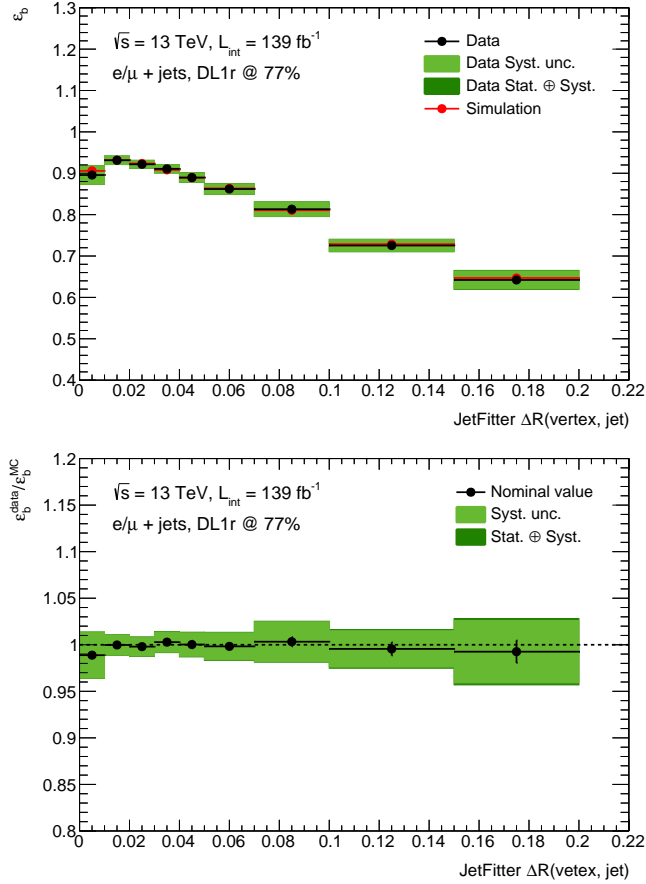


Figure 6.9: Comparison of measured and expected  $b$ -tagging efficiency (top) and data-to-simulation ratio of the  $b$ -tagging efficiency (bottom) as a function of the geometrical distance between the probe-jet axis and the estimated  $b$ -hadron flight direction,  $\Delta R(\text{vertex}, \text{jet})$ .

# 7 Measurement of Higgs boson production at high transverse momentum in the $VH, H \rightarrow b\bar{b}$ channel

This chapter presents a novel measurement of Higgs boson production at high  $p_T^H$  in the  $VH, H \rightarrow b\bar{b}$  channel. After motivating its necessity, a general overview of the whole analysis is given. Subsequently, the individual elements of the measurement, such as the event selection, the treatment of backgrounds and the statistical inference, are explained in more detail. Finally, the results are presented in terms of inclusive signal strength measurements as well as differential cross-section measurements within the STXS framework. The analysis is published in Ref. [5].

## 7.1 Motivation

Differential Higgs boson production cross-section measurements are sensitive probes for new physics. Of particular interest are measurements as a function of  $p_T^H$ . Deviations from the SM could manifest themselves in different regions of the  $p_T^H$  spectrum, depending on the nature of the considered BSM model. A precise measurement of the whole spectrum is therefore necessary.

Existing differential cross-section measurements use analyses that are optimised for the total rate, therefore focusing on the region with  $p_T^H \lesssim 300$  GeV where most of the Higgs bosons are produced [6, 76, 78]. The high  $p_T^H$  region with  $p_T^H \gtrsim 400$  GeV is particularly sensitive to heavy new physics, such as composite Higgs models or heavy additional quarks. At high energies, additional microscopic structures of known interactions will lead to enhanced deviations from the predictions of the SM. Moreover, the region contributes only  $\sim 1\%$  to the total production cross-section, and local deviations of even several times the SM prediction cannot be constrained by the current total rate measurements [69]. With the increasing  $pp$  collision data set delivered by the LHC, dedicated high  $p_T^H$  analyses become feasible.

Figure 7.1 shows the different Higgs boson production modes' fractional contribution to the total production cross-section at  $\sqrt{s} = 13$  TeV, as a function of a lower  $p_T^H$  cut. In contrast to the inclusive production cross-section, which is mainly dominated by gluon-gluon fusion, at high  $p_T^H$  all production modes are important. Especially the fractional contribution of Higgs-strahlung rises with  $p_T^H$ , because of

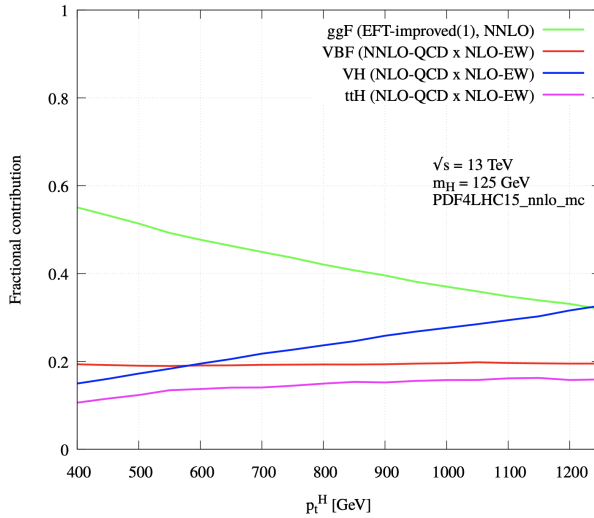


Figure 7.1: The different Higgs boson production mechanisms’ fractional contribution to the total production cross-section as a function of the lower  $p_T^H$  cut. Taken from Ref. [150].

the diagrams with two quarks in the initial state. Whereas inclusively only  $\sim 4\%$  of Higgs bosons are produced via Higgs-strahlung, for  $p_T^H > 400$  GeV it is  $\sim 18\%$ . Above 1.2 TeV, Higgs-strahlung is the dominant production mode.

Higgs-strahlung has an additional advantage with respect to the more prominent gluon-gluon fusion (ggF) and vector boson fusion (VBF) production modes. The vector boson  $V = W, Z$  that is produced in association with the Higgs boson, decays a fraction of times into leptons. The presence of these leptons allows to study hadronic Higgs boson decay signatures. In the case of ggF and VBF production, hadronic Higgs boson decays would lead to a fully hadronic final state, which, at a hadron collider like the LHC, faces irreducible QCD multijet backgrounds several orders of magnitude higher than the signal. In Higgs-strahlung, the leptons create detector signatures that differentiate the signal from the multijet backgrounds. Additionally, the leptonic signatures are rare enough, such that they can be exploited for triggering during data taking.

Of all hadronic decay channels, the decay into a pair of  $b$ -quarks is particularly interesting due to its high branching fraction of  $\sim 58\%$ . It ensures a high signal yield even in rare regions of phase space, such as at high  $p_T^H$ . Consequently,  $pp \rightarrow VH$ , with  $V \rightarrow \text{leptons}$  and  $H \rightarrow b\bar{b}$  is used as a signal to establish a measurement that explicitly targets Higgs boson production at high  $p_T^H$ .



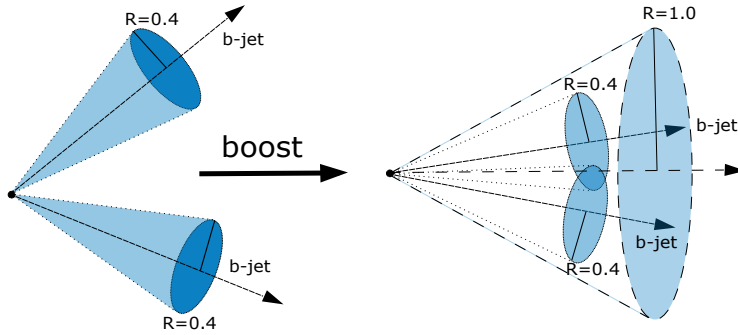


Figure 7.2: Illustration of the reconstruction of a  $H \rightarrow b\bar{b}$  decay using two small- $R$  jets (left) and one large- $R$  jet (right).

## 7.2 Analysis overview

### 7.2.1 The Higgs boson reconstruction

The measurement presented in this section primarily relies on the capability to reconstruct the  $H \rightarrow b\bar{b}$  decay at high  $p_T^H$  as accurately as possible. The two  $b$ -quarks each hadronise and subsequently form a jet in the detector. The geometrical distance  $\Delta R$  between these two jets depends on the Lorentz boost of the Higgs boson, which in turn depends on  $p_T^H$  and the Higgs boson mass  $m_H$ . If the decay happens entirely in the transverse plane, the  $\Delta R$  between the outgoing  $b$ -quarks, and therefore also approximately between the axes of the jets, is

$$\Delta R(b_1, b_2) \sim \frac{m_H}{p_T^H} \frac{1}{\sqrt{z(1-z)}} \sim \frac{2m_H}{p_T^H} \quad , \quad (7.1)$$

where  $z$  is the momentum fraction carried by  $b_1$ .

In the regime below  $p_T^H \sim 300$  GeV, the outgoing  $b$ -jets are well separated and can be reconstructed individually. Because most of the signal events are produced in this region, past analyses in the  $VH, H \rightarrow b\bar{b}$  channel [6, 151, 152] have been optimised for it. These analyses reconstruct the  $H \rightarrow b\bar{b}$  decay with two anti- $k_t$  jets with  $R = 0.4$  (small- $R$  jets). The Higgs boson candidate is then formed by adding the two four-momenta.

For  $p_T^H > 400$  GeV, however, this reconstruction technique is less efficient because the two  $b$ -jets are geometrically closer. If the separation is too small, they can no longer be reconstructed as two individual small- $R$  jets. Therefore, this analysis reconstructs both  $b$ -jets inside one anti- $k_t$  jet with  $R = 1.0$  (large- $R$  jet), whose four-momentum is used as the Higgs boson candidate. The two different reconstruction approaches are sketched in Figure 7.2.

The fraction of events that can be reconstructed with either technique depends on

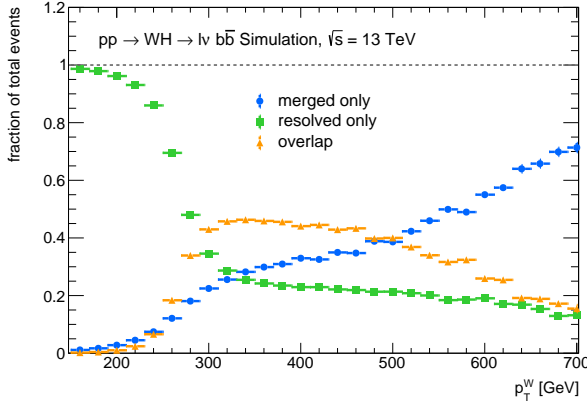


Figure 7.3: Fraction of  $pp \rightarrow W(\rightarrow \ell\nu) H(\rightarrow b\bar{b})$  events after the event selection, for which the Higgs boson candidate can be only reconstructed using two small- $R$  jets (green squares) or one large- $R$  jet (blue dots). The fraction of events for which both reconstruction techniques work is depicted as orange triangles. The fractions are shown as a function of the reconstructed  $p_T^W$ .

$p_T^H$ , and therefore also on  $p_T^V$ . Because the two techniques are not exclusive with respect to each other, for some events both reconstruction approaches work. Three scenarios can be distinguished:

1. **Resolved:** An event can be *solely* reconstructed using two small- $R$  jets.
2. **Merged:** An event can be *solely* reconstructed using one large- $R$  jet.
3. **Overlap:** Both reconstruction techniques work.

The fraction of signal events that falls into each of the three categories is shown in Figure 7.3, as a function of  $p_T^V$ , after applying the event selection. Resolved events are shown in green, merged events in blue and the overlap fraction is shown in orange.

At low  $p_T^V$ , events are solely reconstructed using the resolved technique. In the intermediate region, between 300 GeV and 450 GeV, about 40% of events fall into the overlap category, where both techniques work. Starting from  $p_T^V \sim 450$  GeV, the fraction of events that are reconstructed solely using the merged technique rises significantly, reaching up to 70% at 700 GeV. The higher  $p_T^V$ , and therefore  $p_T^H$ , the higher the chance that the two  $b$ -quarks have a  $\Delta R < 0.4$ .

### 7.2.2 The vector boson reconstruction

The leptonic  $V$  decay signatures that are targeted and to be reconstructed are  $Z \rightarrow \nu\nu$ ,  $W \rightarrow \ell\nu$  and  $Z \rightarrow \ell\ell$ , with  $\ell$  denoting an electron or a muon. Final

states with  $\tau$  leptons are not explicitly targeted but can pass the analysis selection depending on their decay mode.  $\tau$  leptons that pass are treated as signal.

Because each of the three  $V$  decays creates a different detector signature, the analysis is split into three sub-channels. The 0-lepton channel selects events with  $E_{\text{T}}^{\text{miss}}$  from the  $Z \rightarrow \nu\nu$  decay. In the 1-lepton channel, events with exactly one electron or muon and  $E_{\text{T}}^{\text{miss}}$  are selected. The 2-lepton channel selects events with either two electrons or two muons.

In the 0-lepton channel, only information about the transverse component of the  $Z$  boson candidate is available because for neither of the two neutrinos the  $z$ -momentum component is known. In the 1-lepton channel, the  $W$  boson is fully reconstructed from the measured lepton four-vector,  $E_{\text{T}}^{\text{miss}}$  and a  $W$  mass constraint. In the 2-lepton channel, the  $Z$  boson candidate is formed from the two four-vectors of the leptons.

In the absence of initial state radiation, the Higgs boson recoils against the vector boson in the transverse plane. Therefore, if the Higgs boson has high  $p_{\text{T}}$ , so does the vector boson. The close proximity of the decay products, is, however, not a problem for the vector boson reconstruction. For  $Z \rightarrow \nu\nu$ , the two neutrinos can get arbitrarily close because only their summed transverse momentum is measured as  $E_{\text{T}}^{\text{miss}}$ . For  $W \rightarrow \ell\nu$ , only one charged lepton has to be reconstructed in addition to  $E_{\text{T}}^{\text{miss}}$  from the neutrino. Therefore, the lepton is necessarily isolated. In the 2-lepton channel, the signatures of the two electrons or muons are localised enough to be reconstructed individually up to at least  $p_{\text{T}}^V = 800 \text{ GeV}$  without significant signal loss. Therefore, in contrast to the Higgs boson, no special merged vector boson reconstruction techniques are needed.

To summarise, the signal at LO leads to the following experimental signatures:

- **0-lepton channel:** a large- $R$  jet recoiling in the transverse plane against  $E_{\text{T}}^{\text{miss}}$ .
- **1-lepton channel:** a large- $R$  jet recoiling in the transverse plane against an electron or muon and  $E_{\text{T}}^{\text{miss}}$ .
- **2-lepton channel:** a large- $R$  jet recoiling in the transverse plane against two electrons or two muons.

A candidate event for the  $pp \rightarrow WH \rightarrow \mu\nu b\bar{b}$  signal, in the 1-lepton channel, is displayed in Figure 7.4.

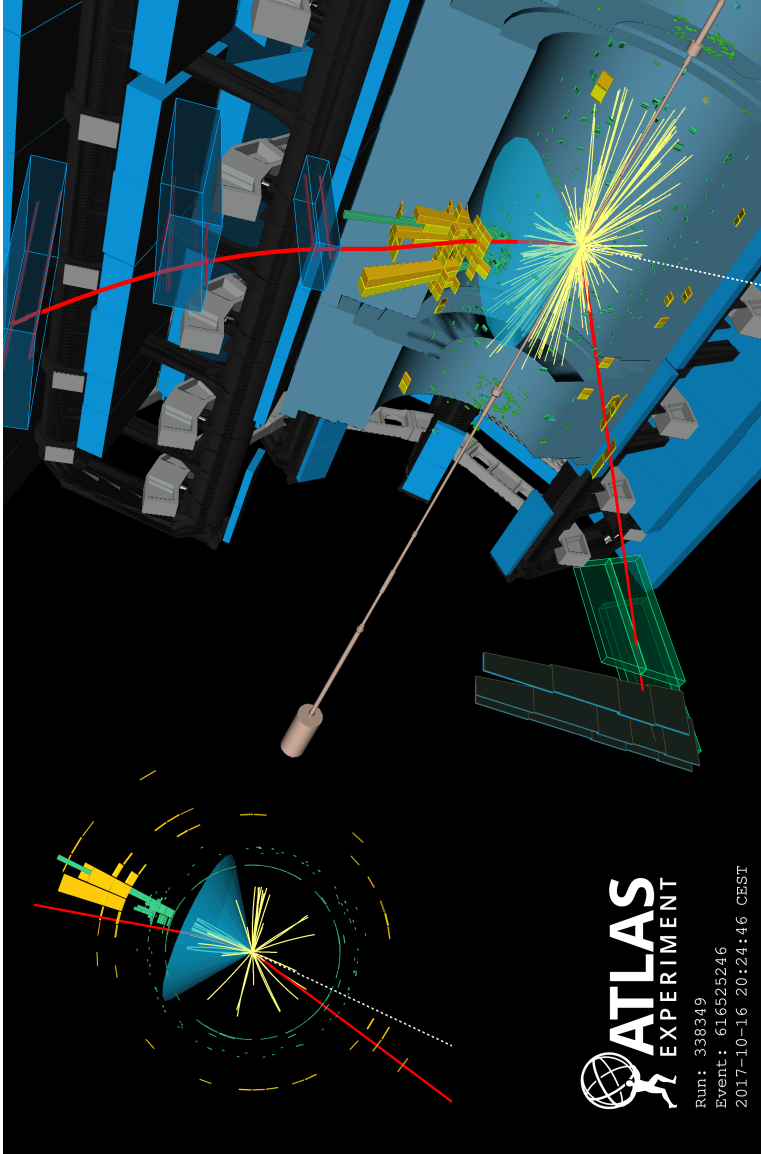


Figure 7.4: Candidate event for the  $pp \rightarrow WH \rightarrow \mu\nu b\bar{b}$  signal. The event was recorded during run 338349 in October 2017. An isolated muon with  $p_T = 196$  GeV and  $\eta = 1.16$  is depicted as the lower red line producing hits in the end-cap muon chambers. The event has  $E_T^{\text{miss}} = 832$  GeV (dashed white line), which together with the muon, forms a  $W$  boson candidate of  $p_T = 1.03$  TeV and  $m = 112$  GeV. The Higgs boson candidate recoiling against the  $W$  candidate shows a two-prong structure with energy deposits both in the ECAL (green) and HCAL (yellow). It has a reconstructed invariant mass of 116 GeV. A second muon with hits in the barrel muon chambers can be found within  $\Delta R = 1.0$  of the Higgs boson candidate (blue cone) and possibly originates from the semi-leptonic  $b$ -hadron decay in one of the two  $b$ -tagged jets. Published in Ref. [5].

### 7.2.3 The main backgrounds

Several other processes can lead to the above mentioned signal signatures and are therefore backgrounds for this analysis. The backgrounds are divided into reducible and irreducible, with different compositions between the three lepton channels.

Irreducible backgrounds have exactly the same final state particle count as the  $VH$  signal. These include diboson and  $V$ +jets production, for which example Feynman diagrams are shown in Figure 7.5 and 7.6, respectively. The  $VZ$  part of the diboson process is particularly similar to the signal. It leads to a mass peak around the  $Z$  boson mass, similar to the mass peak around the Higgs boson mass for the  $VH$  signal. The cross-section of  $VZ$  production is higher than for  $VH$  production, which makes the  $VZ$  peak more prominent. The measurement of the  $VZ$  process is used to cross-check the analysis strategy.

Top quark pair ( $t\bar{t}$ ) production (Figure 7.7), single top production (Figure 7.8) and QCD multijet production (Figure 7.9) constitute the reducible backgrounds. These backgrounds pass the event selection only due to instrumental limitations like limited detector coverage, reconstruction inefficiencies or objects being out of kinematic acceptance. Although such inaccuracies are not very frequent, these processes have typically a cross-section much larger than the signal which causes a significant amount of events to pass the selection. A summary of the different background contributions is given in Table 7.1.

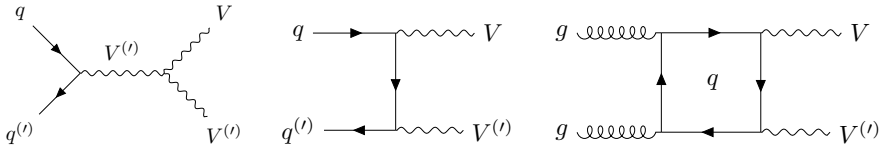


Figure 7.5: Feynman diagrams for diboson production ( $VV^{(\prime)}$ ).

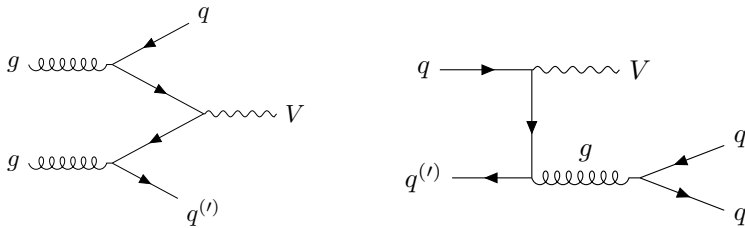


Figure 7.6: Feynman diagrams for  $V$ +jets production.

### 7.2.4 Goal of the measurement

The goal of this analysis is to measure the differential  $p_T$  spectrum of  $VH$  production at high  $p_T^H$ . First, the  $VH$  signal is measured inclusively for  $p_T^V > 250$  GeV, which

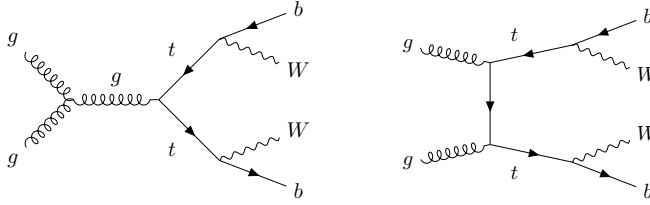


Figure 7.7: Feynman diagrams for  $t\bar{t}$  production with subsequent  $t \rightarrow Wb$  decay.

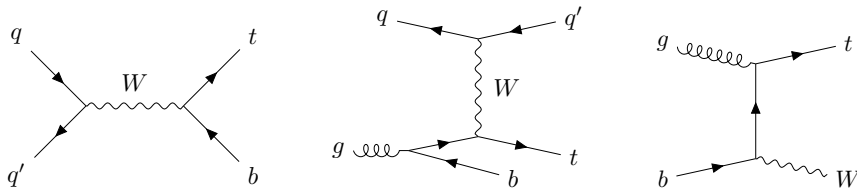


Figure 7.8: Feynman diagrams for single top production in the  $s$ -channel (left) and  $t$ -channel (middle) as well as the  $Wt$ -channel (right).

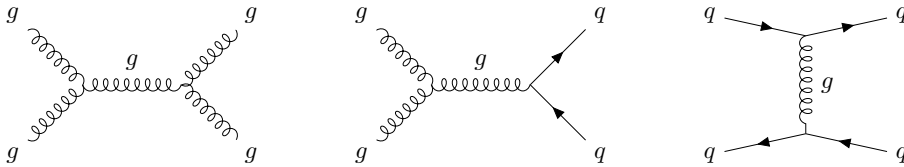


Figure 7.9: Feynman diagrams for QCD multijet production.

Process	0-lepton	1-lepton	2-lepton
$t\bar{t}$	✓	✓	
Single top	✓	✓	
$W$ + jets	✓	✓	
$Z$ + jets	✓		✓
Diboson	✓	✓	✓
QCD multijet		✓	

Table 7.1: Main backgrounds to the  $VH$  signal in the three charged lepton sub-channels of the analysis.

is the region where the merged reconstruction techniques are applicable. The lower cut of  $p_T^V > 250$  GeV marks the point from which on the two  $b$ -quarks are mostly contained within a large- $R$  jet of  $R = 1.0$ . The parameter of interest (PoI) of the measurement, the signal strength, is defined as

$$\mu_{VH} = \frac{[\sigma_{VH} \times \text{BR}(H \rightarrow b\bar{b})]_{\text{measured}}}{[\sigma_{VH} \times \text{BR}(H \rightarrow b\bar{b})]_{\text{predicted}}} . \quad (7.2)$$

In addition, a differential cross-section measurement is performed within the STXS framework. The measured generator-level  $p_T^{V,t}$  bins are  $p_T^{V,t} \in [250, 400)$  GeV and  $p_T^{V,t} > 400$  GeV. The region with  $p_T^{V,t} > 400$  GeV is hereby considered separately due to its enhanced sensitivity to BSM physics. This differential measurement is used to set limits on the Wilson coefficients of dimension 6 operators in a SM effective field theory, especially the ones with  $p_T^H$  dependent effects.

### 7.2.5 A sketch of the event selection and categorisation

The event selection and categorisation is grouped into criteria related to the Higgs boson candidate, criteria related to the vector boson candidate and requirements on additional activity in event. Events are categorised according to their charged lepton multiplicity into a 0-, a 1- and a 2-lepton channel. Figure 7.10 sketches an event passing the 1-lepton event selection and highlights the criteria according to which events are selected.

The two  $b$ -jets from the  $H \rightarrow b\bar{b}$  decay are expected to be close at high  $p_T^H$ , and are therefore reconstructed in a single large- $R$  jet. Consequently, events are required to have at least one such large- $R$  jet built from clustered energy deposits in the calorimeter. To discriminate the  $H \rightarrow b\bar{b}$  system against backgrounds, jet substructure information is used. The presence of two  $b$ -hadrons within the large- $R$  jet is inferred by using flavour tagging algorithms, that search for signatures of these hadrons. The algorithms work on a jet-by-jet basis, and therefore need a direction in the detector along which to look for signs of an individual  $b$ -hadron. Thus, in order to use these algorithms to identify the two  $b$ -hadrons from  $H \rightarrow b\bar{b}$ , sub-jets need to be formed on which the actual  $b$ -tagging is performed.

The analysis uses tracks measured in the Inner Detector to form anti- $k_t$  jets with a variable radius (VR) parameter that shrinks with the jet  $p_T$ . Because of the high spatial resolution of the tracker, these track-jets can become very small and are therefore ideal candidates for collimated boosted environments. The formed track-jets are geometrically matched to the large- $R$  jet, which means that their axis needs to overlap with the large- $R$  jet cone. The two matched track-jets with the highest  $p_T$  have to be  $b$ -tagged for the event to pass the selection.

To perform a differential cross-section measurement, two  $p_T^V$  regions are considered separately:  $p_T^V \in [250, 400)$  GeV and  $p_T^V > 400$  GeV. In general,  $p_T^V$  is used instead of the large- $R$  jet  $p_T$  to bin this measurement because the leptonic signatures from the  $V$  decay can be reconstructed with higher precision. Therefore, the

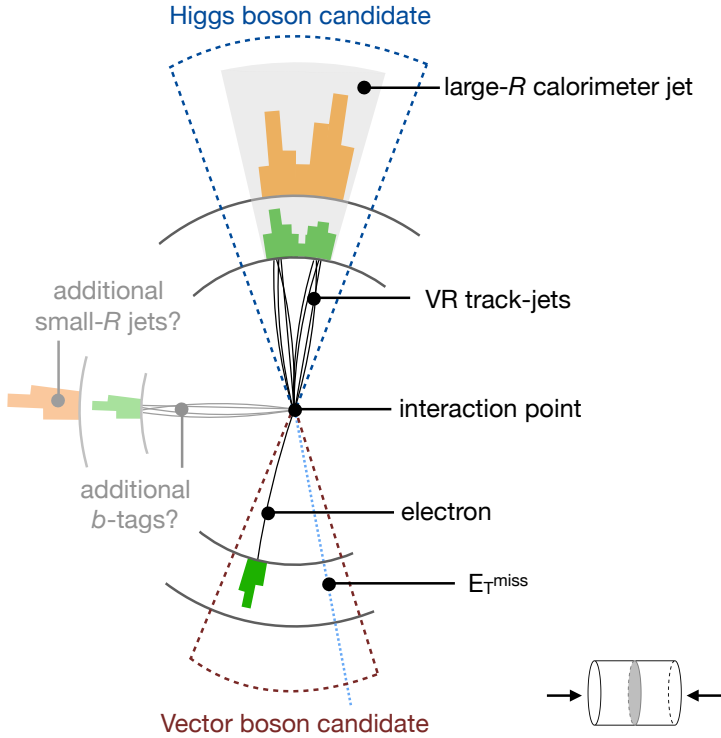


Figure 7.10: Sketched transverse view of an event passing the 1-lepton event selection. The Inner Detector tracks are shown as solid black lines. Energy deposits in the electromagnetic calorimeter are shown as green towers. Hadronic calorimeter energy deposits are shown as orange towers. The  $E_T^{\text{miss}}$  is shown as a dashed blue line. Various event selection requirements are highlighted.



Channel	Categories					
	$p_T^V \in [250, 400) \text{ GeV}$			$p_T^V > 400 \text{ GeV}$		
	0 add. $b$ -track-jets		$\geq 1$ add. $b$ -track-jets	0 add. $b$ -track-jets		$\geq 1$ add. $b$ -track-jets
	0 add. small- $R$ jets	$\geq 1$ add. small- $R$ jets		0 add. small- $R$ jets	$\geq 1$ add. small- $R$ jets	
0-lepton	SR	SR	$t\bar{t}$ CR	SR	SR	$t\bar{t}$ CR
1-lepton	SR	SR	$t\bar{t}$ CR	SR	SR	$t\bar{t}$ CR
2-lepton		SR			SR	

Table 7.2: Analysis region definitions. Signal regions with high signal purity are marked with the label SR. The top background enriched control region is marked as  $t\bar{t}$  CR.

reconstructed  $p_T^V$  is stronger correlated with the generator-level  $p_T^{V,t}$  than the large- $R$  jet  $p_T$  is with  $p_T^H$ .

Additional event information is used to define signal and control regions. To suppress the  $t\bar{t}$  contamination in the 0- and 1-lepton channel, signal regions are formed by vetoing events with additional  $b$ -tagged track-jets that are not matched to the Higgs boson candidate. Additionally, a  $t\bar{t}$  enriched control region with additional  $b$ -tagged jets is formed. The signal regions are split according to their additional small- $R$  jet multiplicity. Since the signal is produced at LO with no additional jets in the final state, a high-purity signal region is formed by requiring zero additional reconstructed small- $R$  jets. A low-purity signal region that allows for additional small- $R$  jets, is considered separately. In the 2-lepton channel, none of these categorisations is applied because  $t\bar{t}$  is a negligible background. The event categorisation is summarised in Table 7.2.

### 7.2.6 The signal extraction

To extract the  $VH$  signal yield, a binned profile-likelihood fit is performed in the 10 signal and 4 control regions. The fit discriminant in each region is the invariant mass  $m_J$  of the large- $R$  jet with the highest  $p_T$ , the Higgs candidate. The  $VZ$  signal is extracted simultaneously with the  $VH$  signal. The normalisations of the main backgrounds are solely determined from data in the fit. The  $t\bar{t}$  contribution is constrained from the dedicated control region and the high- $m_J$  region; the  $V + \text{jets}$  contribution is constrained from the low- $m_J$  region. Experimental and theoretical uncertainties are included as nuisance parameters in the fit.

## 7.3 Data and simulated samples

### 7.3.1 The data sample

The  $pp$  collision data analysed in this measurement was recorded with the ATLAS detector during the second operational run of the LHC from 2015-2018 at a centre-of-mass energy of  $\sqrt{s} = 13$  TeV. Only proton collisions during stable beam conditions have been recorded. Furthermore, it was required that all relevant sub-detectors were fully operational and that the recorded data matches dedicated 'good quality' criteria. The analysed sample corresponds to an integrated luminosity of  $(139 \pm 2) \text{ fb}^{-1}$  [102]. Depending on the analysis sub-channel, a combination of triggers selecting events with high  $E_{\text{T}}^{\text{miss}}$  or single electrons is used.

### 7.3.2 The simulated signal and background samples

The description of the signal process, as well as of the various backgrounds is based on Monte Carlo (MC) simulations. An exception to this is the multijet background, which is estimated from data.

The used MC simulation programs generate events that include a full correlation between the kinematic properties of all final state particles. Subsequently, these events are passed through a simulation of the ATLAS detector. This allows these events to be directly compared to the recorded data. Therefore, these events are used both for the design of the measurement itself and the extraction of the signal strength or the differential cross-sections.

The MC generator setups are mostly NLO QCD accurate in the calculation of the matrix element amplitudes. Furthermore, these generators contain a subsequent parton shower step that is used for shower evolution and hadronisation. In cases where the simulated process relies on an accurate modelling of additional jets, such as for  $V$ +jets, multi-leg techniques are used to obtain (N)LO accuracy in the description of up to  $n$  hard, well separated emissions.

For most processes, cross-section calculations exist at higher order in perturbation theory than what the MC generators provide. When available, these calculations are used to normalise the simulated event yields obtained from the MC generators.

The following sections describe the setup of these generators in detail. Each section is dedicated to either the signal or one of the backgrounds and structured as follows: First, a description of the MC generator setup is given. Second, the cross-section calculations used for the sample normalisation are referenced. Last, any analysis specific selections or modifications are specified.

The generation setup for the nominal signal and background processes is summarised in Table 7.3, together with the fiducial cross-section predictions at  $\sqrt{s} = 13$  TeV.

Process	ME generator	ME PDF	PS and Hadronisation	UE model tune	Cross-section order	$\sigma_{(64)} [\text{pb}]$
Signal ( $m_H = 125 \text{ GeV}$ and $b\bar{b}$ branching fraction set to 58.2%)						
$q\bar{q}/gg \rightarrow WH \rightarrow t\bar{t}b\bar{b}$	POWHEG-Box v2 [153] + GoSAM [157] + MiNLO [158, 159]	NNPDF3.0NLO <sup>(*)</sup> [154]	PYTHIA 8.212 [155]	AZNLO [156]	NNLO(QCD)+ NLO(EW) [160–166]	0.46727
$q\bar{q}/gg \rightarrow ZH \rightarrow \nu\bar{\nu}b\bar{b}/t\bar{t}b\bar{b}$	POWHEG-Box v2 + GoSAM + MiNLO	NNPDF3.0NLO <sup>(*)</sup>	PYTHIA 8.212	AZNLO	NNLO(QCD) <sup>(†)</sup> + NLO(EW)	0.23009
$gg \rightarrow ZH \rightarrow \nu\bar{\nu}b\bar{b}/t\bar{t}b\bar{b}$	POWHEG-Box v2	NNPDF3.0NLO <sup>(*)</sup>	PYTHIA 8.212	AZNLO	NLO+ NLL [167–171]	0.03699
Top quark ( $m_t = 172.5 \text{ GeV}$ )						
$t\bar{t}$	POWHEG-Box v2 [153, 172]	NNPDF3.0NLO	PYTHIA 8.230	A14 [173]	NNLO+NNLL [174]	831.76
$s$ -channel	POWHEG-Box v2 [153, 175]	NNPDF3.0NLO	PYTHIA 8.230	A14	NLO [176, 177]	10.32
$t$ -channel	POWHEG-Box v2 [153, 175]	NNPDF3.0NLO	PYTHIA 8.230	A14	NLO	216.97
$Wt$	POWHEG-Box v2 [153, 178]	NNPDF3.0NLO	PYTHIA 8.230	A14	Approximate NNLO [179]	71.7
Vector boson + jets						
$W \rightarrow \ell\nu$	SHERPA 2.2.1 [180–183]	NNPDF3.0NNLO	SHERPA 2.2.1 [184, 185]	Default	NNLO [186]	20 080
$Z/\gamma^* \rightarrow \ell\bar{\ell}$	SHERPA 2.2.1	NNPDF3.0NNLO	SHERPA 2.2.1	Default	NNLO	2107
$Z \rightarrow \nu\bar{\nu}$	SHERPA 2.2.1	NNPDF3.0NNLO	SHERPA 2.2.1	Default	NNLO	11 373
Diboson						
$q\bar{q}/gg \rightarrow W^+W^-$	SHERPA 2.2.1	NNPDF3.0NNLO	SHERPA 2.2.1	Default	NLO	112.7
$q\bar{q}/gg \rightarrow WZ$	SHERPA 2.2.1	NNPDF3.0NNLO	SHERPA 2.2.1	Default	NLO	50.3
$q\bar{q}/gg \rightarrow ZZ$	SHERPA 2.2.1	NNPDF3.0NNLO	SHERPA 2.2.1	Default	NLO	15.6
$gg \rightarrow VV$	SHERPA 2.2.2	NNPDF3.0NNLO	SHERPA 2.2.2	Default	NLO [187]	6.4

Table 7.3: Signal and background processes with the corresponding generators used for the nominal samples. If not specified, the order of the cross-section calculation refers to the expansion in the strong coupling constant ( $\alpha_s$ ). (\*) The events are generated using the first PDF in the NNPDF3.0NLO set and subsequently reweighted to the PDF4LHC15NLO set [188] using the internal algorithm in POWHEG-Box v2. (†) The NNLO(QCD)+NLO(EW) cross-section calculation for the  $pp \rightarrow ZH$  process includes the  $gg \rightarrow ZH$  contribution. The  $q\bar{q} \rightarrow ZH$  process is normalised using the cross-section for the  $pp \rightarrow ZH$  process, after subtracting the  $gg \rightarrow ZH$  contribution. An additional scale factor is applied to the  $q\bar{q} \rightarrow VH$  processes as a function of the generator-level  $p_T^V$ , to account for electroweak (EW) corrections at NLO, which makes use of the  $VH$  differential cross-section computed with HAWK [189, 190]. Published in Ref. [5].

### 7.3.2.1 Signal

**Simulated samples** The Higgs-strahlung signal samples include three distinct final states depending on the vector boson decay mode:  $ZH \rightarrow \nu\nu H$ ,  $WH \rightarrow \ell\nu H$  and  $ZH \rightarrow \ell\ell H$ , where  $\ell \in \{e, \mu, \tau\}$  and  $H \rightarrow b\bar{b}$ . The  $ZH$  production is furthermore split according to the partonic initial state into either  $qq/qg$ -induced or  $gg(\text{loop})$ -induced. The Higgs boson mass is set to 125 GeV in the calculations.

The  $qq/qg$ -induced Higgs-strahlung samples are simulated with POWHEG-BOX v2 [153, 191–193] making use of the MINLO (Multiscale Improved NLO) [159] prescription for the choice of renormalisation and factorisation scales. This yields NLO QCD and LO EW accuracy for inclusive distributions of both  $VH$  and  $VH + \text{jet}$  production. One-loop amplitudes are generated using the GOSAM [157] interface. Example diagrams for  $qq/qg$ -induced production are shown in Figure 7.11.

The loop-induced diagrams are generated at LO in QCD and EW using POWHEG-BOX v2. Example diagrams are shown in the top row of Figure 7.12. Comparing these diagrams to the diagrams in Figure 7.11, it can be seen that they are formally NNLO in QCD. Because the loop-induced diagrams are gauge invariant, as well as IR and UV finite, they can be generated standalone, which motivates the split according to the initial state.

Although these contributions are NNLO in QCD, it is important to take the loop-induced contribution into account because the gluon PDF is enhanced for low Bjorken  $x$ . The diagrams at the bottom of Figure 7.12 are additional NNLO QCD corrections to the Drell-Yan-like diagrams and are not taken into account in the sample generation.

For both  $qq/qg$ -induced and loop-induced  $VH$  production, the NNPDF3.0NLO [154] set is used for the ME generation. The events are subsequently reweighted to the PDF4LHC15nlo PDF set [188] using the POWHEG-BOX v2 machinery. This reweighting allows to evaluate PDF uncertainties following the PDF4LHC prescriptions.

The matrix elements are matched to the parton shower of PYTHIA 8.212 [155] using the AZNLO set of tuneable parameters [156]. To model their decay, heavy flavour hadrons ( $b$  and  $c$ ) are passed to EVTGEN 1.2.0 [194].

**NLO EW corrections** A comparison of the size of the coupling strengths  $\alpha_{\text{textEW}}$  and  $\alpha_S$  suggests that overall, NLO EW contributions should be similar to NNLO QCD contributions. In specific regions of phase space, such as at high  $p_T$ , NLO EW contributions can have even larger impacts, though. This makes it necessary to include these corrections in order to have a sufficiently accurate modelling of the process under consideration. In the case of  $qq/qg$ -induced production, NLO EW corrections  $\delta_{\text{EW}}$  are applied as a function of the generator-level  $p_T^V$ . The corrections include both real and virtual contributions and are derived using HAWK [189, 190] as the ratio of NLO EW with respect to the Born contribution. The  $p_T^V$ -dependent

correction factors are re-normalised in order not to change the overall sample normalisation. The correction factors are depicted in Figure 7.13 and applied to change the event weight multiplicatively with  $(1 + \delta_{\text{EW}})$ .

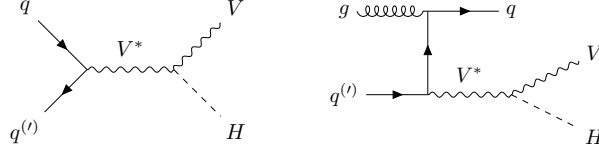


Figure 7.11: Feynman diagrams for quark-quark- (left) and quark-gluon-induced (right) Higgs-strahlung. The quark-gluon-induced diagram appears at NLO in QCD.

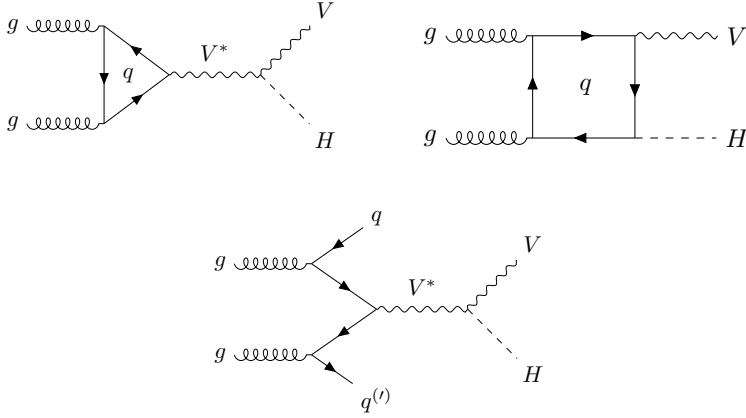


Figure 7.12: Feynman diagrams for gluon-gluon-initiated Higgs-strahlung. The upper diagrams are loop-induced while the lower diagram is a NNLO QCD correction to the Drell-Yan-like diagram.

**Cross-section prediction** The generated signal samples are furthermore normalised to the latest fiducial cross-section calculation, following the prescription from the LHC Higgs cross-section working group [67]. NNLO QCD and NLO EW accuracy is reached by adding individual contributions to the calculated cross-sections as

$$\sigma^{WH} = \sigma_{\text{NNLO QCD}}^{WH, \text{DY}} (1 + \delta_{\text{EW}}) + \sigma_{t\text{-loop}} + \sigma_{\gamma} \quad , \quad (7.3)$$

$$\sigma^{ZH} = \sigma_{\text{NNLO QCD}}^{ZH, \text{DY}} (1 + \delta_{\text{EW}}) + \sigma_{t\text{-loop}} + \sigma_{\gamma} + \sigma^{ggZH} \quad , \quad (7.4)$$

where  $\sigma_{\text{NNLO QCD}}^{VH, \text{DY}}$  contains the Drell-Yan-like processes up to  $\mathcal{O}(\alpha_s^2)$  [160–166]. Terms common to both  $WH$  and  $ZH$  production involving closed top(bottom)-

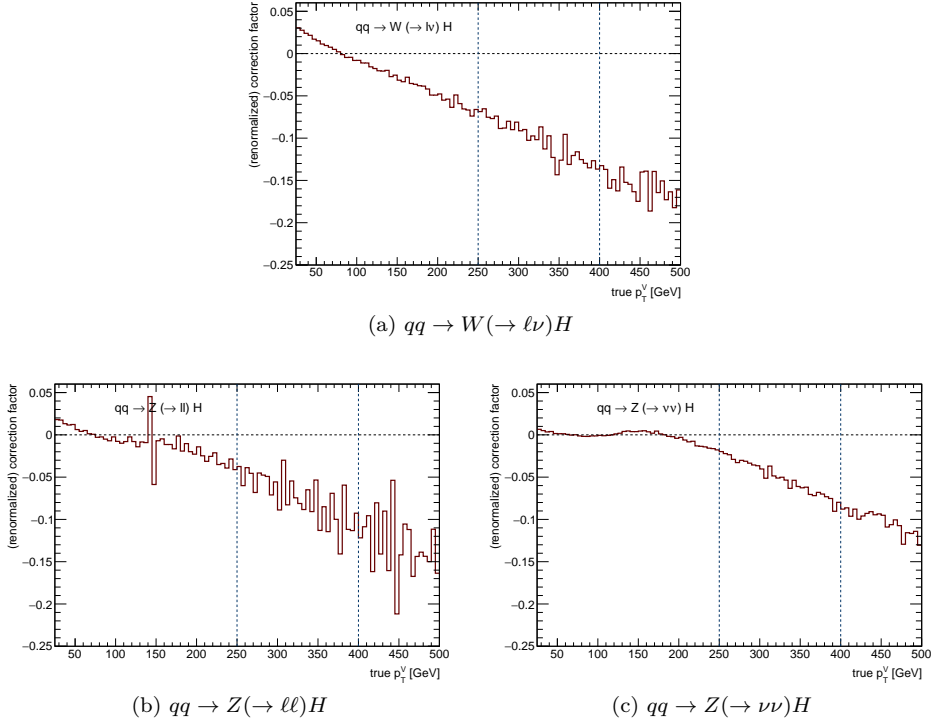


Figure 7.13: NLO EW corrections to quark-initiated Higgs-strahlung as a function of the simulated generator-level  $p_T^V$ . The corrections have been derived as the ratio NLO EW with respect to the Born level using HAWK [189, 190]. The correction factors shown here are renormalised to leave the total cross-section unchanged.

Sample	Cross-section [fb]
$qq/qg \rightarrow W^-(\rightarrow \ell^-\nu)H$	179.49
$qq/qg \rightarrow W^+(\rightarrow \ell^+\nu)H$	282.78
$qq/qg \rightarrow Z(\rightarrow \ell\ell)H$	77.04
$gg \rightarrow Z(\rightarrow \ell\ell)H$	12.42
$qq/qg \rightarrow Z(\rightarrow \nu\nu)H$	153.05
$gg \rightarrow Z(\rightarrow \nu\nu)H$	24.57

Table 7.4: Production cross-sections used to normalise the various signal samples. The leptons  $\ell$  and  $\nu$  are summed over all three generations. The Higgs decay branching ratio is not included.

quark loops are denoted as  $\sigma_{t\text{-loop}}$ . Photon induced contributions ( $\sigma_\gamma$ ) have been calculated with HAWK and are added to the sum. The  $\sigma^{ggZH}$  value contains the  $gg \rightarrow ZH$  process up to NLO in QCD ( $\sim \alpha_S^3$ ) including soft gluon resummation up to next-to-leading logarithms (NLL) [167–171].

The  $qq/qg$ -induced  $WH$  sample is normalised using  $\sigma^{WH}$ . For the  $ZH$  cross-section, the  $qq/qg$ -induced sample is normalised with  $\sigma^{ZH} - \sigma^{ggZH}$ , whereas the  $gg$ -induced sample is normalised with  $\sigma^{ggZH}$ . For this normalisation, a branching ratio  $\text{BR}(H \rightarrow b\bar{b}) = 58.2\%$  is used. It is calculated with HDECAY [195–197] and PROPHECY4F [198–200]. To obtain the final normalisation, and exploiting the assumption of a narrow width for the Higgs boson, the BR is multiplied to the production cross-section.

The cross-section values, without the branching ratio, are listed in Table 7.4.

### 7.3.2.2 Top quark pairs

**Simulated samples** The production of  $t\bar{t}$  is simulated using POWHEG-BOX v2 [153, 172, 192, 193] for the matrix element generation, which yields NLO QCD accuracy. The NNPDF3.0NLO PDF set is used and the  $h_{\text{damp}}$  parameter, which controls the matching and therefore regulates the hardest emission recoiling the  $t\bar{t}$  system, is set to  $1.5 m_t$  [201]. PYTHIA 8.230 [155] is used for the parton shower and hadronisation with the A14 tune [173] and the NNPDF2.3LO set of PDFs [202]. To model their subsequent decay chains,  $b$ - and  $c$ -hadrons are passed to EVTGEN 1.6.0.

**Cross-section prediction** The cross-section value used to normalise the  $t\bar{t}$  sample is calculated at NNLO in QCD and includes NNLL resummation of soft-gluon terms with the TOP++2.0 [174, 203–208] tool. At  $\sqrt{s} = 13 \text{ TeV}$ , the cross-section is  $832 \pm 51 \text{ fb}^{-1}$  assuming  $m_t = 172.5 \text{ GeV}$ . The uncertainties include variations of the PDF,  $\alpha_S$ , the top mass and the QCD scales.

**Analysis specific generation setups** Since the event selection reduces the all-hadronic  $t\bar{t}$  background to a negligible fraction, only events where at least one of the  $W$  bosons decays leptonically are simulated. In addition, to enhance the sample production efficiency, in the 0-lepton channel several  $E_T^{\text{miss}}$ -filtered samples are used to extend the statistical power of the signal-like events that are more likely to pass event the selection cuts. These samples require a certain amount of  $E_T^{\text{miss}}$  already at the generation stage with windows of

$$E_T^{\text{miss}} \in \{[100, 200), [200 - 300), [300 - 400), > 400\} \text{ GeV} \quad .$$

In the 2-lepton channel, events where both  $W$  bosons decay leptonically are simulated separately and added to the non-all-hadronic simulations after removing the overlap.

### 7.3.2.3 Single top

Single top quark production is categorised at LO into three main production modes:  $s$ -channel and  $t$ -channel production, as well as the associated production with a  $W$  boson ( $Wt$ ). Example Feynman diagrams for the three modes are shown in Figure 7.8.

**Sample generation** The  $s$ -channel production is generated using POWHEG-BOX v2 [153, 192, 193, 209] at NLO in QCD in the five-flavour scheme with massless  $b$ -quarks and the NNPDF3.0NLO PDF set.

The  $t$ -channel production also uses POWHEG-BOX v2 at NLO accuracy in  $\alpha_s$  and the NNPDF3.0NLO PDF set. However, the  $t$ -channel process is simulated in the four-flavour scheme, which means the initial state  $b$ -quark always originates from a  $g \rightarrow b\bar{b}$  splitting. The decay of the top quarks is handled at LO with MADSPIN [210, 211] which preserves all spin correlations between the decay products.

In the case of  $Wt$  production, which is also simulated with POWHEG-BOX v2 [153, 178, 192, 193] at NLO in QCD, but instead using the five-flavour scheme with massless  $b$ -quarks and the NNPDF3.0NLO PDF set, some overlap with  $t\bar{t}$  production occurs. At NLO in QCD, these processes have overlapping diagrams and it is no longer possible to keep them formally apart. The diagram removal scheme [212] is used to handle the overlap by removing doubly resonant diagrams from the  $Wt$  sample, i.e. where both top quarks are on-shell. An example of such doubly resonant diagrams is shown in Figure 7.14.

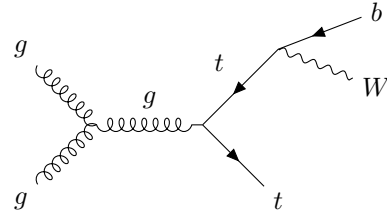


Figure 7.14: Example Feynman diagram of  $Wt$  production at NLO in QCD that overlaps with LO  $t\bar{t}$  production.



A comparison with the alternative diagram subtraction scheme is used to assess systematic uncertainties.

For all three production modes, PYTHIA 8.230 with the A14 tune and the NNPDF2.3LO PDF set is used for parton showering and hadronisation. EVTGEN 1.6.0 models all  $b$ - and  $c$ -hadron decays. In view of the analysis event selection, in the case of  $s$ - and  $t$ -channel, only events with a leptonically decaying  $W$  boson are simulated.

**Cross-section predictions** The fiducial cross-sections for sample normalisation are calculated at NLO in QCD for  $s$ - and  $t$ -channel production using HATHOR v2.1 [176, 177], separately for top and anti-top production. For the  $s$ -channel this results in a cross-section of  $6.35^{+0.23}_{-0.20}$  pb (top) and  $3.97^{+0.19}_{-0.17}$  (anti-top). The  $t$ -channel samples are normalised to  $136.0^{+5.4}_{-4.6}$  pb (top) and  $81.0^{+4.1}_{-3.6}$  pb (anti-top). A branching fraction of 32.5% for leptonic  $W$  boson decays is assumed to scale the cross-sections before sample normalisation. The quoted uncertainties include both PDF+ $\alpha_s$  and QCD scale variations.

The fiducial  $Wt$  production cross-section is calculated with approximate NNLO accuracy from NNLL soft-gluon resummation, resulting in a cross-section of  $71.7 \pm 3.8$  pb [179, 213]. Uncertainties include PDF and QCD scale variations, which are added in quadrature.

### 7.3.2.4 $V$ +jets

**Sample generation**  $V$ + jets production is simulated with SHERPA v2.2.1 [181]. The matrix elements are calculated by making use of the Comix [183] and OPEN-LOOPS [182, 214, 215] libraries. These calculations are NLO accurate in  $\alpha_s$  for final states with up to 2 partons and LO accurate for  $Z + 3$  jets and  $Z + 4$  jets. Example Feynman diagrams for  $Z + 2$  jets are shown in Figure 7.6.

The events are further processed by the SHERPA internal parton shower algorithm based on Catani-Seymour dipole factorisation and the cluster hadronisation model [216]. The PS makes use of the NNPDF3.0NNLO PDF set and has its own set of tuned parameters. The MC@NLO algorithm matches the matrix elements to the parton shower and the MEPS@NLO multijet merging method [185, 217–219] merges all produced samples into a single, inclusive sample. The merging threshold on jets is set to 20 GeV. Decays of  $b$ - and  $c$ -hadrons are handled by SHERPA internally.

In the case of  $Z$ +jets, the simulation includes off-shell photon contributions but applies a lower cut on the dilepton invariant mass of  $m_{\ell\ell} > 40$  GeV to these contributions. This cut is justified by the event selection requiring a reconstructed dilepton mass around the  $Z$  pole.

**Cross-section prediction** The samples are normalised to cross-section predictions at NNLO in QCD obtained with FEWZ [220] and the MSTW2008NNLO PDF set [221]. The values are 20080 pb ( $W \rightarrow \ell\nu$ ), 2107 pb ( $Z \rightarrow \ell\ell$  for  $m_{\ell\ell} > 40$  GeV)

and 11373 pb ( $Z \rightarrow \nu\nu$ ). The first two cross-sections are defined per lepton flavour while the third one is summed over all neutrino flavours. Uncertainties are estimated to be  $\mathcal{O}(5\%)$ , comparing different PDF sets and QCD scale choices [222].

**Analysis specific generation setups** In order to better populate phase spaces that overlap with the analysis region and to ensure good statistical accuracy even at high values of  $p_T^V$ , cuts on  $\max(H_T, p_T^V)$  are introduced at generator level, where  $H_T$  represents the scalar sum of all parton level anti- $k_t$  ( $R = 0.4$ ) jets with  $p_T > 20$  GeV. Separate  $V$ +jets samples are generated for the following regions:

$$\max(H_T, p_T^V) \text{ [GeV]} \in \{[0, 70), [70, 140), [140, 280), [280 - 500), [500, 1000), > 1000\} \quad .$$

The samples below  $\max(H_T, p_T^V) = 500$  GeV are further filtered using different particle-level hadron filters, to enhance the fraction of simulated events with heavy flavour hadrons ( $b$  and  $c$ ). Because these filters are defined without overlap between themselves, the individual contributions can be added to yield the inclusive simulation sample.

### 7.3.2.5 Diboson

**Sample generation** Diboson production, shown in Figure 7.5, is simulated using a setup that is very similar to single boson production. In analogy to the  $VH$  signal samples, it is separated into  $qq/qg$ - and  $gg(\text{loop})$ -induced production modes. In both cases, the simulation is restricted to on-shell  $V$  production with factorised decays. Consequently the samples are split into  $WW$ ,  $WZ$  and  $ZZ$ . Only semi-leptonic final states (one  $V$  decays into leptons and the other one into quarks) are simulated as the other decay modes are sufficiently suppressed by the event selection of the analysis. Off-shell contributions are neglected and the interference with the signal is ignored, which does not affect the analysis at the current level of precision.

The  $qq/qg$ -initiated samples are simulated using SHERPA v2.2.1 at NLO in QCD for  $VV + 0$  and  $VV + 1$  jet and LO accuracy for up to  $VV + 3$  jet. The loop-induced samples are generated with SHERPA v2.2.2 at LO in QCD for up to one additional final state parton.

For the modelling of additional jets in the event, the SHERPA-internal parton shower is used with its default tune of free parameters and with the NNPDF3.0NNLO PDF set. Matching and merging follows the same procedure as for the single boson samples, i.e. improved CKKM using the MEPS@NLO method. The decay of  $b$ - and  $c$ -hadrons is handled by SHERPA internally.

**Cross-section predictions** All  $qq/qg$ -initiated samples are normalised to the SHERPA cross-section prediction at NLO in QCD. For the loop-induced samples, which are simulated at LO, a NLO QCD calculation for  $ZZ$  production is used to derive NLO/LO scale factors that are applied to the SHERPA LO predictions [187].

The resulting cross-sections are 112.7 pb ( $qq/qg \rightarrow WW$ ), 50.3 pb ( $qq/qg \rightarrow WZ$ ), 15.6 pb ( $qq/qg \rightarrow ZZ$ ), 2.8 pb ( $gg \rightarrow WW$ ) and 0.93 pb ( $gg \rightarrow ZZ$ ). Uncertainties are estimated to be  $\mathcal{O}(5\%)$  for the  $qq/qg$ -initiated values and  $\mathcal{O}(10\%)$  for the  $gg$ -initiated values.

**Analysis specific generation setups** In order to enhance the statistical power of the signal-like diboson processes, dedicated samples featuring a  $Z \rightarrow b\bar{b}$  decay are merged with the inclusive ( $Z \rightarrow q\bar{q}$  or  $W \rightarrow q\bar{q}'$ ) semi-leptonic simulations, after removing the overlap between both samples.

All samples are passed through a full GEANT4-based [223] simulation of the ATLAS detector [224]. This chain mimics the complete detector response, which includes the detector material interactions, digitisation, the readout and reconstruction.

Pile-up is simulated by overlaying additional inelastic  $pp$  collisions simulated with PYTHIA 8.186 [225] using the ATLAS A3 tune [226] and the NNPDF2.3LO PDF set. The simulated events are further reweighted such that the distribution of the average number of interactions per bunch-crossing matches the one observed in data [227].

## 7.4 Event reconstruction and selection

The reconstruction of the  $VH, H \rightarrow b\bar{b}$  event topologies requires information from all sub-detectors of the ATLAS experiment, bundled together in *physics objects* like leptons, jets and  $E_T^{\text{miss}}$ . This section first introduces the objects that are used in the analysis, then explains how they are used to reconstruct both the leptonic and hadronic side of the  $VH$  decay and finally introduces the event selection and categorisation. The latter is used to separate the signal from background processes and to define control regions that are especially pure in  $t\bar{t}$  background.

### 7.4.1 Object definitions

In this section, only object definitions that are specific to the presented analysis are described. General information on the reconstruction and calibration of the physics objects is outlined in Chapter 5.

#### 7.4.1.1 The primary vertex

Tracks of charged particles reconstructed in the Inner Detector are used to select collision vertex candidates consisting of at least two tracks. Only good quality tracks with  $p_T > 0.5$  GeV are considered and the vertex with the highest scalar  $p_T$  sum of the associated tracks is denoted the primary vertex [110]. This is done

because the hard scatter, which is the collision of interest, should have the highest momentum transfer out of all collisions in a bunch crossing.

### 7.4.1.2 Leptons

This measurement uses two lepton selection criteria. The number of reconstructed lepton candidates that pass a *baseline* selection defines the categorisation into the 0-, 1- or 2-lepton channel. The 1- and 2-lepton channel face potential contamination from multijet processes that produce fake or non-prompt leptons. Examples are mis-reconstructed jets with high electromagnetic energy deposits (fake) or leptons produced in semileptonic heavy hadron decay chains within a jet (non-prompt). To minimise these multijet contributions, the lepton selection criteria in the 1- and 2-lepton channel are tightened with respect to the *baseline* selection. Events in the 0-lepton channel are required to have zero *baseline* leptons.

**Muons** *Baseline* muons are required to be reconstructed within the Muon Spectrometer acceptance  $|\eta| < 2.7$  and have  $p_T > 7$  GeV. In order to reject non-prompt muons stemming, for example, from the decay chains of heavy flavour hadrons, their tracks have to be compatible with the primary vertex. This compatibility is ensured by requiring their transverse and longitudinal impact parameters  $d_0$  and  $z_0 \sin(\theta)$  to be small. Concretely, the transverse impact parameter significance  $|d_0/\sigma_{d_0}|$ , where  $\sigma_{d_0}$  is the uncertainty on the  $d_0$  measurement<sup>1</sup>, has to be  $< 3$  and additionally it is required that  $|z_0 \sin(\theta)| < 0.5$  mm. *Loose* identification criteria, based on their  $q/p$  significance, the reduced  $\chi^2$  of the track fit, and their  $p_T$  measurement accuracy among other things, are applied [116]. To further suppress the contamination from non-prompt muons, muon candidates are required to additionally pass the *FixedCutLoose* isolation criteria, defined in Ref. [116].

In the 1-lepton channel, *signal* muons are required to pass additional *medium* identification- and tighter track-based isolation-criteria. Because only one lepton is required, the probability for multijet events to pass the 1-lepton selection is higher than for the 2-lepton channel. This motivates the tightening of the identification and isolation criteria in the 1-lepton channel with respect to the 2-lepton channel.

**Electrons** *Baseline* electrons are required to be reconstructed within the precision measurement region of the EM calorimeter  $|\eta| < 2.47$  and have  $p_T > 7$  GeV. Similar to muons, impact parameter requirements are applied requiring  $|d_0/\sigma_{d_0}| < 5$  and  $|z_0 \sin(\theta)| < 0.5$  mm. A *loose* likelihood-based identification criteria, named *LooseAndBLayer* [113], is applied, which requires a hit in the innermost pixel layer. Furthermore, *loose* isolation criteria in both the tracker and the calorimeter need to be passed following the *Fix(Loose)* working point in Ref. [113].

<sup>1</sup>The  $d_0$  measurement is performed with respect to the beamline position which fixes the transverse position of the primary vertex. This is justified because the beam size is usually much smaller than the primary vertex resolution in the transverse plane. In cases where the beam width is not negligible it is taken into account when calculating  $\sigma_{d_0}$ .

To minimise multijet contamination in the 1-lepton channel, *signal* electrons are required to additionally pass *tight* identification- and a tighter calorimeter-based isolation criteria.

**$\tau$  leptons** Hadronically decaying  $\tau$  leptons are not explicitly targeted in the analysis, but are considered in the physics object overlap removal, and also enter the calculation of  $E_{\text{T}}^{\text{miss}}$ . When used,  $\tau$  lepton candidates are required to be central ( $|\eta| < 2.5$ ), excluding the transition region between the barrel and endcap of the electromagnetic calorimeter from  $1.37 < |\eta| < 1.52$ , to have  $p_{\text{T}} > 20$  GeV and to consist of either one or three tracks [228]. The track selection reflects that the dominant hadronically  $\tau$ -lepton decays consist of either one or three charged pions, which leave tracks in the Inner Detector. The  $\tau$  lepton candidates are furthermore required to pass the *medium* working point of a BDT-based  $\tau$ -identification classifier [134].

### 7.4.1.3 Jets

Three types of anti- $k_t$  jets are used in the analysis: *large- $R$*  calorimeter jets with  $R = 1.0$  are used to build the Higgs candidate. *Track-jets* with variable radius are used for  $b$ -tagging inside of the large- $R$  jet, and outside of it to suppress the top background contribution. *Small- $R$*  calorimeter jets with  $R = 0.4$  are used in the event categorisation to improve the overall signal sensitivity and the calculation of  $E_{\text{T}}^{\text{miss}}$ .

**Large- $R$  jets** Large anti- $k_t$  jets with  $R = 1.0$  are formed from topological calorimeter-cell clusters that are calibrated cluster-by-cluster using local cell weighting. To minimise the contamination from pile-up and the underlying event, the clustered jets are trimmed [127]. Only large- $R$  jets with  $p_{\text{T}} > 250$  GeV and  $|\eta| < 2.0$  are considered in this analysis, where the  $p_{\text{T}}$ -requirement marks the point where a significant fraction of the large- $R$  jets contain both  $b$ -hadrons from the  $H \rightarrow b\bar{b}$  decay. The latter requirement arises from the need of tracker coverage to gain information about the jet substructure.

**Track-jets with variable radius (VR)** Although the neutral jet components are missing for track-jets, the high spatial resolution of the tracker makes track-jets ideal candidates in boosted environments, where decay products are very collimated. The radius parameter of the VR track-jets is jet  $p_{\text{T}}$  dependent, where the effective jet size decrease with higher  $p_{\text{T}}$ . The size of the track-jets varies from  $R = 0.4$  at  $p_{\text{T}} = 75$  GeV to  $R = 0.02$  at  $p_{\text{T}} = 1.5$  TeV. VR track-jets are formed from good quality tracks from the Inner Detector with  $p_{\text{T}} > 0.5$  GeV and  $|\eta| < 2.5$ . These jets have to be compatible with the primary vertex and a cut on the longitudinal impact parameter is placed:  $|z_0 \sin(\theta)| < 3$  mm. This requirement reduces the contamination from pile-up interactions. Only central track-jets with  $|\eta| < 2.5$  and  $p_{\text{T}} > 10$  GeV, consisting of at least two tracks are considered.

**Small- $R$  jets** Anti- $k_t$   $R = 0.4$  calorimeter jets with  $p_T > 30$  GeV and within the calorimeter acceptance of  $|\eta| < 4.5$  are used. Jets with  $p_T < 120$  GeV and within the coverage of the tracking detector ( $|\eta| < 2.5$ ) need to furthermore pass the *medium* jet vertex tagger requirement [124]:  $JVT > 0.59$  for  $|\eta| < 2.4$  and  $JVT > 0.11$  else. This requirement suppresses the contamination from pile-up jets.

#### 7.4.1.4 Flavour labelling

The simulated track-jets are labelled as  $b$ -,  $c$ - or light-jets by searching for hadrons with  $p_T \geq 5$  GeV in the vicinity of the jet axis. If a  $b$ -hadron is found within  $\Delta R = 0.3$ , the jet is labelled as a  $b$ -jet. If no  $b$ -hadrons are found,  $c$ -hadrons and afterwards hadronically decaying  $\tau$  leptons are searched for using the same criteria. If neither  $b$ -, nor  $c$ -hadrons and no  $\tau$  leptons are found, the jet is labelled as a light-jet. This flavour labelling is used after the flavour tagging to correct the tagging efficiencies to the values measured in data and to better describe the background compositions.

#### 7.4.1.5 Flavour tagging

To enhance the purity of Higgs boson candidates, flavour tagging is performed on the VR track-jets using the MV2c10 discriminant. The applied working point is tuned to result in an average  $b$ -jet tagging efficiency of 70% per jet in simulated  $t\bar{t}$  events. Using the same simulated events, the light-jet and  $c$ -jet rejection rates are estimated to be 304 and 9, respectively. The tagging and mis-tagging efficiencies are corrected to match the ones measured in data [142]. This correction depends on the flavour label of the track-jet.

#### 7.4.1.6 Missing transverse momentum

The presence of neutrinos is inferred from a momentum imbalance in the transverse plane, the missing transverse momentum  $E_T^{\text{miss}}$ . It is reconstructed as the negative vector sum of  $p_T$  of all leptons, photons,  $\tau$  leptons, and small- $R$  jets. Additionally, it includes a track-based 'soft-term' which is built from good quality tracks that are matched to the primary vertex but not associated with any lepton or small- $R$  jet. The vertex association makes this soft term especially pile-up robust. A separately calculated, entirely track-based  $E_{T, \text{trk}}^{\text{miss}}$  is used in the 0-lepton channel to suppress multijet and non-collision background. It is built using all the tracks from the primary vertex and is therefore especially pile-up independent, despite missing all neutral particles.

#### 7.4.1.7 Overlap removal

The different physics objects that have been described are reconstructed independently of each other. It is therefore possible that some objects are partially or

completely overlapping. To avoid this double counting a dedicated overlap removal procedure is performed.

- $\tau$  leptons are removed if they are closer than  $\Delta R = 0.2$  to a loose electron or a loose muon.
- Small- $R$  jets are removed if they are closer than  $\Delta R = 0.2$  to a  $\tau$  lepton.
- If a loose muon shares a track with a loose electron in the Inner Detector, the electron is removed, unless the muon is *calorimeter-tagged*. Then the muon is removed.
- If a small- $R$  jet is found closer to a loose electron than  $\Delta R = 0.2$ , the jet is removed because energy deposits in the electromagnetic calorimeter will also be clustered as jets. For any surviving jets, the electron is removed if  $\Delta R < 0.4$  as it most likely originates from a semileptonic heavy hadron decay inside the jet.
- If a small- $R$  jet is found closer to a loose muon than  $\Delta R = 0.2$ , or the muon track is associated to the jet, then the jet is removed if it has less than three tracks with  $p_T > 500$  MeV or both of the following conditions are met: The  $p_T$  ratio of the loose muon and the jet is larger than 0.5 and the ratio of the muon  $p_T$  and the  $p_T$  sum of all tracks with  $p_T > 500$  MeV associated to the jet is larger than 0.7. In these cases it is unlikely that the jet is a real jet. For any surviving jets, the muon is removed if  $\Delta R < 0.4$ , to suppress muons from semileptonic heavy hadron decays.
- If a loose electron is found closer to a large- $R$  jet than  $\Delta R = 1.2$ , the large- $R$  jet is removed.
- A dedicated overlap removal between muons and large- $R$  jets is not necessary.

## 7.4.2 Event reconstruction

The following section details the reconstruction techniques used for the leptonic  $V$  and the hadronic  $H$  decay of the  $VH, H \rightarrow b\bar{b}$  signal process.

### 7.4.2.1 Vector boson candidate reconstruction

In the 0-lepton channel, the  $Z$  boson candidate can only be partially reconstructed as the momentum in the  $z$ -direction of the two neutrinos is missing. The transverse momentum of the  $Z$  boson,  $p_T^Z$ , is approximated with  $E_T^{\text{miss}}$ . In the 1-lepton channel, only one neutrino is present in the final state. Its  $z$ -momentum is therefore calculated from the  $W$ -mass constraint up to a potential twofold ambiguity that is solved by choosing the solution that minimises  $|\beta_z^W - \beta_z^H|$ , where  $\beta_z = p_z / \sqrt{p_z^2 + m^2}$  [229]. In cases where, due to inaccuracies, the reconstructed  $m_T^W$  is larger than the nominal  $W$ -boson mass, the quadratic equation has no solution and  $m_T^W$  is set to the nominal  $W$ -boson mass. In the 2-lepton channel, the  $Z$  boson can be fully reconstructed from the two charged leptons.

### 7.4.2.2 Higgs boson candidate reconstruction

The hadronic  $H \rightarrow b\bar{b}$  decay is reconstructed identically in all three lepton channels of the analysis. The large- $R$  jet with the highest  $p_T$  in each event is defined as the Higgs boson candidate, motivated by the LO final state topology of the signal.

At least two VR track-jets are required to be matched to the Higgs boson candidate using the ghost association procedure [130, 131]. This procedure adds the track-jet 4-vectors as 'ghosts' with zero energy to the large- $R$  jet clusters and reruns the jet clustering algorithm. If the clustering algorithm includes a certain track-jet axis in the final large- $R$  jet, the track-jet is said to be matched to the large- $R$  jet. From the  $H \rightarrow b\bar{b}$  signal, at LO only two VR track-jets are expected to be matched to the large- $R$  jet. Additional track-jets beyond that could stem from FSR or pile-up, due to the large size of the Higgs boson candidate, and therefore no upper cut on the number of matched track-jets is placed.

For  $VH, H \rightarrow b\bar{b}$  events, the Higgs boson candidate is required to contain two  $b$ -hadrons. To check their presence, the two VR track-jets with the highest  $p_T$  are required to be  $b$ -tagged using the MV2c10 tagger at the 70% efficiency working point. This tagging strategy slightly outperforms an alternative strategy, which considers all matched track-jets for  $b$ -tagging. Given the chosen working point, on average  $\sim 50\%$  of signal events pass this criteria. The advantage of this flavour tagging procedure, i.e. tagging individually for each of the two track-jets, is that the calibration can be performed independently of the  $VH, H \rightarrow b\bar{b}$  signal on any sample of track-jets. The calibration approach assumes that the boosted environment does not influence the per-jet tagging efficiency. At the level of the precision of the analysis and for the chosen working point, this assumption is verified to be valid.

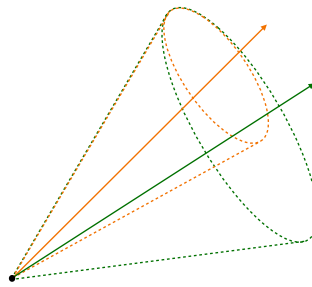


Figure 7.15: Illustration of concentric jets with variable radius.

Due to the  $p_T$ -dependent size of the VR track-jets, these jets can potentially overlap or even be concentric as sketched in Figure 7.15. These overlaps create problems with the flavour labelling, which is based on the  $\Delta R$  between the heavy flavour hadron and the jet axis. An accurate labelling is needed to apply the correct simulation-to-data corrections for the  $b$ -tagging efficiencies. To avoid this overlap,



events are removed where

$$\Delta R(\text{jet}_i, \text{jet}_j) < \min(R_{\text{jet}_i}, R_{\text{jet}_j}) \quad . \quad (7.5)$$

In this formula, index  $i$  labels the two tracks-jets with highest  $p_T$ , which are considered for  $b$ -tagging, and index  $j$  labels all VR track-jets with  $p_T > 5$  GeV that consist of at least one track<sup>2</sup>.

### 7.4.2.3 The combined jet mass

Since the Higgs candidate mass is used as the final discriminant in the analysis, it needs to be reconstructed as precisely as possible. For the signal process it clusters around the Higgs boson mass, whereas for the backgrounds the distribution either shows different peaks (diboson or  $t\bar{t}$ ) or a non-resonant shape ( $V$ +jets). For high  $p_T$  large- $R$  jets, the calorimeter-based mass suffers from the coarse size of the calorimeter cells, which don't allow for a precise determination of the opening angle of the jet constituents if they are very close. Therefore, the *combined jet mass*, which is calculated as a weighted sum of tracker and calorimeter mass as

$$m_{\text{comb}} = w_{\text{calo}} \times m_{\text{calo}} + w_{\text{TA}} \times m_{\text{tracker}} \times \frac{p_T^{\text{calo}}}{p_T^{\text{tracker}}} \quad , \quad (7.6)$$

is used [129]. The weights for the calorimeter- and the track-assisted (TA) mass-terms are chosen to minimise the variance of  $m_{\text{comb}}$ . The jet mass resolution of the combined mass in the analysis phase space ranges between 9-14% and is found to slightly outperform the calorimeter-based mass. For  $m_{\text{comb}} < 50$  GeV, the numerical inversion procedure used to calibrate the jet mass response fails and therefore only Higgs candidates with  $m_{\text{comb}} > 50$  GeV are used.

### 7.4.2.4 Custom corrections to the candidate mass

To further improve the mass resolution and thereby the sensitivity of the analysis, two analysis specific corrections are applied.

**Muon-in-jet correction** Because the analysis specifically selects large- $R$  jets with enriched heavy hadron content, due to the requirement of two  $b$ -tags, the number of leptons from semileptonic decay chains is significant: In about 10% of cases, a  $b$ -hadron decay will contain a muon and a neutrino [13]. The muon will only deposit little energy in the calorimeter, the neutrino will leave the ATLAS detector undetected. Because of the 2-tag requirement, the fraction of Higgs candidates that have at least one such muon is about 20%. In cases where these muons are reconstructed, their 4-vector is added back to the jet, improving the jet's mass resolution. This correction is performed independently of the lepton selection and

---

<sup>2</sup>This overlap removal is also applied for the VR track-jets outside of the Higgs candidate that are used for event categorisation, see Section 7.4.3.

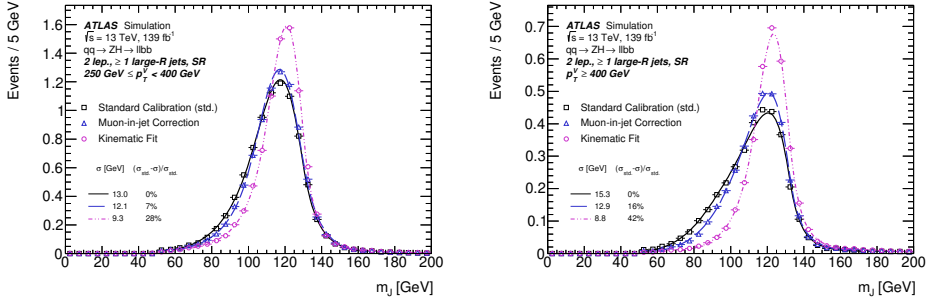


Figure 7.16: Reconstructed Higgs boson candidate (combined) mass of simulated  $qq \rightarrow ZH \rightarrow \ell\ell\nu\nu$  events for  $250 \text{ GeV} \leq p_T^Z < 400 \text{ GeV}$  (left) and  $p_T^Z > 400 \text{ GeV}$  (right). Only events passing the event selection of the 2-lepton channel, described in Section 7.4.3, are shown. The combined mass distribution after the standard calibration is shown in black, after the muon-in-jet correction in blue and after the kinematic fit in violet. A Bukin function [231] is fitted to each distribution and the resolution  $\sigma$  is extracted from FWHM/2.36. Published in Ref. [5].

the overlap removal, using *medium* quality muons with  $p_T > 10 \text{ GeV}$  and  $|\eta| < 2.7$ . Such muons are searched for within the vicinity of the VR track-jets associated to the Higgs candidate, i.e.  $\Delta R < \min(0.4, 0.04 + 10/p_T^\mu [\text{GeV}])$ . If a muon candidate is found, the calorimeter mass of the large- $R$  jet (see Eq. 7.6) is corrected by adding the muon 4-vector, after subtracting the muon's energy deposits in the calorimeter. Subsequently, the updated  $m_{\text{calo}}$  and the updated calorimeter jet  $p_T$  is used to recompute  $m_{\text{comb}}$ . The effect of this correction on the  $m_{\text{comb}}$  distribution is shown in Figure 7.16. With respect to the uncorrected calibration, the jet mass resolution is improved by 6%-17%, depending on the lepton channel and the analysis region.

**Kinematic fit** In the 2-lepton channel, where the vector boson can be fully reconstructed, a kinematic likelihood fit is performed for every event to improve the estimate of the large- $R$  jet energy [230]. The fit balances the well-measured leptonic system against the less well measured hadronic system in the transverse plane and also applies a constraint on the reconstructed dilepton mass. The Higgs candidate, all small- $R$  jets outside of it, the leptons and the  $E_T^{\text{miss}}$  'soft-term' enter into the likelihood definition. With the information from the fit, the large- $R$  jet mass is scaled by the ratio of its fitted transverse momentum with respect to its input value. Applying this correction improves the  $m_{\text{comb}}$  resolution in the 2-lepton channel by 28%-42% with respect to the standard calibration, depending on the analysis region, as shown in Figure 7.16.

### 7.4.3 Event selection and categorisation

The number of reconstructed *baseline* electrons and muons is used to categorise events into a 0-, 1- and 2-lepton channel, targeting  $ZH \rightarrow \nu\nu b\bar{b}$ ,  $WH \rightarrow \ell\nu b\bar{b}$  and  $ZH \rightarrow \ell\ell b\bar{b}$  respectively.

#### 7.4.3.1 Triggers

Events in the 0-lepton channel are selected using a disjunction of unprescaled triggers with  $E_T^{\text{miss}}$  thresholds varying from 70 GeV for data taken in 2015 and the first part of 2016 to 110 GeV for the rest of Run 2. Trigger thresholds are adjusted to cope with the increase in instantaneous luminosity provided by the LHC such that the triggers remain unprescaled at the lowest possible threshold.

In the 1-lepton channel, electron events are required to pass at least one of several unprescaled single electron triggers. The  $E_T$  threshold of the lowest triggers varies from 24 GeV – 26 GeV. These trigger algorithms each require dedicated identification criteria. In addition to the low threshold triggers with relatively tight identification (and isolation) criteria, higher  $E_T$  threshold triggers are deployed which have looser identification working points. Muon events are selected using the same  $E_T^{\text{miss}}$  triggers as in the 0-lepton channel. Because the  $E_T^{\text{miss}}$  triggers use information from the calorimeters only, and muons deposit marginal energy there,  $W \rightarrow \mu\nu$  events look to the  $E_T^{\text{miss}}$  trigger like events with  $E_T^{\text{miss}} \sim p_T^W$ . In the considered analysis phase space ( $p_T^V > 250$  GeV), the  $E_T^{\text{miss}}$  trigger is nearly 100% efficient. In addition, the single muon trigger suffers from inefficiencies due to uninstrumented regions in the Muon Spectrometer. These points motivate the decision to use  $E_T^{\text{miss}}$  triggers instead of single muon triggers.

In the 2-lepton channel, electron events are required to trigger at least one of the same single electron triggers that are used in the 1-lepton channel. For muon events, the  $E_T^{\text{miss}}$  triggers are used. With respect to the single muon triggers a 5% increase in the number of selected signal events is found.

#### 7.4.3.2 Common event selection

Events are required to have at least one large- $R$  jet with  $p_T > 250$  GeV and  $|\eta| < 2.0$ . The large- $R$  jet with highest  $p_T$  is assumed to be the Higgs boson candidate, and at least two VR track-jets with  $p_T > 10$  GeV and  $|\eta| < 2.5$ , consisting of at least two tracks, have to be ghost associated to it. The leading two track-jets are required to be  $b$ -tagged using the MV2c10 tagger at a 70% efficiency working point. Both track-jets have to pass the overlap removal for concentric VR track-jets. The combined mass of the Higgs candidate must be larger than 50 GeV. Only events with  $p_T^V > 250$  GeV are considered, reflecting the comparable requirement on  $p_T^H$ .

### 7.4.3.3 0-lepton selection

The 0-lepton channel selects events with no *baseline* leptons. Since  $E_T^{\text{miss}}$  is equal to  $p_T^V$ ,  $E_T^{\text{miss}} > 250 \text{ GeV}$  is required. Multijet production is a background in this channel mostly due to energy mismeasurements of jets. In events with misreconstructed jets, where the energy of the jet is measured too low,  $E_T^{\text{miss}}$  points into the direction of the mismeasured jet. Three dedicated cuts are therefore applied to reduce the multijet contamination:

- $\Delta\phi(E_T^{\text{miss}}, H_{\text{cand}}) > 120^\circ$
- $\Delta\phi(E_T^{\text{miss}}, E_{T, \text{trk}}^{\text{miss}}) < 90^\circ$
- $\min[\Delta\phi(E_T^{\text{miss}}, \text{small-}R \text{ jets})] > 30^\circ$

The first cut requires  $E_T^{\text{miss}}$  to be in opposite direction of the Higgs candidate, as expected under the signal hypothesis. The second cut requires the object-based missing transverse momentum and the track-based missing transverse momentum to be approximately aligned, to increase the probability that  $E_T^{\text{miss}}$  does not solely arise from calorimeter jet energy mismeasurements. The third cut requires  $E_T^{\text{miss}}$  to be to some extent isolated from any additional small- $R$  jets with  $p_T > 70 \text{ GeV}$  that are not matched to the Higgs candidate.

### 7.4.3.4 1-lepton selection

The 1-lepton channel selects events with exactly one *baseline* lepton that also passes the *signal* criteria. Electrons are required to have  $p_T > 27 \text{ GeV}$ . This cut is chosen slightly higher than the trigger threshold to exclude the turn-on region that is subject to large uncertainties. For muons, a  $p_T > 25 \text{ GeV}$  cut is applied. Events with electrons are further required to pass  $E_T^{\text{miss}} > 50 \text{ GeV}$ , to suppress the contribution from multijet production. The absolute value of the rapidity difference between the Higgs boson- and the vector boson candidate is found to further discriminate between the signal and background and an upper cut of  $|\Delta Y(V, H_{\text{cand}})| < 1.4$  is placed.

### 7.4.3.5 2-lepton selection

The 2-lepton channel selects events with exactly two *baseline* leptons, at least one of which additionally satisfies  $p_T > 27 \text{ GeV}$ . Under the signal hypothesis, the two leptons are expected to come from a  $Z$  boson decay, and are therefore required to be of the same flavour, i.e. either two electrons or two muons. In the case of two muons, the tracks are required to be reconstructed with opposite charge sign, consistent with the  $Z \rightarrow \mu\mu$  expectation. For electrons, this requirement is dropped due to a higher charge misidentification probability at high  $p_T$ , which would lead to a significant fraction of the signal being rejected. To suppress the  $t\bar{t}$  contamination, for both electrons and muons, the reconstructed dilepton mass  $m_{\ell\ell}$  needs to lie within a window around the nominal  $Z$  boson mass, i.e.

$66 \text{ GeV} < m_{\ell\ell} < 116 \text{ GeV}$ . The  $qq/qq$ - and loop-induced  $ZH$  production processes differ from the  $Z$ + jets background in terms of  $Z$  boson polarisation [232], which manifests itself e.g. in the  $p_T$  difference between the two leptons in the laboratory frame. A cut of  $(p_T^{\ell_1} - p_T^{\ell_2})/p_T^Z < 0.8$  is found to optimise the analysis sensitivity. The vector boson can be fully reconstructed and therefore, as in the 1-lepton channel, a  $|\Delta Y(V, H_{\text{cand}})| < 1.4$  cut is applied to further decrease the background contamination.

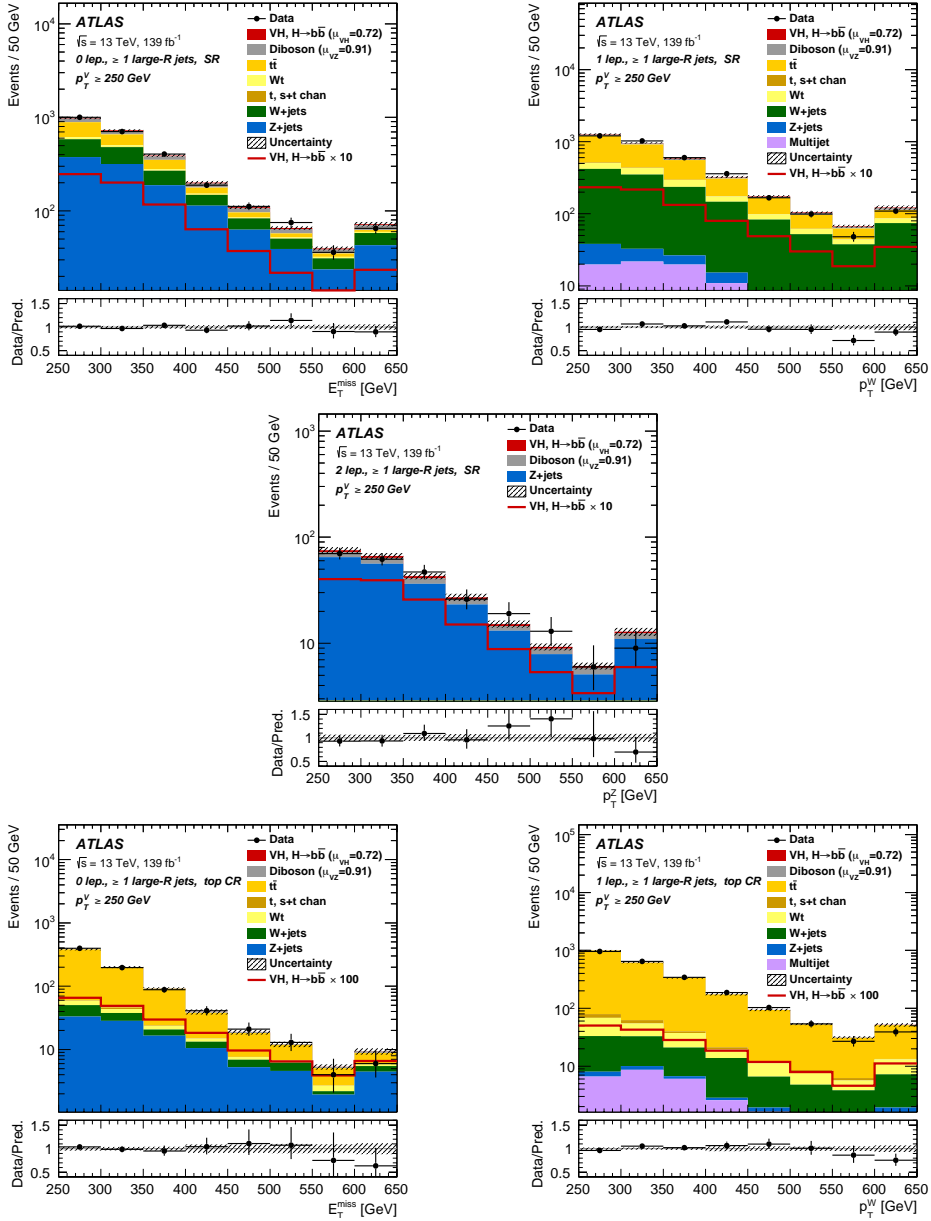
#### 7.4.3.6 Event categorisation

Two  $p_T^V$  regions are considered separately in the analysis: a *medium*  $p_T^V$  region with  $p_T^V \in [250, 400) \text{ GeV}$  and a *high*  $p_T^V$  region with  $p_T^V > 400 \text{ GeV}$ . This is motivated both by the fact that the signal-to-background ratio increases with  $p_T^V$  as well as that a variety of BSM models predict enhanced deviations at high  $p_T^V$ . The boundaries are chosen to match the pre-defined measurement bins of the STXS framework. This minimises extrapolation uncertainties for the differential measurement. The  $p_T^V$  distribution in the signal and control regions of the three lepton sub-channels is shown in Figure 7.17 post-fit, i.e. the result of the profile-likelihood fit.

In both the 0- and 1-lepton channel,  $t\bar{t}$  production is one of the main backgrounds. For these events, the Higgs candidate is mainly formed from a true  $b$ -jet as well as a mistagged  $c$ -jet from the hadronically decaying  $W$  boson. In such events, a second  $b$ -jet from the other top-quark is present and often not associated to the Higgs candidate. A  $t\bar{t}$ -enriched control region is therefore formed by requiring additional  $b$ -tagged VR track-jets outside of the Higgs candidate. Similarly, the signal region is defined orthogonally by vetoing such events. The post-fit distribution of additional  $b$ -tagged VR track-jets outside of the Higgs candidate is shown in Figure 7.18. As can be seen, the fraction of signal events with additional tags is negligible whereas the region with  $\geq 1$  tags is especially pure in  $t\bar{t}$ .

The signal regions in the 0-lepton and 1-lepton channels are further split according to the number of small- $R$  jets that are not matched to the Higgs candidate. A *high purity* signal region with no such jets and a *low purity* signal region allowing for such jets to be present are defined. This distinction helps to further discriminate against  $t\bar{t}$ , making use of the fact that even in cases where the second  $b$ -jet is not tagged or also inside of the large- $R$  jet, the average jet multiplicity of  $t\bar{t}$  is higher than for the signal. As in the case of the  $b$ -tagging veto, no such categorisation is applied in the 2-lepton channel because of the negligible  $t\bar{t}$  contamination. The post-fit distribution of the number of additional non-matched small- $R$  jets is displayed in Figure 7.19.

The resulting 10 signal and 4 control regions are summarised in Table 7.2. The complete event selection and categorisation is summarised in Table 7.5.



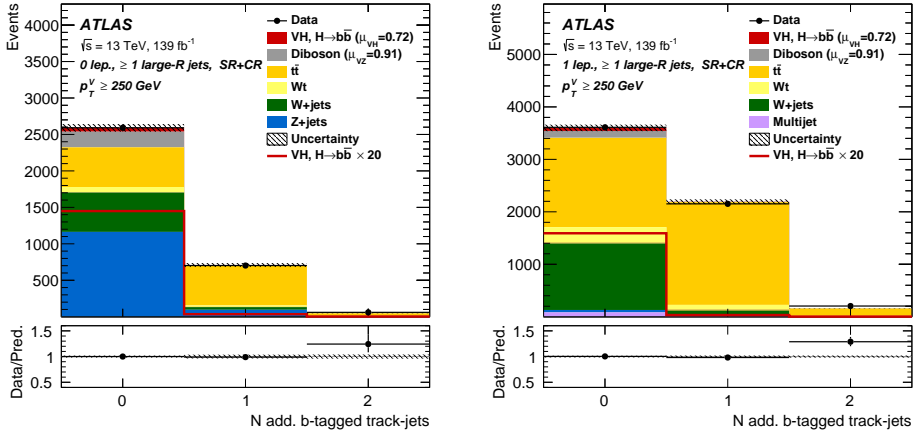


Figure 7.18: Number of additional  $b$ -tagged VR track-jets that are not matched to the Higgs candidate large- $R$  jet in the 0-lepton (left) and 1-lepton channel (right), inclusively for  $p_T^V \geq 250$  GeV. The background and signal contributions are shown as filled histograms and are scaled to match the result of the analysis fit (with the exception of the MC statistical nuisance parameters for which the fit result cannot be applied). Additionally, the signal scaled to 20 times its SM expectation is overlaid as a red line. The uncertainty band contains the combined statistical and systematic uncertainty after the fit. Published in Ref. [5].

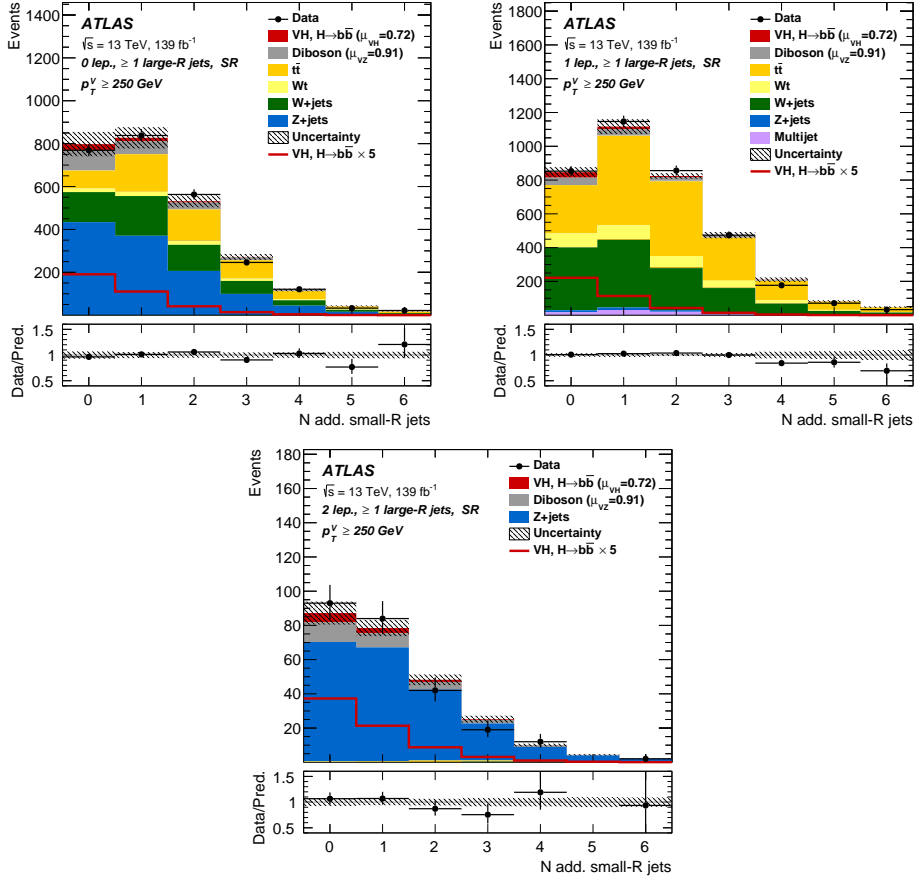


Figure 7.19: Number of additional small- $R$  jets non-matched to the Higgs candidate large- $R$  jet in signal regions of the 0-lepton (top left), 1-lepton (top right) and 2-lepton channel (bottom), inclusively for  $p_T^V \geq 250$  GeV. The background and signal contributions are shown as filled histograms and are scaled to match the result of the analysis fit (with the exception of the MC statistical nuisance parameters for which the fit result cannot be applied). Additionally, the signal scaled to 20 times its SM expectation is overlaid as a red line. The uncertainty band contains the combined statistical and systematic uncertainty after the fit. Published in Ref. [5].



Selection	0 lepton channel	1 lepton channel	2 lepton channel
	$e$ sub-channel	$\mu$ sub-channel	$\mu$ sub-channel
Trigger	$E_T^{\text{miss}}$	Single electron	Single electron
Leptons	0 <i>baseline</i> lepton	1 <i>signal</i> lepton	2 <i>baseline</i> leptons
		$p_T > 27 \text{ GeV}$	$\geq 1$ lepton with $p_T > 27 \text{ GeV}$
		no second <i>baseline</i> lepton	both leptons of the same flavour
			opposite charge sign
$E_T^{\text{miss}}$	$> 250 \text{ GeV}$	$> 50 \text{ GeV}$	-
Large- $R$ jet		at least one large- $R$ jet, $p_T > 250 \text{ GeV}$ , $ \eta  < 2$	
Track-Jets		at least two track-jets, $p_T > 10 \text{ GeV}$ , $ \eta  < 2.5$ , matched to the leading large- $R$ jet	
$b$ -jets		leading two track-jets matched to the leading large- $R$ jet must be $b$ -tagged (MV2c10, 70%)	
$m_J$		$> 50 \text{ GeV}$	
$\min[\Delta\phi(E_T^{\text{miss}}, \text{small-}R \text{ jets})]$	$> 30^\circ$	-	-
$\Delta\phi(E_T^{\text{miss}}, H_{\text{cand}})$	$> 120^\circ$	-	-
$\Delta\phi(E_T^{\text{miss}}, E_{T, \text{trk}}^{\text{miss}})$	$< 90^\circ$	-	-
$ \Delta Y(V, H_{\text{cand}}) $	-	$ \Delta Y(V, H_{\text{cand}})  < 1.4$	$ \Delta Y(V, H_{\text{cand}})  < 1.4$
$m_{\ell\ell}$	-	-	$66 \text{ GeV} < m_{\ell\ell} < 116 \text{ GeV}$
lepton $p_T$ imbalance	-	-	$(p_T^{\ell_1} - p_T^{\ell_2})/p_T^Z < 0.8$
$p_T^V$ regions		$250 \text{ GeV} < p_T^V < 400 \text{ GeV}$ and $p_T^V > 400 \text{ GeV}$	
Signal regions	0 add. small- $R$ jets	$> 1$ add. small- $R$ jets	-
	0 add. $b$ -tagged track-jets		
Control regions	$> 1$ add. $b$ -tagged track-jets		-

Table 7.5: Summary of the event selection and categorization. Published in Ref. [5].

Process	Cross-section $\times$ BR [fb]	Acceptance [%]		
		0-lepton	1-lepton	2-lepton
$qq/qg \rightarrow ZH \rightarrow \ell\ell b\bar{b}$	29.9	0.09	0.31	2.96
$gg \rightarrow ZH \rightarrow \ell\ell b\bar{b}$	4.8	0.05	0.23	2.57
$qq \rightarrow WH \rightarrow \ell\nu b\bar{b}$	269.0	0.45	2.04	-
$qq/qg \rightarrow ZH \rightarrow \nu\nu b\bar{b}$	89.1	3.83	< 0.01	-
$gg \rightarrow ZH \rightarrow \nu\nu b\bar{b}$	14.3	3.17	-	-

Table 7.6: The signal production cross-section times decay branching ratio and the analysis acceptance per lepton sub-channel. The branching fractions include decays into electrons and muons for  $Z \rightarrow \ell\ell$ , decays into all three lepton flavours for  $W \rightarrow \ell\nu$  and decays into all three neutrino flavours for  $Z \rightarrow \nu\nu$ . The analysis acceptance is defined as the number of simulated events remaining after the event selection (signal + control region) divided by the total number of simulated signal events.

### 7.4.3.7 Signal acceptance

The acceptances of the event selection with respect to the total  $VH$  signal is shown in Table 7.6, separately for each of the lepton channels and signal components. The acceptances range from two to four permille. The non-negligible fraction of  $WH$  events passing the 0-lepton selection consists of  $W \rightarrow \tau\nu$  decays where the  $\tau$  lepton further decays hadronically. The different acceptance numbers for the gluon-loop induced  $ZH$  production with respect to the quark induced one can be explained by the different  $p_T^V$  spectrum of the latter, see Ref. [168].

To illustrate the effect of the various event selection cuts on the simulated signal, the acceptance times efficiency is shown for each subsequent cut as a function of the generator-level 'true'  $p_T^V$  for the three lepton sub-channels in Figure 7.20. Acceptance times efficiency is defined as the number of events passing a specific cut divided by the total number of events before any cut is applied. For the 0-lepton channel, only the  $qq/qg$ -initiated  $Z(\rightarrow \nu\nu)H(\rightarrow b\bar{b})$  signal is considered. Similarly, the 1-lepton plot only includes the targeted  $qq/qg$ -initiated  $W(\rightarrow \ell\nu)H(\rightarrow b\bar{b})$  process and the plot for the 2-lepton channel only considers  $qq/qg$ -initiated  $Z(\rightarrow \ell\ell)H(\rightarrow b\bar{b})$ .

In the 1- and 2-lepton channel, the acceptance times efficiency values reach a plateau below unity due to the  $\tau$ -lepton decays that are not targeted by the event selection and due to non-reconstructed electrons/muons. The turn-on curve of the reconstructed  $p_T^V > 250$  GeV cut is significantly steeper for the 2-lepton channel because the  $Z$  boson is reconstructed from two charged leptons there. The effect of the large- $R$  jet related cuts is similar for the three lepton channels. The efficiency of most event selection cuts increases with the true  $p_T^V$ . An exception is the VR overlap

removal which removes about 10% of events at true  $p_T^V \sim 500$  GeV. Although the overlap removal is also applied to track-jets whose axes do not overlap with the Higgs boson candidate, this effect is nearly exclusively coming from overlapping VR track-jets inside of the Higgs candidate. The  $b$ -tagging efficiency decreases as well as a function of the true  $p_T^V$ .

## 7.5 Background composition and estimation

This section provides an overview of the background composition, which varies between the three lepton sub-channels of the analysis. The background composition in each of the 14 analysis regions is summarised in Figure 7.21. The main backgrounds in the three lepton sub-channels are:

- **0-lepton:**  $Z$ +jets,  $W$ +jets and  $t\bar{t}$
- **1-lepton:**  $t\bar{t}$ , single top production and  $W$ +jets
- **1-lepton:**  $Z$ +jets

In the following, various simulated processes are separated according to the flavour labelling of the two leading VR track-jets matched to the Higgs candidate. For example  $Z + b\bar{b}$  means that both track-jets have a  $b$ -hadron matched to them. The term hf, e.g.  $Z + hf$ , refers to the sum of  $b\bar{b}$ ,  $bc$ ,  $bl$  and  $cc$  components.

### 7.5.1 Top quark pair production

The  $t\bar{t}$  production is a main background in the 0- and 1-lepton channel. Due to the requirement on  $E_T^{\text{miss}}$  and the presence of one charged lepton, the contamination from all-hadronically decaying  $t\bar{t}$  is negligible in both cases. In the 2-lepton channel, the  $Z$  candidate is typically reconstructed from the leptons of the two different  $W$  bosons in dilepton  $t\bar{t}$ , which results in a rather soft  $p_T^V$  spectrum. Therefore, the  $p_T^V > 250$  GeV requirement, together with the  $Z$  boson mass window cut, suppresses the  $t\bar{t}$  contamination to a negligible amount.

**0-lepton channel** Over 95% of  $t\bar{t}$  events that pass the 0-lepton event selection have one hadronically and one leptonically decaying  $W$ -boson (1-lepton  $t\bar{t}$ ). In about 70% of these events, the leptonically decaying  $W$  boson decays into a  $\tau$  lepton and a neutrino. The remaining cases are equally split between  $W \rightarrow e\nu$  and  $W \rightarrow \mu\nu$  decays in which the lepton is either out of the detector acceptance, or not reconstructed.

**1-lepton channel** About 85% of  $t\bar{t}$  events that pass the 1-lepton selection have one leptonically decaying  $W$  boson that meets the event selection requirements, and one hadronically decaying  $W$  boson. Of those events, about 40% contain

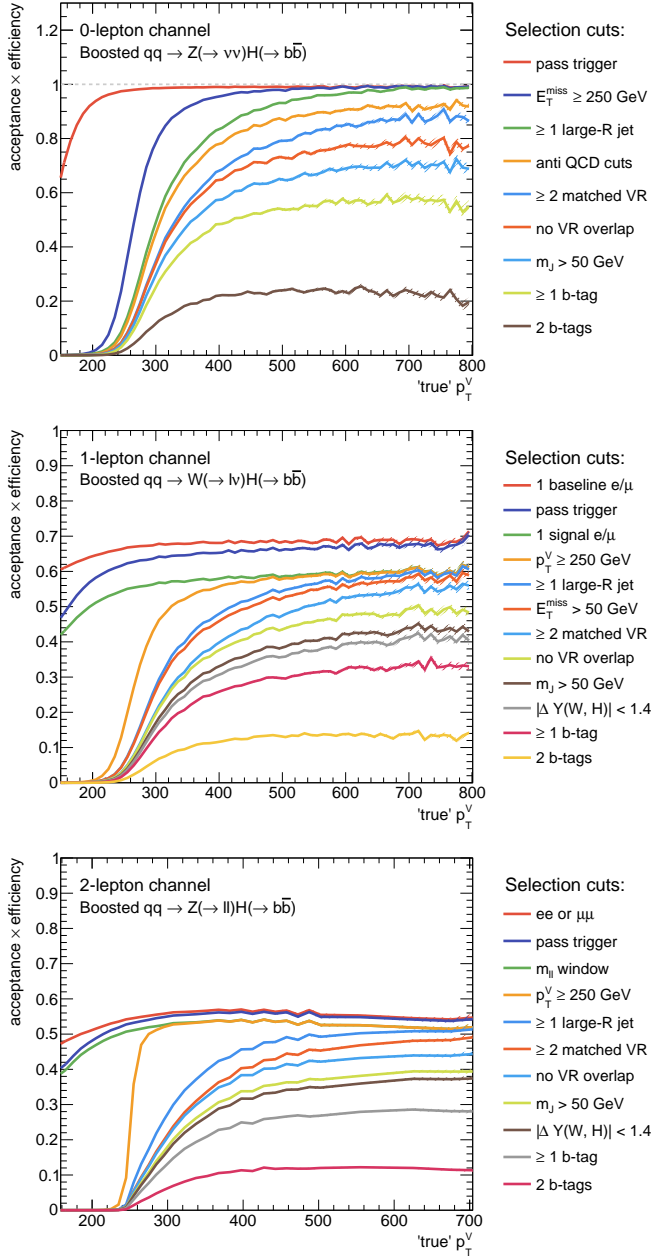


Figure 7.20: Acceptance times efficiency of the event selection cuts as a function of the generator-level 'true'  $p_T^V$ . All curves are shown separately for the 0- (top), 1- (middle) and 2-lepton channel (bottom).

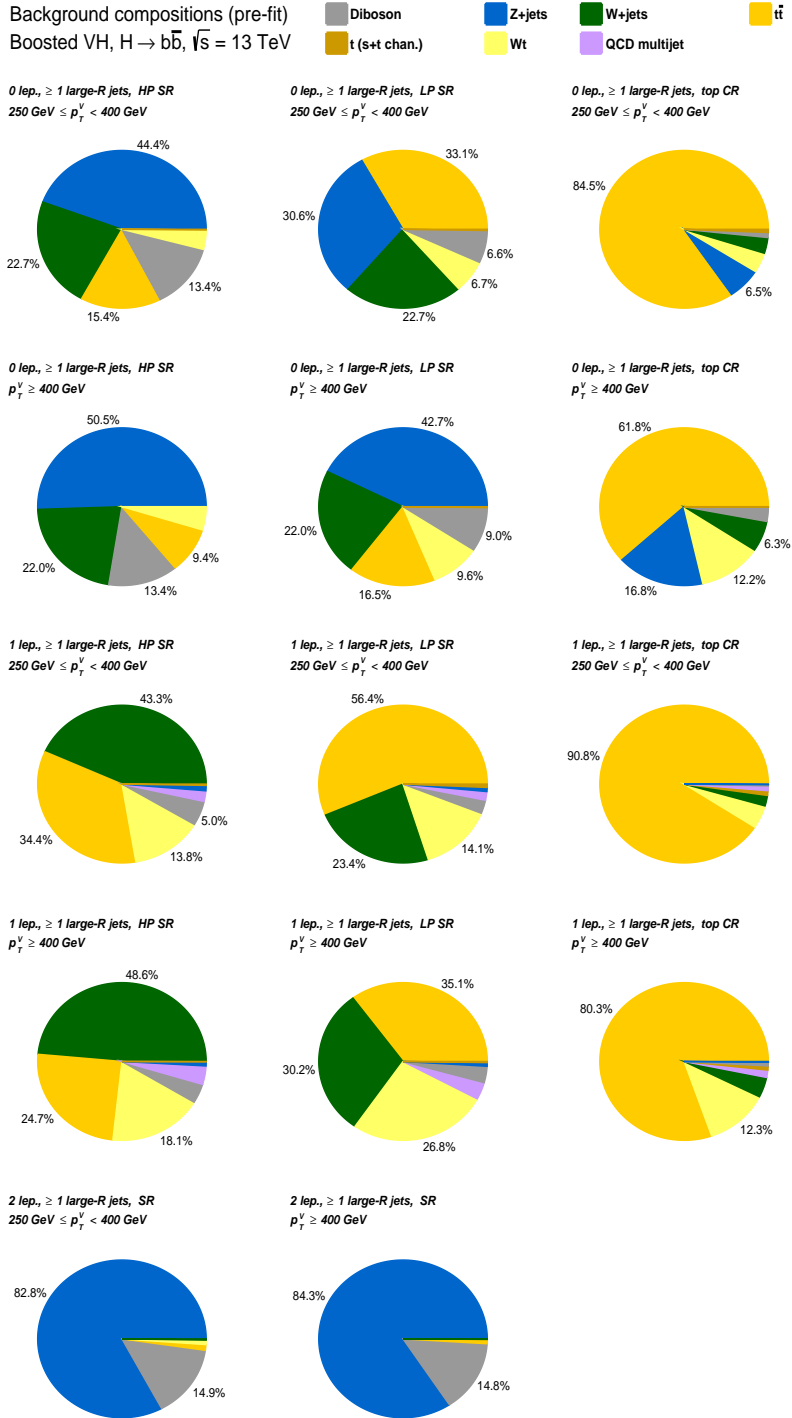


Figure 7.21: Estimated background composition of the 14 analysis regions.

electrons and 40% contain muons. In 5% of cases, a  $W \rightarrow \tau\nu$  decay is present. The remaining 15% of events have two leptonically decaying  $W$  bosons.

**Higgs candidate flavour composition** The Higgs candidate flavour composition is similar for the 0- and 1-lepton channel. For 75% of the events, the two VR track-jets with highest  $p_T$  are labelled  $bc$ , which suggests that the Higgs candidate contains the  $b$ -jet and the  $c$ -jet from the hadronically decaying  $W$  boson. Especially for high  $p_T$  top quarks, the two decay products are likely to be geometrically separated, which decreases the probability of both  $b$ -quarks to form the Higgs boson candidate. Only about 7%-10% of events are labelled  $bb$ . For about 10%-15% of events, the Higgs boson candidate is labelled  $bl$ . This fraction is lower compared to the  $bc$  label because of the lower  $b$  mistagging probability for light flavour jets compared to  $c$ -jets.

### Jet containment and Higgs candidate mass

For  $t\bar{t}$  events in both the 0- and 1-lepton channel, the Higgs candidate is likely formed from the hadronically decaying side of 1-lepton  $t\bar{t}$  production, i.e.  $t \rightarrow Wb \rightarrow qq'b$ . The invariant mass distribution of the Higgs candidate strongly depends on how many subjets are contained within the large- $R$  jet. For cases where two VR track-jets can be matched to it, the  $m_{\text{comb}}$  distribution is broad, with a peak at about 100 GeV to 120 GeV. In cases where three or more track-jets are matched to the Higgs candidate,  $m_{\text{comb}}$  peaks around the top mass, as expected. An example  $m_{\text{comb}}$  distribution from the 1-lepton channel is shown in Figure 7.22. In the medium  $p_T^V$  regions, the fraction of Higgs candidates with exactly two matched VR track-jets is about 45%, dropping to 30% in the high  $p_T^V$  regions. This is expected, because the higher the  $p_T^V$ , the higher the Lorentz boost of the top quark and the more collimated are the top quark decay products.

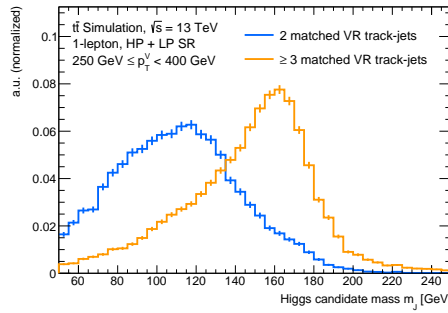


Figure 7.22: Higgs candidate mass for the  $t\bar{t}$  process in the SR (HP+LP) of the 1-lepton channel for  $250 \text{ GeV} \leq p_T^V < 400 \text{ GeV}$ , split according to the number of matched VR track-jets.

## 7.5.2 Single top production

Single top events contribute to the background in the 0- and 1-lepton channel. Of the three production mechanisms, the  $Wt$ -channel contaminates the signal regions the most. The contribution from  $s$ - and  $t$ -channel production is less than 1%. Due to the similar topology of the  $Wt$ -channel single top production and  $t\bar{t}$  production,

their background composition is similar too. In the medium  $p_T^V$  regions of both the 0- and 1-lepton channel, the  $Wt$  contribution is about one quarter of the  $t\bar{t}$  contribution, rising to up to 70% at high  $p_T^V$ .

**Higgs candidate flavour composition** The  $Wt$  production process overlaps with  $t\bar{t}$  production at NLO in QCD. The diagram removal scheme is used as a baseline to treat this overlap. A comparison with the alternative diagram subtraction scheme is performed to assess the systematic uncertainty associated with this step. The Higgs candidate flavour composition significantly depends on the choice of the overlap treatment. For the baseline diagram removal sample of simulated events, the medium  $p_T^V$  signal region contains Higgs candidates with about 60%  $bb$ , 35%  $bc$  and 5%  $bl$  labels. In the high  $p_T^V$  signal region this changes to about 70% for  $bb$ , 20% for  $bc$  and 10%  $bl$ . In the control region, which requires additional  $b$ -tagged track-jets outside of the Higgs candidate, the fraction of  $bb$  labels is reduced to 25% at medium  $p_T^V$  and 40% at high  $p_T^V$ . For the events with  $bb$  labelling, one of the  $b$ -hadron is coming from the top decay whereas the other one from other sources. For the alternative simulation with the diagram subtraction scheme, the fraction of  $bb$  labelled Higgs candidates is significantly lower, about 20%.

### 7.5.3 $V$ +jets production

In all three lepton channels,  $V$ +jets production is a main background. In the 0-lepton channel, the main contribution is  $Z \rightarrow \nu\nu$  (+jets) with a smaller contribution from  $W \rightarrow \tau\nu$  and  $W \rightarrow \ell\nu$  with unreconstructed leptons. In the 1-lepton channel, the main contribution is  $W \rightarrow \ell\nu$ . In the 2-lepton channel, the main contribution is  $Z \rightarrow \ell\ell$ .

The majority, 70% - 80% of Higgs candidates in the signal regions of the three lepton channels, are labelled  $bb$ . Together with the other labels that include at least one heavy hadron, i.e.  $bc$ ,  $bl$ , or  $cc$ , these events make up  $\sim 95\%$  of the  $V$ +jets background. In the  $t\bar{t}$  control regions of the 0- and 1-lepton channel, the  $bb$  fraction is slightly lower due to the requirement of the additional  $b$ -tagged track-jet outside of the Higgs candidate, but still between 60% and 70%. The  $V$ +jet contamination in the 1-lepton control region is below 1%.

### 7.5.4 Diboson production

In the on-shell production of heavy vector boson pairs, the  $ZZ, WZ$  and  $WW$  processes are distinguished. The Higgs candidate is most likely formed by reconstructing a  $Z \rightarrow b\bar{b}$  decay and the invariant mass distribution therefore shows a peak around the  $Z$  boson mass. In the 0-lepton channel, the  $ZZ$  process contributes about 80% to 90%, where in addition to the hadronically decaying  $Z$  boson, the second  $Z$  boson decays into a pair of neutrinos that are reconstructed as  $E_T^{\text{miss}}$ . A smaller contribution of about 10% - 20% originates from  $WZ$  production, where  $W \rightarrow \tau\nu$ . In the 1-lepton channel, about 90% of the diboson contribution is

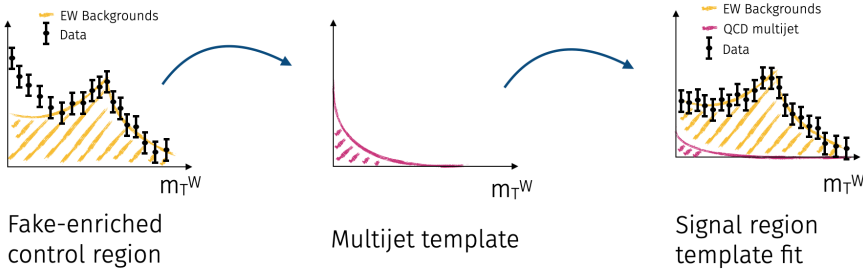


Figure 7.23: Sketch of the template fit method used to extract the multijet contamination in the 1-lepton channel.

$WZ$  events, where the leptonic signature is created by a  $W \rightarrow \ell\nu$  decay. The remaining 10% of events are nearly exclusively  $ZZ$  production, with  $Z \rightarrow \ell\ell$ . In the 2-lepton channel, more than 98% of the diboson contamination originates from  $ZZ$  production. The contribution from  $WW$  production is suppressed by the 2  $b$ -tag requirement.

### 7.5.5 QCD multijet production

Multijet production is a reducible background in the analysis. The event selection has a high rejection rate for multijet events, which makes it difficult to estimate this contribution from simulation. Instead, special techniques are applied to estimate the contribution directly from data. In the 0- and 2-lepton channels, these techniques are used to verify that the contribution is small enough to be neglected. For electron events in the 1-lepton channel, a dedicated template distribution is derived from data and included in the signal extraction fit.

#### 7.5.5.1 0-lepton channel

In the 0-lepton channel, a set of anti-multijet cuts is included in the event selection. These cuts are tuned to lower the multijet contribution to about 1%. This remaining rate is estimated by removing the cut on  $\min[\Delta\phi(E_T^{\text{miss}}, \text{small-}R \text{ jets})]$  and performing a template fit in this observable to extract the multijet yield. An exponential shape is assumed for the multijet template distribution. This choice is validated using simulated events. Because the contribution after these cuts is about 1%, the multijet process is neglected in the 0-lepton channel. Due to its similarity in shape with the non-resonant  $V$ +jets background, the residual contribution is absorbed by the fitted  $V$ +jets normalisation factor.



### 7.5.5.2 1-lepton channel

Semi-leptonic heavy hadron decays inside a poorly reconstructed jet can cause multijet events to pass the 1-lepton event selection. For electron events, jets with a high electromagnetic component that are misidentified as electron candidates are an additional source of multijet background. The isolation criteria applied in the lepton selection suppress these sources, but the remaining contamination needs to be estimated. As in the 0-lepton channel, the multijet contamination is estimated via a template fit to data. The transverse  $W$  boson mass  $m_T^W$  has a high separation between multijet production and other electroweak backgrounds, with multijet events expected to peak at low values. In order to obtain a template shape, the lepton isolation criteria are inverted and the cut on  $E_T^{\text{miss}}$  is removed. The multijet shape is then extracted using this region by subtracting the electroweak background simulation from the data, separately for electron- and muon events. A template fit to the  $m_T^W$  distribution in the signal region estimates a negligible amount of multijet production in the muon sub-channel and a 2% contribution in the electron sub-channel with an uncertainty of 55%. A sketch summarising the template fit method is shown in Figure 7.23.

### 7.5.5.3 2-lepton channel

It is unlikely for multijet events to pass the 2-lepton event selection, since it requires the production or false identification of two leptons. Since these 'fake' leptons are expected to be independent in terms of charge with respect to each other, in the muon-channel, the requirement of two oppositely charged leptons is explicitly introduced. After inverting this requirement, i.e. selecting events with two muons of the same charge sign, no events pass the selection. In the electron channel, no requirement on the reconstructed lepton charges is made. Selecting only the subset of events with two electrons of the same reconstructed charge sign, the data is described well by the included simulation, showing no signs of missing multijet contamination.

## 7.5.6 Contamination from other Higgs boson processes

The contamination from different Higgs production modes and decay channels, for example from  $t\bar{t}H$  production, is found to be negligibly small.

## 7.6 Systematic uncertainties

In addition to the statistical uncertainties of the measurement, a variety of systematic uncertainties are considered, which are grouped into experimental uncertainties and theoretical uncertainties related to the modelling of either the signal or the background processes. Experimental uncertainties are linked to the performance of

the ATLAS detector, in particular to the reconstruction, identification and calibration of physics objects. Modelling uncertainties are linked to the assumptions made in the MC simulation of the signal and the background processes, as well as their cross-section calculations.

### 7.6.1 Experimental uncertainties

The experimental systematic uncertainties are determined in dedicated performance measurements. In order to assess their impact on the observable distributions used in the analysis, the simulation settings are varied to the  $\pm 1\sigma$  bounds that are obtained from the performance measurements.

### 7.6.2 Luminosity and pile-up modelling

The integrated luminosity measurement for the full Run 2 data taking period from 2015 to 2018 yields a central value of  $139 \text{ fb}^{-1}$  with an uncertainty of 1.7% [102]. The largest sources of uncertainty arise from the calibration extrapolation from the low pile-up conditions of the Van-der-Meer scans to the physics data taking conditions and the long-term stability of the calibration. Both are determined by comparing the LUCID-2 measurements to other luminosity-sensitive detectors, such as the tracker and the calorimeter.

The measured inelastic cross-section differs from the values assumed in the pile-up simulation by 3% and a correction factor is applied [227]. A systematic uncertainty of the same size as the correction is assigned.

### 7.6.3 Electrons

Systematic uncertainties on the trigger, reconstruction, identification and isolation efficiencies are considered. Additional sources of systematic uncertainties are the electron energy scale and resolution [112]. All electron-related uncertainties are determined to have a negligible impact on the final result.

### 7.6.4 Muons

Similarly to electrons, reconstruction, identification and isolation efficiency uncertainties are considered. Together with an additional track-to-vertex association uncertainty, they are split into a statistical and a systematic component. No trigger uncertainties are considered because the  $E_{\text{T}}^{\text{miss}}$  trigger is used for muon events in both the 1- and 2-lepton channel. Uncertainties on the muon momentum scale and resolution are also considered [116]. All muon-related uncertainties are determined to have a negligible impact on the final result.

### 7.6.5 Small- $R$ jets

Systematic uncertainties related to small- $R$  jets can impact the jet energy scale (JES), the jet energy resolution (JER) as well as the efficiency of the jet vertex tagger (JVT), which is used to suppress pile-up [123, 233, 234]. The JES uncertainties have several contributions, ranging from balance measurements using data, the non-closure of the  $\eta$  intercalibration procedure, the pile-up dependence, the flavour composition and response to uncertainties related to punch-through. A dedicated additional uncertainty for the behaviour of high  $p_T$  jets is also taken into account. To facilitate combinations with other measurements, the uncertainties from the balance measurements are split according to their origin into a statistical category, a detector-related category, a category for uncertainties from the MC simulation of physics processes and a category for the remaining sources. The JES uncertainties range from  $\sim 3\%$  at  $p_T = 40$  GeV to  $\sim 1\%$  for small- $R$  jets with  $p_T = 200$  GeV and are rather flat in the central region with  $|\eta| < 3.0$ . The dominant sources are pile-up at low  $p_T$  together with the flavor response and uncertainties from the balance measurements in data. A dedicated JER smearing is applied to match the resolution measured in data. Uncertainties on this smearing are about 1.5% for central jets at 40 GeV dropping to less than 1% at 200 GeV.

### 7.6.6 Large- $R$ jets

Of all experimental systematic uncertainties, the ones related to the large- $R$  jets have the highest impact on the result. They are grouped into scale uncertainties on the jet energy (JES) and jet mass (JMS) and resolution uncertainties on both energy (JER) and mass (JMR) of the large- $R$  jet. The scale uncertainties are determined using the rTrack procedure [125]. This procedure compares the mass/ $p_T$  scale ratio of a measurement that uses only the calorimeter with one that uses only the tracker. It is performed in a sample of dijet events, which, due to the high cross-section of the process, has a sufficient statistical power to provide scale measurements up to a jet  $p_T$  of several TeV. The systematic uncertainties that are derived from this measurement are be grouped into four categories:

1. **Baseline:** The difference between the measured data and the dijet simulation by PYTHIA.
2. **Modelling:** The maximum of the differences between the PYTHIA MC generator and HERWIG or SHERPA.
3. **Tracking:** Uncertainties related to the tracks that are used in the measurement.
4. **TotalStat:** The statistical uncertainty of the measurement.

In the regime that is considered by the analysis, the Baseline and Modelling uncertainties have the largest impact on the result. The tracking uncertainties are sub-dominant and given the high dijet cross-section, the statistical uncertainties are negligible. The uncertainties themselves depend on the mass and  $p_T$  of the jet

and range from  $\mathcal{O}(1\%)$  to  $\mathcal{O}(5\%)$  in the analysis phase space.

The impact of the JER and JMR uncertainties is assessed by smearing the jet resolution in the simulation. For JER, an absolute smearing by 2% is performed whereas for JMR the resolution is smeared such that the relative mass resolution increases by 20%. These values have been obtained from previous measurements with trimmed large- $R$  jets [129, 235].

### 7.6.7 Flavour tagging

The  $b$ -tagging efficiency in simulation is corrected to the efficiency measured in data by applying scale factors that depend on the flavour and  $p_T$  of the jet. The extraction of these scale factors is subject to uncertainties that are propagated as systematic uncertainties to the measurement.

The tagging efficiency measurements are performed separately for  $b$ -,  $c$ - and light-flavour jets [142, 144, 236]. The mistagging efficiency for hadronically decaying  $\tau$  leptons is extrapolated from  $c$  jets. The total uncertainty on the  $b$ -jet scale factors is about 5%, mostly dominated by uncertainties related to the simulation of  $t\bar{t}$ . For  $c$ -jets the uncertainties are about 10%, dominated as well by uncertainties related to the simulation of  $t\bar{t}$  but also the accuracy of the light mistagging efficiency measurement. For light-flavour jets, the uncertainties are about 50%, with the largest component being the extrapolation uncertainty from the efficiency measurement tagging conditions to the analysis tagging conditions.

For hadronic  $\tau$ -jets, an additional extrapolation uncertainty is added to the uncertainties from the  $c$ -jet measurement. The measurements provide scale factors up to a jet  $p_T$  of 250 GeV for  $b$ -jets, 140 GeV for  $c$ -jets and 300 GeV for light-flavour jets. For jets with higher  $p_T$ , an additional,  $p_T$ -dependent extrapolation uncertainty is added.

### 7.6.8 Missing transverse energy

Uncertainties related to electrons, muons and small- $R$  jets are propagated to the calculation of  $E_T^{\text{miss}}$ . Dedicated uncertainties on the scale and resolution of the soft term are also considered [135, 237]. The latter is split into a component parallel and one perpendicular to  $E_T^{\text{miss}}$ . These uncertainties also impact  $E_{T, \text{trk}}^{\text{miss}}$  and the effect is treated as fully correlated with  $E_T^{\text{miss}}$ . An additional uncertainty on  $E_{T, \text{trk}}^{\text{miss}}$  is based on the observed track mismodelling. The  $E_T^{\text{miss}}$  trigger is fully efficient in the regime considered by the analysis, and no related systematic uncertainties are assigned.

### 7.6.9 $\tau$ leptons

The effect of systematic uncertainties related to  $\tau$  leptons, which enter via the calculation of  $E_T^{\text{miss}}$ , is found to be negligibly small and is therefore not considered.

### 7.6.10 Principle component analysis of uncertainties

In cases where the number of individual uncertainties is high and where the effects of the variations are correlated, e.g. for the jet- and flavour tagging-related uncertainties, a principal component analysis (PCA) is performed to obtain orthogonal variations. To reduce the number of total uncertainties, the eigenvectors with the smallest uncertainties are added in quadrature to form a single uncertainty component. Due to the PCA, the original meaning of the uncertainties is lost. For this reason, in the case of the jet-related uncertainties, the PCA is performed in subgroups. The uncertainty sources of each subgroup share a common physics origin like process modelling or detector-related uncertainties.

### 7.6.11 Modelling uncertainties

The simulation packages used to model both the signal and background processes in the analysis phase space, as well as the cross-section calculations used to normalise the MC samples, rely on various assumptions. Examples of such assumptions are the choice of renormalisation and factorisation scale, the choice of PDFs, the NLO+PS matching algorithm, the choice of parton shower and the hadronisation model and the experimental input parameters like  $\alpha_S$  or  $m_b$ . These assumptions cause additional modelling uncertainties that need to be quantified. This is done by either varying the internal parameters of the nominal simulation, if available, or by comparing the nominal simulation result to one obtained with an alternative generator setup. The modelling uncertainties are grouped into three categories:

**Normalisation uncertainties** The overall normalisation of the main backgrounds,  $t\bar{t}$  and  $V+\text{hf}$ , is solely determined from data by introducing a global scale factor for each background that is not associated to any auxiliary measurement in the the likelihood fit. The minor backgrounds, such as  $V + c\bar{c}$ ,  $V + l\bar{l}$  or single top, are scaled to the SM prediction. The uncertainty on the cross-section prediction for these processes is considered as an overall normalisation uncertainty, treated separately for each process, but implemented coherently over all analysis regions.

**Acceptance uncertainties** Acceptance uncertainties affect the relative normalisation of backgrounds between analysis regions, for example 0- vs. 1-lepton, medium  $p_T^V$  vs. high  $p_T^V$  or high purity SR vs. low purity SR. As such, they parameterise the uncertainty to which the relative acceptance of the analysis to a certain process between two measurement regions is known. These uncertainties are calculated by a comparison of the acceptance between two regions  $A$  and  $B$  with the nominal simulation setup and an alternative setup, either a change of internal parameters or a different generator. The double ratio

$$\mathcal{R} = \left( \frac{N_{\text{alternative}}}{N_{\text{nominal}}} \right)_B / \left( \frac{N_{\text{alternative}}}{N_{\text{nominal}}} \right)_A - 1 \quad (7.7)$$

is used to calculate these acceptance uncertainties, where  $N$  is the number of events that falls in each category. The usage of the double ratio removes any overall normalisation effects and prevents double counting with the normalisation uncertainties. In addition to acceptance uncertainties between analysis regions for a certain process, acceptance uncertainties on the flavour composition are introduced. They allow to change the relative normalisation of different flavour compositions e.g. the relative contribution of  $V + bb$ ,  $V + bc$ ,  $V + bl$  and  $V + cc$  to the  $Z + \text{hf}$  background.

**Shape uncertainties** The impact of the modelling uncertainties on the fit discriminant distribution  $m_J$  is assessed by comparing the nominal simulation setup with alternative simulation setups. To decouple the  $m_J$  shape effects from acceptance effects, the distributions are normalised to the same yield in the comparison.

The exact simulation setup differs from process to processes and therefore, the uncertainty treatment is summarised separately for the signal and the various background processes in what follows. The guiding principles to determine the normalisation, acceptance and shape uncertainties are the same.

### 7.6.11.1 Signal modelling

Several sources of uncertainties on the  $VH, H \rightarrow b\bar{b}$  signal simulation are considered: uncertainties on the assumed value of the  $H \rightarrow b\bar{b}$  branching ratio, uncertainties on the  $p_T^{V,t}$ -dependent NLO EW correction factors, uncertainties on the parton shower modelling, variations of the renormalisation and factorisation scales and uncertainties on the used parton distribution functions and the value of  $\alpha_s$ .

**Branching ratio** The theoretical uncertainty on the calculation of the  $H \rightarrow b\bar{b}$  branching ratio is 1.6% [67]. The largest contributions to the uncertainty are the limited knowledge of  $m_b(m_b)$  in the  $\overline{\text{MS}}$  scheme ( $\sim 0.7\%$ ), the limited knowledge of  $\alpha_s(m_Z)$  ( $\sim 0.8\%$ ) and the estimated effect of missing higher order corrections ( $\sim 0.7\%$ ).

**NLO EW corrections** To account for missing higher order EW corrections, in addition to the applied NLO EW correction factors  $\kappa_{\text{EW}}^{\text{NLO}}$ , a  $p_T^V$ -dependent systematic uncertainty  $\Delta_{\text{EW}}$  is added to the  $qq$ -initiated  $VH$  samples, following the prescription in Ref. [67].

$$\Delta_{\text{EW}} = \max\{\alpha, (\kappa_{\text{EW}}^{\text{NLO}})^2\} \quad , \quad (7.8)$$

where  $\alpha$  represents the estimated size of neglected higher order EW effects plus the uncertainty on the contribution of photon-induced  $VH$  production:  $\alpha = 1.5\%$  in the case of the  $WH$  process and  $\alpha = 1.0\%$  for the  $ZH$  process. The factor  $(\kappa_{\text{EW}}^{\text{NLO}})^2$  parameterises a possible systematic enhancement of NNLO EW effects due to large

Sudakov logarithms. At  $p_T^V = 400$  GeV,  $\kappa_{\text{EW}}^{\text{NLO}}$  is between -8% and -15%, depending on the lepton channel that is considered.

**Parton shower** To assess uncertainties arising from the choice of the PS, the hadronisation model and the UE, the nominal generation setup using POWHEG-BOX v2 and PYTHIA 8 is compared to an alternative setup where instead of PYTHIA 8.212, HERWIG 7.1.3 is used with the HERWIG internal set of tuned parameters [238, 239] and the MMHT2014LO PDF set [240]. Both acceptance uncertainties and shape uncertainties on  $m_J$  are derived for each of the signal regions. The acceptance uncertainties vary between 1% and 7% and are generally higher for the low purity SR than for the high purity SR, as expected from a change of the PS that models additional real emissions beyond NLO.

**QCD scales** To assess uncertainties related to the choice of renormalisation and factorisation scale, the scales are varied by a factor 2 up and down in both a correlated and uncorrelated way. These variations cause a change both in the overall normalisation, as well as in the relative signal acceptance between analysis regions. To separate these effects from each other, the individual variations are rearranged following the long-range Stuart-Tackmann procedure [241–243] into the following set:

- $\Delta_Y$ : affects the overall cross-section
- $\Delta_{75}, \Delta_{150}, \Delta_{250}, \Delta_{400}$ : migration acceptances between STXS  $p_T^{V,t}$  bins
- $\Delta_0, \Delta_1$ : jet migration acceptances

The overall normalisation uncertainty  $\Delta_Y$  represents the QCD scale uncertainty for the total production cross-section calculation [67]. For the migration uncertainties, the subscripts indicate either the  $p_T^{V,t}$  or  $n_{\text{jet}}$  boundaries, respectively, where  $n_{\text{jet}}$  denotes the number of additional small- $R$  jets. These migration uncertainties are evaluated on the full stage-1.2 STXS split, separately for the  $qq$ - and  $gg$ -initiated signal, which makes them re-usable once the sensitivity of the measurement allows for a measurement in smaller fiducial regions. The values of the various migration uncertainties are listed in Table 7.7 for the  $p_T^{V,t}$  boundaries and in Table 7.8 for the  $n_{\text{jet}}$  boundaries. The  $p_T^{V,t}$  migration uncertainties range from 0.4% to 3.3% for  $qq$ -initiated samples and range from 10% to 30% for the  $gg$ -initiated samples. This difference in magnitude is expected, given that these  $gg$ -initiated samples are only simulated at LO in QCD and the dependence of the result on the choice of renormalisation and factorisation scales decreases the higher the perturbative order of the calculation. In contrast, the  $qq$ -initiated samples are simulated at (Mi)NLO in QCD. The same behaviour is seen for the  $n_{\text{jet}}$  migration uncertainties, which are 4% to 8% for  $qq$ -initiated samples and up to 100% for the  $gg$ -initiated samples. The impact of the QCD scale uncertainties on the  $m_J$  shape is found to be negligible.

$p_T^{V,t}$ range	$\Delta_Y^{qq}$	$\Delta_{75}^{qq}$	$\Delta_{150}^{qq}$	$\Delta_{250}^{qq}$	$\Delta_{400}^{qq}$	$\Delta_Y^{gg}$	$\Delta_{75}^{gg}$	$\Delta_{150}^{gg}$	$\Delta_{250}^{gg}$	$\Delta_{400}^{gg}$
[150, 250) GeV	0.7%	3.3%	1.3%	-0.41%	-	25%	26%	13%	-2.6%	-
[250, 400) GeV	0.7%	3.3%	1.3%	1.4%	-0.38%	25%	26%	13%	14%	-1.3%
[400, $\infty$ ) GeV	0.7%	3.3%	1.3%	1.4%	1.8%	25%	26%	13%	14%	15%

Table 7.7: Acceptance uncertainties due to QCD scale changes, arising from the signal split in  $p_T^{V,t}$  and calculated using the long-range Stewart-Tackmann method.

$p_T^{V,t}$ range	$\Delta_1^{qq}$			$\Delta_2^{qq}$		
	0 jet	1 jet	$\geq 2$ jets	0 jet	1 jet	$\geq 2$ jets
[150, 250) GeV	-4.1%	5.1%	5.1%	-	-5.0%	8%
[250, 400) GeV	-5.4%	5.3%	5.3%	-	-5.0%	6.7%
[400, $\infty$ ) GeV	-6.8%	5.5%	5.5%	-	-5.7%	6.7%

$p_T^{V,t}$ range	$\Delta_1^{gg}$			$\Delta_2^{gg}$		
	0 jet	1 jet	$\geq 2$ jets	0 jet	1 jet	$\geq 2$ jets
[150, 250) GeV	-50%	26%	26%	-	-20%	26%
[250, 400) GeV	-100%	28%	28%	-	-38%	28%
[400, $\infty$ ) GeV	-100%	30%	30%	-	-66%	30%

Table 7.8: Acceptance uncertainties due to QCD scale changes, arising from the signal split in the number of additional small- $R$  jets and calculated using the long-range Stewart-Tackmann method.

**PDF and  $\alpha_s$**  To assess systematic uncertainties due to limited data statistics in the PDF extraction, due to the extraction methodology itself, as well as due to the precision to which  $\alpha_S(m_Z)$  is known, the PDF4LHC15.30 set [188] of PDFs is used. It consists of 30 PDF replicas that are compared to the nominal PDF in order to quantify the uncertainty. Additionally, two variations of  $\alpha_S(m_Z)$  within its measurement bounds of  $0.1180 \pm 0.0015$  are averaged into a single  $\alpha_s$  uncertainty. The QCD scale variations are treated separately between  $qq$ - and  $gg$ -initiated  $ZH$  and  $WH$  production and their acceptance impact is evaluated on each of the stage-1.2 STXS bins. The variations change the acceptance in each STXS bin by 1%-2% and are found to have a negligible impact on the  $m_J$  shape.

**Residual acceptance uncertainties** The signal uncertainties are derived for the full stage-1.2 STXS split, which is a finer granularity than the STXS measurement



itself. These signal uncertainties already cover the majority of potential relative acceptance differences. The jet migration uncertainty  $\Delta_1$ , for instance, almost directly maps to an acceptance uncertainty between the high purity and low purity SRs. At the same time, the uncertainties on the STXS predictions do not consider changes inside of an STXS bin, e.g. due to a different lepton or jet  $p_T$  spectrum. This residual effect inside the bins is studied and found to be small with respect to the acceptance uncertainties between STXS bins. Therefore, this effect is not further considered.

### 7.6.11.2 Background modelling

**$t\bar{t}$**  Systematic uncertainties on the simulation of  $t\bar{t}$  production are assessed by a comparison of different setups for the NLO+PS matching, the PS and hadronisation model as well as by varying the amount of QCD radiation, both for ISR and FSR. The followed procedure is similar to the description in Ref. [244, 245]. The NLO+PS matching choice of the nominal POWHEG-BOX+PYTHIA 8 generator is compared to an alternative setup with MADGRAPH5\_aMC@NLO 2.6.0 +PYTHIA 8.230, with otherwise identical settings. The uncertainties related to the PS, hadronisation and the UE are assessed via a comparison of the nominal POWHEG-BOX+PYTHIA 8 generator to a setup with POWHEG-BOX+HERWIG 7.1.3 [238, 246], using the HERWIG internal set of tuned parameters [238, 239] and the MMHT2014LO PDF set [240]. From these variations, acceptance uncertainties between the high purity and low purity SRs, the SR and CR, as well as from medium to high  $p_T^V$  are derived. The sub-jet containment of the Higgs candidate is also studied and an uncertainty on the fraction of 2 vs.  $\geq 3$  track-jets, that are matched to the Higgs candidate, is added. Additionally, the impact of the considered variations on the prediction of the  $m_J$  shape is assessed. The NLO+PS matching variation, as well as the alternative PS, contribute most to the acceptance uncertainties. The  $m_J$  shape uncertainties are driven by the ISR and the PS variation. Uncertainties on the total cross-section prediction are not included, since the normalisation is determined from data.

**Single top** Modelling uncertainties for single top production are derived in analogy to the  $t\bar{t}$  procedure. Due to the small contamination from  $s$ - and  $t$ -channel production, only the nominal  $Wt$  sample is compared to alternative generator setups. The nominal  $Wt$  sample is simulated using POWHEG-BOX+PYTHIA 8. The same set of alternative generators as for  $t\bar{t}$  production is used, with slightly different versions of HERWIG 7 (PS variation) and MADGRAPH5\_aMC@NLO 2.6 (NLO+PS matching). As in the case of the nominal  $Wt$  sample, for MADGRAPH5\_aMC@NLO, the five-flavour scheme is used, however with the NNPDF2.3NLO PDF set. Uncertainties related to the treatment of the overlap with  $t\bar{t}$  production are derived by a comparison of the nominal diagram removal scheme to an alternative simulation using the diagram subtraction scheme. A large difference between the schemes is observed, which is traced back to the description of  $b$ -jets that do not originate from the top quark decay and are reconstructed inside the Higgs

candidate. Cross-section uncertainties, acceptance uncertainties, as well as  $m_J$  shape uncertainties are derived. In addition to the acceptance uncertainties that are also present for the  $t\bar{t}$  simulation, an acceptance uncertainty between the 0- and 1-lepton channels is added. This additional uncertainty arises from the fact that an overall normalisation uncertainty for both channels is considered. For the  $t\bar{t}$  simulation the normalisation is determined from data, with separate normalisation factors measured in the 0- and 1-lepton channel.

**V+jets** Systematic uncertainties on the  $V$ +jets simulation are derived by the variation of the renormalisation and factorisation scales in the hard scatter calculation. Alternative PDF sets and changes in the merging and resummation scale are also considered, but are found to have a negligible impact on the process description in the analysis phase space. The nominal NLO+PS generator setup with SHERPA is additionally compared to an alternative LO multi-leg approach with MADGRAPH5\_aMC@NLO 2.2.2 [247] for up to four partons in the final state, using the NNPDF2.3NLO PDF set. These events are subsequently passed to PYTHIA 8.186 for parton showering, hadronisation and the UE modelling, making use of the CKKW-L merging procedure to remove the overlap. For the  $W$ +hf and  $Z$ +hf samples, the overall normalisation is determined from data and therefore no dedicated normalisation uncertainties are included. Since the contributions from  $V + cl$  and  $V + l$  are smaller, a dedicated normalisation uncertainty for these contributions is estimated. Acceptance uncertainties are derived for the heavy flavour compositions, between the high purity and low purity SR, the SR and CR as well as from medium to high  $p_T^V$ . Finally, shape uncertainties on the  $m_J$  distribution are derived from all considered variations for the  $W$ +jets and  $Z$ +jets simulations.

**Diboson** The systematic uncertainties that are considered for the diboson process are derived in analogy to the ones for the  $V$ +jets background, motivated by the similarity in the simulation setup. The renormalisation and factorisation scales in the hard scatter calculation are varied, and a comparison with alternative PDF sets and changes in the merging and resummation scale are evaluated. Similar to what is found for the  $V$ +jets process, the latter three sources are found to have a negligible impact on the phase space targeted by the analysis. An alternative generation setup, based on POWHEG-BOX v2 and PYTHIA 8.186 with the AZNLO tune, is compared to the nominal SHERPA setup. In the alternative setup, the CT10 PDF set [248] is used for the hard scatter and the CTEQ6L1 PDF set [249] is used for the PS. In contrast to the SHERPA multi-leg setup, POWHEG-BOX is an inclusive NLO generator which implements e.g. the off-shell  $V$ -decay contribution. Cross-section uncertainties, acceptance uncertainties, as well as  $m_J$  shape uncertainties are derived. The acceptance uncertainties allow for relative acceptance changes between the high purity and low purity SRs, between the medium and high  $p_T^V$  regions, as well as for acceptance changes between the three lepton sub-channels. No SR to CR acceptance uncertainty is applied, given the low fraction of diboson events in the CR.

**Multijet** Based on the results of the template fit in the 1-lepton channel for electron events, a normalisation uncertainty of 55% is applied to the multijet contamination, separately for each analysis region. Extrapolation uncertainties are found to be negligible with respect to the normalisation uncertainty.

## 7.7 Statistical treatment and inference

The  $VH$  and  $VZ$  signals are extracted from the data through a binned profile likelihood fit. A likelihood function  $\mathcal{L}$  is constructed and encodes the probability of the data under the signal hypothesis. This signal hypothesis is furthermore tested against a null hypothesis that assumes that no signal is present. The likelihood fit is performed to the binned  $m_J$  distribution, simultaneously in all 14 analysis regions. Its technical implementation builds on HISTFACTORY [250] together with the ROOFIT [251] and ROOSTATS [252] software packages.

### 7.7.1 The likelihood function definition

The likelihood function is built from a set of Poissonian probability terms that assume a counting experiment in each bin of the  $m_J$  distribution:

$$\mathcal{L}_{\text{phys}}(\text{data}|\mu) = \mathcal{L}_{\text{phys}}(\mu) = \prod_{i \in \text{bins}} \text{Pois}(N_i | \mu s_i + b_i) = \prod_{i \in \text{bins}} \frac{(\mu s_i + b_i)^{N_i}}{N_i!} e^{-(\mu s_i + b_i)} \quad , \quad (7.9)$$

where  $N_i$  is the number of observed data events in bin  $i$ , and  $s_i$  and  $b_i$  are the expected signal and background counts, respectively. The likelihood is introduced here with only one signal strength parameter  $\mu$ . In practice, multiple PoIs  $\vec{\mu}$  are fit simultaneously. The default fit configuration for this analysis extracts both  $\mu_{VH}$  and  $\mu_{VZ}$ . For the STXS measurements, the number of PoIs is increased to one PoI per fiducial measurement region.

The systematic uncertainties are incorporated into the likelihood via a set of nuisance parameters (NPs)  $\vec{\theta}$  that modify both the expected signal and background yield, i.e.  $\{s_i, b_i\} \rightarrow \{s_i(\vec{\theta}), b_i(\vec{\theta})\}$ . The central value and uncertainty of a NP  $\theta$  are often determined beforehand in auxiliary measurements, for example the JES or JMS calibration measurements. In these cases, the constraint from such an auxiliary measurement is propagated to the likelihood by multiplying  $\mathcal{L}_{\text{phys}}$  with a term  $\mathcal{L}_{\text{aux}}$ , which parameterises the auxiliary measurements using Gaussian functions. The NPs  $\vec{\theta}$  are rescaled to have a mean of zero and a unit variance. Consequently,

$$\mathcal{L}_{\text{aux}}(\vec{\theta}) = \text{Gauss}(0 | \vec{\theta}, 1) = \prod_{\theta \in \vec{\theta}} \frac{1}{\sqrt{2\pi}} e^{-\theta^2/2} \quad . \quad (7.10)$$

Minimising the product  $\mathcal{L}_{\text{phys}} \times \mathcal{L}_{\text{aux}}$  with respect to a NP  $\theta$  corresponds to a joint measurement of  $\theta$ , where  $\mathcal{L}_{\text{phys}}$  can provide additional constraining power, if the measurement is particularly sensitive to a specific NP. The fit is allowed to change the values of the NPs within uncertainties. Not all of the auxiliary measurement terms correspond to actual measurements but also the theoretical modelling uncertainties are implemented in the same way. Some NPs, usually connected to the overall normalisation of certain samples, have no auxiliary measurement, and these are constrained from  $\mathcal{L}_{\text{phys}}$  alone.

Given the limited size of the MC simulation samples, the expected number of signal and background events in each bin is only known within uncertainties. These MC statistical uncertainties are parameterised in the likelihood, too. Due to the fact that the analysis selection is tailored to have a high signal efficiency combined with a high background rejection, these uncertainties are neglected for the  $VH$  signal. For the backgrounds, and the  $VZ$  signal<sup>3</sup>, the uncertainties are sizeable and are therefore included. To regularise the number of NPs, the different background samples are treated as a joint set, following the light version of the Barlow and Beeston procedure [250, 253]. So-called  $\gamma$ -parameters  $\gamma_i$  are introduced in each bin  $i$  and are allowed to modify the expected total background yields as  $b_i(\vec{\theta}) \rightarrow \gamma_i b_i(\vec{\theta})$ . They are constrained by

$$\mathcal{L}_{\text{bkg stat}}(\vec{\gamma}) = \prod_{i \in \text{bins}} \text{Gauss}(\beta_i | \gamma_i \beta_i, \sqrt{\gamma_i \beta_i}) \quad , \quad (7.11)$$

that are multiplied to the likelihood. The parameter  $\beta_i$  approximates the total number of background events and is calculated as  $\beta_i = 1/\sigma_{\text{rel}}$ , where  $\sigma_{\text{rel}}$  is the relative statistical uncertainty on the expected total background yield. According to first principles, the penalty terms should be Poissonians, however, in the presented analysis the fit result is unchanged when Gaussian penalty terms are used instead. This choice decreases the time needed for the fit to converge in a minimum.

The full likelihood is schematically written as

$$\mathcal{L}(\mu, \vec{\theta}, \vec{\gamma}) = \prod_{i \in \text{bins}} \text{Pois}(N_i | \mu s_i(\vec{\theta}) + \gamma_i b_i(\vec{\theta})) \times \prod_{\theta \in \vec{\theta}} \frac{1}{\sqrt{2\pi}} e^{-\theta^2/2} \times \prod_{i \in \text{bins}} \text{Gauss}(\beta_i | \gamma_i \beta_i, \sqrt{\gamma_i \beta_i}) \quad . \quad (7.12)$$

The signal estimate is obtained by minimising  $-\ln(\mathcal{L})$  with respect to all parameters  $\vec{\mu}$ ,  $\vec{\theta}$  and  $\vec{\gamma}$ . This can not be done analytically and instead a gradient-descent-based method is used, implemented in the MINUIT package [254].

The likelihood is also used to test the background-only hypothesis ( $\mu = 0$ ). A

---

<sup>3</sup>In what follows the  $VZ$  process is included in the term background.

profile likelihood ratio  $\lambda(\mu)$  is defined in analogy to the Neyman-Pearson ratio as

$$\lambda(\mu) = \frac{\mathcal{L}(\mu, \hat{\hat{\theta}}, \hat{\hat{\gamma}})}{\mathcal{L}(\hat{\mu}, \hat{\hat{\theta}}, \hat{\hat{\gamma}})} \quad , \quad (7.13)$$

where  $\{\hat{\mu}, \hat{\hat{\theta}}, \hat{\hat{\gamma}}\}$  are the values that maximise the likelihood overall and  $\{\hat{\hat{\theta}}, \hat{\hat{\gamma}}\}$  the ones that maximise  $\mathcal{L}$  for a chosen value of  $\mu$ , in this case  $\mu = 0$ . Based on this ratio, the discovery test statistic  $q_0$  is constructed as

$$q_0 = \begin{cases} -2 \ln(\lambda(0)) & \hat{\mu} \geq 0 \\ 2 \ln(\lambda(0)) & \hat{\mu} < 0 \end{cases} \quad . \quad (7.14)$$

Assuming the null hypothesis, the  $p$ -value quantifies the probability of finding data that is less compatible with the null hypothesis than the data that is measured. It is defined as

$$p_0 = \int_{q_0, \text{obs.}}^{\infty} f(q_0 | \mu = 0) dq_0 \quad , \quad (7.15)$$

where  $f(q_0 | \mu = 0)$  is the PDF of the test statistic under the assumption that the hypothesis  $\mu = 0$  is true. This PDF is a priori unknown and can be estimated from MC simulations. In the limit of large sample sizes, it approaches a  $\chi^2$  distribution [255] for one degree of freedom.

In what follows, the  $p$ -value is given in terms of Gaussian standard deviations  $Z$ , calculated as

$$Z = \Phi^{-1}(1 - p_0) = \sqrt{q_0} \quad , \quad (7.16)$$

where  $\Phi^{-1}$  is the inverse Gaussian CDF.

## 7.7.2 The fit model

**Fit inputs** The likelihood function is constructed from the one-dimensional  $m_J$  histograms in the 10 signal and 4 control regions of the analysis. The range of the histograms is kept as large as possible, while avoiding empty bins in both data and the simulation based templates. The binning is optimised to maximise signal sensitivity, while keeping the MC statistical uncertainty in each bin below 20% in order not to bias the fit result. Events that end up out of the histogram range are added to the first or last bin, respectively. The binning and range of the used histograms is summarised in Table 7.9

**Inter- and extrapolation** To determine the impact of experimental and modelling systematics, the associated NP  $\theta$  is varied to its  $\pm 1\sigma$  value and the resulting  $m_J$  shape is stored in a separate (systematic) histogram. The likelihood function,

Channel	$p_T^V \in [250, 400)$ GeV				$p_T^V \in [400, \infty)$ GeV			
	HP		LP		HP		LP	
0L	SR	[50,210] GeV in 10 GeV	[50,220] GeV in 10 GeV		[50,240] GeV in 10 GeV		[50,280] GeV in 10 GeV	
	CR	[50,230] GeV in 20 GeV			[50,250] GeV in 20 GeV			
1L	SR	[50,210] GeV in 10 GeV	[50,220] GeV in 10 GeV		[50,240] GeV in 10 GeV		[50,280] GeV in 10 GeV	
	CR	[50,230] GeV in 10 GeV			[50,260] GeV in 10 GeV			
2L	SR	[50,200] GeV in 10 GeV			[50,240] GeV in 10 GeV			

Table 7.9: Summary of fit regions including the used binning and fit ranges.

however, requires a continuous description of the effect of each NP. Therefore, functions are used to interpolate between the central value and the  $\pm 1\sigma$  bounds, as well as to extrapolate to variations that are large than  $1\sigma$ . A polynomial interpolation and exponential extrapolation is used. This has the advantage that both the first and second derivative are continuous and at the same time avoids that yields become negative.

**Symmetrisation** For some NPs, e.g. the large- $R$  jet resolution uncertainty, only a one-sided variation histogram exists. This absence of a second alternate template originates from a technical limitation, because it is not possible to un-smear the resolution of the simulation to make it better. In these cases, where only a  $+1\sigma$  variation exists, the effect of the NP on the  $m_J$  distribution is symmetrised to obtain the  $-1\sigma$  variation.

**Smoothing** The effect of systematic uncertainties on the  $m_J$  distribution is estimated in two ways. For some uncertainties, like the ones related to  $b$ -tagging, the event weight of each event that passes the analysis selection is altered. For other variations, such as the ones related to the large- $R$  jet scale and resolution, the kinematic properties of each jet are altered and the full analysis chain is rerun. Due to their altered kinematic properties, events can migrate from one analysis region to an other, from one  $m_J$  bin to another, or entirely in or out of the analysis acceptance. Therefore, the effect of these variations is correlated with the size of the simulation sample. Especially in sparsely populated regions of phase space, such as at high  $p_T^V$ , this can lead to large statistical fluctuations with unwanted effects on the fit. To reduce the impact of these statistical fluctuations in the templates, an iterative smoothing algorithm is applied to this type of systematic variations. The basic assumption behind this algorithm is that the effect of the variations should be monotonic and correlated between neighbouring bins. A parabolic smoothing algorithm is chosen, given that the invariant Higgs candidate mass is used as fit discriminant.

**Pruning** Only a small subset of all NPs has a non-negligible impact on the fit result. To stabilise the fit and reduce the fitting time, a pruning technique is applied to reduce the number of NPs that are considered in the likelihood. The

pruning algorithm removes e.g. normalisation uncertainties if their effect on a certain sample in a certain region is less than  $\pm 0.5\%$ . Shape uncertainties are removed if none of the variations exceeds  $\pm 0.5\%$ . Additional pruning steps are applied to small backgrounds that contribute less than 2% to the total background in a region.

**The Asimov data set** A common tool to investigate the fit performance and to estimate the expected sensitivity of the analysis is the Asimov data set [256]. The pre-fit Asimov set is built by adding the nominal signal and background predictions with all NPs set to their (input) central value. Although a fit to this data set will by construction extract the input central values, it can be used to study the NP constraints and correlations. The post-fit Asimov set is built by taking the central values of the background NP's from an unconditional fit to data, while the signal NPs and PoIs are fixed to their SM expectation. It is used to calculate the expected significances.

## 7.8 Results

In this sections, the results of the measurements are presented. Several scenarios are investigated and to better differentiate the results of these scenarios, the results are labelled according to the number of  $VH$  PoIs ( $N_{VH}$ ) and the number of  $VZ$  PoIs ( $N_{VZ}$ ) as  $(N_{VH} + N_{VZ})$ -PoI fits.

The combined (1+1)-PoI fit of all three lepton channels measures the  $VZ$  and  $VH$  signal strengths to be

$$\mu_{VZ}^{bb} = 0.92^{+0.29}_{-0.23} = 0.92^{+0.15}_{-0.15} (\text{stat.})^{+0.25}_{-0.17} (\text{syst.}) \quad , \quad (7.17)$$

$$\mu_{VH}^{bb} = 0.72^{+0.39}_{-0.36} = 0.72^{+0.29}_{-0.28} (\text{stat.})^{+0.26}_{-0.22} (\text{syst.}) \quad . \quad (7.18)$$

Both measurements agree with the SM expectation of unity within uncertainties. Furthermore, the semileptonic  $VZ$  signal strength measurement for  $p_T^Z > 250$  GeV is in agreement with an other measurement for  $p_T^Z > 220$  GeV in the dileptonic final state of  $WZ$  production [257]. For  $\mu_{VZ}$ , the systematic contribution to the total uncertainty is larger than the statistical one. For the  $\mu_{VH}$  measurement, conversely, the statistical uncertainty is the largest source of uncertainties and is slightly larger than the combined impact of all systematic uncertainties. With respect to the background-only hypothesis, a data excess for the  $VH$  signal is observed that corresponds to a significance of  $Z_{\text{obs}}(VH)$  of 2.1 standard deviations, where 2.7 are expected from a SM Higgs boson. For the  $VZ$  signal a data excess over the background-only hypothesis is observed that corresponds to a significance of  $Z_{\text{obs}}(VZ) = 5.4$  standard deviations, where 5.7 are expected from the SM.

The data excesses are visualised in Figure 10.4, that shows the Higgs candidate mass distribution,  $m_J$ , combining all the signal regions of the 0-, 1- and 2-lepton channel after a fit to data. The observed data and the hypothesis including signal

and background contributions agree. Additionally, two background subtracted plots are shown. In one of them, the regions are weighted according to their  $VH$  signal-to-background ratio before adding them. With respect to adding the regions without weighting, this procedure is closer to the figure of merit that the fit optimises. The  $VZ$  peak is prominently visible in the background subtracted data. The  $VH$  peak next to it is visibly smaller. The  $VH$  and  $VZ$  simulations, scaled to their post-fit prediction, are overlaid as coloured histograms to guide the eye.

The  $VZ$  and  $VH$  peaks in the  $m_J$  distribution are partially overlapping and correlations between the two maximum likelihood estimates of the PoIs are expected. Figure 7.25 shows the profile likelihood ratio contours at the 68% and 95% CL, obtained from a two-dimensional scan of fixed values of  $\mu_{VH}$  and  $\mu_{VZ}$ . The correlation between the two PoIs is estimated to be 11%. Whereas from two overlapping peaks, a negative correlation is naively expected, a positive correlation is observed between  $\mu_{VH}$  and  $\mu_{VZ}$  and can be traced back to the anti-correlation of both PoIs with the background normalisation.

## 7.8.1 Validation of the maximum likelihood fit

Given the complexity of the fit model, a thorough validation is performed to ensure both the validity of the likelihood function and of the maximum that is found. To not introduce a bias on the results, this validation is initially performed on a 'blinded' setup. This means, that in all plots, the data in the region around the nominal Higgs boson mass is not looked at. Additionally, only 'conditional' fits are performed to data, where the PoIs are fixed at unity and the pulls and constraints of signal-related NPs are not looked at. Once the blinded setup is validated, the signal is extracted from an 'unconditional' fit that is allowed to adjust the PoIs. The following section presents a more detailed study of the likelihood fit performance.

### 7.8.1.1 Post-fit distributions

Post-fit distributions are shown for all signal and control regions of the 0-lepton channel in Figure 7.26, for the 1-lepton channel in Figure 7.27, and for the 2-lepton channel in Figure 7.28. In each of the plots, the data is compared to the background prediction, which is adjusted to the NP values determined by the likelihood maximisation. The different background components are shown as stacked histograms and their pre-fit contribution is shown as a dashed blue line. The  $VH$  and  $VZ$  signals are added to the stack, scaled by their best-fit  $\mu$  and  $\vec{\theta}$ , respectively. Additionally, a scaled version of the  $VH$  signal is overlaid without stacking. The lower panel of each plot shows the ratio between the data and the post-fit signal and background predictions. In both panels, the combined statistical and systematic uncertainty (post-fit) is indicated as a hashed grey band.

Overall, good agreement between the data and the fitted prediction is observed in all regions. The pre-fit prediction shows a worse agreement with the measured data,



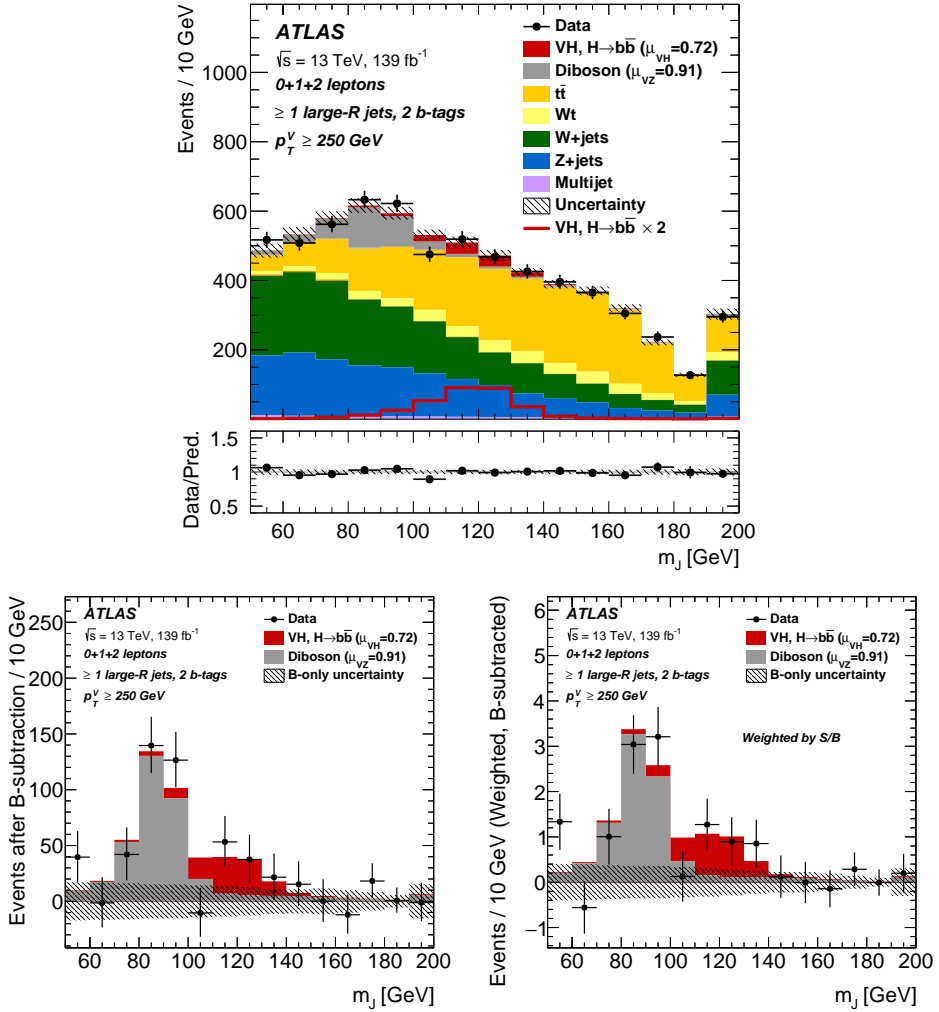


Figure 7.24: The Higgs candidate mass distribution  $m_J$ , combining all SRs of the 0-, 1- and 2-lepton channel, after the profiled likelihood fit to data. Top: All regions are stacked. The hatched grey uncertainty band shows the total uncertainty (signal + background). Bottom left: Subtracting the post-fit background prediction from the data. The  $VH$  and  $VZ$  contribution is not subtracted but shown as red and grey histograms, respectively. The grey uncertainty band includes only the post-fit uncertainty on the background. Bottom right: Same as bottom left but each region is weighted by their  $VH$  signal over background ratio before adding them. Published in Ref. [5].

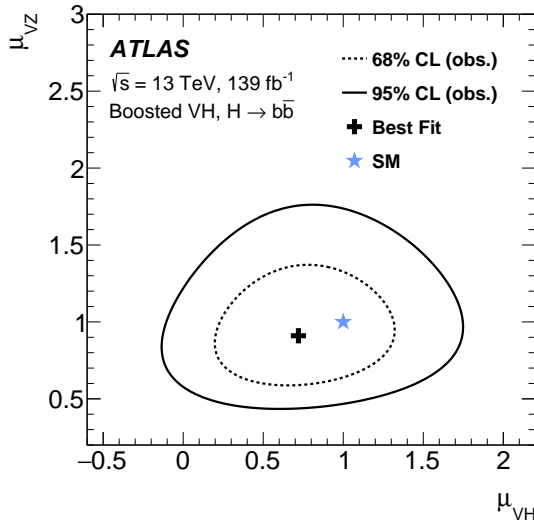


Figure 7.25: Two dimensional profile likelihood ratio scan in the  $(\mu_{VH}, \mu_{VZ})$ -plane. Indicated are the profile likelihood ratio contours at 68% and 95% CL. The cross marks the best-fit value, the star indicates the SM prediction. The Pearson correlation between the two PoIs is 11%. Published in Ref. [5].

which is traced back to known mismodellings that the fit adjusts for. Examples of such mismodellings are the simulated  $t\bar{t}$   $p_T$  spectrum, the single top -  $t\bar{t}$  interference, or the missing in-situ calibrations for the large- $R$  jet mass.

### 7.8.1.2 Nuisance parameter pulls and constraints

The NPs are adjusted by the fit to the data and their variations are studied in terms of their pull. The NP pull is defined as

$$\text{pull} = \frac{\hat{\alpha} - \alpha_0}{\sigma_{\alpha_0}} = \hat{\alpha} \quad , \quad (7.19)$$

where  $\hat{\alpha}$  is the best fit value of  $\alpha$ ,  $\alpha_0$  is its pre-fit central value and  $\sigma_{\alpha_0}$  its pre-fit uncertainty. The likelihood is constructed such that  $\alpha_0 = 0$  and  $\sigma_{\alpha_0} = 1$ .

The post-fit uncertainty for each NP is taken from the diagonal elements of the covariance matrix  $\sigma_{\alpha_i}^2 = \text{cov}(\alpha_i, \alpha_i)$ , with

$$\text{cov}(\alpha_i, \alpha_j) = H_{ij}^{-1} = \left( -\frac{\partial^2 \ln(\mathcal{L})}{\partial \alpha_i \partial \alpha_j} \right)^{-1} . \quad (7.20)$$

The inverse Hessian  $H_{ij}^{-1}$  is calculated at the minimum of  $-\ln \mathcal{L}$ . If the fit model is

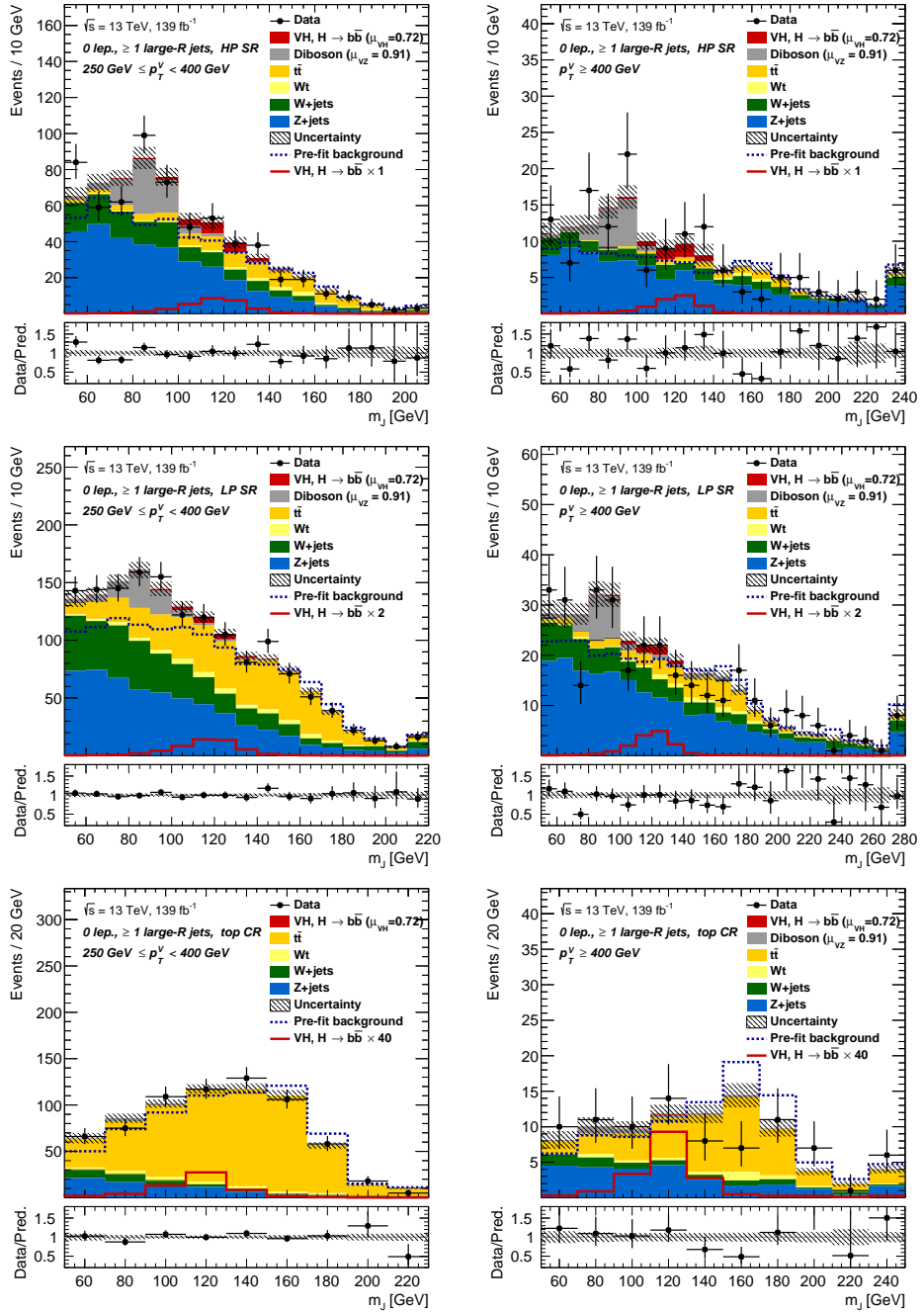


Figure 7.26: Post-fit distributions for the 0-lepton channel obtained from the unconditional fit to data. The overflow bin is added to the last bin of the shown plot range. Similar plots have been published in Ref. [5].

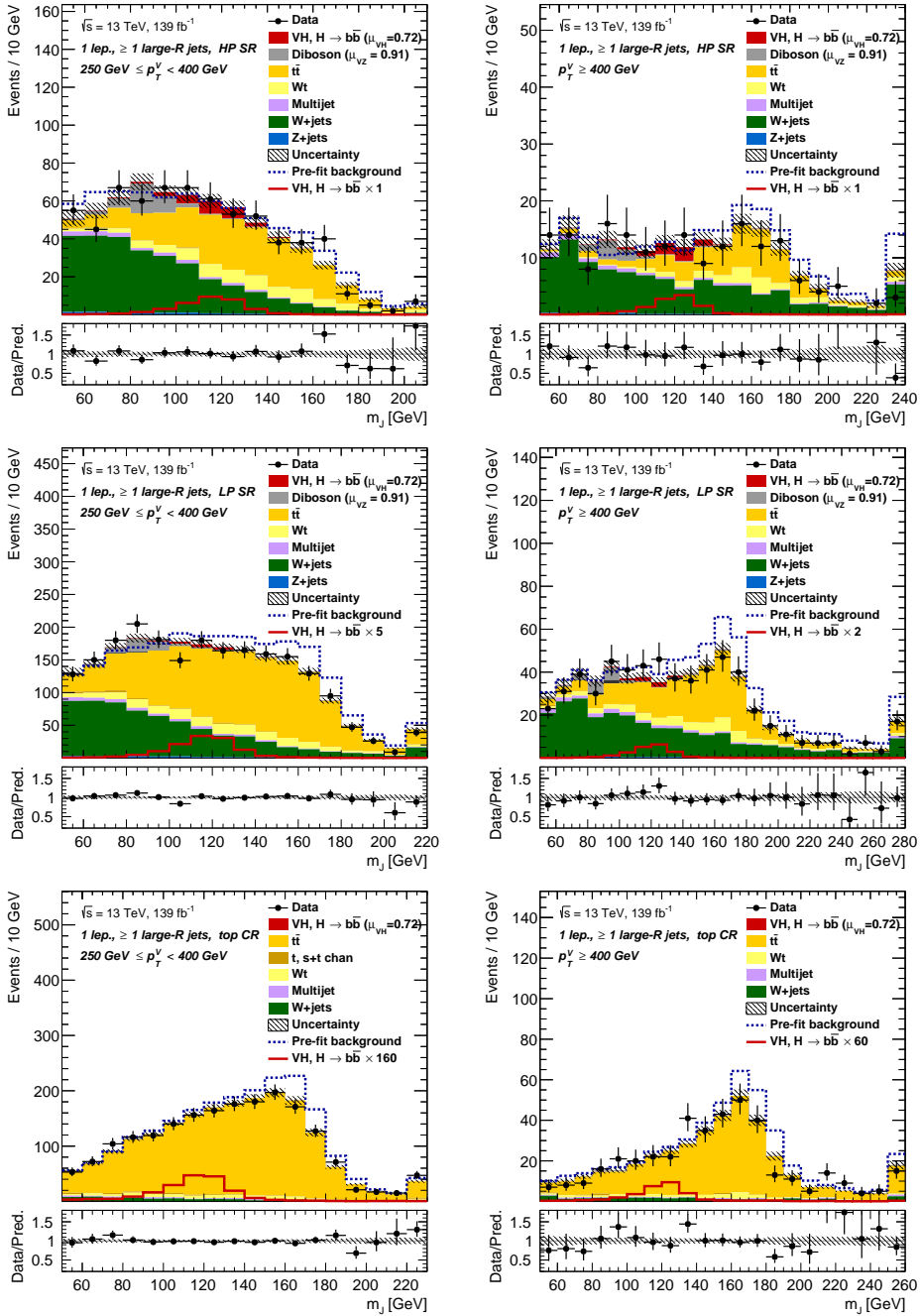


Figure 7.27: Post-fit distributions for the 1-lepton channel obtained from the unconditional fit to data. The overflow bin is added to the last bin of the shown plot range. Similar plots have been published in Ref. [5].

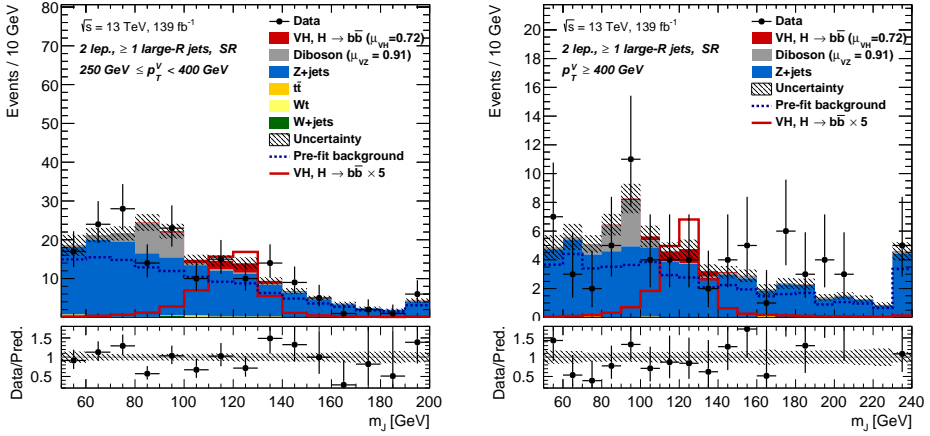


Figure 7.28: Post-fit distributions for the 2-lepton channel obtained from the unconditional fit to data. The overflow bin is added to the last bin of the shown plot range. Similar plots have been published in Ref. [5].

sensitive to a specific NP, its uncertainty is constrained and the post-fit uncertainty is smaller than the pre-fit uncertainty  $\sigma_{\alpha_0}$ . If not, the post-fit uncertainty remains the pre-fit uncertainty for that NP.

The floating normalisations of the  $W$ +hf,  $Z$ +hf and  $t\bar{t}$  backgrounds are not associated to any auxiliary constraint but purely determined from data. Two separate normalisation factors are used for the  $t\bar{t}$  background in the 0- and 1-lepton channel, as both channels have their own  $t\bar{t}$  CR. The measured values are  $0.88 \pm 0.10$  and  $0.83 \pm 0.09$  for the 0- and 1-lepton channel, respectively. The  $W$ +hf normalisation factor is fitted to  $1.12 \pm 0.14$  and the  $Z$ +hf normalisation factor is  $1.32 \pm 0.16$  post fit. For  $Z$ +hf, a common normalisation factor is used for both the 0- and 2-lepton channel. This notably increases the signal sensitivity of the 0-lepton regions, because the  $Z$ +jets background is additionally constrained from the 2-lepton channel.

### 7.8.1.3 Correlations

The correlation between pairs of NPs  $\alpha_i$  and  $\alpha_j$  is studied and the correlation matrix  $\rho_{ij}$  is obtained from the covariance matrix  $\text{cov}_{ij}$  as

$$\rho_{ij} = \frac{1}{\sigma_i \sigma_j} \text{cov}_{ij} \quad . \quad (7.21)$$

High correlations are found e.g. between the  $b$ -tagging uncertainties and the background normalisation factors, as expected because both SR and CR pose requirements on the number of  $b$ -tagged track-jets. These correlations are similar between the unconditional fit to data and the unconditional Asimov fit, which

provides an additional validation of the simulation approach.

#### 7.8.1.4 Nuisance parameter rankings

Out of the large set of NPs, it is important to determine which ones have the highest impact on the sensitivity to a certain PoI  $\mu$ . To quantify the impact of a NP  $\alpha$ , a likelihood scan is performed. First, the result of an unconditional fit is used to determine  $\hat{\alpha}$ . Starting from this best fit value,  $\alpha$  is varied away from the minimum in steps. For each step, the fit is redone, fixing  $\alpha$  at its scan point value. The change in  $-\ln(\mathcal{L})$  is monitored and the points where  $\Delta \ln(\mathcal{L}) = 1/2$  mark the  $\pm 1\sigma_\alpha$  positions. At these two points, the change in the fit value for the PoI  $\Delta\hat{\mu}$  is checked and used as a figure of merit to order the NPs.

The NP ranking, together with the corresponding NP pulls and constraints are shown for the  $VH$  signal strength in Figure 7.29(a). The uncertainty with the largest impact on the  $VH$  signal strength is the large- $R$  jet JMR for the signal process. It is neither significantly pulled, nor constrained by the fit. Because it is a signal uncertainty, it mainly affects the uncertainty of the measured signal strength, but has a lower impact on the statistical significance of the excess. Other highly ranked uncertainties are the  $Z$ +hf normalisation, which is constrained only by the physics measurement, the  $VZ$  PoI, the large- $R$  JMS/JES for the  $V$ +jets background and various other background modelling uncertainties. These NPs have the highest correlation to the  $VH$  PoI. Compared to the individual impacts of the NPs, the data statistical uncertainty (0.25) dominates. The ranking obtained from the unconditional fit to data and the fit to the Asimov set agree well, which provides additional validation of the fit model and the underlying simulation approach. The top peak in both the SRs and CRs of the 0- and 1-lepton channel helps to constrain the top quark background shape uncertainty on the  $m_J$  distribution for the  $t\bar{t}$  background. The uncertainties related to the large- $R$  jet calibration are sizeable and are constrained by the fit, which is explained by the fact that the input uncertainties have been derived only on a subset of the full Run 2 data set.

For the  $VZ$  signal strength, the NP ranking, together with the corresponding NP pulls and constraints are shown in Figure 7.30(a). The NPs with the highest impact on  $\mu_{VZ}$  are related to the  $VZ$  signal prediction, overall acceptance uncertainties and extrapolation uncertainties among channels and among additional jet multiplicities.

#### 7.8.1.5 Uncertainty breakdown

While the nuisance parameter ranking identifies single NPs that have a high impact on a PoI, an impact breakdown into larger, physics-inspired categories is studied, too. The NPs are grouped according to the origin of the corresponding systematic uncertainty. First, the nominal fit is run and the uncertainty on the PoI  $\sigma_{\hat{\mu}}$  is extracted via a likelihood scan. Then, for each group  $g$  an additional fit is run with all NPs from the group fixed to their central values. The uncertainty on the PoI from this fit,  $\sigma_{\hat{\mu}}^g$ , is then subtracted in quadrature from  $\sigma_{\hat{\mu}}$  to obtain

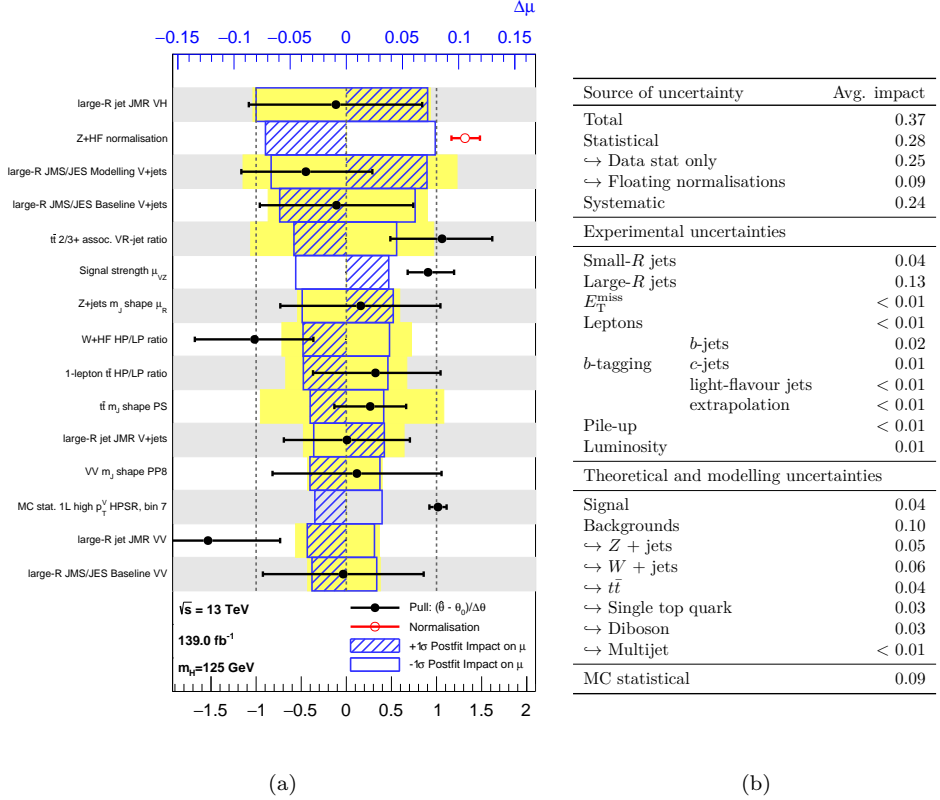


Figure 7.29: (a): The impact of individual NPs on the fitted  $VH$  signal strength parameter  $\hat{\mu}$ , sorted in decreasing order. The blue boxes show the post-fit impact on  $\hat{\mu}$  (top  $x$ -axis), obtained from fixing the NP to its  $\pm 1\sigma$  post-fit uncertainty and monitoring the change in  $\hat{\mu}$ . The pre-fit impact is overlaid as yellow boxes. The black points show the deviation of the NP's central value with respect to its pre-fit value (pull) in standard deviations (bottom  $x$ -axis). The error bars show the post-fit uncertainties of each NP with respect to its pre-fit value (constraints). The red points show the fitted values for normalisation parameters or PoIs. Their SM expectation is unity. (b): Breakdown of the contribution of groups of NPs to the uncertainty on the  $VH$  PoI. The sum in quadrature of the individual contributions differs from the total uncertainty due to correlations between the NPs. Both Figures are obtained from a (1+1)-PoI fit. Published in Ref. [5].

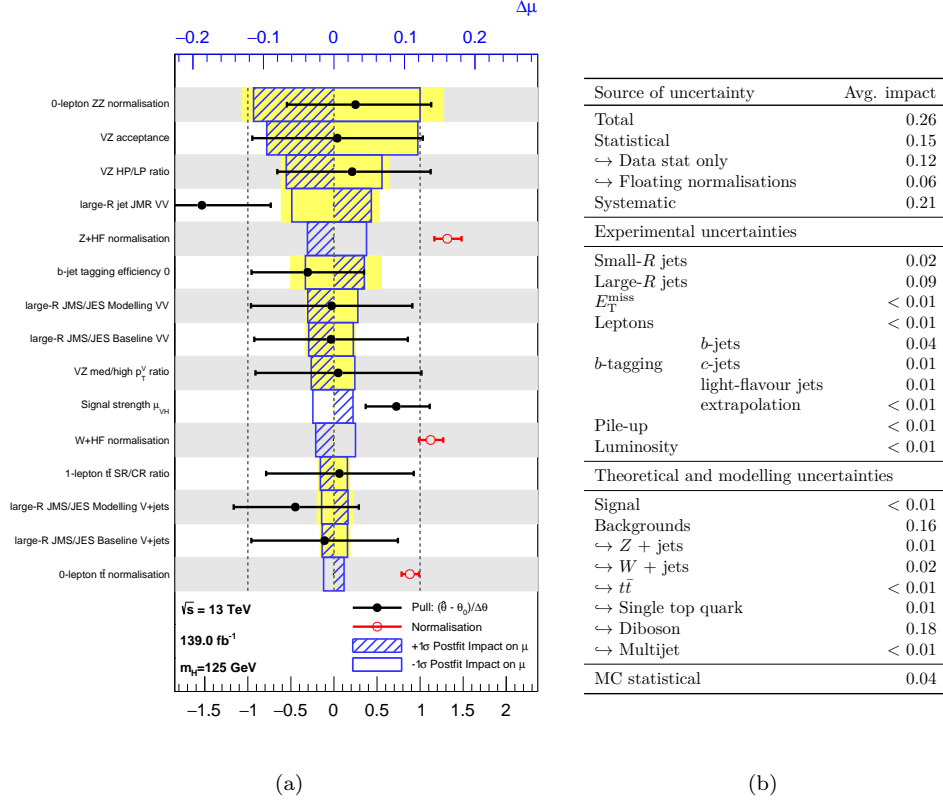


Figure 7.30: (a): The impact of individual NPs on the fitted  $VZ$  signal strength parameter  $\hat{\mu}$ , sorted in decreasing order. The blue boxes show the post-fit impact on  $\hat{\mu}$  (top  $x$ -axis), obtained from fixing the NP to its  $\pm 1\sigma$  post-fit uncertainty and monitoring the change in  $\hat{\mu}$ . The pre-fit impact is overlaid as yellow boxes. The black points show the deviation of the NP's central value with respect to its pre-fit value (pull) in standard deviations (bottom  $x$ -axis). The error bars show the post-fit uncertainties of each NP with respect to its pre-fit value (constraints). The red points show the fitted values for normalisation parameters or PoIs. Their SM expectation is unity. (b): Breakdown of the contribution of groups of NPs to the uncertainty on the  $VZ$  PoI. The sum in quadrature of the individual contributions differs from the total uncertainty due to correlations between the NPs. Both Figures are obtained from a (1+1)-PoI fit.



the impact,

$$\text{impact} = \sqrt{(\sigma_{\hat{\mu}})^2 - (\sigma_{\hat{\mu}}^g)^2} . \quad (7.22)$$

When testing the expected impact on one PoI, the other PoIs are freely adjusted in the fit. The total statistical impact is defined as the uncertainty of the fit with all NPs fixed to their nominal value except for the floating normalisations. The total systematic impact is calculated as the quadratic difference of the statistical impact to the nominal uncertainty. The “data stat only” contribution is defined as the uncertainty of the fit with all NPs fixed to their nominal expectation value. The “floating normalisations” contribution is the quadratic difference between the total error and the error from fit with only the normalisation factors fixed to best fit value.

The uncertainty breakdown for the  $VH$  signal strength is shown in Figure 7.29(b). Statistical and systematic sources have an equal impact on the uncertainty of the  $VH$  signal strength. The statistical component is dominated by the limited size of the data set (0.25), two times more than the impact of the floating normalisations of the backgrounds (0.09). The systematic uncertainties are further broken down into experimental and theoretical uncertainties. The uncertainties related to large- $R$  jets have the highest impact out of all groups of experimental uncertainties (0.13). The largest contribution from theoretical and modelling uncertainties is the limited size of the simulation samples (0.09), followed by the modelling uncertainties of the various backgrounds (0.03-0.06).

For the  $VZ$  signal strength, the breakdown is shown in Figure 7.30(b). As in the case for  $VH$  production, the statistical component of the uncertainty on  $\mu_{VZ}$  is dominated by the limited size of the data set (0.12). The impact of the floating normalisations of the backgrounds, which is also grouped to the statistical uncertainties, has a half as large impact (0.06). Out of all systematic uncertainties the ones related to the modelling of  $VZ$  (0.18) and the ones related to the large- $R$  jets (0.09) are the most important ones.

#### 7.8.1.6 Compatibility of fit results

It is important to ensure the measurement results are compatible between the various regions and that the combined result is e.g. not driven by a single potentially biased region. To study the compatibility of the fit result between different analysis regions  $i$ , the PoI  $\mu$  can be decorrelated between them, i.e.  $\mu \rightarrow \{\mu_i\}$ . The difference in  $-\ln(\mathcal{L})$  at the two minima is expected to be  $\chi^2$  distributed with  $N - 1$  degrees of freedom, where  $N$  is the number of analysis regions. This allows to calculate a  $p$ -value to quantify the compatibility of the PoIs between the various regions. Additionally, the PoI decorrelation allows to obtain separate significances and is used to investigate how much each analysis channel contributes to the total result.

A comparison between the expected and observed  $VH$  significances between the

Fit	Expected sig. (Post-fit)	Observed sig.
Combined	2.7	2.1
0-lepton	1.9	1.4
1-lepton	2.0	2.0
2-lepton	1.2	-0.1

Table 7.10: Expected and observed  $VH$  significances for the combined (1+1)-PoI fit and a combined fit where each channel has an independent signal strength, i.e. a (3+1)-PoI fit. The  $VZ$  PoI is not fixed when calculating the significances.

Fit	Expected sig. (Post-fit)	Observed sig.
Combined	5.7	5.4
0-lepton	4.8	4.7
1-lepton	2.7	2.8
2-lepton	2.3	1.2

Table 7.11: Expected and observed  $VZ$  significances for the combined (1+1)-PoI fit and a combined fit where each channel has an independent signal strength, i.e. a (3+1)-PoI fit. The  $VH$  PoI is not fixed when calculating the significances.

three lepton sub-channels of the analysis is listed in Table 7.10. The expected  $VH$  significances for the 0- and 1-lepton channel are larger than for the 2-lepton channel, given the higher expected event yields and relatively equal with respect to each other. The observed  $VH$  significances in the 0- and 2-lepton channel are lower than expected. Figure 7.31 shows the  $VH$  signal strength  $\mu_{VH}^{bb}$ , decorrelated into the  $WH$  and  $ZH$  contributions, as well as decorrelated into various analysis regions. Overall, good compatibility between the various decorrelation scenarios is observed. A compatibility test between the default (1+1)-PoI fit and the (2+1)-PoI fit with separate  $WH$  and  $ZH$  PoI yields a  $p$ -value of 37%. Similarly, a fit with separate PoIs per lepton channel yields good compatibility with the combined fit, quantified by a  $p$ -value of 49%. Decorrelating between the different  $p_T^V$  regions and comparing to the combined fit results in a  $p$ -value of 47% and similarly a full decorrelation into a (6+1)-PoI fit is compatible with the (1+1)-PoI fit, having a  $p$ -value of 81%.

A comparison between the expected and observed  $VZ$  significances between the three lepton sub-channels of the analysis is listed in Table 7.11. Figure 7.32 shows the  $VZ$  signal strength  $\mu_{VZ}^{bb}$  decorrelated into the  $WZ$  and  $ZZ$  contributions, as well as decorrelated into various analysis regions. Good compatibility between the various decorrelation scenarios is observed. This has been verified by performing  $\chi^2$  compatibility tests between the various PoI setups.

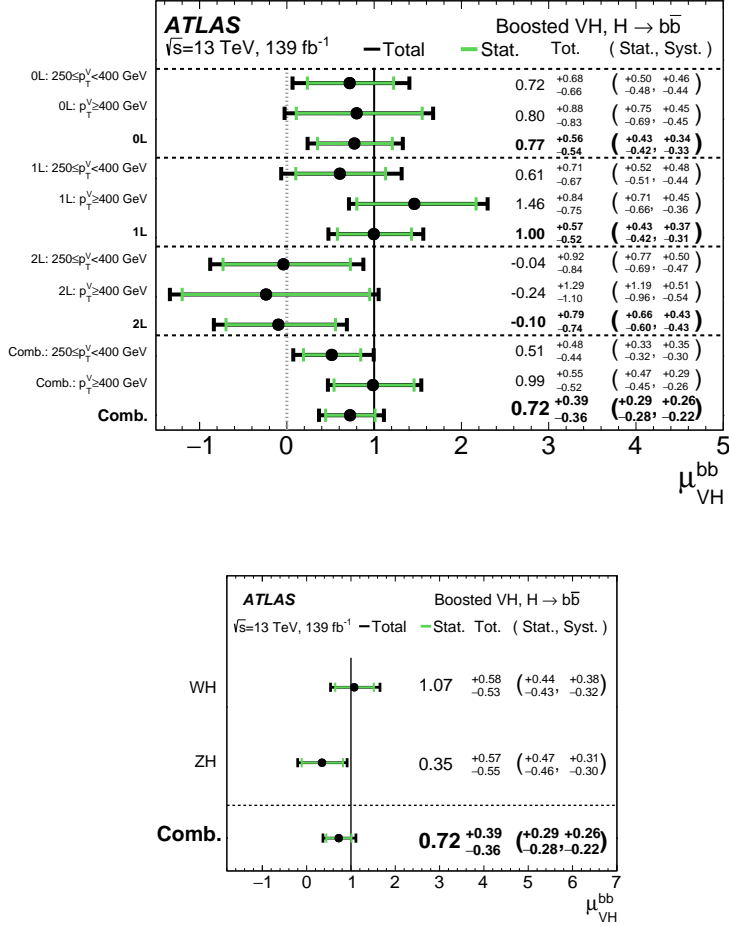


Figure 7.31: Left: Fitted values of the  $VH$  signal strength parameter  $\mu_{VH}^{bb}$  for the 0-, 1- and 2-lepton channel, the medium and high  $p_T^V$  region as well as combinations. The combined value is obtained from a (1+1)-PoI fit. The  $p_T^V$  split combined results are obtained from a (2+1)-PoI fit. The results split in lepton channel are obtained from a (3+1)-PoI fit and a (6+1)-PoI in the case of the additional  $p_T^V$  split, respectively. Right: Fitted signal strength parameters for  $WH$  and  $ZH$  production, obtained from a (2+1)-PoI fit. Published in Ref. [5].

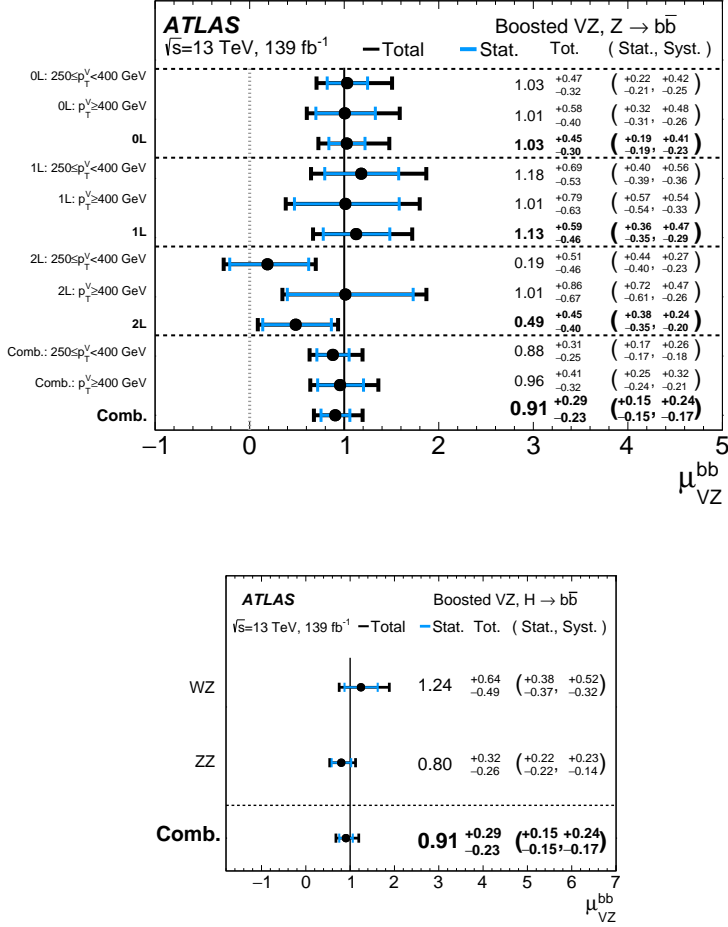


Figure 7.32: Left: Fitted values of the  $VZ$  signal strength parameter  $\mu_{VZ}^{bb}$  for the 0-, 1- and 2-lepton channel, the medium and high  $p_T^V$  region as well as combinations. The combined value is obtained from a (1+1)-PoI fit. The  $p_T^V$  split combined results are obtained from a (1+2)-PoI fit. The results split in lepton channel are obtained from a (1+3)-PoI fit and a (1+6)-PoI in the case of the additional  $p_T^V$  split, respectively. Right: Fitted signal strength parameters for  $WZ$  and  $ZZ$  production, obtained from a (1+2)-PoI fit. Published in Ref. [5].

## 7.9 Simplified Template Cross-Section measurement

To fully exploit the potential of the high  $p_T^V$  analysis, the  $VH$  measurement is modified to yield additional differential information, in this case fiducial cross-sections within the STXS framework. To avoid confusion, throughout this section, generator-level quantities are labelled with a superscript  $t$ , whereas reconstructed quantities have a superscript  $r$ . Basis for the definition of the fiducial regions is the reduced stage-1.2 STXS splitting used e.g. in Ref.s [6, 242] and defined in Chapter 3.3. In light of the increased acceptance at high  $p_T^V$ , the 'reduced splitting' is extended in this analysis by introducing an additional generator-level split at  $p_T^{V,t} = 400$  GeV. Motivated by the analysis regions, only cross-section bins with a generator level  $p_T^{V,t} > 250$  GeV are considered, which results in the following 4 bins:

$$p_T^{W,t} \in [250, 400) \text{ GeV}, \quad p_T^{W,t} \geq 400 \text{ GeV}, \quad (7.23)$$

$$p_T^{Z,t} \in [250, 400) \text{ GeV}, \text{ and } p_T^{Z,t} \geq 400 \text{ GeV} \quad (7.24)$$

The  $p_T^{V,r}$  categorisation of the analysis is designed to match this splitting. In contrast to the analysis region splitting in the 0- and 1-lepton channel, no fiducial splitting according to the jet multiplicity of the final state is used, given the limited experimental sensitivity.

The signal simulation is split according to  $p_T^{V,t}$  into the four templates that match the STXS measurement bins. An additional generator-level category from  $p_T^{V,t} \in [150, 250)$  GeV is introduced because a small fraction of signal events from this region will end up in the analysis due to a mismeasurement of  $p_T^{V,r}$ . Figure 7.33 shows how much signal of each  $p_T^{V,t}$  category falls into which analysis region. Three figure of merits are shown: the actual event yield, the fraction of events normalised per analysis category and the acceptance times efficiency normalised to the total signal yield of each  $p_T^{V,t}$  category. Due to the good resolution of the vector boson reconstruction, these migration matrices have a majority of diagonal contributions, where the  $p_T^{V,t}$  and  $p_T^{V,r}$  categories match. This is especially visible in the signal fraction plot. As expected, the diagonality is best for the 2-lepton channel, where two charged leptons are reconstructed. Over 95% of events end up in an analysis region that matches the STXS range. In the one lepton channel, this number drops to 80%-90%, because the neutrino is only indirectly reconstructed via  $E_T^{\text{miss}}$ , which is subject especially to the resolution of all the jets in the event. The analysis regions of the 0-lepton channel, which are designed for the  $Z \rightarrow \nu\nu$  decay, have about 20% contamination from the  $WH$  signal. In these cases, the  $W$  boson decays in to a  $\tau$ -lepton and a neutrino, and the  $\tau$ -lepton subsequently decays into one of the hadronic final states. The acceptance times efficiency for the diagonal entries rises from 2%-4% for  $p_T^{V,t} \in [250, 400)$  GeV to 5%-6% for  $p_T^{V,t} \geq 400$  GeV in the 0- and 1-lepton channel. For the 2-lepton channel they are slightly smaller rising from 2% to 4%. These observations match the behaviour shown in Figure 7.20. The contribution from the region  $p_T^{V,t} \in [150, 250)$  GeV is small in the considered analysis regions. Due to the lack of experimental sensitivity to this signal with

$p_T^{V,t} \in [150, 250)$  GeV, its contribution in the fit is fixed to the SM prediction.

The fit setup for the STXS measurement is similar to the one used to measure the inclusive signal strengths. The signal uncertainty scheme for the latter already takes into account the stage-1.2 STXS bins in the maximal split scenario and therefore does not need to be adjusted. For each STXS bin, a dedicated PoI is introduced. The separate  $VZ$  PoI is kept and fitted simultaneously, resulting in (4+1)-PoIs. Given that the STXS PoIs measure cross-sections and not signal strengths, the theory uncertainty on the cross-section prediction of each measurement bin  $g$  is removed from the total set of uncertainties. The theory uncertainty on the measurement bin  $g$  is calculated from the individual uncertainties of the underlying STXS bins  $\delta_i$  and their fiducial cross-sections  $\sigma_i$  as

$$\delta_g = \frac{\sum_{i \in g} \delta_i \sigma_i}{\sum_{i \in g} \sigma_i} . \quad (7.25)$$

The residual uncertainty on the individual STXS bins  $i$  inside of the measurement bin  $g$  is then calculated as  $\delta_{i,\text{res}} = \delta_i - \delta_g$ . This subtraction, that is illustrated for a simple example in Figure 7.34, is performed for each of the QCD scales and PDF+ $\alpha_S$  uncertainties separately.

The measured  $VH$  STXS cross-sections, multiplied by the  $V \rightarrow \text{leptons}$  and  $H \rightarrow b\bar{b}$  BRs, are summarised in Table 7.12 and plotted in Figure 7.35, together with their SM expectations. The measured  $\sigma \times \text{BR}$  for each bin with respect to the SM expectation is shown in Figure 7.36, as well as the correlation between the  $VH$  STXS PoIs. Compared to the inclusive signal strength, the relative contribution of the statistical uncertainty becomes larger, as expected from a measurement with a finer binning. The highest correlation between STXS PoIs is observed between the PoIs for  $p_T^{W,t} \geq 400$  GeV and  $p_T^{Z,t} \geq 400$  GeV, with a correlation coefficient of -14%. This correlation originates from the already mentioned  $WH$  contribution to the SRs of the 0-lepton channel. Given that the 4 PoIs have relatively similar relative uncertainty, based on the event yield migrations shown in Figure 7.33, higher anticorrelations are expected, namely of  $\sim 2\epsilon$  for a relative yield migration of  $\epsilon$  between two bins. These anticorrelations are absorbed, however, by other nuisance parameters in the fit, such as the floating normalisations. A full breakdown of systematic uncertainties for each of the four STXS measurement bins is shown in Figure 7.13. A NP ranking is listed in Figures 7.37 and 7.38, and is qualitatively similar to the one from the inclusive signal strength fit.

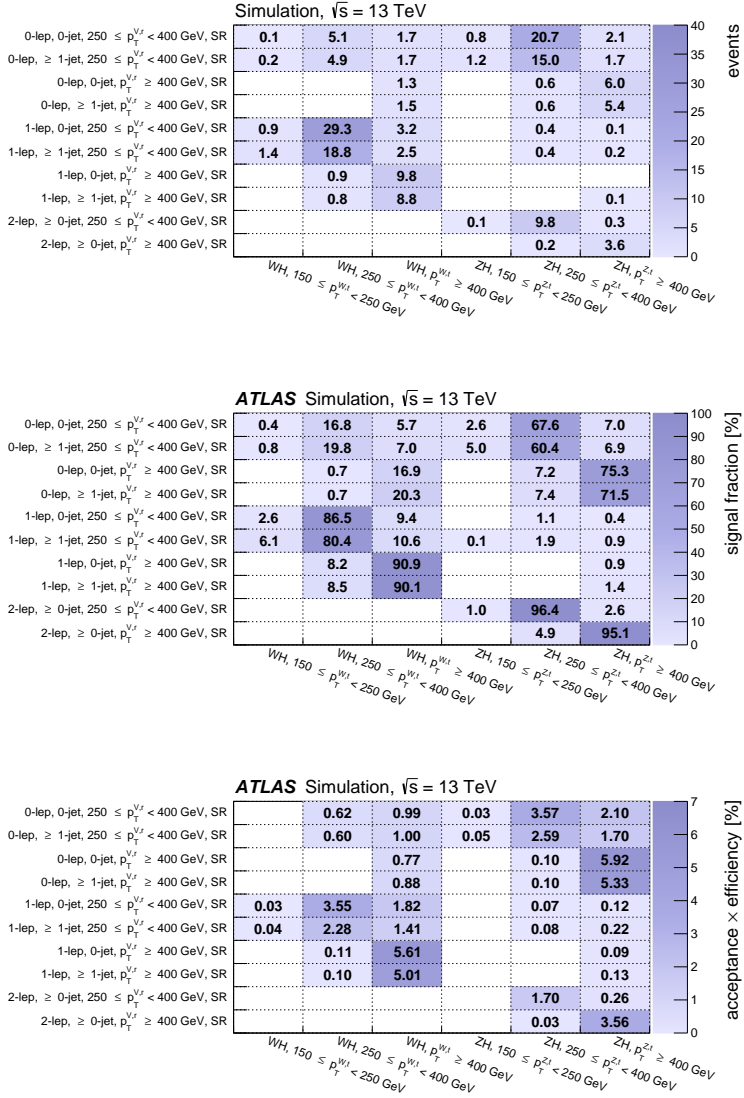


Figure 7.33: Matching between fiducial STXS measurement regions ( $x$ -axis) and analysis categories ( $y$ -axis) for the signal yields (top), the signal fraction in % (middle) and the signal acceptance times efficiency in % (bottom). The signal acceptance times efficiency is to be understood as the number of signal events from a certain STXS region falling into an analysis region normalised to the total number of events in that STXS region. Entries with signal yields  $< 0.1$ , fractions  $< 0.1\%$  and acceptance times efficiency values below  $0.01\%$  are not shown. Middle and bottom plots published in Ref. [5].

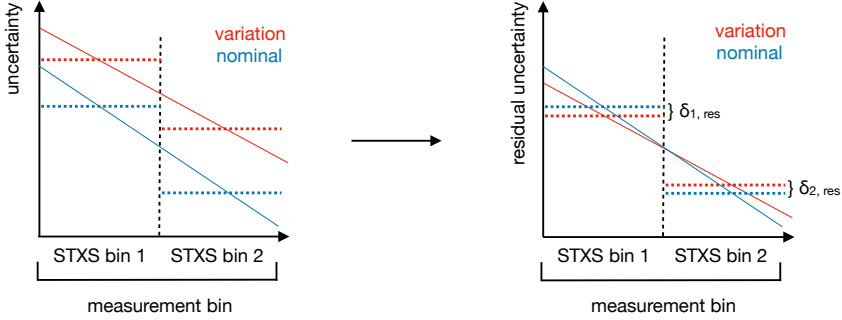


Figure 7.34: Calculation of the residual theory uncertainties  $\delta_{i,\text{res}}$  for a hypothetical measurement bin that consists of two finer STXS bins.

STXS region ( $ y_H  < 2.5, H \rightarrow b\bar{b}$ )	SM prediction [fb]	Result	(Tot.)	(Stat.)	(Syst.) [fb]
$W \rightarrow \ell\nu; p_T^{W,t} \in [250, 400) \text{ GeV}$	$5.83 \pm 0.26$	3.3	+4.8 -4.6	+3.6 -3.4	+3.2 -3.0
$W \rightarrow \ell\nu; p_T^{W,t} \in [400, \infty) \text{ GeV}$	$1.25 \pm 0.06$	2.1	+1.2 -1.1	+1.0 -0.9	+0.6 -0.5
$Z \rightarrow \ell\ell, \nu\nu; p_T^{Z,t} \in [250, 400) \text{ GeV}$	$4.12 \pm 0.45$	1.4	+3.1 -2.9	+2.4 -2.3	+1.9 -1.7
$Z \rightarrow \ell\ell, \nu\nu; p_T^{Z,t} \in [400, \infty) \text{ GeV}$	$0.72 \pm 0.05$	0.2	+0.7 -0.6	+0.6 -0.5	+0.3 -0.3

Table 7.12: Measured  $VH, V \rightarrow \text{leptons}$  reduced stage-1.2 simplified template cross sections times the  $H \rightarrow b\bar{b}$  and  $V \rightarrow \text{leptons}$  branching fractions and comparison with their SM predictions. Published in Ref. [5].



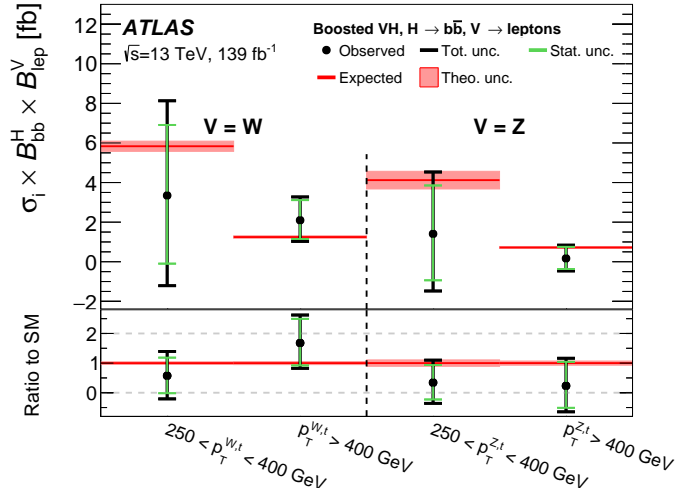


Figure 7.35: Measured  $VH$  reduced stage-1.2 simplified template cross-sections times the  $H \rightarrow b\bar{b}$  and  $V \rightarrow \text{leptons}$  branching fractions and comparison with their SM predictions. Published in Ref. [5].

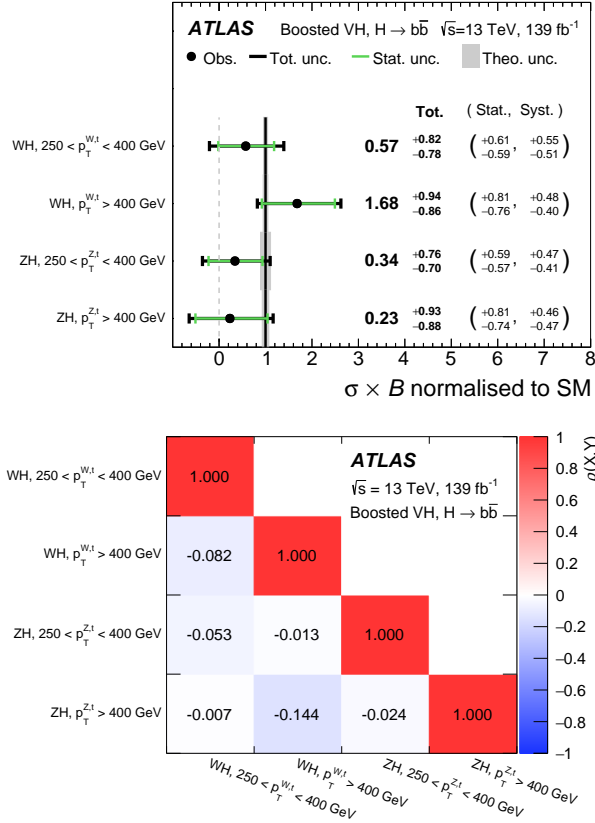


Figure 7.36: Top: Measured values of the reduced stage-1.2 simplified template  $VH, H \rightarrow b\bar{b}$  cross-sections, normalised to the Standard Model predictions. The grey error bands correspond to the theoretical uncertainty on the normalised  $\sigma \times \text{BR}$ . Bottom: Observed correlations between the measured cross-sections. Published in Ref. [5].

Source of uncertainty	$ZH, p_T^{Z,t} \in [250, 400] \text{ GeV}$	Avg. impact on normalized STXS $\sigma \times \text{BR}$ $ZH, p_T^{Z,t} \in [400, \infty) \text{ GeV}$ $WH, p_T^{W,t} \in [250, 400] \text{ GeV}$		$WH, p_T^{W,t} \in [400, \infty) \text{ GeV}$
Total	0.73	0.90	0.80	0.90
Statistical	0.58	0.78	0.60	0.79
$\hookrightarrow$ Data stat only	0.50	0.72	0.54	0.73
$\hookrightarrow$ Floating normalisations	0.26	0.22	0.11	0.18
Systematic	0.44	0.46	0.53	0.44
Experimental uncertainties				
Small-R jets	0.10	0.09	0.12	0.10
Large-R jets	0.27	0.27	0.22	0.14
$E_T^{\text{miss}}$	0.03	0.05	0.02	$\leq 0.01$
Leptons	0.02	0.02	$\leq 0.01$	0.05
$b$ -tagging ( $b$ -jets)	0.02	0.04	0.03	0.09
$b$ -tagging ( $c$ -jets)	$\leq 0.01$	0.02	$\leq 0.01$	0.03
$b$ -tagging (light-flavour jets)	0.02	$\leq 0.01$	0.02	0.02
$b$ -tagging (extrapolation)	$\leq 0.01$	$\leq 0.01$	0.02	0.03
Pile-up	$\leq 0.01$	$\leq 0.01$	$\leq 0.01$	0.02
Luminosity	$\leq 0.01$	0.02	$\leq 0.01$	0.03
Theoretical and modelling uncertainties				
Signal modelling	0.06	0.07	0.04	0.14
Background modelling	0.22	0.26	0.19	0.22
$\hookrightarrow Z$ +jets	0.18	0.21	0.04	0.04
$\hookrightarrow W$ +jets	0.08	0.08	0.11	0.15
$\hookrightarrow t\bar{t}$	$\leq 0.01$	$\leq 0.01$	0.09	0.04
$\hookrightarrow$ Single top	$\leq 0.01$	0.03	0.07	0.10
$\hookrightarrow$ Diboson	0.05	0.04	0.03	0.03
$\hookrightarrow$ Multijet	$\leq 0.01$	0.02	0.06	0.07
MC statistical	0.18	0.23	0.20	0.22

Table 7.13: Breakdown of the contribution to the uncertainty on the STXS POIs obtained from an unconditional (4+1)-POI STXS fit ( $\mu_{VH}, \mu_{VZ}$ ) to data. The sum in quadrature of the individual contributions differs from the total uncertainty due to correlations between the nuisance parameters.

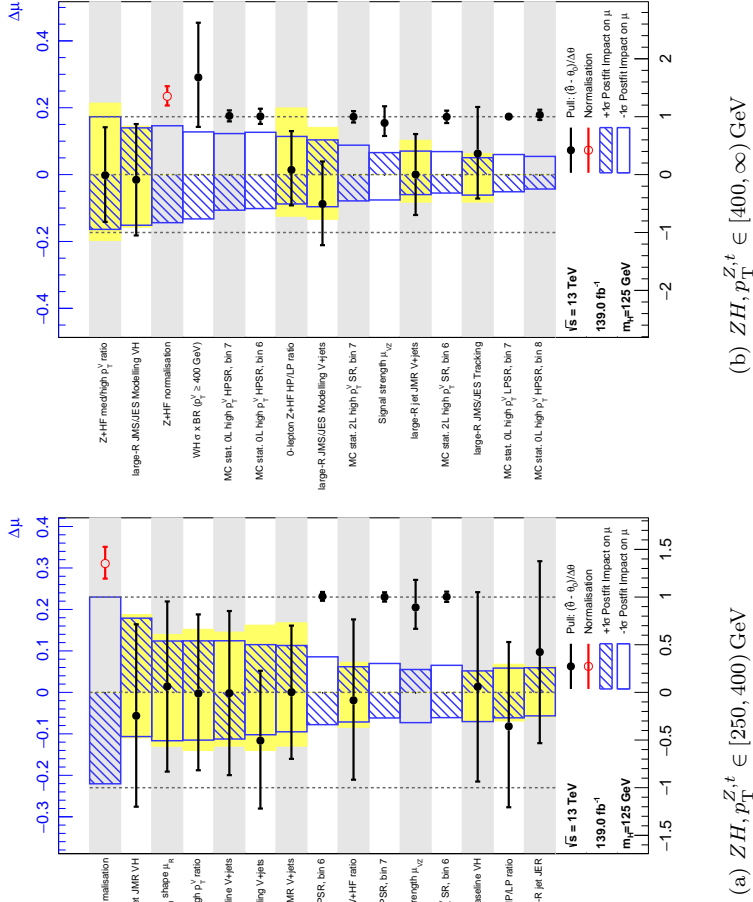


Figure 7.37: The impact of individual NPs to on the fitted STXS PoIs for  $ZH$  production, sorted in decreasing order. The blue boxes show the post-fit impact on the PoI (top  $x$ -axis), obtained from fixing the NP to its  $\pm 1\sigma$  post-fit uncertainty and monitoring the change in PoI. The pre-fit impact is overlaid as yellow boxes. The black points show the deviation of the NP's central value with respect to its pre-fit value (pull) in standard deviations (bottom  $x$ -axis). The error bars show the post-fit uncertainties of each NP with respect to its pre-fit value (constraints). The red points show the fitted values for normalisation parameters or PoIs. Their SM expectation is unity. Published in Ref. [5].

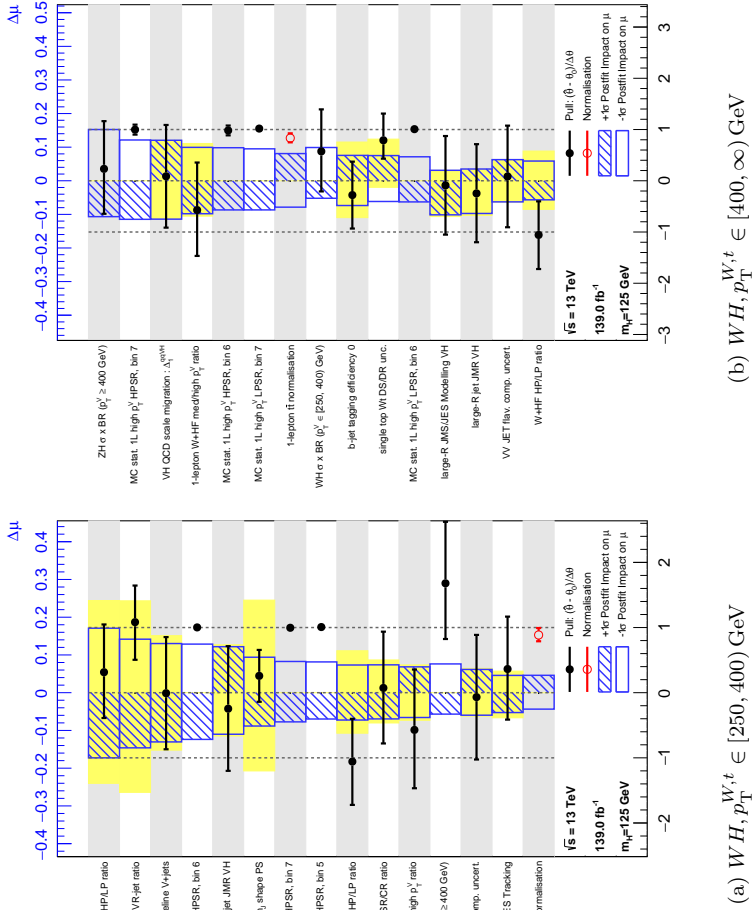


Figure 7.38: The impact of individual NPs to on the fitted STXS PoLs for  $WH$  production, sorted in decreasing order. The blue boxes show the post-fit impact on the PoL (top  $x$ -axis), obtained from fixing the NP to its  $\pm 1\sigma$  post-fit uncertainty and monitoring the change in PoL. The pre-fit impact is overlaid as yellow boxes. The black points show the deviation of the NP's central value with respect to its pre-fit value (pull) in standard deviations (bottom  $x$ -axis). The error bars show the post-fit uncertainties of each NP with respect to its pre-fit value (constraints). The red points show the fitted values for normalisation parameters or PoLs. Their SM expectation is unity. Published in Ref. [5].



## 8 (SM) EFT interpretation

This chapter presents an interpretation of the high  $p_T$   $VH, H \rightarrow b\bar{b}$  differential STXS measurement within the framework of a Standard Model Effective Field Theory (SMEFT). Since the measurement results are in agreement with the prediction of the SM, the differential information is used to constrain the free parameters of the SMEFT, the Wilson coefficients.

Ultimately, SMEFT is a global scheme. Its true power lies in being able to connect possible effects of new physics across measurements. Before combining measurements globally, however, it is important to understand the local sensitivity of each measurement to the set of effective operators and associated Wilson coefficients. The high  $p_T$   $VH, H \rightarrow b\bar{b}$  analysis provides for the first time exclusive STXS measurements for the region with  $p_T^{V,t} \geq 400$  GeV, where the sensitivity to short-distance physics is enhanced. This chapter quantifies the sensitivity to potential modifications of the SM in terms of limits on the respective Wilson coefficients.

### 8.1 Simulation of the SMEFT impact

Only the leading terms relevant for LHC Higgs physics, i.e. the ones with mass dimension 6, are considered in the EFT expansion of the SM Lagrangian, which takes the form

$$\mathcal{L}_{\text{SMEFT}} = \mathcal{L}_{\text{SM}} + \sum_i \frac{1}{\Lambda^2} c_i^{(6)} \mathcal{Q}_i^{(6)} \quad . \quad (8.1)$$

The energy scale  $\Lambda$  suppresses the effect of the dimension-6 operator  $\mathcal{Q}_i$  that is scaled by its respective coupling constant  $c_i$ , the Wilson coefficient. If  $\Lambda$  is much greater than the vacuum expectation value, then this expansion captures the generalised IR limit of  $\Lambda$ -scale BSM physics at low energies (i.e.  $E \ll \Lambda$ ). The ratio  $c_i/\Lambda^2$  is a priori undetermined and can only be constrained from experimental data. In the SM,  $c_i = 0$  and therefore the expectation for this ratio is zero, too. In principle, each Wilson coefficient can have its own suppression scale  $\Lambda$ , because not all BSM physics necessarily needs to have the same energy scale. Conventionally and hereinafter, a global suppression scale  $\Lambda$  is chosen and set to 1 TeV, motivated by theoretical arguments such as the hierarchy problem. The experimental constraints are consequently presented as limits on the Wilson coefficients  $c_i$  at  $\Lambda = 1$  TeV, but a re-scaling to different values of  $\Lambda$  is straightforward. Ultimately, the ratio of  $c_i$  and  $\Lambda$  needs to be matched to the coupling strength and the energy scale of the

UV-complete theory under consideration.

### 8.1.1 Parameterising the STXS cross-sections

SMEFT operators with non-zero coefficients will modify the predicted cross-section for the signal in each STXS bin  $k$ , which becomes a function of the Wilson coefficients  $c_i$ . To interpret the observed data in terms of Wilson coefficients, the likelihood, expressed so far in parameters  $(\sigma \times \text{BR})_k$  must be re-expressed in terms of the Wilson coefficients  $c_i$ , substituting each measured  $(\sigma \times \text{BR})$  with its corresponding SMEFT prediction. Assuming that the Higgs boson width is narrow also in the SMEFT, the cross-section for  $pp \rightarrow V(\rightarrow \text{leptons}) H(\rightarrow b\bar{b})$  factorises into a production cross-section and a decay branching ratio as

$$\sigma[pp \rightarrow V(\rightarrow \text{leptons}) H(\rightarrow b\bar{b})] = \sigma[pp \rightarrow V(\rightarrow \text{leptons}) H] \times \text{BR}[H \rightarrow b\bar{b}] \quad , \quad (8.2)$$

which greatly simplifies the process of expressing cross-sections in terms of Wilson coefficients.

#### 8.1.1.1 Production cross-section

The dimension-6 operators in the SMEFT Lagrangian lead to modifications of scatter amplitudes  $\mathcal{M}$ , e.g. via insertion of effective vertices that either already exist in the SM or are novel contact interactions. Additionally, they can also lead to re-definitions of SM fields or a change in the value of experimental input parameters. Every vertex insertion into a Feynman diagram comes with a suppression factor of  $\Lambda^{-2}$ . Restricting to Feynman diagrams with only one SMEFT insertion each, the production cross-section is written as

$$\sigma \propto |\mathcal{M}|^2 = \left| \mathcal{M}_{\text{SM}} + \sum_i M_i^{(6)} \right|^2 \quad , \quad (8.3)$$

where  $M_i^{(6)}$  are the scatter amplitudes proportional to  $c_i/\Lambda^2$ . After expanding this term, the cross-section separates into

$$\sigma = \sigma_{\text{SM}} + \sigma_{\text{int}} + \sigma_{\text{BSM}} \quad , \quad (8.4)$$

where  $\sigma_{\text{SM}}$  is the SM cross-section,  $\sigma_{\text{int}}$  an interference term between SM amplitudes and SMEFT amplitudes, and  $\sigma_{\text{BSM}}$  is a term involving only SMEFT amplitudes. Consequently,  $\sigma_{\text{SM}}$  is suppressed by  $\Lambda^0$ ,  $\sigma_{\text{int}}$  by  $\Lambda^{-2}$  and  $\sigma_{\text{BSM}}$  by  $\Lambda^{-4}$ .

Of the two additional terms that are added to the SM cross-section,  $\sigma_{\text{int}}$  is generically expected to be dominant, because the  $\sigma_{\text{BSM}}$  terms are suppressed by two additional powers of  $\Lambda$  with respect to  $\sigma_{\text{int}}$ . This generic statement is not true for regions of phase space where the energy scale  $E$  is very large. For this reason, interpretations



are provided both without and with  $\sigma_{\text{BSM}}$  terms, to provide a measure of the impact of  $\Lambda^{-4}$  terms.

In contrast to the  $\sigma_{\text{int}}$  contribution, which forms a complete set of all possible terms that are suppressed by  $\Lambda^{-2}$ ,  $\sigma_{\text{BSM}}$  is not the only contribution that is suppressed by  $\Lambda^{-4}$ . Interference terms of SM amplitudes and (dimension-6) SMEFT amplitudes with two inserted vertices, and interference terms of SM amplitudes with SMEFT amplitudes of dimension-8 operators, both of which are suppressed at  $\Lambda^{-4}$ , are only starting to become understood [258] and are therefore not considered in this interpretation.

The SMEFT contributions are usually known at lower order in perturbation theory than the SM ones. To reduce the impact of this difference, the parameterisation of the cross-section is computed as a relative correction to the SM prediction at the highest available perturbative order as

$$\sigma_{\text{SMEFT}} = \sigma_{\text{STXS}}^{(\text{N})\text{NLO}} \times \left( 1 + \frac{\sigma_{\text{int}}^{\text{LO}}}{\sigma_{\text{SM}}^{\text{LO}}} + \frac{\sigma_{\text{BSM}}^{\text{LO}}}{\sigma_{\text{SM}}^{\text{LO}}} \right) . \quad (8.5)$$

This strategy relies on the assumption that the relative SMEFT effects with respect to the SM prediction are similar at higher perturbative orders. For the  $VH$  process, this is studied for NLO/LO QCD and holds within  $O(10\%)$  [259], which is significantly smaller than the measurement uncertainty. Therefore, this approximation is justified.

The ratios in equation 8.5 can be expressed as a function of the Wilson coefficients  $c_i$ :

$$\frac{\sigma_{\text{int}}}{\sigma_{\text{SM}}} \sim \sum_i \frac{2\text{Re} \left( \mathcal{M}_{\text{SM}}^* \mathcal{M}_i^{(6)} \right)}{|\mathcal{M}_{\text{SM}}|^2} = \sum_i \alpha_i c_i \quad \text{and} \quad (8.6)$$

$$\frac{\sigma_{\text{BSM}}}{\sigma_{\text{SM}}} \sim \sum_{i,j} \frac{\left( \mathcal{M}_i^{(6)} \right)^* \mathcal{M}_j^{(6)}}{|\mathcal{M}_{\text{SM}}|^2} = \sum_{i,j} \beta_{ij} c_i c_j . \quad (8.7)$$

The constants  $\alpha_i$  and  $\beta_{ij}$  are estimated for each STXS bin using MC simulations. These constants express the sensitivity of each STXS bin to cross-section deviations introduced by SMEFT operators, therefore the values of  $\alpha_i$  include the  $\Lambda^{-2}$  suppression and the values of  $\beta_{ij}$  include the  $\Lambda^{-4}$  suppression. Conventionally, the terms proportional to  $\alpha_i$  are referred to as linear (in the Wilson coefficients) whereas the terms proportional to  $\beta_{ij}$  are referred to as quadratic, although they also include cross-terms between two different Wilson coefficients  $c_i$  and  $c_j$ .

### 8.1.1.2 Decay branching ratio

Similar parameterisations are found for the decay BR, because

$$\text{BR}(H \rightarrow b\bar{b}) = \frac{\Gamma_H^{b\bar{b}}}{\Gamma_H^{\text{tot.}}} \quad \text{with } \Gamma \propto |\mathcal{M}|^2 \quad . \quad (8.8)$$

The partial Higgs boson decay width  $\Gamma_H^{b\bar{b}}$  and the total Higgs boson decay width  $\Gamma_H^{\text{tot.}}$  are parameterised linearly with coefficients  $A_i^{(\text{tot.}/b\bar{b})}$  and quadratically with coefficients  $B_{ij}^{(\text{tot.}/b\bar{b})}$ , analogously to the coefficients  $\alpha_i$  and  $\beta_{ij}$  for the cross-section.

A multitude of operators that only affect the total width  $\Gamma_H^{\text{tot.}}$  leads to a degeneracy that can not be resolved with this measurement alone. Therefore, in an additional alternative approach, the BR is factored out as one single ad-hoc parameter which is linearised and added to yield

$$\sigma \times \text{BR} = [\sigma \times \text{BR}]_{\text{SM}} \times \left( 1 + \sum_i \alpha_i c_i + \mathcal{I}_{\text{BR}} \right) \quad . \quad (8.9)$$

The parameter  $\mathcal{I}_{\text{BR}}$  quantifies the relative deviation of the  $H \rightarrow b\bar{b}$  BR from its SM expectation.

In later SMEFT interpretations [260], the total expression for  $\sigma \times \text{BR}$  is expanded in orders of  $\Lambda^{-2}$ , which improves upon this ad-hoc solution. The SMEFT limits reported in this interpretation, however, are generally found to not depend significantly on the addition of the BR terms.

## 8.1.2 Selection of effective operators

The Warsaw basis of dimension-6 operators [54] is used, and the considered set of operators is reduced as motivated in Chapter 2 by taking into account only the baryon- and lepton-number conserving operators and imposing a  $U(3)^5$  flavour symmetry. Furthermore, only CP-even operators are considered because  $VH$  STXS cross-section measurements are analysed, which only measure a CP-even observable: the  $p_T^V$  distribution. From the resulting 59 operators, 13 are found to affect the  $pp \rightarrow V(\rightarrow \text{leptons})H$  rate more than 1‰ at  $c = 1$ . From the multitude of operators that affect the  $H \rightarrow b\bar{b}$  decay, one operator,  $\mathcal{Q}_{dH}$ , modifies the Yukawa coupling  $y_b$ . Because the analysis specifically targets the  $H \rightarrow b\bar{b}$  decay, the real value of the associated coefficient  $c_{dH}$  is considered in addition.

The definition of the 13 + 1 operators, the names of their corresponding Wilson coefficient and example vertices that are modified by them are shown in Figure 8.1. Operators generally have different effects on the resulting signal cross-section predictions in each of the STXS bins:

- The  $\mathcal{Q}_{Hq}^{(3)}$  operator, for example, induces cross-section deviations that are

proportional to the squared energy transfer  $\sqrt{s} = m_{VH}$ , which leads to deviations that scale with  $(p_T^{V,t})^2$  for both  $WH$  and  $ZH$  production.

- The  $\mathcal{Q}_{Hu}$  operator also shows quadratic deviations with  $p_T^{V,t}$ , but only for  $ZH$  production. It has no effect on the  $WH$  production cross-section.
- The  $\mathcal{Q}_{HW}$  operator has a constant effect on both  $WH$  and  $ZH$  production, with an additional component that grows roughly linearly with  $p_T^{V,t}$ .
- The operators  $\mathcal{Q}_{H\Box}$  and  $\mathcal{Q}_{HDD}$ , additionally lead to a redefinition of the Higgs field, which impacts the inclusive  $VH$  cross-section, without changing the predicted  $p_T^{V,t}$  spectrum.
- The operator associated with  $c'_{\ell\ell}$  affects the extraction of the Fermi constant  $G_F$  from the muon lifetime measurement, which enters the calculation of the amplitudes. It therefore impacts the inclusive  $VH$  cross-section prediction and has no  $p_T^{V,t}$ -dependent effect.

The last two points demonstrate one of the advantages of the SMEFT approach, as all of these effects are taken into account consistently. The studied  $p_T^V$ -dependences of the operator effects agree with the expectation from LO helicity amplitudes, e.g. reported in Ref. [261].

Of the  $13 + 1$  operators that affect the  $pp \rightarrow V(\rightarrow \text{leptons}) H(\rightarrow b\bar{b})$  process, the analysis phase space is particularly sensitive to deviations from the SM induced by non-zero values of  $c_{Hq}^{(3)}$ ,  $c_{Hu}$ ,  $c_{HW}$  and  $c_{HWB}$ . The coefficient  $c_{Hu}$  has degenerate effects on the cross-section predictions with  $c_{Hd}$  and  $c_{Hq}^{(1)}$  because the analysis cannot distinguish the types and handedness of incoming quarks. Therefore,  $c_{Hu}$  is chosen as a representative coefficient for all effects of this type. Results for these four coefficients and the real part of  $c_{dH}$  are presented in this chapter. The results for the full set of  $13 + 1$  operators are shown in Appendix A.

### 8.1.3 Technical setup

Each of the three terms in Equation 8.4 is simulated separately at LO using MADGRAPH with the SMEFTSIM package [57] and the  $\{m_W, m_Z, G_F\}$  scheme of EW input parameters. Events are interfaced to PYTHIA 8 for showering and hadronisation. Further details on the simulation setup can be found in Ref. [262]. The events are not passed through a simulation of the ATLAS detector, but studied at generator level within the fiducial volumes of each STXS measurement bin. The fiducial selection is technically implemented via the RIVET software [263].

As indicated in Equation 8.5, the parameterisation in each of the STXS bins is subsequently obtained with respect to the LO SM prediction from MADGRAPH + PYTHIA 8 and multiplied to the nominal prediction from POWHEG-BOX v2 and PYTHIA 8, including the simulation of the ATLAS detector and a full set of residual corrections such as the NLO EW differential- and the NNLO QCD inclusive cross-section correction. This assumes that the SM signal acceptance times efficiency in each STXS bin is not significantly changed by the EFT contributions, which

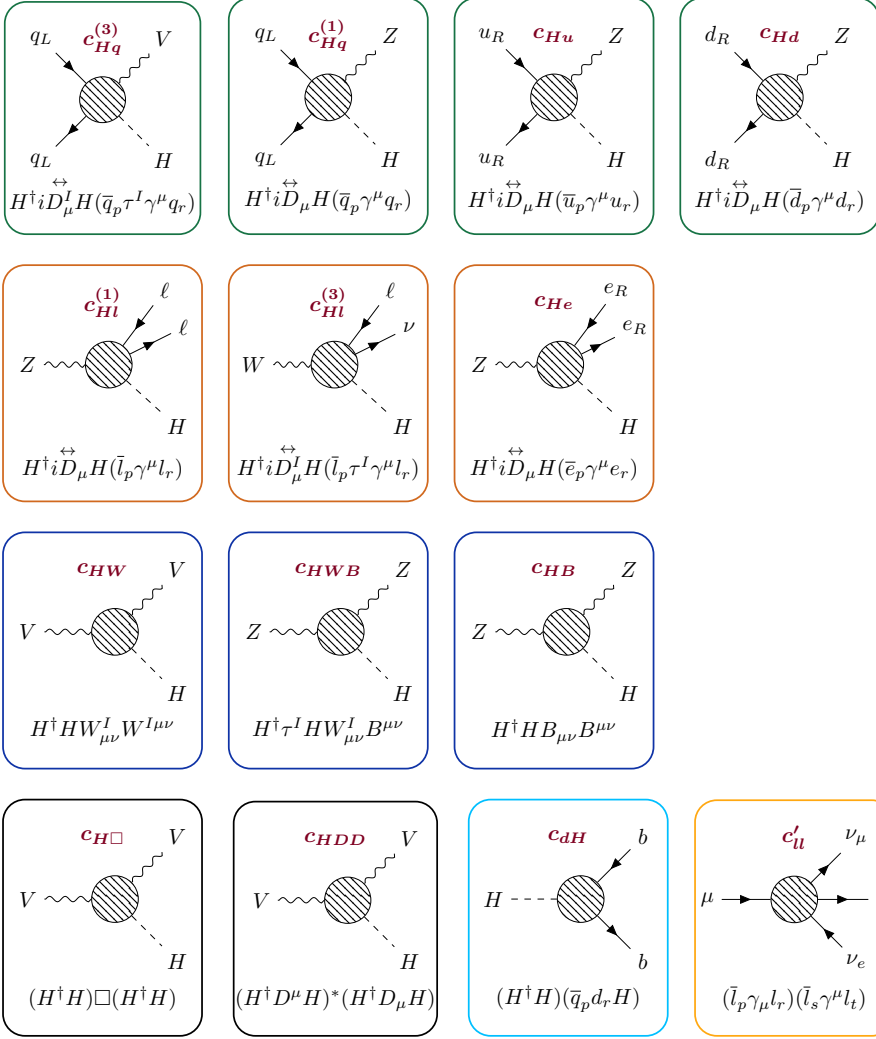


Figure 8.1: Example SMEFT operators of mass dimension 6 in the Warsaw basis that affect the  $pp \rightarrow V(\rightarrow \text{leptons})H$  cross-section at LO. Shown is the definition of the operator, adapted from Ref. [57], the name of the associated Wilson coefficient as well as an example vertex that the operator modifies. The operators are grouped according to their structure in colored boxes. The operator in the light blue box modifies the  $y_b$  Yukawa coupling. The operators in the black box also lead to a redefinition of the Higgs field and the operator in the orange box influences the value of the Fermi constant  $G_F$ .

is explicitly studied and summarised in Section 8.5.1. Additionally, the full set of theoretical uncertainties on  $\sigma_{\text{STXS}}^{(N)NLO}$  are considered in the statistical inference procedure. To suppress the contribution of statistical noise, only modifications to the cross-section that are larger than 1‰ at  $c_i = 1$  are taken into account.

Since the simulation is performed at LO in QCD, only  $qq$ -initiated  $ZH$  production is considered. Modifications of the  $gg$ -initiated  $ZH$  production cross-section are either introduced by operators of mass dimension  $\geq 8$  or by corrections that are formally NNLO in QCD. Therefore, the expected  $gg \rightarrow ZH$  contribution is fixed to the SM prediction within uncertainties in the fit. Given the small contribution in the analysis phase space, however, this assumption does not affect the limits on the Wilson coefficients significantly.

## 8.2 1D and 2D limits

To study the analysis sensitivity to each of the 13 + 1 SMEFT operators separately, one-dimensional scans of the profile likelihood-ratio

$$q(c_i) = -\ln \left( \frac{\mathcal{L}(c_i | \hat{\hat{\alpha}})}{\mathcal{L}(\hat{c}_i | \hat{\hat{\alpha}})} \right) \quad (8.10)$$

are performed as a function of the Wilson coefficients. The parameters  $\hat{\hat{\alpha}}$  are the nuisance parameters that maximise the likelihood for a given  $c_i$ , whereas the set  $\{\hat{c}_i, \hat{\hat{\alpha}}\}$  maximises the likelihood overall.

For the 1D scans, only one Wilson coefficient is varied at a time and the contribution of the other Wilson coefficients is fixed to their SM prediction at zero. The resulting likelihood landscapes are shown in Figures 8.2 and 8.3 as functions of the  $c_{Hq}^{(3)}$ ,  $c_{Hu}$ ,  $c_{HW}$ ,  $c_{HWB}$  and  $c_{dH}$  coefficients. The blue curves show the likelihood when only considering the interference terms between the SM and the SMEFT and therefore only taking into account the linear terms. The orange curves show the result when including the quadratic terms. The thresholds for the 68% and 95% confidence level intervals are indicated, too and the confidence intervals themselves are summarised separately in Figure 8.4. The confidence intervals for the remaining operators are summarised in Appendix A.

The analysis has the largest sensitivity to operators that induce a  $p_T^{V,t}$ -dependent modification of the signal cross-section. This is reflected in  $c_{Hq}^{(3)}$  and  $c_{Hu}$  having the tightest individual constraints, as their effect on the SM cross-section grows quadratically with  $p_T^{V,t}$ . The next best constraint operators are  $c_{HW}$  and  $c_{HWB}$ , which show an effect that grows linearly with  $p_T^{V,t}$ . The real part of the  $b$ -Yukawa modifier  $c_{dH}$  can only be constrained very poorly.

The difference between the limits obtained from a linear and a linear + quadratic parameterisation, shows that effects that are  $\Lambda^{-4}$  suppressed have non-negligible impact on the interpretation. In some cases, e.g. for  $c_{Hq}^{(3)}$ , including the quadratic

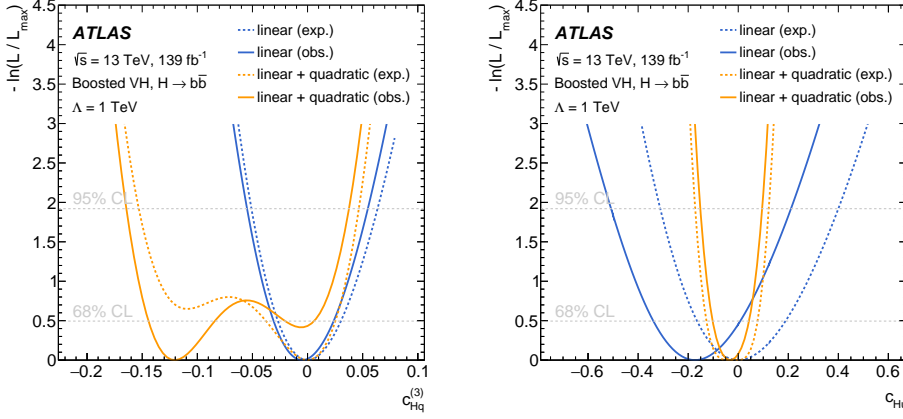


Figure 8.2: Scanned profile of the negative log-likelihood-ratio as a function of the Wilson coefficients  $c_{Hq}^{(3)}$  and  $c_{Hu}$ . The scans are performed using either a linear parameterisation of the  $VH$  production cross-section, the partial  $H \rightarrow b\bar{b}$  decay width, as well as the total width of the Higgs boson (blue line), or a parameterisation including quadratic terms (orange line). The value of all other Wilson coefficients is fixed to their SM expectation of zero. The observed shape is drawn as solid curves, the expected shape is drawn using dashed curves. The 68% and 95% CL thresholds are indicated. Published in Ref. [5].

terms introduces an ambiguity with a second minimum appearing at negative values of the Wilson coefficient. At the same time, the interpretation of the linear + quadratic limits is complicated by the absence of double SMEFT vertex insertions and the dimension-8 interference terms with the SM, which are also  $\Lambda^{-4}$  suppressed.

The similarity of the effect of the SMEFT operators on the  $p_T^{V,t}$  distribution causes the measurements of the individual operators to be correlated. These correlations are studied by performing two dimensional profile likelihood ratio scans as a function of pairs of Wilson coefficients. Two example scans are shown in Figure 8.5 for  $c_{Hu}$  vs.  $c_{Hq}^{(3)}$  and in Figure 8.6 for  $c_{HW}$  vs.  $c_{Hq}^{(3)}$ . The strength of the correlation is found to depend on whether the quadratic terms are included or not. The observed 2-dimensional 68% confidence intervals include the SM prediction.

### 8.3 Effect of the STXS split at 400 GeV

A unique feature of the dedicated high  $p_T$   $VH, H \rightarrow b\bar{b}$  analysis presented in the previous chapter, is the increased experimental acceptance at high  $p_T^V$ . As a result of this, the fiducial cross-section for  $p_T^{V,t} \geq 400$  GeV is measured for the first

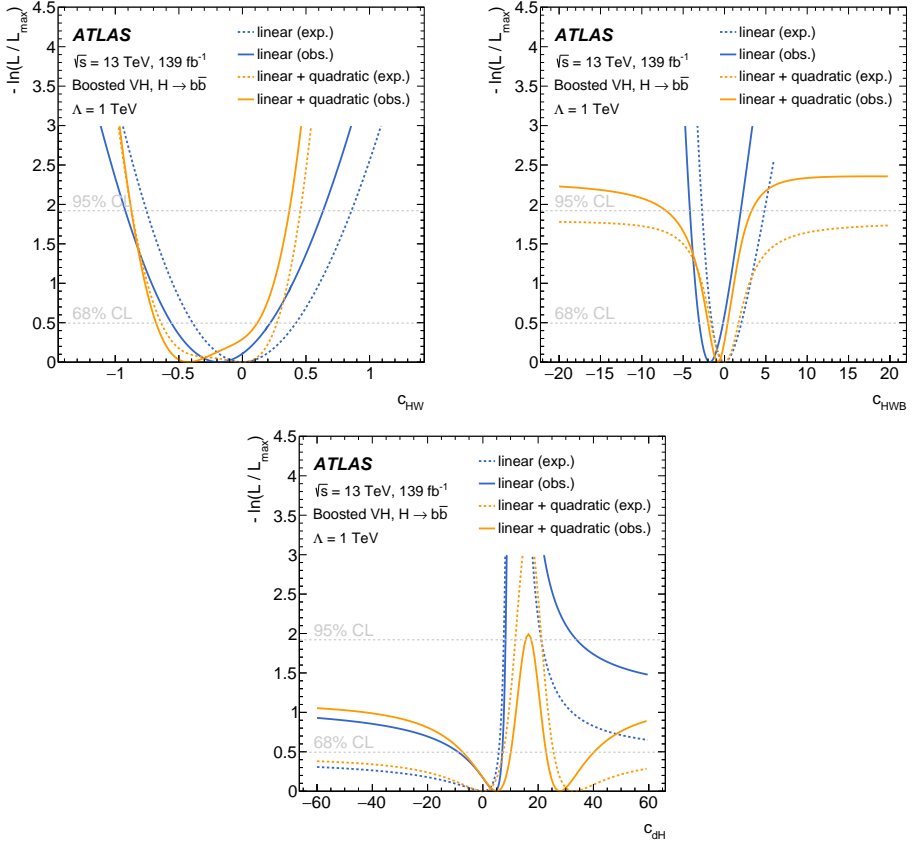


Figure 8.3: Scanned profile of the negative log-likelihood-ratio as a function of the Wilson coefficients  $c_{HW}$ ,  $c_{HWB}$  and  $c_{dH}$ . The scans are performed using either a linear parameterisation of the  $VH$  production cross-section, the partial  $H \rightarrow b\bar{b}$  decay width, as well as the total width of the Higgs boson (blue line), or a parameterisation including quadratic terms (orange line). The value of all other Wilson coefficients is fixed to their SM expectation of zero. The observed shape is drawn as solid curves, the expected shape is drawn using dashed curves. The 68% and 95% CL thresholds are indicated. Published in Ref. [5].

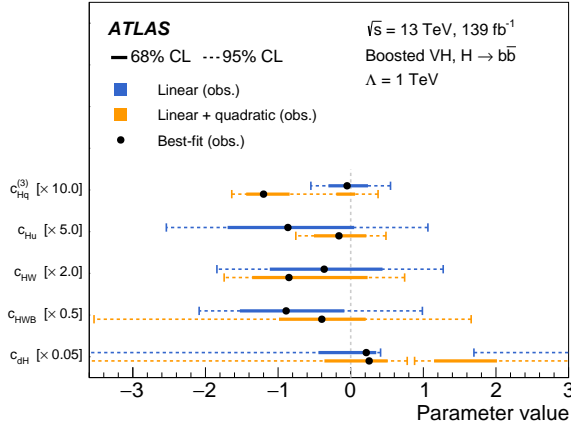


Figure 8.4: Summary of observed confidence intervals at 68% and 98% CL from profile likelihood ratio scans as a function of either  $c_{Hq}^{(3)}$ ,  $c_{Hu}$ ,  $c_{HW}$ ,  $c_{HWB}$  or the real part of  $c_{dH}$ . Only one Wilson coefficient is varied at a time and the remaining ones are fixed to their SM prediction at zero. The blue lines show the intervals obtained considering only the interference effects and therefore a linear parameterisation. The orange lines indicate the limits when including the terms quadratic in the Wilson coefficients. Published in Ref. [5].

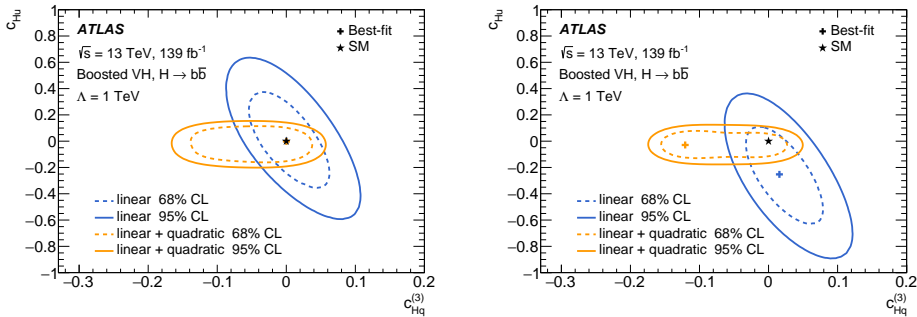


Figure 8.5: Expected (left) and observed (right) confidence intervals at 68% (dashed curves) and 95% (solid curves) CL on  $c_{Hu}$  and  $c_{Hq}^{(3)}$ . They are obtained from two dimensional scan of the profile negative log-likelihood-ratio. The contribution of other Wilson coefficients is fixed to their SM expectation at zero. Contours are obtained from a linear parameterisation of  $\sigma \times \text{BR}$  in blue and including the quadratic terms in orange. The best fit point is marked with a cross. Published in Ref. [5].



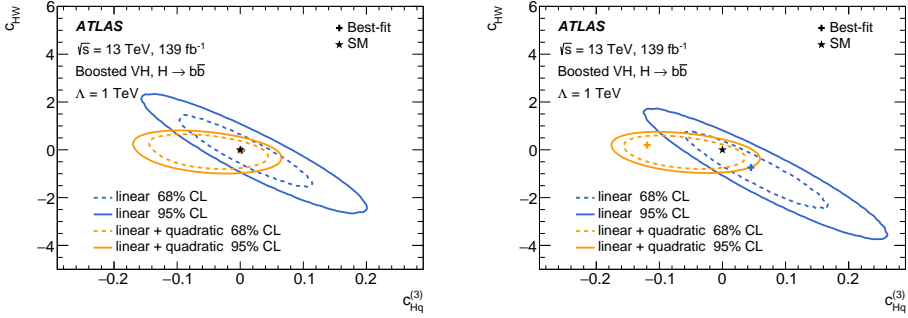


Figure 8.6: Expected (left) and observed (right) confidence intervals at 68% (dashed curves) and 95% (solid curves) CL on  $c_{HW}$  and  $c_{Hq}^{(3)}$ . They are obtained from two dimensional scan of the profile negative log-likelihood-ratio. The contribution of other Wilson coefficients is fixed to their SM expectation at zero. Contours are obtained from a linear parameterisation of  $\sigma \times \text{BR}$  in blue and including the quadratic terms in orange. The best fit point is marked with a cross. Published in Ref. [5].

time. This section studies the effect that this additional differential information at high  $p_T^{V,t}$  has on the limits on Wilson coefficients. To do this, the SMEFT limits from the measurement using 4 STXS bins are compared to limits obtained when using only 2 STXS bins that are inclusive in  $p_T^{V,t} \geq 250 \text{ GeV}$ , one for  $ZH$  and one for  $WH$ . Additional differential information is only useful if the operator that is considered produces a  $p_T^{V,t}$ -dependent effect, therefore  $c_{Hq}^{(3)}$ ,  $c_{Hu}$  and  $c_{HW}$  are studied as proxies of possible deviations that grow linear/ quadratically with  $p_T^{V,t}$ . To be able to better compare the resulting limits, this test is performed on the simulation of the SM expectation (pre-fit Asimov set). Example results are shown in Figure 8.7 for the split scenario in orange and the merged scenario in blue. As can be seen, the expected limits increase significantly when more differential information is available, especially at high  $p_T^V$ .

## 8.4 EFT limits in the analysis eigenspace

To obtain limits on Wilson coefficients that do not make the assumption that all other coefficients are zero, a simultaneous fit needs to be performed. However, the large correlations that are already observed in the two-dimensional case become prohibitively problematic in higher dimensional fits. This renders such an approach impossible using only the high  $p_T$   $VH, H \rightarrow b\bar{b}$  measurements.

This section presents an alternative approach, where instead of the original Wilson coefficients, linear combinations of Wilson coefficients that are designed to be uncorrelated are constrained. A Principal Component Analysis (PCA) is used to identify these orthogonal combinations and order them according to their

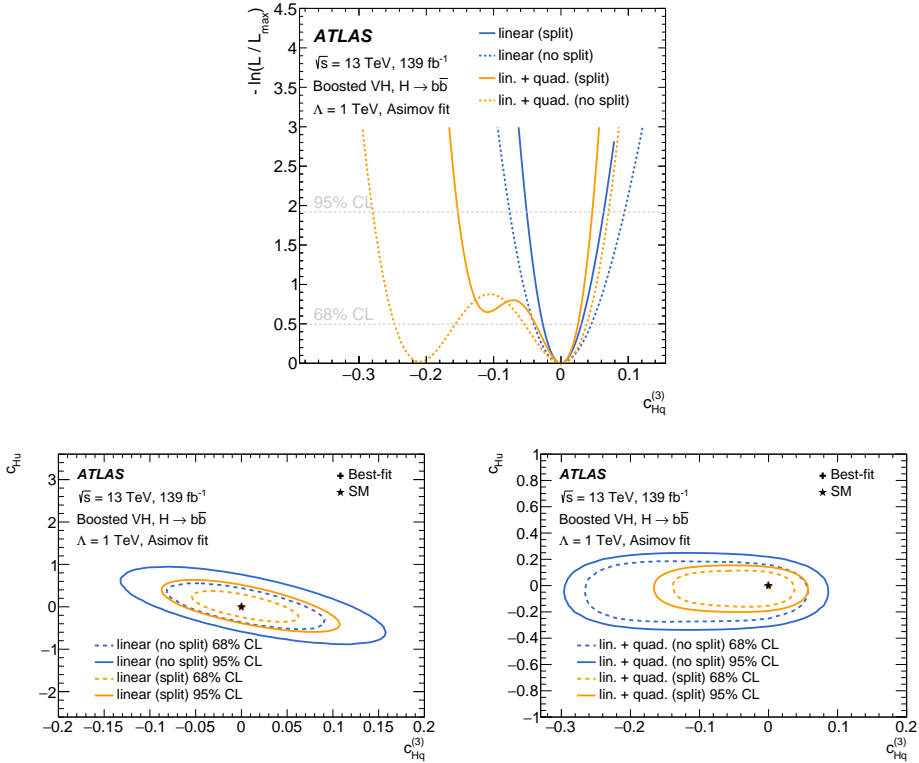


Figure 8.7: Expected shape of the profile likelihood ratio obtained from a one dimensional scan over  $c_{Hq}^{(3)}$  (top) and two dimensional scans of  $c_{Hu}$  vs.  $c_{Hq}^{(3)}$  (bottom left) and  $c_{Hu}$  vs.  $c_{HW}^{(3)}$  (bottom right). The likelihood shape (1D case) and contours (2D case) are shown comparing the two times two  $p_T^{V,t}$  STXS bins in the analysis (solid) with an alternative binning inclusive for  $p_T^{V,t} \geq 250 \text{ GeV}$  (dashed). Published in Ref. [5].

expected uncertainty. The methodology is an extension of the approach presented in Ref. [262].

Ideally, the PCA is performed on the Fischer information matrix of the reparameterised SMEFT likelihood, which in the limit of Gaussian measurements is the inverse of the covariance matrix

$$(H_{\text{SMEFT}})_{ij} = (C_{\text{SMEFT}}^{-1})_{ij} = \frac{\partial^2 - \ln(\mathcal{L})}{\partial c_i \partial c_j} \quad . \quad (8.11)$$

$H_{\text{SMEFT}}$  is obtained from the Hessian of the STXS fit<sup>1</sup> to the SM expectation (pre-fit Asimov) via a transformation of variables from STXS signal strengths  $\mu_i$  to Wilson coefficients  $c_i$ :

$$(H_{\text{SMEFT}})_{ij} = (H_{\text{STXS}})_{ab} \frac{\partial \mu_a}{\partial c_i} \frac{\partial \mu_b}{\partial c_j} \rightarrow H_{\text{SMEFT}} = P^T C_{\text{STXS}}^{-1} P \quad , \quad (8.12)$$

where  $P = (\alpha_i)_j$  is the parameterisation matrix consisting of the linear coefficients  $\alpha_i$  for each STXS bin  $j$ . The linear parameterisation is used to obtain the orthogonal measurement directions in the parameter space. The linearised decay branching ratio  $\mathcal{I}_{\text{BR}}$  is used to parameterise the  $H \rightarrow b\bar{b}$  decay. The initial eigenvectors are determined from SM simulated data in order to not let the choice of eigenvector depend on the details of the observed data.

The matrix  $H_{\text{SMEFT}}$  is diagonalised to obtain the eigenvectors  $E_a$  with their corresponding eigenvalues  $\lambda_a$ . In the Gaussian approximation, the precision to which the eigenvector  $E_a$  can be measured is given by  $1/\sqrt{\lambda_a}$ . Eigenvectors with high eigenvalue can therefore be constrained tightly. This procedure leads to four eigenvectors with eigenvalues  $\geq 0.1$ . The remaining eigenvectors express quasi-flat directions in the likelihood landscape, as they can only be weakly constraint to values  $> 1/\sqrt{0.1} \sim 3$ . These four eigenvectors of Wilson coefficients are afterwards fit to data, which leads to residual correlations of up to 13%.

In a second step, these correlations are removed by diagonalising again the inverse covariance matrix of the fit to data, which results in slightly changed eigenvectors. However, as the new eigenvectors are just linear combinations of the old ones, this second diagonalisation does not change the eigenspace that the analysis is sensitive to.

The definition of the eigenvectors as linear combinations of the original Wilson coefficients and the decay branching ratio modifier  $\mathcal{I}_{\text{BR}}$  is listed in Table 8.1. For readability, Wilson coefficients entering each eigenvector expression with a coefficient of less than 0.1 have been omitted. A complete table is listed in Appendix A. The best constrained direction in the parameter space,  $c_{EA}$ , aligns nearly perfectly with the Wilson coefficient  $c_{Hq}^{(3)}$ , which is also the coefficient that has the strongest linear constraint in the one dimensional scans. The subleading combination  $c_{EB}$  is an

---

<sup>1</sup>The theory uncertainties on the signal prediction in each STXS bin are included in this fit, in contrast to the STXS measurement.

Coefficient	Eigenvalue	Eigenvector combination
$c_{EA}$	1500.0	$0.99 \cdot c_{Hq}^{(3)} + 0.11 \cdot c_{Hu}$
$c_{EB}$	26.9	$0.82 \cdot c_{Hu} - 0.49 \cdot c_{Hq}^{(1)} - 0.24 \cdot c_{Hd} - 0.13 \cdot c_{Hq}^{(3)}$
$c_{EC}$	2.2	$0.67 \cdot \mathcal{I}_{BR} + 0.66 \cdot c_{HW} + 0.18 \cdot c_{Hq}^{(1)} - 0.16 \cdot c_{Hl}^{(3)} + 0.14 \cdot c_{HWB} + 0.12 \cdot c'_{ll}$
$c_{ED}$	0.1	$0.70 \cdot c_{Hq}^{(1)} + 0.52 \cdot c_{HWB} + 0.27 \cdot c_{Hu} - 0.27 \cdot c_{HW} - 0.24 \cdot c_{Hd} + 0.13 \cdot c_{HB}$

Table 8.1: Definition of the principal components of the analysis in terms of linear combinations of Wilson coefficients. The eigenvalues corresponding to the eigenvector combinations are shown, too. Coefficients less than 0.1 have been dropped. Published in Ref. [5]. Full table in Appendix A.

admixture of  $c_{Hq}^{(1)}$ ,  $c_{Hu}$  and  $c_{Hd}$ , which all have comparable (and almost degenerate) effects on the  $ZH$  STXS bins. In addition to the general  $(p_T^{V,t})^2$ -dependent effect, the eigenvector  $c_{EB}$  allows for a  $ZH$  vs.  $WH$  difference. The coefficients  $c_{EC}$  and  $c_{ED}$  are combinations of many Wilson coefficients, showing large contributions of  $\mathcal{I}_{BR}$ ,  $c_{HW}$  and  $c_{HWB}$  and  $c_{Hq}^{(1)}$ , respectively.

Since the eigenvectors per definition are orthogonal on data, the leading four can be fit simultaneously. Their best fit value, together with their confidence intervals at 68% and 95% CL are shown in Figure 8.8. The exact values of the confidence intervals are listed in Appendix A, obtained from profile likelihood ratio scans over each eigenvector, while profiling over the remaining three. The impact of the eigenvectors on the expected signal cross-section in the four STXS bins is shown in Figure 8.9.

## 8.5 Miscellaneous considerations

The interpretation presented in this chapter must be seen in the larger context of developing a global SMEFT scheme that allows to both make quantitative statements about a multitude of measurements and to combine them in a consistent way. In the absence of resonantly produced new physics and with limits from direct searches being pushed further beyond the electroweak scale, this approach meets increasing interest also from the energy frontier community at colliders. As such, development in these areas is ongoing. This section touches several aspects of the interpretation procedure that are less well understood but deserve a closer look.

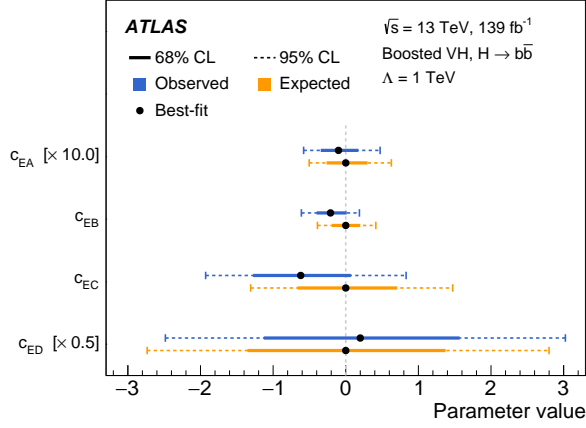


Figure 8.8: Summary of the expected (orange) and observed (blue) confidence intervals at 68% and 95% CL for the four leading eigenvectors of the PCA. Published in Ref. [5].

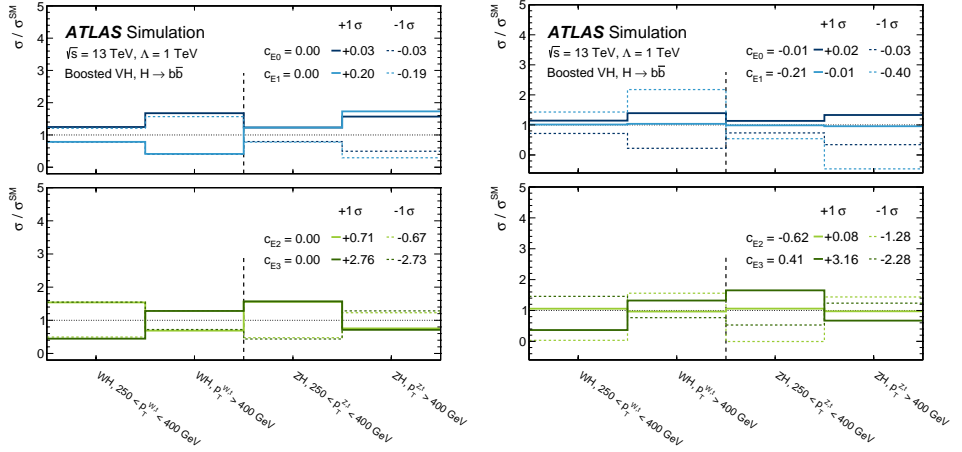


Figure 8.9: The expected (left) and observed (right) impact of the four leading eigenvectors of the PCA at their  $+1\sigma$  (solid) and  $-1\sigma$  variations on the four STXS bins measured by the analysis. The central values are indicated in the legend. Published in Ref. [5].

### 8.5.1 SMEFT effects on experimental acceptance

Many of the effective operators that affect the  $VH, H \rightarrow b\bar{b}$  signal process do not only affect the total rate of the process, but modify kinematic distributions, such as e.g. the  $p_T^{V,t}$  spectrum. This can impact the interpretation in two possible ways:

1. If the effective operators modify the shape of the Higgs candidate jet mass  $m_J$  significantly with respect to the SM prediction, the simple scaling of the SM shapes by the SMEFT cross-section change is no longer valid.
2. Some SMEFT operators alter the signal kinematics. Due to the STXS partitioning, changes in the  $p_T^V$  spectrum across STXS bins are taken into account. But inside of each STXS bin, SM kinematics are assumed. If acceptance-sensitive distributions inside of an STXS bin get changed too much by an effective operators, the estimated yield change is not valid.

Potential changes to the predicted  $m_J$  shape are studied at generator-level for the operators that the analysis is most sensitive to and found to be negligible. Similarly, the effect of the analysis selection on the SMEFT parameterisation is studied on generator level. One example for an operator that changes the predicted distribution of kinematic variables is  $\mathcal{Q}_{Hq}^{(3)}$ , which introduces cross-section modifications from the SM prediction that grow  $\sim (p_T^{V,t})^2$ . As shown in Figure 7.20, the analysis acceptance times efficiency is  $p_T^{V,t}$ -dependent. A change in the predicted  $p_T^{V,t}$  shape is found to be the main cause of change in the analysis acceptance. It impacts the limits by less than 20%, and most of the time the confidence intervals at 95% CL become more tight when the acceptance effect is included, which implies that the limits without acceptance effects are (if different) more conservative than limits with acceptance corrections. Figure 8.10 illustrates the effect of (not) including acceptance effects on the operator  $c_{Hq}^{(3)}$ <sup>2</sup>.

### 8.5.2 SMEFT effects on background processes

A complex analysis like the search for  $VH, H \rightarrow b\bar{b}$  faces backgrounds from a variety of EW and QCD processes. This makes a consistent SMEFT interpretation difficult, as not only the signal but in principle also all important backgrounds need to be parameterised as a function of the Wilson coefficients. In addition to a total increase in the number of Wilson coefficients that need to be considered, the same Wilson coefficients that affect the  $VH$  signal also impact some of the backgrounds. Experimentally, the analysis fit model tries to rely as little on MC predictions for the background as possible. For example, the normalisations of all major backgrounds are measured in data, which allows partially to absorb potential effects on the backgrounds. The impact of the operators selected for the  $VH, H \rightarrow b\bar{b}$  analysis has been evaluated for the diboson process, which has an invariant mass just below that of the Higgs signal. In the same range of  $p_T^{V,t}$ ,

<sup>2</sup>This scan is performed using a simple  $\chi^2$  ansatz instead of the full experimental likelihood. Both procedures are shown to yield consistent results.

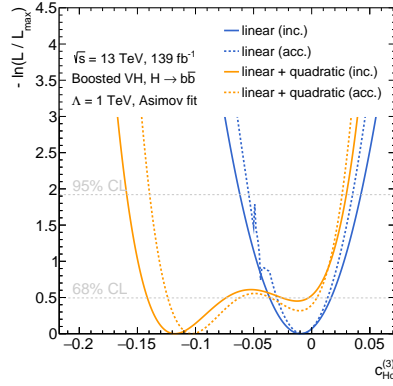


Figure 8.10: Effect of acceptance changes on the Wilson coefficient constraints.

that is in the same STXS bin, the relative modification of the fiducial diboson production cross-section with respect to the SM prediction is three to four times smaller than the effect on the  $VH$  cross-section in the same range, for the same Wilson coefficient value. Although  $ZZ$  and  $WZ$  production are measured with up to twice better precision, the effect on the limits of the most constrained coefficients is up to  $\sim 10\%$  and therefore within the range of the impact of other assumptions that are made for this interpretation.

### 8.5.3 Validity of the SMEFT

The extended  $p_T^V$  reach of the dedicated high  $p_T$   $VH, H \rightarrow b\bar{b}$  analysis enables to assess regions where the effect of many SMEFT operators is relatively enhanced. At the same time, events that fall into these regions have a high energy transfer  $\sqrt{s} = m_{VH}$ . Especially for operators with momentum-dependent effects, the region where  $\sqrt{s} \sim \Lambda/\sqrt{c}$  leads to SMEFT effects that are comparable to the SM contribution, which breaks the convergence of the SMEFT expansion. This imposes constraints on the validity and interpretability of the SMEFT results. In the region just below the generic limit of  $\sqrt{s} \sim \Lambda/\sqrt{c}$ , interpretability is limited to a class of strongly coupled UV completions [264].

Furthermore, the limits that are set on the Wilson coefficients and the correlation between Wilson coefficients change when the quadratic terms are included in the parameterisation. Although the parameter intervals that are derived from the linear and linear + quadratic parameterisation are not in contradiction with each other, for some Wilson coefficients the inclusion of the quadratic terms changes the intervals significantly.

The quadratic terms are not the only terms that are  $\Lambda^{-4}$  suppressed, however. Interference terms of the SM with dimension 8 operators, or double insertions of dimension 6 operators, for example, are also  $\Lambda^{-4}$  suppressed and therefore

of the same generic size as the quadratic dimension 6 terms. These terms are currently neglected, however, and including them or not might impact the limits significantly, too. This statement carries a fine print, however, since depending on the actual BSM structure of the theory, the dimension 8 interference terms could be suppressed or enhanced with respect to the squared dimension 6 contributions.

Additional considerations on the validity of the SMEFT for the case of the presented  $VH, H \rightarrow b\bar{b}$  measurements are given in Section 9.1.6.



# 9 Combination of measurements of Higgs boson decays to heavy-flavour quarks

This chapter presents two combinations of measurements of Higgs boson decays to heavy-flavour quarks. The first combines the novel  $VH, H \rightarrow b\bar{b}$  analysis at high  $p_{\text{T}}^V$  with the standard  $VH, H \rightarrow b\bar{b}$  analysis to measure the  $VH, H \rightarrow b\bar{b}$  cross-section consistently over the whole  $p_{\text{T}}^V$  range with as many bins as possible. The combination is published in Ref. [7]. The second combination simultaneously measures the  $VH, H \rightarrow b\bar{b}$  and the  $VH, H \rightarrow c\bar{c}$  processes by combining the two individual analyses.

## 9.1 Combination of resolved and boosted $VH, H \rightarrow b\bar{b}$

Measurements of the  $VH, H \rightarrow b\bar{b}$  cross-section as a function of the vector boson's transverse momentum  $p_{\text{T}}^V$  are an important test of the SM. The ATLAS collaboration provides two such differential measurements in the STXS framework, using the full Run 2 data set of  $139\text{ fb}^{-1}$ . Depending on the magnitude of the  $p_{\text{T}}^V$ , different strategies are used to maximise the acceptance to the signal.

A first analysis targets  $VH, H \rightarrow b\bar{b}$  events with  $p_{\text{T}}^V > 75\text{ GeV}$  and reconstructs the  $H \rightarrow b\bar{b}$  decay using two separate small- $R$  jets with a radius parameter of  $R = 0.4$ . This analysis is referred to as the *resolved* analysis and constitutes the most precise inclusive measurement of the  $VH, H \rightarrow b\bar{b}$  signal strength to date. As is shown in Figure 9.1, the  $VH, H \rightarrow b\bar{b}$  cross-section is extracted in 3 STXS categories for  $ZH$  production and 2 categories for  $WH$  production. In both cases, the highest STXS category includes all events with  $p_{\text{T}}^{V,t} > 250\text{ GeV}$ .

The second analysis is specifically tailored towards the high transverse momentum regime with  $p_{\text{T}}^V > 250\text{ GeV}$ , where the two  $b$ -jets from the  $H \rightarrow b\bar{b}$  decay are geometrically close due to the high Lorentz boost of the Higgs boson. Consequently, the Higgs boson decay is reconstructed using a single large- $R$  jet with a radius parameter of  $R = 1.0$ . The analysis has already been described in detail in Chapter 7 and is referred to as the *boosted* analysis in what follows. As is shown in Figure 9.1, the  $VH, H \rightarrow b\bar{b}$  cross-section is extracted in 2 STXS categories for both  $ZH$  and  $WH$  production. The increased signal acceptance of the boosted Higgs boson

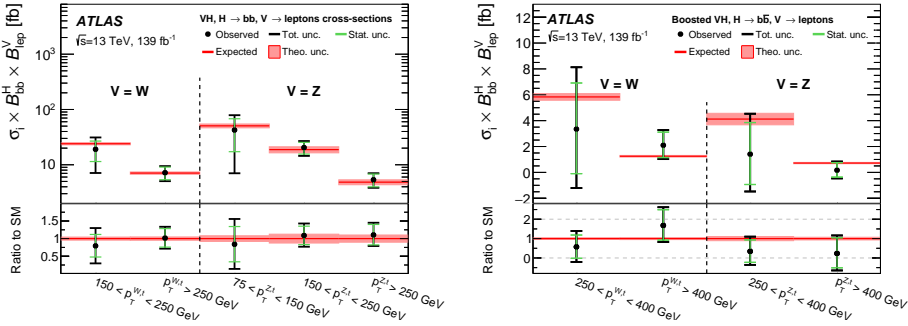


Figure 9.1: Measured  $VH$  reduced stage-1.2 simplified template cross-sections times the  $H \rightarrow b\bar{b}$  and  $V \rightarrow$  leptons branching fractions and comparison with their SM predictions. Left shows the results obtained from the resolved analysis [6] and right shows the results obtained from the boosted analysis [5].

reconstruction technique allows to increase the granularity of the cross-section measurement at high  $p_T^V$  and to provide a measurement in the BSM-sensitive STXS category that only contains events with  $p_T^{V,t} > 400$  GeV.

Due to their complementary, a combination of the resolved and boosted analyses could provide both a high precision in the STXS categories at low and intermediate  $p_T^V$ , and additional differential measurements at high  $p_T^V$ . The additional differential information with respect to the resolved analysis is expected to improve the constraints on a variety of BSM physics, as suggested in Ref. [261]. Such a combination of the two analyses cannot be achieved trivially, however, because the two analysis share a significant fraction of the selected data events. This is due to the fact that for  $p_T^V \sim 300$  GeV, Higgs boson candidates can be reconstructed both with the resolved and with the boosted approach.

The overlap between the two analyses is shown in Figure 9.2 for the 1-lepton channel as a function of the reconstructed  $p_T^V$ . Especially in the  $p_T^V$  regime between 250 and 400 GeV, about 25%-50% of the signal events that pass the resolved analysis selection also pass the boosted selection. Vice versa, 60%-80% of the signal events falling into the signal regions of the boosted analysis are also selected by the resolved analysis. This section presents a consistent combination of the resolved and boosted  $VH, H \rightarrow b\bar{b}$  analyses, that resolves the overlap by using exclusively the resolved analysis for events with  $p_T^V < 400$  GeV and the boosted analysis selection for events with  $p_T^V > 400$  GeV. This combination results in the most granular differential measurement of the  $VH$  cross-section to date.

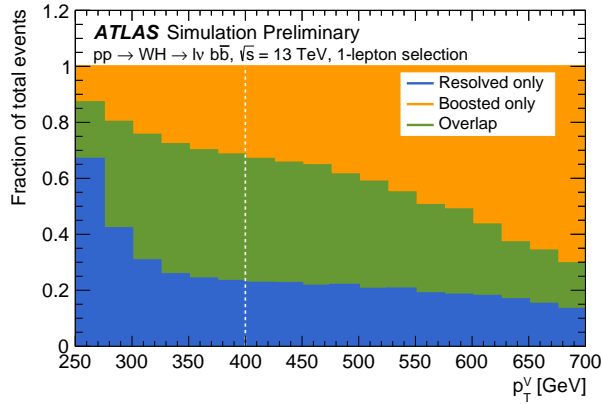


Figure 9.2: Predicted fraction of selected  $WH, H \rightarrow b\bar{b}$  events in the 1-lepton channel of both analyses. Events that can only be reconstructed with the resolved analysis strategy are shown in blue, events that can only be reconstructed with the boosted analysis strategy are shown in orange and events for which both reconstruction strategies work are shown in green. Only events with  $p_T^V > 250$  GeV are shown, because the boosted reconstruction cannot be applied below this threshold [7].

### 9.1.1 The resolved $VH, H \rightarrow b\bar{b}$ analysis

Before presenting the combined measurements, this section introduces briefly the resolved  $VH, H \rightarrow b\bar{b}$  analysis. A more detailed description is given in Ref. [6].

Similar to the boosted analysis, the resolved  $VH, H \rightarrow b\bar{b}$  analysis categorises events according to the charged-lepton multiplicity into three channels: A 0-lepton channel targeting  $ZH \rightarrow \nu\nu b\bar{b}$  events, a 1-lepton channel targeting  $WH \rightarrow \ell\nu b\bar{b}$  events and a 2-lepton channel targeting  $ZH \rightarrow \ell\ell b\bar{b}$  events, where  $\ell$  is either a muon or an electron. The definition of the leptons and  $E_T^{\text{miss}}$ , and as a consequence also the reconstruction of the vector-boson candidate, is identical to the boosted analysis.

The magnitude of the reconstructed  $p_T^V$  is used to further split the events into separate categories that match with the STXS categories for which the analysis provides measurements. Three categories are defined:  $75 \text{ GeV} < p_T^V < 150 \text{ GeV}$ ,  $150 \text{ GeV} < p_T^V < 250 \text{ GeV}$  and  $p_T^V > 250 \text{ GeV}$ . The first category, from 75 to 150 GeV, is only considered in the 2-lepton channel, because in the 0-lepton channel the trigger thresholds are too high and in the 1-lepton channel the background contamination is too high to access this region.

Due to the difference in the Higgs boson reconstruction, events in the resolved analysis are characterised by the presence of small- $R$  calorimeter jets with a radius parameter of  $R = 0.4$ . Exactly two such jets with  $p_T > 20 \text{ GeV}$  and  $|\eta| < 2.5$  are required to be flagged by a multivariate  $b$ -tagging algorithm to have originated

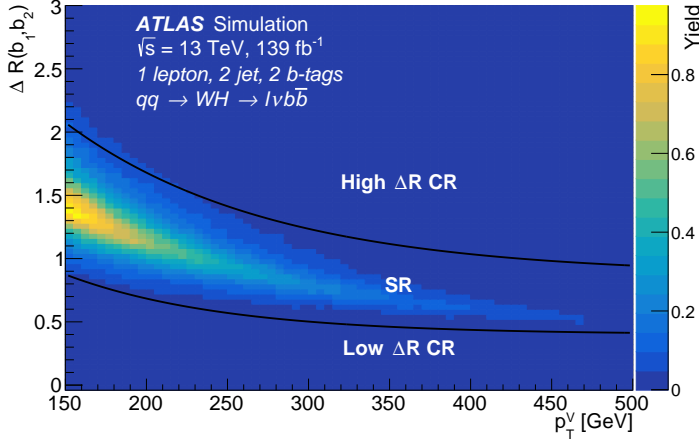


Figure 9.3: The geometrical distance  $\Delta R(b, b)$  between the two  $b$ -tagged jets of the resolved analysis as a function of the reconstructed  $p_T^V$ . The black lines show the  $p_T^V$ -dependent cuts that are used to define the signal region and a low- and high  $\Delta R$  control region. Taken from Ref. [6].

from final state  $b$ -quarks. These two jets are used to reconstruct the Higgs boson candidate. To improve the signal purity, events are further classified according to the total number of jets in the event. If only the two  $b$ -tagged jets are present, the event is categorised as a 2-jet event. In the 0- and 1-lepton channel, events with one additional jet form the 3-jet categories. Events with higher jet multiplicities are not considered, due to the high background contamination from  $t\bar{t}$  production. In the 2-lepton channel, where the  $t\bar{t}$  background is less prominent, this upper cut on the jet multiplicity is dropped and events are categorised as 2-jet or  $\geq 3$ -jet events.

The geometrical distance  $\Delta R(b, b)$  between the two  $b$ -tagged jets is used to define signal and control regions. As shown in Figure 9.3,  $p_T^V$ -dependent cuts on  $\Delta R(b, b)$  are introduced to separate the events into a SR and CRs with low- and high  $\Delta R$ . The low  $\Delta R$  CR is enriched in  $V$ +jet events, whereas the high  $\Delta R$  CR is enriched in events from  $t\bar{t}$  background.

In the SRs, a boosted decision tree (BDT) is used to separate the signal from the backgrounds. The BDT uses a variety of kinematic event information as input, such as the invariant dijet mass  $m_{bb}$ , the  $\Delta R(b, b)$  and variables that are sensitive to e.g. the  $Z$ -boson polarisation in the 2-lepton channel. A total of 10 to 15 variables is used, depending on the considered lepton channel. A binned profile likelihood fit is performed, using the BDT shape in the SRs and the total event yield in each CR simultaneously to extract the signal.

### 9.1.2 The modifications to the input analyses and the combination strategy

Because the resolved and the boosted analysis reconstruct the vector-boson candidate in the same way, the magnitude of  $p_T^V$  can be used to achieve orthogonality between the two analyses. This combination places a cut at  $p_T^V = 400$  GeV. Below this cut, the resolved analysis strategy is applied and the Higgs boson candidate is reconstructed as two small- $R$  jets. Above this cut, the boosted analysis strategy is used and the Higgs boson candidate is reconstructed as a large- $R$  jet.

The decision to use the resolved analysis strategy in the overlap region with  $250 \text{ GeV} < p_T^V < 400 \text{ GeV}$  is driven by the fact that the acceptance of the boosted reconstruction is not yet maximal at  $p_T^V \sim 250$  GeV, as can be seen in Figure 7.20. An other reason is that the resolved analysis uses a BDT-based discriminant which showed improvements of 20%-55% with respect to a resolved analysis using only the reconstructed Higgs mass. The upper cut at  $p_T^V = 400$  GeV removes about 8%-14% of data events and 14%-18% of signal events. In the region with  $p_T^V > 400$  GeV, the boosted analysis has a  $\sim 30\%$  higher signal acceptance with respect to the resolved analysis. For the combination, the regions of the boosted analysis with  $250 \text{ GeV} < p_T^V < 400 \text{ GeV}$  are dropped.

Furthermore, the split at  $p_T^V = 400$  GeV ensures that the  $p_T^V$  categories match with the fiducial STXS categories for which cross-sections are measured. This correspondence, together with a sketch of the combination strategy, is shown in Figure 9.4. It is important that the events that fall into a certain reconstructed  $p_T^V$  category also have a generator-level truth  $p_T^V$  from the corresponding STXS category in order to minimise the correlations between the measured STXS cross-sections. Therefore, to quantify the correspondence between the reconstructed  $p_T^V$  categories of the analysis and the STXS categories, Figure 9.5 shows the matching matrix between the analysis and STXS categories for the signal yield and the signal fraction. Overall, a very good correspondence between the STXS categories and the  $p_T^V$  categories of the analysis is observed. This correspondence is best in the 2-lepton channel, where the presence of the two charged leptons guarantee a precise reconstruction of the  $Z$ -boson candidate. In the 0-lepton channel, there is significant cross-contamination from  $WH$  events, where the  $W$ -boson decays into a  $\tau$  lepton, which in turn decays hadronically, and a neutrino.

### 9.1.3 Statistical treatment and inference

The statistical inference of the combination is similar to the procedure used in the individual analyses. A likelihood function is defined from binned histograms and incorporates systematic uncertainties as nuisance parameters  $\vec{\theta}, \vec{\gamma}$ . The signal is

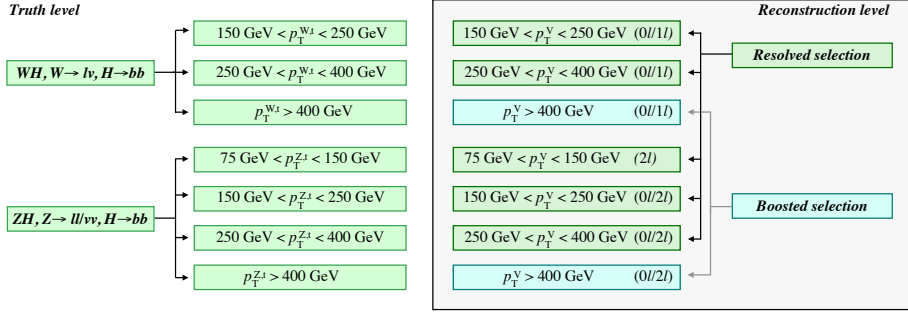


Figure 9.4: Illustration of the resolved + boosted analysis combination strategy together with a sketch of the STXS categories for which cross-sections are extracted. Published in Ref. [7].

extracted by maximising the profile likelihood-ratio

$$\lambda(\vec{\mu}) = \frac{\mathcal{L}(\vec{\mu}, \hat{\hat{\theta}}, \hat{\hat{\gamma}})}{\mathcal{L}(\hat{\hat{\mu}}, \hat{\hat{\theta}}, \hat{\hat{\gamma}})} \quad , \quad (9.1)$$

where  $\{\hat{\hat{\mu}}, \hat{\hat{\theta}}, \hat{\hat{\gamma}}\}$  are the values that maximise the likelihood unconditionally and  $\{\hat{\hat{\theta}}, \hat{\hat{\gamma}}\}$  the values that maximise  $\mathcal{L}$  conditional on a fixed set of values of the parameters of interest  $\vec{\mu}$ . Different fits are performed for different sets of parameters of interest, ranging from a single, global  $VH, H \rightarrow b\bar{b}$  signal strength  $\mu_{VH}^{b\bar{b}}$  to a fit with seven PoIs that correspond to the cross-sections times branching ratio in each STXS category.

In contrast to the boosted analysis, the  $VZ$  signal strength is not extracted together with the  $VH$  signal strength, due to the fact that the resolved regions make use of a BDT that is trained to discriminate the  $VH$  signal from the backgrounds. Instead a  $VZ$  cross-check fit is performed to validate the analysis strategy, by exchanging the  $VH$  BDT in the resolved regions by a different BDT that is trained to separate the  $VZ$  process from the background. No change of fit discriminant is needed for the boosted regions because the large- $R$  jet mass is used as a fit discriminant, which has enough separation power between the  $VH$  process, the  $VZ$  process and the backgrounds.

The normalisations of the main backgrounds,  $t\bar{t}$ ,  $W$ +jets and  $Z$ +jets, are solely determined from the fit to data with the help of dedicated control regions. They do not have associated auxiliary measurement terms and are consequently referred to as 'floating normalisations'. A summary of the deployed normalisation factor scheme of the combination is shown in Figure 9.6. The scheme has been re-evaluated with respect to the individual analyses to accommodate the changes that arise from the overlap removal. In addition, the fit model of the combination has an increased set of floating normalisations in order to reduce the reliance on MC simulations.

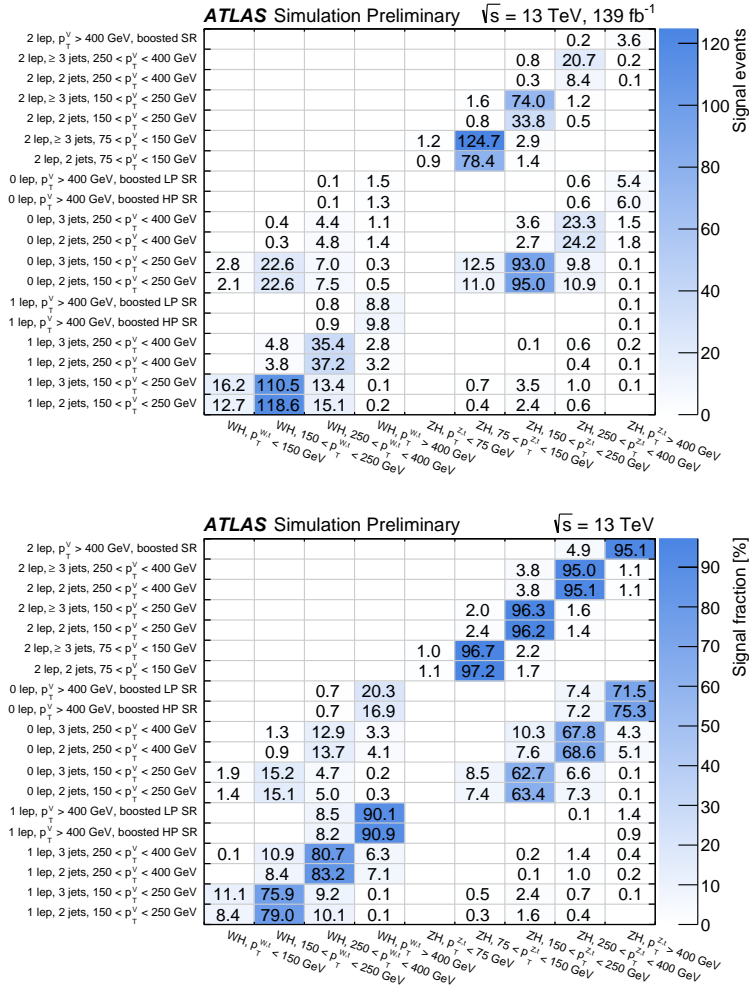


Figure 9.5: Matching matrix between fiducial STXS measurement regions ( $x$ -axis) and analysis categories ( $y$ -axis) for the signal yields (top) and the signal fraction in % (bottom). Entries with signal yields  $< 0.1$  and fractions  $< 0.1\%$  are not shown. Published in Ref. [7].

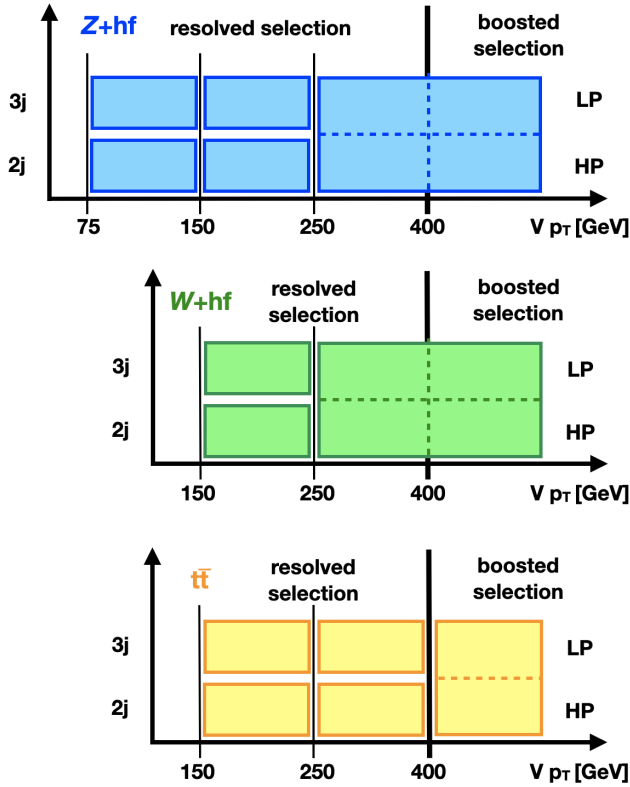


Figure 9.6: Sketch of the floating normalisation factors implemented for the main backgrounds  $t\bar{t}$ ,  $W+\text{hf}$  and  $Z+\text{hf}$ . Regions that are separated with a dashed line share a common normalisation factor and uncertainties are implemented that quantify possible acceptance differences between the regions. Published in Ref. [7].



For the  $V$ +jets background, separate normalisation factors are applied for each  $p_T^V$  region below 250 GeV, further split into individual factors for 2-jet and ( $\geq$ )3-jet events. Since the boosted analysis regions with  $250 \text{ GeV} < p_T^V < 400 \text{ GeV}$  are removed, the resolved regions in the same  $p_T^V$  range are used to help constrain the boosted  $V$ +jets backgrounds and consequently, they share a common normalisation factor with the boosted  $p_T^V \geq 400 \text{ GeV}$  region. Uncertainties are added to take into account potential acceptance differences between the resolved and boosted selection, in addition to the uncertainties related to the  $p_T^V$  extrapolation. The normalisation factor for events with  $p_T^V \geq 250 \text{ GeV}$  is not further split according to the jet multiplicity, given the limited amount of data in these regions. Instead, the relative difference between 2-jet and  $\geq 3$ -jet events is taken from simulation and extrapolation uncertainties are added that quantify the dependence of this difference on the MC generation settings.

For the  $t\bar{t}$  background in the 0- and 1-lepton channel, a separate normalisation factor is applied in the boosted region, because of the presence of the dedicated boosted top CR. This normalisation factor split between the resolved and boosted regions is further motivated by the different event topology and flavour composition of the selected  $t\bar{t}$  events, which are both a consequence of the different selection criteria. Below 400 GeV, separate normalisation factors are applied for each  $p_T^V$  and  $n_{\text{jet}}$  category. In the 2-lepton channel, the  $t\bar{t}$  contamination of the resolved regions is estimated from data. In the boosted 2-lepton region, the  $t\bar{t}$  contamination is negligible.

Uncertainties related to the signal modelling are treated as correlated between the two analysis regions of the combination. The uncertainties for the background modelling are treated as decorrelated between the two analysis regions, given that the two analyses follow different modelling approaches driven e.g. by the discriminants that are used in the fit (BDT output score vs.  $m_J$ ). An exception to this decorrelated modelling are nuisance parameters related to inclusive cross-section predictions of sub-leading backgrounds and the flavour composition of the  $V$ +jet backgrounds, which are fully correlated between the resolved and boosted regions.

Experimental systematic uncertainties are correlated between the two analyses whenever the same physics objects are used. This is the case e.g. for the triggering criteria, the used luminosity value and the lepton reconstruction, identification and isolation. Conversely the uncertainties related to flavour tagging are not correlated due to the usage of different jet collections, calorimeter jets vs. track jets. Even though the flavour tagging is performed using tracks and vertices, it relies to some extent on input variables from the jet collections, which prohibits a full correlation<sup>1</sup>. Similarly, uncertainties related to the small- $R$  and large- $R$  jets are kept uncorrelated as different calibration procedures are used.

---

<sup>1</sup>A proper treatment, correlating the underlying sources of uncertainty that enter the flavour-tagging uncertainty eigenvectors, has been performed and no impact the measurement was observed.

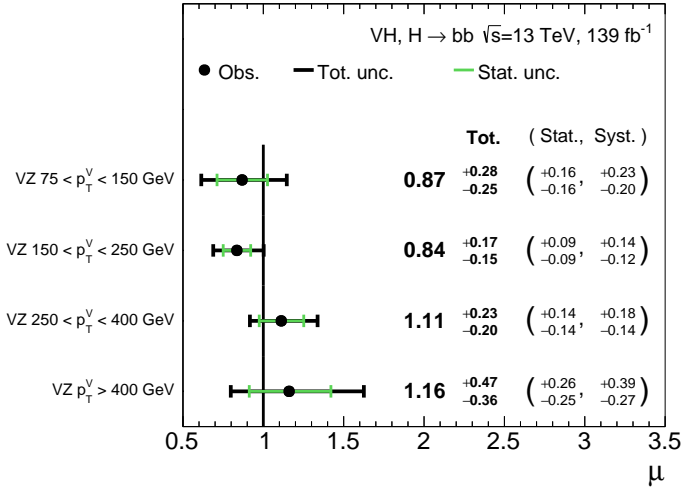


Figure 9.7: Observed  $VZ$  signal strengths obtained from the diboson cross-check fit of the resolved + boosted combination, decorrelated according to the reconstructed  $p_T^V$  regions.

### 9.1.4 $VZ$ cross-check measurement

Due to its similarity with the  $VH$  signal, the  $VZ$  process ( $WZ$  and  $ZZ$ ) is used as a validation of the analysis design. A  $VZ$  fit with a single signal strength parameter yields

$$\mu_{VZ}^{bb} = 0.96^{+0.15}_{-0.13} = 0.96^{+0.07}_{-0.07} (\text{stat.})^{+0.13}_{-0.11} (\text{syst.}) \quad , \quad (9.2)$$

which agrees with the SM prediction of unity and therefore validates the analysis strategy. Additionally, a cross-check fit is performed in which the  $VZ$  signal strength is decorrelated according to the reconstructed  $p_T^V$  regions that are considered in the analysis. The result of this fit is shown in Figure 9.7. All measured values are in good agreement with the SM prediction and with the results that were obtained from the  $VZ$  cross-checks of the individual analyses.

### 9.1.5 Measurement results

The resolved and boosted combination yields a  $VH, H \rightarrow b\bar{b}$  signal strength of

$$\mu_{VH}^{b\bar{b}} = 1.00^{+0.18}_{-0.17} = 1.00^{+0.12}_{-0.11} (\text{stat.})^{+0.14}_{-0.13} (\text{syst.}) \quad , \quad (9.3)$$

which agrees with the SM expectation of unity. Figure 9.8 shows post-fit distributions for the resolved signal regions with  $250 < p_T^V < 400\text{ GeV}$ , which are the regions that have been modified with respect to the standalone resolved analysis.

A good agreement between the measured data and the SM expectation is observed in all regions. Further post-fit plots for the remaining regions are found in Ref. [7] and are qualitatively similar to the post-fit plots of the individual resolved and boosted analyses.

When further splitting the  $VH$  signal into its  $WH$  and  $ZH$  components, separate signal strengths of

$$\mu_{WH}^{b\bar{b}} = 1.03_{-0.27}^{+0.28} = 1.03 \pm 0.19 \text{ (stat.)}_{-0.19}^{+0.21} \text{ (syst.)} \quad (9.4)$$

$$\mu_{ZH}^{b\bar{b}} = 0.97_{-0.23}^{+0.25} = 0.97 \pm 0.17 \text{ (stat.)}_{-0.15}^{+0.18} \text{ (syst.)} \quad (9.5)$$

are observed. Both signal strength are in good agreement with the SM prediction and the observed values from the resolved analysis. This is expected, given that the removal of the resolved events with  $p_T^V > 400$  GeV and their replacement by the corresponding region of the boosted analysis is only a small change with respect to the whole phase space that is probed by the resolved analysis. The observed correlation between the  $WH$  and  $ZH$  signal strengths is +2%.

The measured  $VH, V \rightarrow \text{leptons}$  cross-sections times the  $H \rightarrow b\bar{b}$  BR in each STXS category are plotted in Figure 9.9 and summarised in Table 9.1. The  $\sigma \times \text{BR}$  values, normalised by their SM expectation is shown in Figure 9.10, together with the correlation between the various PoIs. The measured cross-sections are in agreement with their SM expectation, with uncertainties ranging from 30% to 300% of the measured values, depending on the STXS category that is considered. The statistical component of the uncertainty is the leading single contribution to the total uncertainty in each STXS category. It includes the uncertainty due to background normalisations which are determined from data. A breakdown of the total uncertainty into physics categories is shown in Table 9.2. Especially in the STXS categories with  $p_T^{V,t} < 250$  GeV, systematic uncertainties related to small- $R$  jets or uncertainties from the modelling of the main backgrounds are sizeable. The correlations between the extracted cross-section values are of the order of a few percent for adjacent STXS categories, reaching up to -15% for the bins with  $p_T^{V,t} > 400$  GeV.

A comparison of the measured  $VH, V \rightarrow \text{leptons}$  cross-sections times the  $H \rightarrow b\bar{b}$  BR in each STXS category of the combination with the values obtained from the resolved and boosted analyses is shown in Figure 9.11. Good agreement is observed between the different measurements.

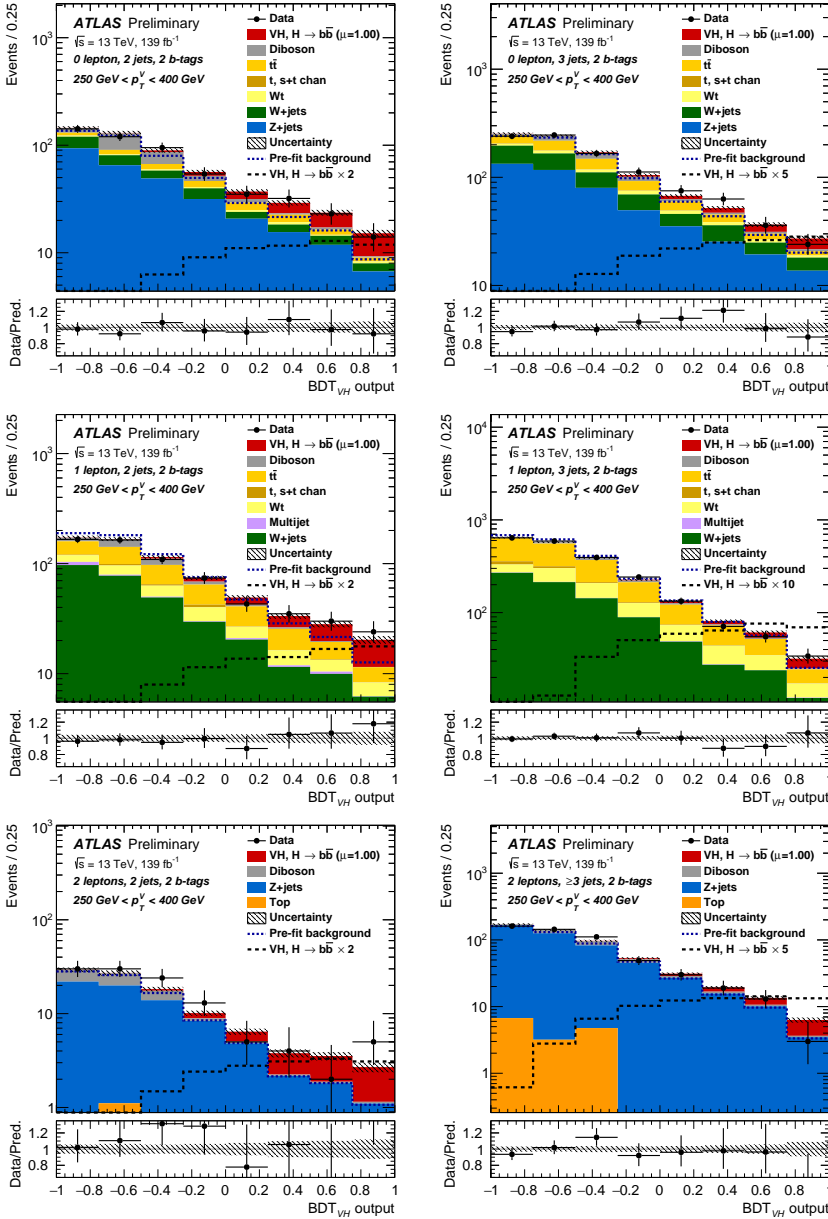


Figure 9.8: The BDT distribution after the profiled likelihood ratio fit to data for the signal regions with  $250 \text{ GeV} < p_T^V < 400 \text{ GeV}$  of the resolved regime. The left column shows 2-jet events, the right column shows events with  $(\geq)3$ -jet events for the 0- (top row), 1- (middle row) and 2-lepton channels (bottom row). Published in Ref. [7].

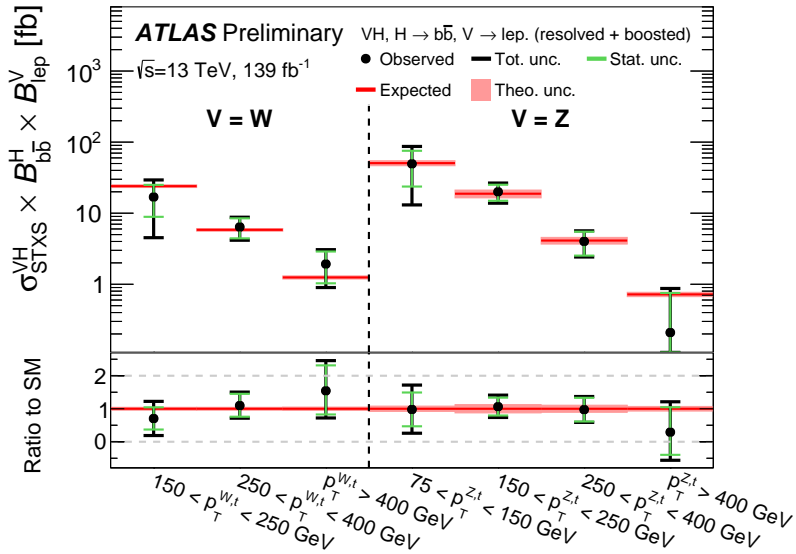


Figure 9.9: Measured  $VH$  simplified template cross-sections times the  $H \rightarrow b\bar{b}$  and  $V \rightarrow$  leptons branching fractions and comparison with their SM predictions. The values are obtained from the resolved + boosted analysis combination. Published in Ref. [7].

STXS region		SM prediction [fb]	Measurement [fb]	Stat. unc. [fb]	Syst. unc. [fb]		
Process	$p_T^{V, t}$ interval				Th. sig.	Th. bkg.	Exp.
$W(\ell\nu)H$	150–250 GeV	$24.0 \pm 1.1$	$16.9 \pm 12.4$	8.1	0.8	7.3	5.7
$W(\ell\nu)H$	250–400 GeV	$5.8 \pm 0.3$	$6.4 \pm 2.3$	2.0	0.3	0.9	0.6
$W(\ell\nu)H$	$> 400$ GeV	$1.3 \pm 0.1$	$1.9 \pm 1.1$	0.9	0.2	0.4	0.3
$Z(\ell\ell/\nu\nu)H$	75–150 GeV	$50.6 \pm 4.1$	$49.5 \pm 36.9$	25.9	6.3	18.5	20.6
$Z(\ell\ell/\nu\nu)H$	150–250 GeV	$18.8 \pm 2.4$	$20.0 \pm 6.4$	5.1	1.8	2.5	2.2
$Z(\ell\ell/\nu\nu)H$	250–400 GeV	$4.1 \pm 0.5$	$4.0 \pm 1.6$	1.5	0.4	0.4	0.3
$Z(\ell\ell/\nu\nu)H$	$> 400$ GeV	$0.7 \pm 0.1$	$0.2 \pm 0.6$	0.5	0.1	0.3	0.2

Table 9.1: Measured  $VH$  simplified template cross sections times the  $H \rightarrow b\bar{b}$  and  $V \rightarrow$  leptons branching fractions and comparison with their SM predictions. Published in Ref. [7].

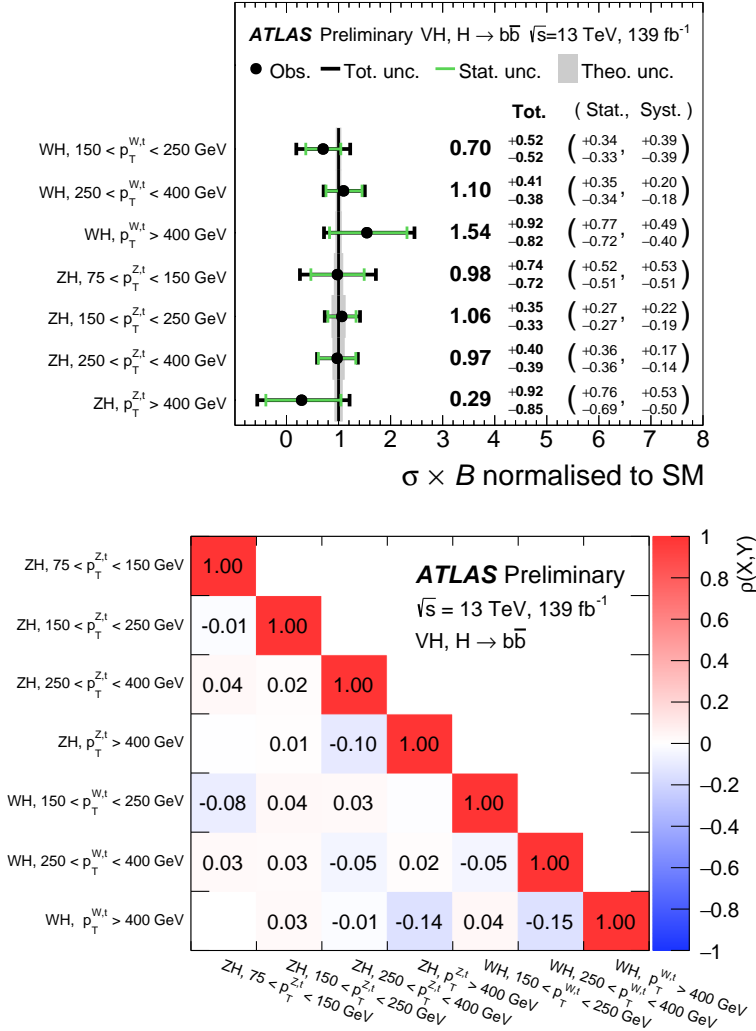


Figure 9.10: Top: Measured values of the simplified template  $VH, H \rightarrow b\bar{b}$  cross-sections, normalised to the SM expectation. The grey error bands correspond to the theoretical uncertainty on the normalised  $\sigma \times BR$  values. Bottom: Observed correlations between the measured cross-sections. Published in Ref. [7].

Category	$WH, 150 - 250$	$WH, 250 - 400$	$WH, > 400$	$ZH, 75 - 150$	$ZH, 150 - 250$	$ZH, 250 - 400$	$ZH, > 400$
Total	0.52	0.40	0.87	0.73	0.34	0.39	0.89
Statistical	0.34	0.35	0.74	0.51	0.27	0.36	0.72
Systematic	0.39	0.19	0.45	0.52	0.20	0.16	0.51
Statistical uncertainties							
Data stat only	0.31	0.32	0.69	0.43	0.25	0.33	0.70
Floating normalisations	0.18	0.10	0.22	0.21	0.11	0.10	0.17
$t\bar{t}$ $e\mu$ control region	0.03	<0.01	0.01	0.23	0.04	0.08	<0.01
Experimental uncertainties							
Total experimental	0.24	0.10	0.22	0.41	0.12	0.07	0.28
$\hookrightarrow$ lepton	0.03	0.02	0.05	0.03	<0.01	0.01	0.01
$\hookrightarrow E_{T}^{\text{miss}}$	0.17	<0.01	0.02	0.24	0.03	0.01	0.02
$\hookrightarrow$ Small- $R$ jets	0.12	0.07	0.09	0.28	0.07	0.04	0.05
$\hookrightarrow$ Large- $R$ jets	<0.01	<0.01	0.14	<0.01	<0.01	<0.01	0.26
$\hookrightarrow$ Calo $b$ -tagging ( $b$ -jets)	0.05	0.02	0.01	0.18	0.08	0.05	0.02
$\hookrightarrow$ Calo $b$ -tagging ( $c$ -jets)	0.10	0.06	0.02	0.02	0.02	<0.01	<0.01
$\hookrightarrow$ Calo $b$ -tagging (light-flavour jets)	<0.01	<0.01	0.01	0.01	0.01	0.02	<0.01
$\hookrightarrow$ Calo $b$ -tagging (extrap. from charm)	<0.01	<0.01	<0.01	<0.01	<0.01	<0.01	<0.01
$\hookrightarrow$ VR $b$ -tagging ( $b$ -jets)	<0.01	0.02	0.11	<0.01	<0.01	<0.01	0.04
$\hookrightarrow$ VR $b$ -tagging ( $c$ -jets)	<0.01	<0.01	0.03	<0.01	<0.01	<0.01	0.02
$\hookrightarrow$ VR $b$ -tagging (light-flavour jets)	<0.01	<0.01	0.02	<0.01	<0.01	<0.01	0.06
$\hookrightarrow$ VR $b$ -tagging (extrap. from charm)	<0.01	<0.01	0.02	<0.01	<0.01	<0.01	<0.01
$\hookrightarrow$ Pile-up	0.02	<0.01	0.01	0.05	<0.01	<0.01	<0.01
$\hookrightarrow$ Luminosity	0.02	0.02	0.03	0.01	0.02	0.01	0.02
Theoretical and modelling uncertainties							
Signal	0.03	0.05	0.13	0.13	0.10	0.09	0.07
Backgrounds	0.30	0.15	0.36	0.37	0.13	0.11	0.42
$\hookrightarrow$ single top	0.12	0.09	0.13	0.05	0.01	0.02	0.01
$\hookrightarrow t\bar{t}$	0.16	0.03	0.14	0.10	0.04	0.03	0.04
$\hookrightarrow W$ +jets	0.18	0.07	0.12	0.02	0.02	0.01	0.04
$\hookrightarrow Z$ +jets	0.05	0.02	0.08	0.29	0.09	0.06	0.33
$\hookrightarrow$ Diboson	0.04	0.04	0.04	0.09	0.05	0.04	0.08
$\hookrightarrow$ Multi-jet	<0.01	0.01	0.04	<0.01	<0.01	<0.01	0.01
$\hookrightarrow$ MC statistical	0.12	0.09	0.21	0.17	0.06	0.07	0.22

Table 9.2: Breakdown of the contributions to the uncertainty in the cross-section for the three WH and four ZH STXS measurements. The sum in quadrature of the systematic uncertainties attached to the categories differs from the total systematic uncertainty due to correlations. The uncertainty is divided by the SM predictions.



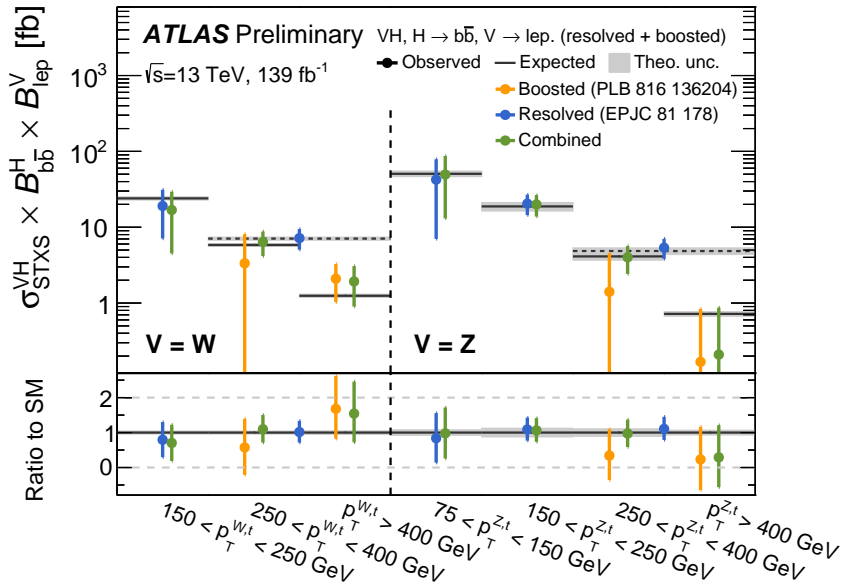


Figure 9.11: Measured  $VH$  simplified template cross-sections times the  $H \rightarrow b\bar{b}$  and  $V \rightarrow \text{leptons}$  branching fractions and comparison with their SM predictions. The values from the resolved + boosted analysis combination [7] (green) are compared to the values from the resolved analysis [6] (blue) and the boosted analysis [5] (orange). Published in Ref. [7].

### 9.1.6 Constraints on effective interactions

As suggested in Ref. [261], additional STXS categories at high  $p_T^{V,t}$  can enhance the sensitivity to a variety of new physics scenarios. In order to benchmark the gain from the additional differential information through the resolved + boosted combination, the combination is used to constrain effective interactions of a SMEFT. These constraints are then compared to the ones obtained from the individual analyses to quantify the improvement. Effective operators with mass dimension 6 are added to the SM Lagrangian and their impact on the  $VH, H \rightarrow b\bar{b}$  signal is evaluated following the methodology described in Chapter 8. Results are shown for both the case when considering only the BSM-SM interference (linear terms) and when including the pure BSM contributions (linear + quadratic terms).

Three operators that induce a  $p_T^{V,t}$ -dependent modification of the signal cross-section are considered:  $\mathcal{Q}_{Hq}^3$ , which shows a strong  $p_T^{V,t}$ -dependent effect for both the  $WH$  and  $ZH$  processes,  $\mathcal{Q}_{Hu}$  which also shows a strong  $p_T^{V,t}$  dependence but only affects  $ZH$  and  $\mathcal{Q}_{HW}$ , which mainly leads to an overall change in the  $WH$  and  $ZH$  cross-section with a slight  $p_T^V$  dependence. The effect that these operators have on the seven STXS categories that the combination analysis measures is shown in Figure 9.12 for both the linear and the linear + quadratic parameterisation. The value of the Wilson coefficients for which the effect is visualised is similar to the upper end of the expected 95% confidence interval obtained from the combination. The two plots also illustrate the advantage of having the additional differential information at high  $p_T^{V,t}$  by comparing the operator effect in the STXS categories with  $250 \text{ GeV} < p_T^{V,t} < 400 \text{ GeV}$  and  $p_T^{V,t} > 400 \text{ GeV}$  to the effect on an inclusive category with  $p_T^{V,t} > 250 \text{ GeV}$ , as considered by the resolved analysis. The less precise cross-section measurement for the category with  $p_T^{V,t} > 400 \text{ GeV}$  is compensated by the larger relative deviation with respect to the SM at the same Wilson coefficient value.

Profile likelihood-ratio scans are performed as a function of one or two Wilson coefficients to benchmark the improvements from the combination. Wilson coefficients that are not scanned over are fixed at their SM expectation of zero. Figure 9.13 shows both the expected and observed profile likelihood ratio contours for the  $c_{Hq}^{(3)}$  coefficient for the linear and the linear + quadratic parameterisations and compares them to the results obtained from the resolved and boosted analyses. In both cases, the combination leads to a narrower likelihood shape which corresponds to a better constraint on the SMEFT effect. Furthermore, in the case of the linear + quadratic parameterisation, the combination removes the second local minimum at negative values of  $c_{Hq}^{(3)}$ . A summary of the expected and observed confidence intervals at 68% and 98% CL for the three operators that are considered is shown in Figure 9.14 and compared to the intervals obtained from the resolved and boosted analyses. The combination tightens the individual intervals, especially for the Wilson coefficients that correspond to operators with  $p_T^{V,t}$ -dependent effects and when considering also quadratic terms in the parameterisation of the SMEFT effects.

Figures 9.15 and 9.16 show the expected and observed profile likelihood ratio

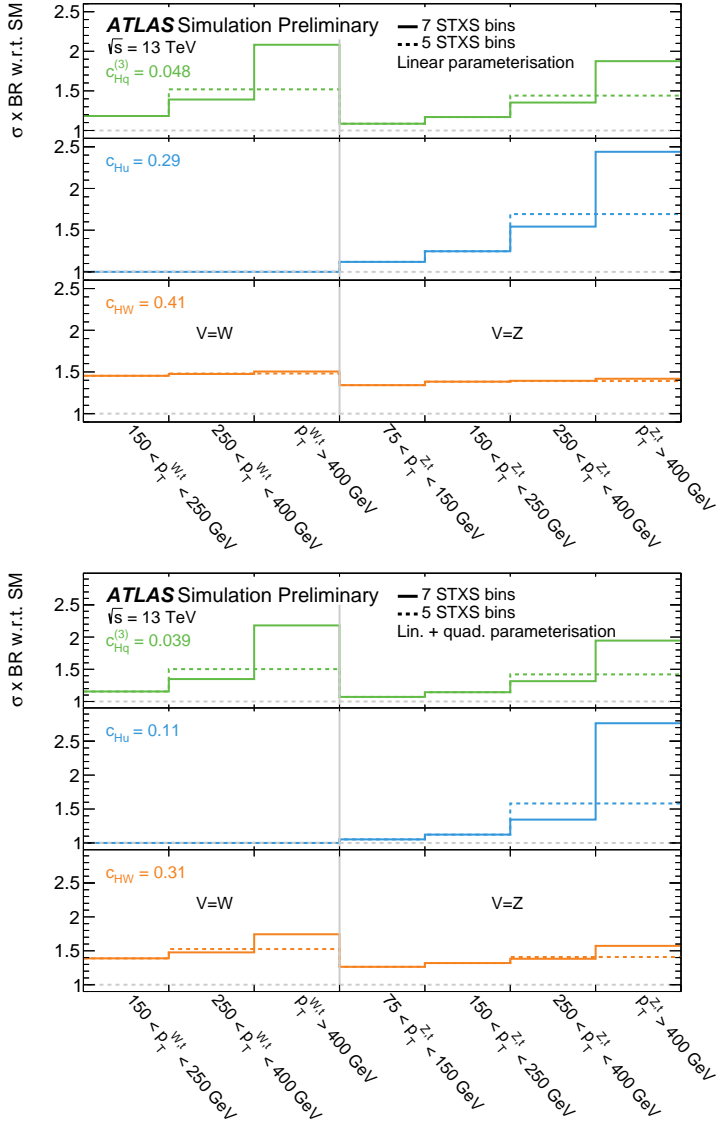


Figure 9.12: The predicted modification of the signal  $\sigma \times \text{BR}$  in the STXS regions considered in the analysis for the three operators  $\mathcal{Q}_{Hq}^3$ ,  $\mathcal{Q}_{Hu}$  and  $\mathcal{Q}_{HW}$ . The solid line illustrates the case where each STXS bin receives an independent parameterisation (7 STXS bins). For the dotted line, a common parameterisation is computed for the  $p_T^{V,t} > 250 \text{ GeV}$  (5 STXS bins). The values chosen for the Wilson coefficient correspond to the upper end of the expected 95% confidence interval obtained by the combination analysis. Published in Ref. [7].

contours at 95% CL for 2D scans of  $c_{Hq}^{(3)}$  vs.  $c_{HW}$ , and  $c_{Hq}^{(3)}$  vs.  $c_{Hu}$ , respectively. The contours from the combination are compared to the ones obtained from the individual resolved and boosted analyses. The correlation between the two operators differs between the analyses and the combination leads to smaller contours. The additional differential information helps to distinguish constant from linear from quadratic effects in  $p_T^{V,t}$ . This distinction power will become especially useful in global fits, where currently the number of coefficients that can be fit simultaneously is limited due to large correlations between them. An example of such a fit that uses the  $VH, H \rightarrow b\bar{b}$  combination as an input is given in Section 9.1.7.

With the increased  $p_T^V$  reach of the combination analysis, the validity of the dimension-6 truncated SMEFT expansion approach is challenged, especially for  $p_T^{V,t}$ -dependent effects. What to do in such cases is still subject to ongoing discussions. Three approaches are conventionally considered:

1. Restricting the range of UV-complete models for which the extracted constraints apply a posteriori.
2. Introducing one or multiple upper cuts on the energy range that is probed in the analysed events and presenting the limits as a function of these upper cuts. The upper cuts exclude regions where higher order contributions of  $\mathcal{O}(\Lambda^{-4})$ , which are neglected in the current SMEFT truncation, might be sizeable [265, 266].
3. Including theory uncertainties into the likelihood fit that account for the uncertainty due to the missing higher order SMEFT contributions.

The first approach has the caveat that it goes against the spirit of SMEFT, which aims at publishing limits that are as universally valid as possible.

The second approach is not favourable from an experimentalist point of view as it would require a redesign of the analysis, introducing an upper cut on the momentum transfer in  $VH$  events, i.e. on  $\sqrt{\hat{s}} = m_{VH}$ .

Instead, the STXS framework allows to restrict the interpretation to certain STXS categories. In the case of  $VH, H \rightarrow b\bar{b}$ , it is possible to place an upper cut on the  $p_T^{V,t}$  of the events that are used for the interpretation. This represents a quasi-cut on the upper energy of the events that are used for the interpretation, because  $p_T^{V,t}$  is strongly correlated with  $m_{VH}$ . Figure 9.17 demonstrates this procedure for a cut at  $p_T^{V,t} = 400$  GeV. The combination analysis has an increased number of STXS categories at high  $p_T^{V,t}$  for which cross-sections are measured with respect to the individual  $VH, H \rightarrow b\bar{b}$  measurements. This increases the number of potential upper cuts that can be considered, depending on the model that is to be constrained. This binned approach is by no means limited to  $p_T^{V,t}$  and different binnings, e.g. directly in  $m_{VH}$  or multi-dimensional binnings that include angular observables can be considered, too.

The third approach is simpler than the second approach because it does not require to perform the interpretation for (multiple) upper cuts on the energy range of the

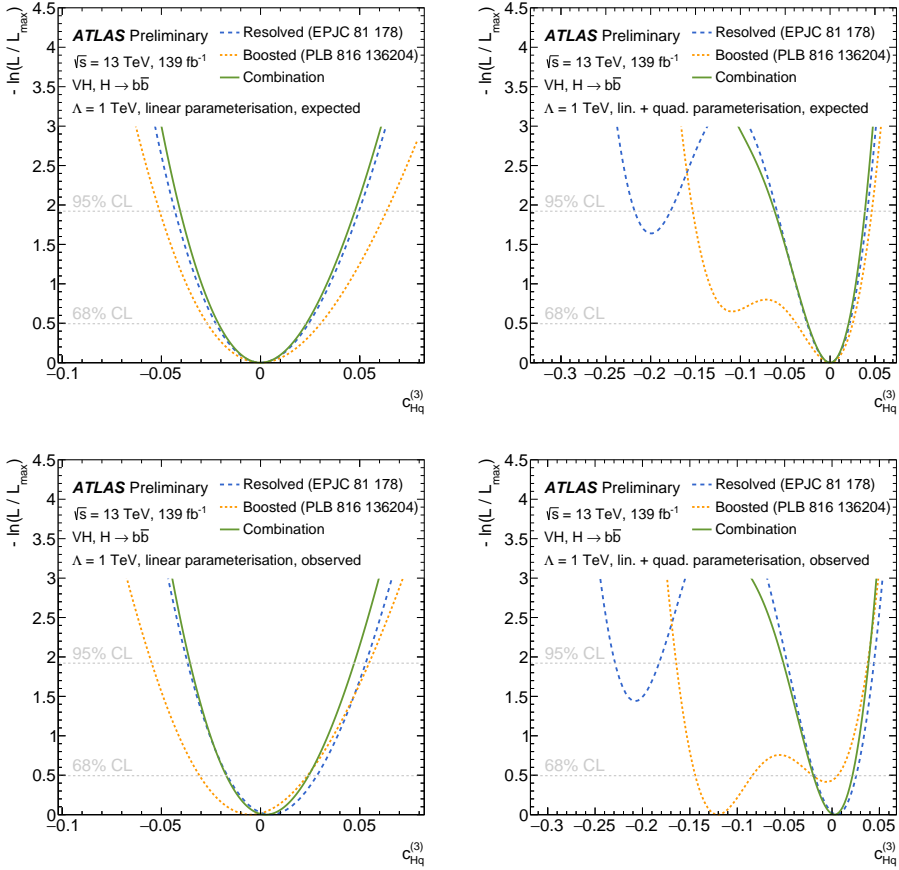


Figure 9.13: Scanned profile of the expected (top row) and observed (bottom row) negative log-likelihood-ratio as a function of the Wilson coefficient  $c_{Hq}^{(3)}$ . The scans are performed using either a linear parameterisation of the  $VH$  production cross-section, the partial  $H \rightarrow b\bar{b}$  decay width, as well as the total width of the Higgs boson (left), or a parameterisation including quadratic terms (right). The value of all other Wilson coefficients is fixed to their SM expectation of zero. The profile obtained from the combination analysis [7] is shown in green, the one from the resolved analysis [6] in blue and the profile from the boosted analysis [5] in orange. The 68% and 95% CL thresholds are indicated. Published in Ref. [7].

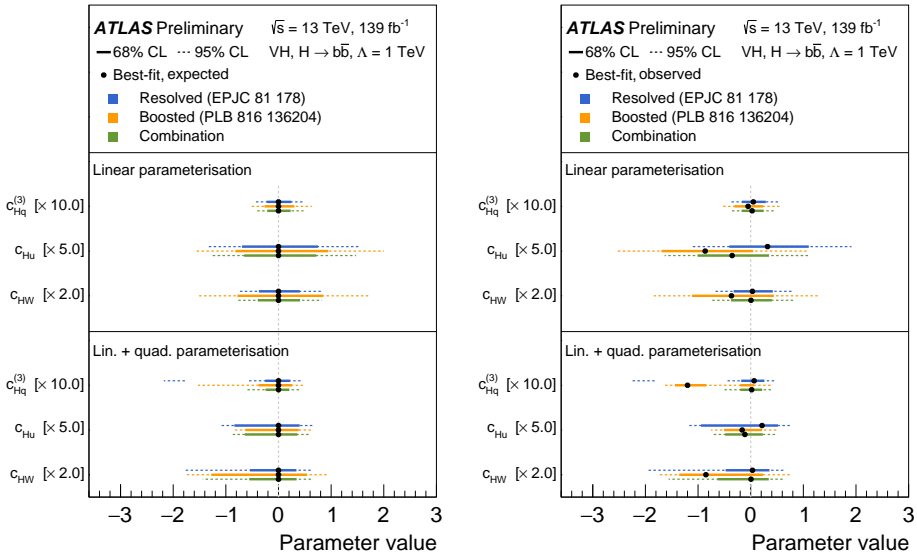


Figure 9.14: Summary of expected (left) and observed (right) confidence intervals at 68% and 95% CL from profile likelihood ratio scans as a function of either  $c_{Hq}^{(3)}$ ,  $c_{Hu}$  or  $c_{HW}$ . Only one Wilson coefficient is varied at a time and the remaining ones are fixed to their SM prediction at zero. The intervals obtained from the combination [7] are shown in green, the resolved intervals [6] in blue and the boosted intervals [5] in orange. Published in Ref. [7].

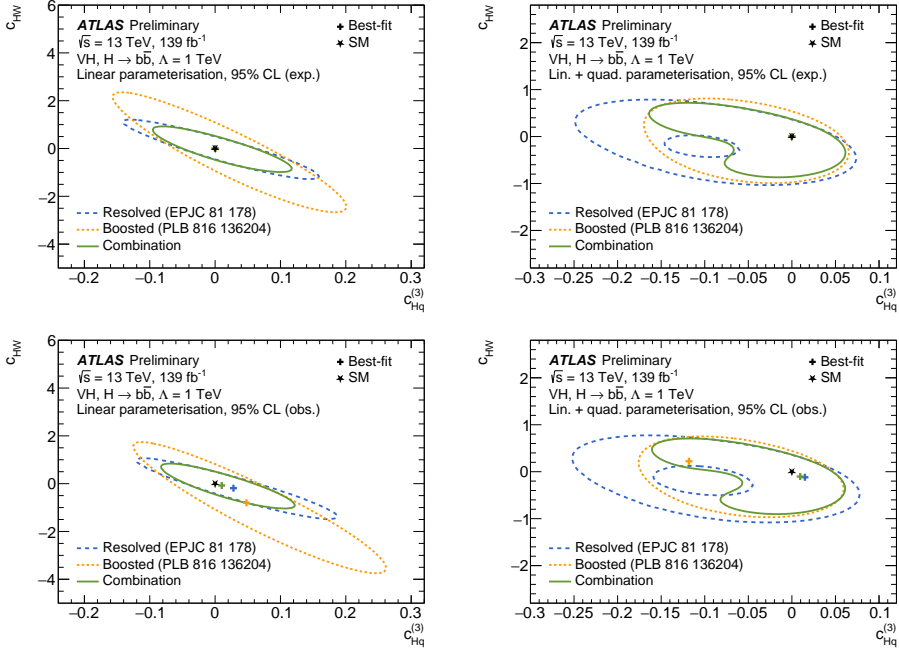


Figure 9.15: Expected (top row) and observed (bottom row) contours of the confidence interval at 95% CL as a function of the two Wilson coefficients  $c_{Hq}^{(3)}$  and  $c_{HW}$ . The contribution of other Wilson coefficients is fixed to their SM expectation at zero. Contours are obtained both from a linear parameterisation of  $\sigma \times \text{BR}$  (left) and when including the quadratic terms (right). The best fit point is marked with a cross. The contour obtained from the combination analysis [7] is shown in green, the one from the resolved analysis [6] in blue and the contour from the boosted analysis [5] in orange. Published in Ref. [7].

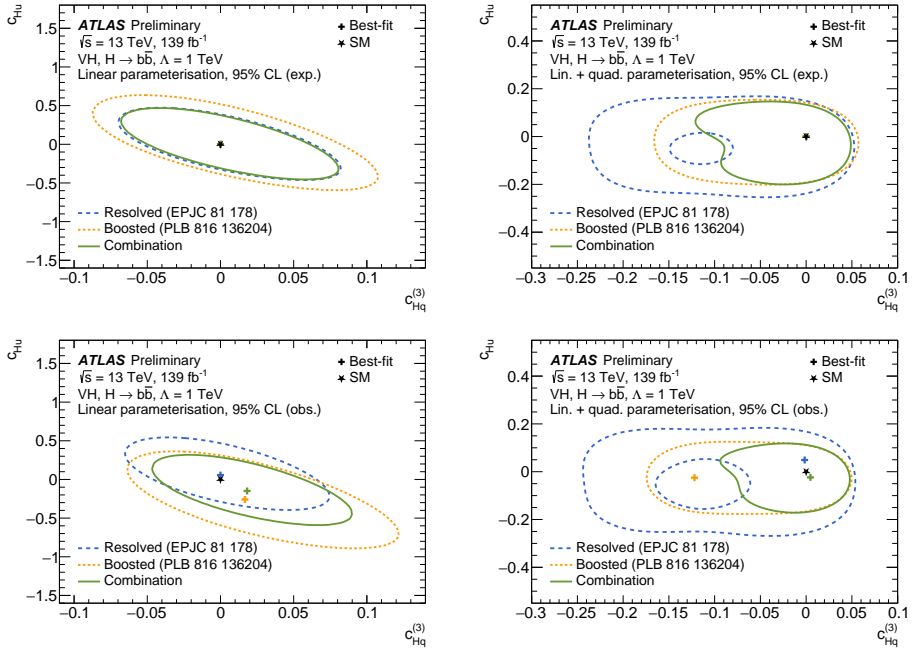


Figure 9.16: Expected (top row) and observed (bottom row) contours of the confidence interval at 95% CL as a function of the two Wilson coefficients  $c_{Hq}^{(3)}$  and  $c_{Hu}$ . The contribution of other Wilson coefficients is fixed to their SM expectation at zero. Contours are obtained both from a linear parameterisation of  $\sigma \times \text{BR}$  (left) and when including the quadratic terms (right). The best fit point is marked with a cross. The contour obtained from the combination analysis [7] is shown in green, the one from the resolved analysis [6] in blue and the contour from the boosted analysis [5] in orange. Published in Ref. [7].



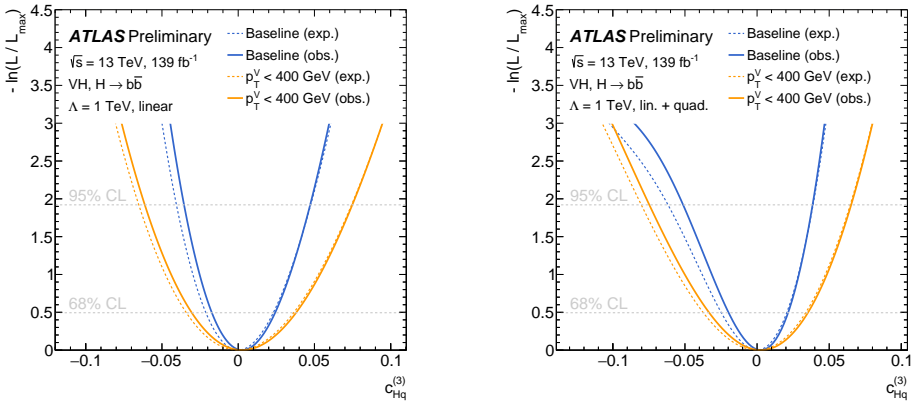


Figure 9.17: Profiled negative log-likelihood ratio scan as a function of the Wilson coefficient  $c_{Hq}^{(3)}$  when considering the full combination (blue) and when only parameterising the cross-section for  $p_T^V < 400$  GeV, which effectively restricts the energy range that is used for the interpretation. The solid lines show the observed contours, whereas the dashed lines indicate the expected ones. The left plot shows the results when only the linear parameterisation is used and the right plot is obtained by including the quadratic terms. Published in Ref. [7].

measurement. Instead, only one likelihood fit is required. However, the problem is shifted to the question of how to reliably estimate the uncertainties due to missing higher order terms [267]. Furthermore, these truncation uncertainties are folded into the measurement and once updated calculations become available, the measurement has to be redone.

### 9.1.7 Inclusion in the ATLAS-wide combination of Higgs boson measurements

The combination of  $VH, H \rightarrow b\bar{b}$  measurements is subsequently used as input to ATLAS-wide combinations of Higgs boson measurements. Figure 9.18 shows differential measurements of Higgs boson production cross-sections in the STXS framework that are obtained from a global fit to measurements of  $H \rightarrow \gamma\gamma$ ,  $H \rightarrow ZZ^*$ ,  $H \rightarrow WW^*$ ,  $H \rightarrow \tau\tau$  and  $H \rightarrow b\bar{b}$  [4]. The usage of the  $VH, H \rightarrow b\bar{b}$  combination within the global combination allows also there an exclusive cross-section measurement for  $p_T^V > 400$  GeV. Furthermore, the precision of the  $qq \rightarrow H\ell\nu$  and  $qq \rightarrow H\ell\ell$  measurements with  $p_T^V > 150$  GeV is dominated by the  $VH, H \rightarrow b\bar{b}$  combination. Similarly, in the ATLAS-wide SMEFT interpretation of Higgs boson measurements, shown in Figure 9.19, the sensitivity to the  $c_{Hq}^{(3)}$  Wilson coefficient, which parameterises  $VH$  cross-section changes that grow quadratically with  $p_T^V$ , is nearly exclusively determined by the  $VH, H \rightarrow b\bar{b}$  combination.

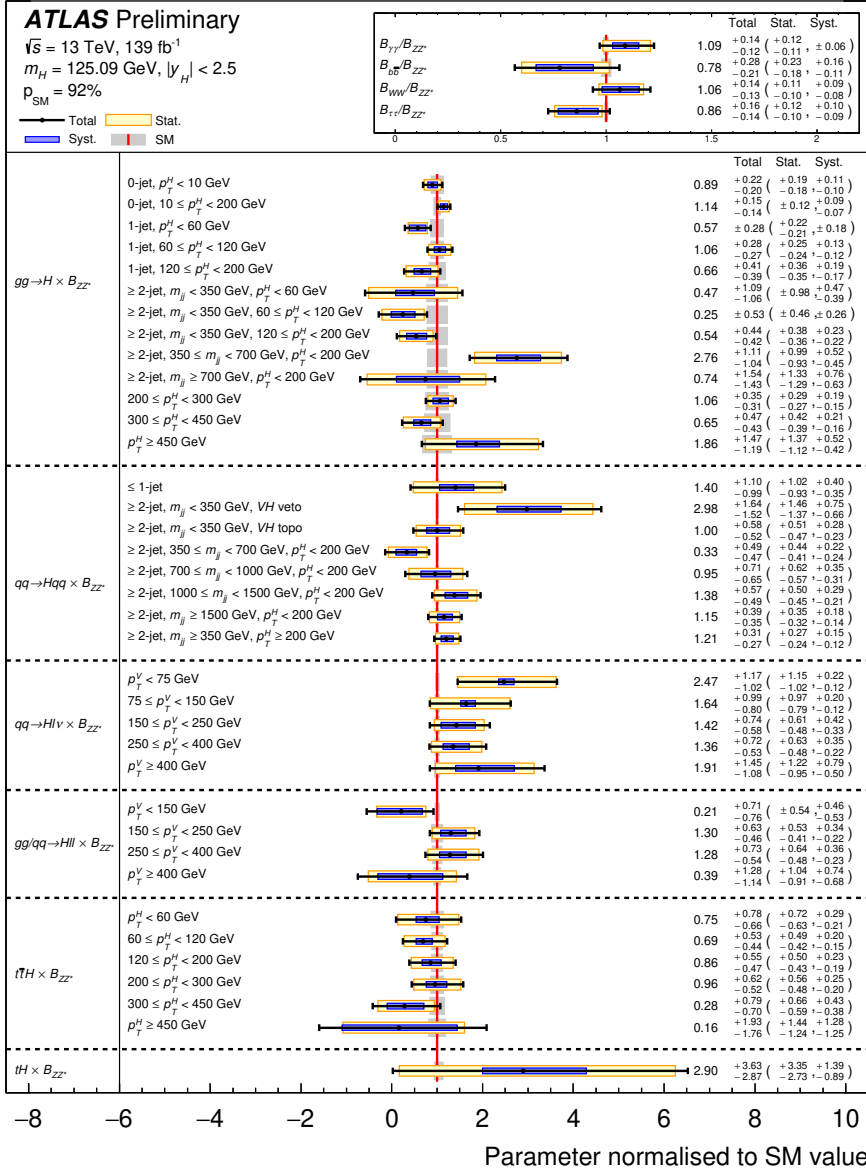


Figure 9.18: Cross-section measurements in STXS categories obtained from a combination of Higgs boson measurements and normalised to their SM predictions. For all the cross-section measurements, the  $H \rightarrow ZZ^*$  branching ratio is used as a common reference and the ratios of branching ratios  $B_f/B_{ZZ^*}$  are shown on the top of the plot. Taken from Ref. [4].

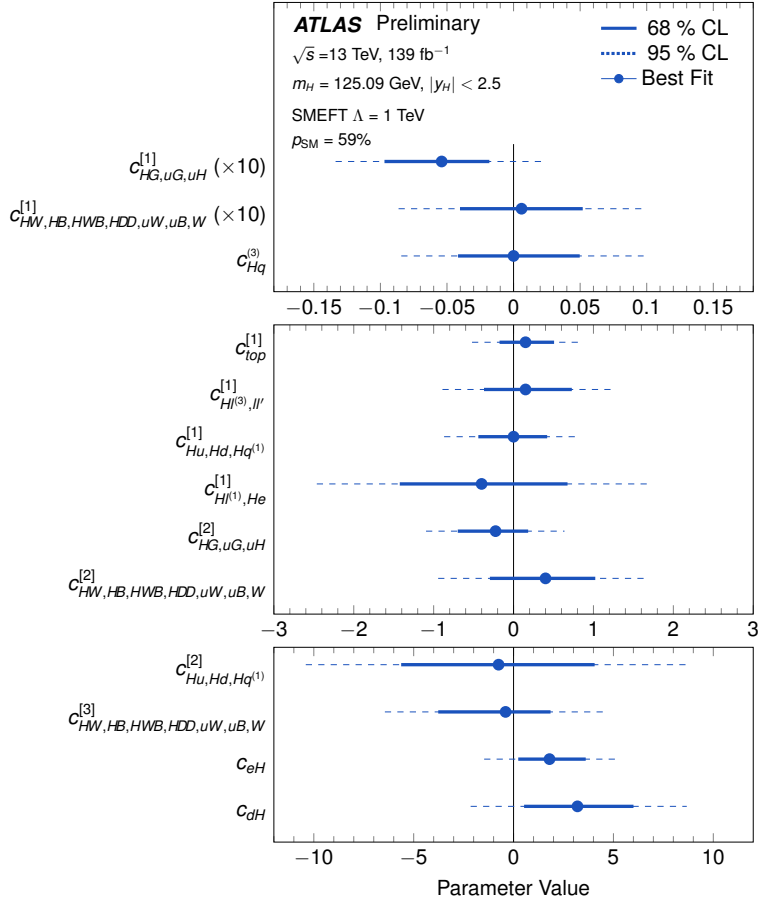


Figure 9.19: Summary of observed confidence intervals at 65% and 95% CL, together with the best fit value of combinations of Wilson coefficients. The measurements are obtained from a combination of Higgs boson measurements. Only linear terms proportional to  $\Lambda^{-2}$  are included when parameterising the SMEFT effects. Taken from Ref. [4].

## 9.2 Combination of $VH, H \rightarrow b\bar{b}$ and $VH, H \rightarrow c\bar{c}$

The  $VH, H \rightarrow b\bar{b}$  and  $VH, H \rightarrow c\bar{c}$  processes lead to similar detector signatures. At leading order in both cases, two jets from the Higgs boson decay recoil in the transverse plane against the (leptonic) signatures from the  $V$ -boson decay. Flavour tagging is used to distinguish the  $b$ -jets from the  $c$ -jets and to keep the two processes apart. However, because flavour tagging is not perfect, there is a cross-contamination of  $b$ -jets that are wrongly labelled as  $c$ -jets and vice versa. As a consequence,  $VH, H \rightarrow b\bar{b}$  events enter the SRs of the  $VH, H \rightarrow c\bar{c}$  analysis and  $VH, H \rightarrow c\bar{c}$  events enter the SRs of the  $VH, H \rightarrow b\bar{b}$  analysis. This section presents a combination of the resolved  $VH, H \rightarrow b\bar{b}$  analysis described in Section 9.1.1 and an analysis targeting  $VH, H \rightarrow c\bar{c}$  decays. The combination allows to measure both processes consistently across the two analyses and is used to set model-independent constraints on the ratio of the Higgs coupling to  $c$ -quarks and  $b$ -quarks.

### 9.2.1 The $VH, H \rightarrow c\bar{c}$ analysis

This section introduces the  $VH, H \rightarrow c\bar{c}$  analysis. A detailed description of the analysis is given in Ref. [8].

To maximise trigger efficiency and signal purity, similar to the  $VH, H \rightarrow b\bar{b}$  analysis, only leptonic decays of the vector boson are considered. Depending on the number of charged leptons in the final state, events are categorised into a 0-, 1- and 2-lepton channel targeting  $ZH \rightarrow \nu\nu c\bar{c}$ ,  $WH \rightarrow \ell\nu c\bar{c}$  and  $ZH \rightarrow \ell\ell c\bar{c}$ , respectively. The Higgs boson decay is captured with two separate calorimeter jets with a radius parameter of  $R = 0.4$ . To achieve orthogonality with  $VH, H \rightarrow b\bar{b}$ , the  $c$ -tagging of jets is performed in combination with a  $b$ -veto that uses the same tagger and working point as the  $VH, H \rightarrow b\bar{b}$  analysis. Signal candidate events that have one or two such  $c$ -tagged and  $b$ -vetoed jets are considered in the analysis. Dedicated event selection criteria are applied to reduce the background contamination that arises from  $W$ +jets,  $Z$ +jets,  $t\bar{t}$ , single-top and QCD multijet production. Because of its similarity with the  $VH$  signal, the diboson process is used to validate the analysis strategy. The analysis signal regions are further split according to the  $p_T^V$  and the number of additional jets in the event. Dedicated control regions are constructed to constrain the normalisations and shapes of the main backgrounds and a binned profile-likelihood fit to both signal and control regions is used to extract the  $VH, H \rightarrow c\bar{c}$  signal. The invariant dijet mass is used as a fit discriminant in the signal regions, where the signal is expected to peak at the Higgs boson mass. The signal strengths for diboson processes involving at least one final state  $c$ -quark are extracted together with the  $VH, H \rightarrow c\bar{c}$  signal strengths. They are in agreement with the SM prediction within uncertainties, which validates the analysis strategy.

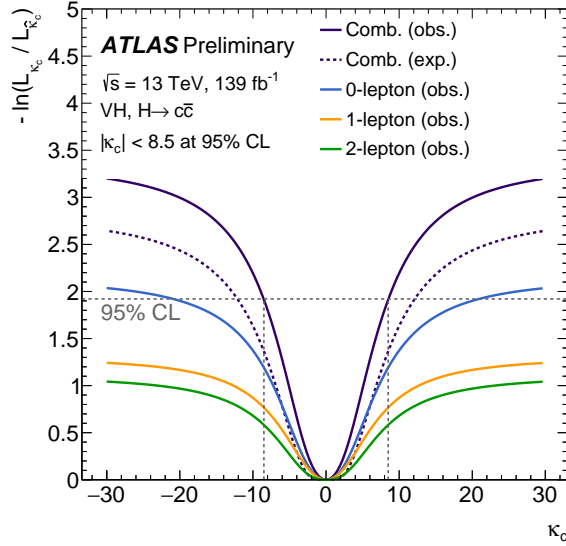


Figure 9.20: Profile likelihood ratio scan as a function of  $\kappa_c$  for a combined fit to all three lepton channels of the analysis. The individual contours per lepton channel are obtained from a combined fit with separate signal strengths. Published in Ref. [8].

The best-fit  $VH, H \rightarrow c\bar{c}$  signal strength is measured to be

$$\mu_{VH}^{c\bar{c}} = -9 \pm 15 = -9 \pm 10 \text{ (stat.)} \pm 12 \text{ (syst.)} \quad , \quad (9.6)$$

and an upper limit of 26 times the SM prediction is set at 95% CL using the CL<sub>s</sub> method [268].

The measurement is further used to place constraints on modified values of the Higgs to  $c$ -quark coupling within the  $\kappa$  framework. Assuming only a modified Higgs to  $c$ -quark coupling  $\kappa_c$  and not considering any Higgs boson decays to BSM particles, the signal strength is reparameterised as

$$\mu_{VH}^{c\bar{c}} = \frac{\kappa_c^2}{1 - \text{BR}(H \rightarrow c\bar{c}) + \text{BR}(H \rightarrow c\bar{c}) \kappa_c^2} \quad , \quad (9.7)$$

where  $\text{BR}(H \rightarrow c\bar{c}) = 2.89\%$  is the SM value of the  $H \rightarrow c\bar{c}$  branching ratio [67]. A profile likelihood-ratio scan as a function of  $\kappa_c$  is shown in Figure 9.20. Under the aforementioned assumptions, the measurement excludes values of  $|\kappa_c| > 8.5$  at 95% CL. The combination presented in this section allows interpretations that rely on less assumptions.

Tagger working point	Tagging efficiency			
	$b$ -jets	$c$ -jets	$\tau$ -jets	light jets
$b$ -tagging of the $VH, H \rightarrow b\bar{b}$ analysis	70%	11%	1.6%	0.2%
$c$ -tagging and $b$ -tag veto of the $VH, H \rightarrow c\bar{c}$ analysis	8%	27%	25%	1.6%

Table 9.3: Expected tagging efficiencies for the flavour taggers used in the  $VH, H \rightarrow b\bar{b}$  and  $VH, H \rightarrow c\bar{c}$  analyses for jets with different flavours. The values are obtained from simulated jets and represent an average over all the jets in a simulated 1-lepton  $t\bar{t}$  sample.

### 9.2.2 The signal cross-contamination

Due to the different branching ratios of  $H \rightarrow b\bar{b}$  and  $H \rightarrow c\bar{c}$ , there are about 20 times more  $VH, H \rightarrow b\bar{b}$  events expected to be produced in the  $pp$  collisions than  $VH, H \rightarrow c\bar{c}$  events. The two analyses apply dedicated flavour-tagging algorithms to select  $H \rightarrow b\bar{b}$  and  $H \rightarrow c\bar{c}$  candidates. The expected efficiency for a jet of a certain flavour to pass the flavour-tagging working point of each analysis is shown in Table 9.3.

The  $b$ -tagging of the  $VH, H \rightarrow b\bar{b}$  analysis is performed at an operating point that has a 70% efficiency for true  $b$ -jets and a mistagging efficiency for true  $c$ -jets of 11%. Given that the SRs require events with two  $b$ -tagged jets, the expected fraction of  $VH, H \rightarrow c\bar{c}/VH, H \rightarrow b\bar{b}$  in the  $VH, H \rightarrow b\bar{b}$  analysis is about 0.2%. The cross-contamination is shown on a selection of post-fit plots of the BDT score for the  $VH, H \rightarrow b\bar{b}$  SRs in Figure 9.21. The BDT output score shapes of the  $VH, H \rightarrow c\bar{c}$  and  $VH, H \rightarrow b\bar{b}$  processes are roughly similar for the SRs in the 2-lepton channel. In the 0- and 1-lepton channels, the tagger score of the jets is used as an input variable to the BDT, which leads to a stronger difference between the output scores of the two processes.

The  $c$ -tagging +  $b$ -veto that is used in the  $VH, H \rightarrow c\bar{c}$  analysis has a 27% efficiency for true  $c$ -jets and a mistagging efficiency for true  $b$ -jets of 8%. These efficiencies are closer together compared to the efficiency differences in the  $VH, H \rightarrow b\bar{b}$  analysis. The  $VH, H \rightarrow c\bar{c}$  analysis also uses events where only one jet is  $c$ -tagged. Together with the larger BR, it follows that the  $VH, H \rightarrow b\bar{b}$  contamination in the  $VH, H \rightarrow c\bar{c}$  analysis is more important than vice versa. The number of  $VH, H \rightarrow b\bar{b}$  events that are categorised into the  $VH, H \rightarrow c\bar{c}$  SRs are two to seven times larger than the actual  $VH, H \rightarrow c\bar{c}$  signal. The cross-contamination is shown on a selection of post-fit plots of the invariant dijet mass for the  $VH, H \rightarrow c\bar{c}$  SRs in Figure 9.22. The mass peaks for both processes are similar in shape, although the  $VH, H \rightarrow b\bar{b}$  events peak at lower dijet mass values because  $b$ -hadron decay chains are more likely to feature leptonic decays, which produce neutrinos.

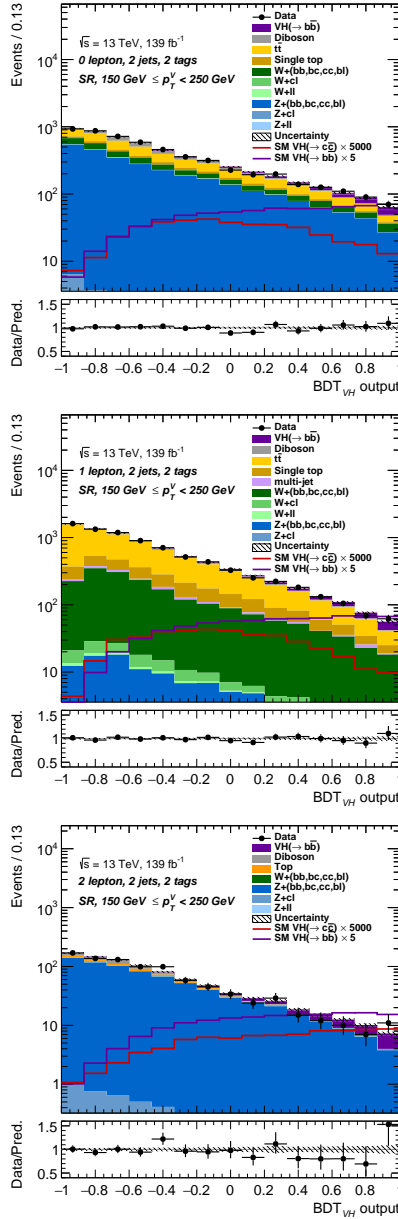


Figure 9.21: Post-fit distributions of the BDT score in the SRs of the  $VH, H \rightarrow b\bar{b}$  analysis in the 0- (top), 1- (middle) and 2-lepton channel (bottom). Only the regions with exactly two jets, which also pass the  $b$ -tagging working point, are shown. The magnified  $VH, H \rightarrow c\bar{c}$  signal is shown in red and to be compared to the  $VH, H \rightarrow b\bar{b}$  signal in violet. Different magnification factors are used.

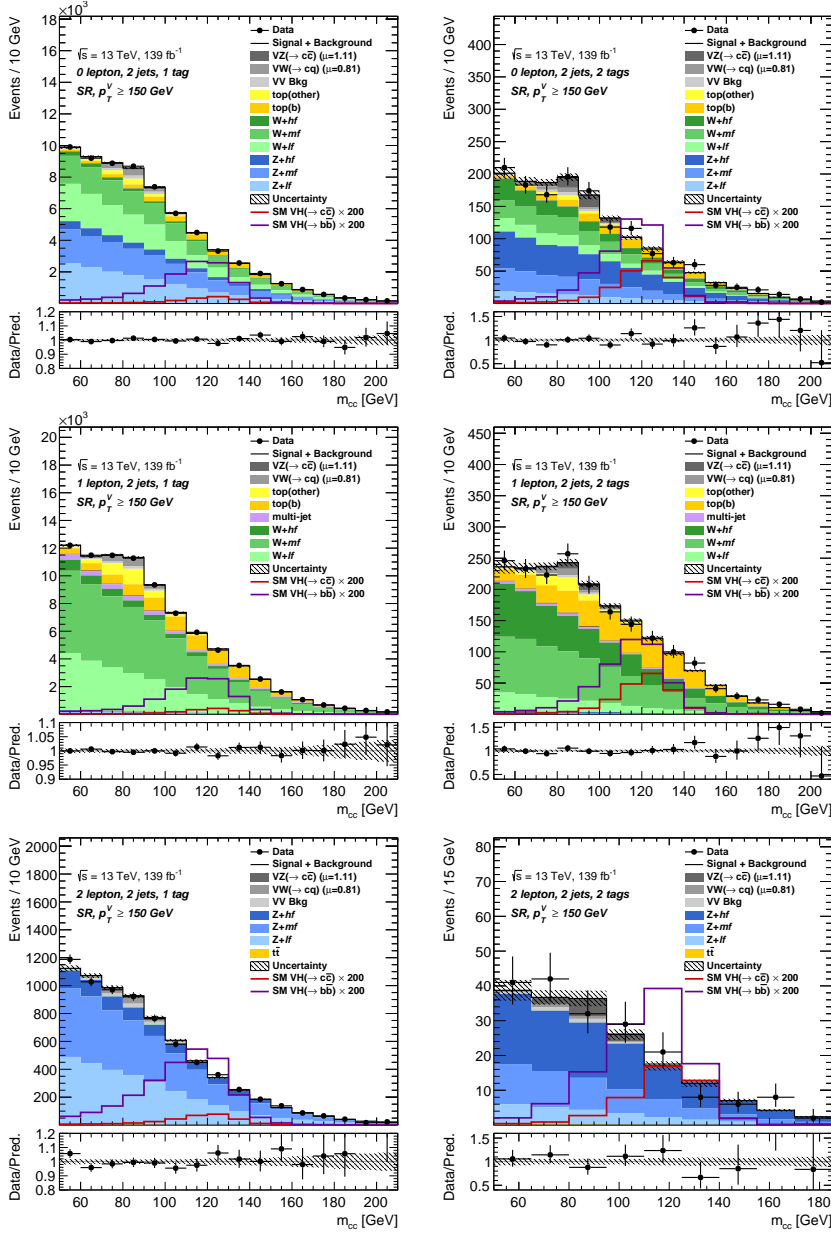


Figure 9.22: Post-fit distributions of the dijet mass in the SRs of the  $VH, H \rightarrow c\bar{c}$  analysis in the 0- (top), 1- (middle) and 2-lepton channel (bottom). Only regions with exactly two jets are shown. The regions on the left have one jet passing the  $c$ -tagging +  $b$ -veto working point, for the regions on the right it is both jets. The magnified  $VH, H \rightarrow c\bar{c}$  signal is shown in red and to be compared to the  $VH, H \rightarrow b\bar{b}$  signal in violet. The same magnification factors are used.



### 9.2.3 The combination procedure

To combine the  $VH, H \rightarrow c\bar{c}$  and  $VH, H \rightarrow b\bar{b}$  analyses, a joint likelihood function is created as a multiplication of the two individual likelihoods. Common signal strength parameters, that affect the signal in both analyses, are introduced for both  $VH, H \rightarrow c\bar{c}$  and  $VH, H \rightarrow b\bar{b}$ . The normalisation factors of the main backgrounds and all process-modelling uncertainties are kept decorrelated between the two analyses, given that the two analyses followed different modelling approaches, that are driven e.g. by the discriminant that is used in the fit (BDT output score vs. dijet mass) and the different flavour compositions of the backgrounds. Experimental nuisance parameters that correspond to uncertainties related to the detector performance are correlated between the two analyses. An exception are the flavour tagging uncertainties for the  $b$ -tagging in  $VH, H \rightarrow b\bar{b}$  and the  $b$ -veto in  $VH, H \rightarrow c\bar{c}$ , which are kept decorrelated because different nuisance parameter schemes are used by the individual analyses.

Although the SRs of the two analyses are orthogonal by design due to the usage of the  $b$ -veto in the  $VH, H \rightarrow c\bar{c}$  analysis, a small fraction of events with 2  $b$ -tags enters the control regions of the  $VH, H \rightarrow c\bar{c}$  analysis. This fraction differs slightly from region to region and amounts to maximally 6%. The impact of this potential overlap is assessed by removing the events with 2  $b$ -tags from the control regions: it does not impact the measurement results. The post-fit agreement between data and simulation in all analysis regions is similar to the agreement that is obtained in the individual analysis fits.

### 9.2.4 Results and interpretation

The combination measures the  $VH, H \rightarrow b\bar{b}$  and  $VH, H \rightarrow c\bar{c}$  signal strengths to be

$$\mu_{VH}^{c\bar{c}} = -9 \pm 15 \quad , \text{ and } \mu_{VH}^{b\bar{b}} = 1.06_{-0.17}^{+0.19} \quad . \quad (9.8)$$

These results agree with the signal strengths of  $\mu_{VH}^{c\bar{c}} = -9 \pm 15$  and  $\mu_{VH}^{b\bar{b}} = 1.02_{-0.17}^{+0.18}$  that are obtained from the individual analyses. The change in the central value for  $\mu_{VH}^{b\bar{b}}$  is traced back to its correlation with the jet-related nuisance parameters, which in the combination are correlated between the two analyses which leads to slightly different values compared to the ones obtained from the  $VH, H \rightarrow b\bar{b}$  analysis. Figure 9.23 shows the likelihood landscape in the  $(\mu_{VH}^{b\bar{b}}, \mu_{VH}^{c\bar{c}})$ -plane, obtained from a two-dimensional profile likelihood-ratio scan. The observed (expected) correlation between the two signal strengths is -12% (-11%) and driven by the  $VH, H \rightarrow b\bar{b}$  events in the SRs of the  $VH, H \rightarrow c\bar{c}$  analysis.

The combined measurement is further interpreted as constraints on modified Higgs couplings using the  $\kappa$  framework. With respect to the  $\kappa$  interpretation of the

<sup>2</sup>The addition of a dedicated extrapolation uncertainty due to the different analysis selections has been tested and found to not impact the results.

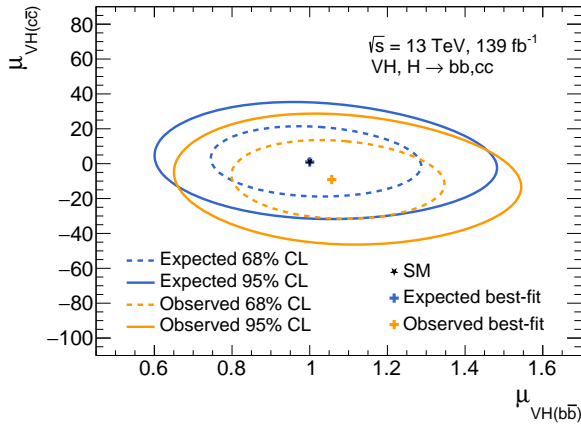


Figure 9.23: Expected and observed profile likelihood ratio contours at the 68% and 95% CL for the  $VH, H \rightarrow b\bar{b}$  and  $VH, H \rightarrow c\bar{c}$  signal strengths. The best-fit value is indicated with a cross. The observed (expected) linear correlation coefficient between the two signal strengths is -12% (-11%).

standalone  $VH, H \rightarrow c\bar{c}$  analysis, the combination allows to relax the assumptions and consider in addition to non-SM values of  $\kappa_c$  also modified Higgs to  $b$ -quark couplings manifesting themselves as  $\kappa_b \neq 1$ . Again, no BSM Higgs decays are assumed and all other Higgs couplings are fixed to their SM expectation.

The different contributions to the  $VH$  cross-section are parameterised as described in Section 3.4. This parameterisation does not consider  $c$ -quark contributions to the  $gg \rightarrow ZH$  production, however, these contributions are expected to be negligible in the range of  $\kappa_c$  values that are probed. The same argument holds for  $VH$  production, where the Higgs boson couples directly to initial-state  $c$ -quarks, which is shown to only become significant for  $\kappa_c \sim \mathcal{O}(100)$  [269]. Because  $\kappa_b$  is included in the parameterisation of  $gg \rightarrow ZH$  and  $\kappa_c$  is not, the likelihood is symmetric around  $\kappa_c = 0$  but not around  $\kappa_b = 0$ . The likelihood difference between positive and negative values of  $\kappa_b$  is negligibly small, however, given the small contribution that the interference terms featuring  $\kappa_b$  have to the  $gg \rightarrow ZH$  production.

Figure 9.24 shows the profile likelihood ratio contours as a function of  $\kappa_c$  and  $\kappa_b$ , together with the best-fit values obtained from the combination. Given the negative observed  $VH, H \rightarrow c\bar{c}$  signal strength, the observed likelihood has a minimum at  $\kappa_c = 0$ . Additionally, the observed  $VH, H \rightarrow b\bar{b}$  signal strength that is slightly larger than unity leads to the best-fit value being at negative  $\kappa_b$ . This preference over positive values of  $\kappa_b$  is insignificant, however. The valleys of low likelihood occur e.g. when the effect of an enhanced  $\kappa_c$  in the  $H \rightarrow c\bar{c}$  partial width is compensated in the branching ratio by an enhanced  $\kappa_b$  which increases the total Higgs width. The constraints are complementary to those obtained from measurements of the Higgs boson  $p_T$  spectrum, e.g. from  $H \rightarrow ZZ \rightarrow 4\ell$  decays [78]

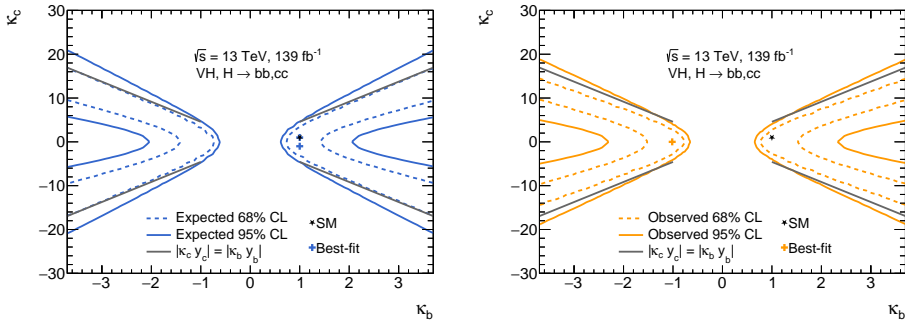


Figure 9.24: Expected (left) and observed (right) profile likelihood ratio contours at the 68% and 95% CL for the coupling modifiers  $\kappa_c$  and  $\kappa_b$ . The best-fit value is indicated with a cross. The SM expectation is indicated with a star.

as shown in Figure 9.25.

A common limitation of  $\kappa$  interpretations of Higgs boson measurements is that the total width of the Higgs boson  $\Gamma_H$  enters in all measurements via the branching ratio. While direct experimental constraints on  $\Gamma_H$  remain weak, assumptions need to be made on the coupling modifier  $\kappa_H$ . Common assumptions include the absence of any non-SM Higgs boson decays and, as in the case of this combination, allowing only a subset of  $\kappa$  modifiers to be different from unity. The ratio of coupling modifiers, however, is independent of any assumptions on  $\Gamma_H$ . Therefore, the  $VH, H \rightarrow b\bar{b}$  and  $H \rightarrow c\bar{c}$  combination is used to constrain the ratio  $\kappa_c/\kappa_b$ .

In the SM, the Higgs couplings to charm and bottom quarks are uniquely defined. Any significant deviation from the prediction of  $\kappa_c = \kappa_b = 1$  would be a direct sign of new physics. Several extensions of the SM can lead to enhanced Higgs boson couplings to the light quarks of the first and second generation, such as Two Higgs Doublet Models (2HDMs) [270, 271] or TeV-scale vector-like quarks (VLQs) [272] with suppressed Higgs-mediated flavour changing interactions. In these scenarios, the light quark Yukawa couplings, including the coupling to charm quarks, can be significantly enhanced with respect to their SM prediction, up to the point where they are comparable in strength with the third generation Yukawa couplings.

To benchmark the performance of the combination, the point where the modified charm Yukawa coupling  $\kappa_c y_c$  is of the same size as the modified bottom Yukawa coupling  $\kappa_b y_b$ , is chosen. This is the case for

$$\kappa_c y_c = \kappa_b y_b, \text{ with } y_f = \sqrt{2} \frac{m_f}{v} \rightarrow \frac{\kappa_c}{\kappa_b} = \frac{m_b}{m_c}. \quad (9.9)$$

The quark-mass ratio  $m_b/m_c$  can be determined ab initio using lattice QCD methods. It is a dimensionless quantity and to good approximation independent of the renormalisation scheme and scale choice and is therefore calculated with good

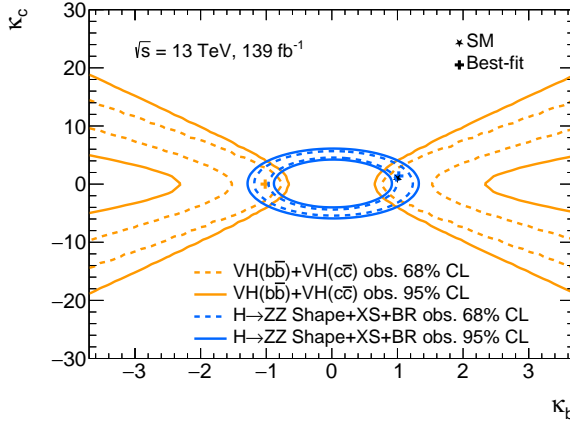


Figure 9.25: Observed profile likelihood ratio contours at the 68% and 95% CL for the coupling modifiers  $\kappa_c$  and  $\kappa_b$  obtained from the  $VH, H \rightarrow b\bar{b}$  and  $VH, H \rightarrow c\bar{c}$  combination (orange) and a measurement of the Higgs boson  $p_T$  spectrum from  $H \rightarrow ZZ^* \rightarrow 4\ell$  decays (blue). For the latter measurement, both the shape and the normalisation are used to constrain  $\kappa_c$  and  $\kappa_b$ . Blue contour taken from Ref. [78].

precision. The  $c/b$  universality benchmark happens at [273]

$$\frac{\kappa_c}{\kappa_b} = \frac{m_b}{m_c} = 4.578 \pm 0.008 \quad . \quad (9.10)$$

For values larger than that, the modified charm Yukawa coupling would be larger than the modified bottom Yukawa coupling.

A profile likelihood ratio scan from the combination as a function of  $\kappa_c/\kappa_b$  is shown in Figure 9.26. When performing the scan,  $\kappa_b$  is not fixed. The  $c/b$  universality benchmark is indicated as vertical green lines. Since the partial decay widths for  $H \rightarrow b\bar{b}$  and  $H \rightarrow c\bar{c}$  are proportional to  $\kappa^2$ , both positive and negative values of  $\kappa_c/\kappa_b$  are considered. As can be seen, the combination is able to exclude that the magnitude of the Higgs boson coupling to charm quarks is larger or equal to the magnitude of the Higgs boson coupling to bottom quarks at the 95% CL.

### 9.2.5 Inclusion in the ATLAS-wide combination of Higgs boson measurements

In contrast to the  $\kappa_c/\kappa_b$  interpretation, interpretations that aim at constraining individual coupling modifiers require assumptions to be made on the total width of the Higgs boson. To relax these assumptions, the  $VH, H \rightarrow c\bar{c}$  search has to be included in the ATLAS-wide combination of all Higgs boson measurements.

To benchmark the expected sensitivity of such a combination to the coupling

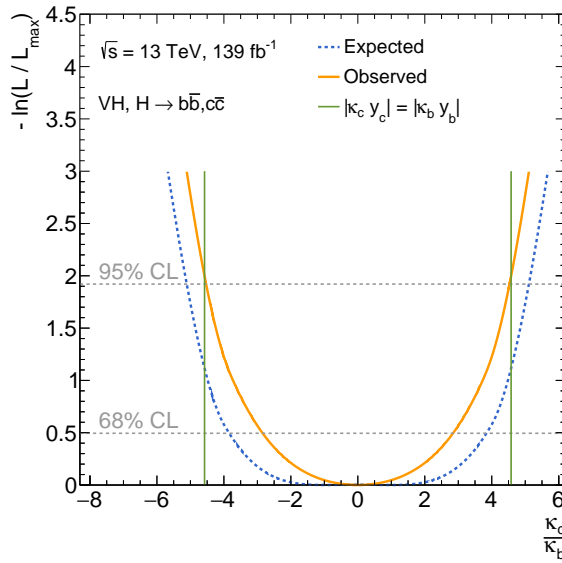


Figure 9.26: Expected and observed profile likelihood ratio scans for  $\kappa_c/\kappa_b$ . The 68% and 95% CL thresholds are indicated. The green lines mark the values at which the Higgs coupling to  $c$ -quarks is equal to the Higgs coupling to  $b$ -quarks.

modifiers  $\kappa_c$  and  $\kappa_b$ , a preliminary combination is performed assuming Gaussian measurements. Starting from the inclusive  $\sigma \times \text{BR}$  measurements of the most recent ATLAS combination of measurements of  $H \rightarrow \gamma\gamma$ ,  $H \rightarrow ZZ^*$ ,  $H \rightarrow WW^*$ ,  $H \rightarrow \tau\tau$ ,  $H \rightarrow b\bar{b}$  and  $H \rightarrow \mu\mu$  [4], a likelihood is constructed as

$$-2\ln(\mathcal{L}) = (\vec{x} - \vec{\mu}(\vec{\kappa}))^T V^{-1} (\vec{x} - \vec{\mu}(\vec{\kappa})) \quad . \quad (9.11)$$

In this equation,  $\vec{x}$  describes the central values of the  $\sigma \times \text{BR}$  normalised to the SM prediction and  $\vec{\mu}(\vec{\kappa})$  parameterises the expectation of this ratio as a function of the coupling modifiers  $\kappa$ . The covariance matrix  $V$  is built from the correlation matrix of the combined measurement and the symmetrised uncertainties on the central  $\sigma \times \text{BR}$  values.

The  $VH, H \rightarrow c\bar{c}$  search is included by extending  $\vec{x}, \vec{\mu}$  and  $V$ . For this inclusion, the measured signal strength of the individual  $VH, H \rightarrow c\bar{c}$  analysis [8] is used. It is assumed that the  $VH, H \rightarrow c\bar{c}$  signal strength is not correlated with any other measurement, apart from  $VH, H \rightarrow b\bar{b}$  where the measured correlation from the  $VH, H \rightarrow b\bar{b}$  and  $VH, H \rightarrow c\bar{c}$  combination of  $-12\%$  is taken.

The parameterisation of the individual signal strengths  $\mu$  in terms of the coupling modifiers  $\kappa$  is based on the scenario considered for Figure 3.10. In particular, that means that only Higgs boson couplings to SM particles are considered, i.e. SM loops and  $\text{BR}_{\text{inv.}} = \text{BR}_{\text{undet.}} = 0$ . The following coupling modifiers are considered:  $\kappa_Z, \kappa_W, \kappa_b, \kappa_t, \kappa_\tau, \kappa_\mu$  and since  $VH, H \rightarrow c\bar{c}$  is included also  $\kappa_c$ . The  $\kappa_s$  modifier is fully correlated with  $\kappa_b$  and the coupling modifiers of first generation quarks are fixed to unity.

The profile likelihood-ratio contours as a function of  $\kappa_c$  and in two dimensions for  $\kappa_b$  and  $\kappa_c$  from this combination is shown in Figure 9.27. As can be seen, at the 95% CL, values of  $|\kappa_c| > 5.7$  are excluded. Furthermore, the combination of Higgs boson measurements leads to closed profile likelihood-ratio contours at the 68% and 95% CL in the  $\kappa_c$  vs.  $\kappa_b$  plane. Although this preliminary study does not replace a proper combination based on the full likelihoods of the individual measurements, it already indicates that the inclusion of  $VH, H \rightarrow c\bar{c}$  in the ATLAS-wide combination of Higgs boson measurements will allow to set more stringent limits on  $\kappa_c$  with at the same time less assumptions.

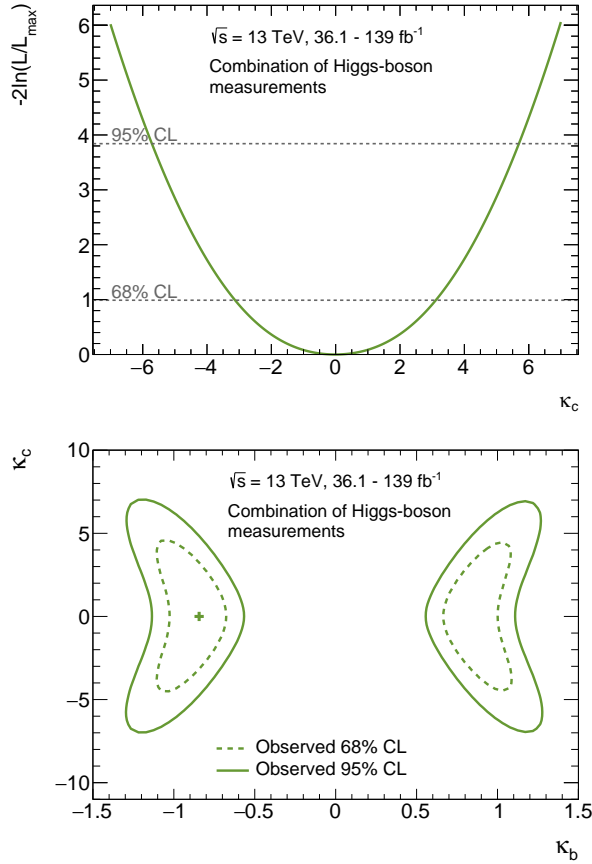


Figure 9.27: The observed profiled negative-log-likelihood ratio for the Higgs to charm-quark coupling modifier  $\kappa_c$  (top) and the contours at the 68% and 95% CL for both  $\kappa_c$  and the Higgs to bottom-quark coupling modifier  $\kappa_b$ . The likelihoods are built by combining signal strength measurements into a multivariate Gaussian. The input values for this combination are taken from Ref. [8] and Ref. [4]. A correlation of  $-12\%$  is assumed between the  $VH, H \rightarrow b\bar{b}$  and  $VH, H \rightarrow c\bar{c}$  signal strength measurements.





# 10 Conclusion and outlook

Precise measurements of the Higgs boson's properties are a powerful tool to look for deviations from the predictions of the SM. The  $139\text{ fb}^{-1}$  of proton-proton collision data that have been collected by the ATLAS experiment during Run 2 of the LHC, offer an unprecedented opportunity to investigate rare Higgs boson topologies that are particularly sensitive to new physics scenarios, but experimentally difficult to access. Several such measurements, that target Higgs boson decays to heavy-flavour quarks, and their combinations are presented in this thesis.

Of particular interest is the study of differential quantities, such as the transverse momentum distribution of the Higgs boson,  $d\sigma/dp_T^H$ . Even if the collision energy of the LHC is too low to directly probe new physics, many new physics models predict relative deviations from the SM that are enhanced at high  $p_T^H$ . Due to the low cross-section in this phase space, even large deviations would not conflict with existing measurements.

This thesis reports a novel analysis that measures  $VH$ ,  $V \rightarrow \text{leptons}$  and  $H \rightarrow b\bar{b}$  events with high  $p_T^H$ . To enhance the signal sensitivity in this extreme phase space, dedicated reconstruction techniques are applied to deal with the highly Lorentz-boosted decay products. In particular, the Higgs boson is reconstructed from a single jet with large radius parameter  $R$  and, furthermore, jet substructure is used to identify the signatures of the two  $b$ -hadrons from the  $H \rightarrow b\bar{b}$  decay inside of the large- $R$  jet. The analysis techniques are validated on semi-leptonic  $VZ$ ,  $Z \rightarrow b\bar{b}$  events where a significance of 5.4 (5.7) standard deviations is observed (expected). The observed significance of the high- $p_T$   $VH$  signal is 2.1 standard deviations, compared to a SM expectation of 2.7. Cross-sections are measured in the framework of simplified template cross-sections (STXS) for two regions of the transverse momentum of the vector boson  $p_T^V$ :  $250\text{ GeV} < p_T^V < 400\text{ GeV}$  and for the first time exclusively for  $p_T^V > 400\text{ GeV}$ . The results agree with the predictions of the SM within uncertainties.

The high- $p_T$   $VH$ ,  $H \rightarrow b\bar{b}$  measurement is further combined with an other  $VH$ ,  $H \rightarrow b\bar{b}$  measurement that targets the low- and intermediate  $p_T^H$  regime. The overlap between the two measurements is resolved via a cut at  $p_T^V = 400\text{ GeV}$ . Below this value, the Higgs boson is reconstructed using two small- $R$  jets. Above this value the Higgs boson is reconstructed using one large- $R$  jet. This combination allows to measure the  $VH$  cross-sections, where  $H \rightarrow b\bar{b}$  and  $V \rightarrow \text{leptons}$ , over the largest possible range of the vector-boson transverse momentum. Within the

STXS framework, the  $ZH$  cross-section is measured in four separate categories and the  $WH$  cross-section in three categories. This measurement represents the most precise differential  $VH, H \rightarrow b\bar{b}$  cross-section measurement to date, with uncertainties ranging from 30 to 300%, depending on the  $p_T^V$  range and the vector-boson type.

The  $VH, H \rightarrow b\bar{b}$  measurements are used to constrain the coupling strength of possible new physics interactions of a Standard Model Effective Field Theory (SMEFT). Out of all considered Wilson coefficients of CP-even operators with mass dimension 6, the ones that lead to  $p_T^V$ -dependent modifications of the  $VH$  cross-section can be constrained particularly well with the differential cross-section measurement. The additional exclusive cross-section measurement for  $p_T^V > 400$  GeV improves the limits on these coefficients and at the same time reduces the correlation between the coefficients. This proves particularly useful also in ATLAS-wide SMEFT interpretations of Higgs boson measurements, to which the  $VH, H \rightarrow b\bar{b}$  combination is used as an input.

Finally, to constrain the ratio of the Higgs boson couplings to  $c$ - and  $b$ -quarks without assumptions on the Higgs boson width, a combination of the  $VH, H \rightarrow b\bar{b}$  measurement and a direct search for  $VH, H \rightarrow c\bar{c}$  is reported. The ratio of couplings is constrained to be smaller than 4.5 at the 95% CL, and as a consequence it is excluded for the first time that the Higgs boson couples stronger or equally strong to  $c$ -quarks than it does to  $b$ -quarks.

The Run 2 Higgs boson measurements have set new precision records in the determination of the boson's properties. The analyses presented in this thesis significantly improve the experimental knowledge of high- $p_T$  Higgs bosons and establish the coupling strength hierarchy between the Higgs boson and quarks of the second and third generation. In all aspects, the initial sensitivity expectations have been exceeded through improvements of the analysis strategies.

In the future, the high- $p_T$  Higgs boson measurements will benefit from a more complex analysis strategy. The usage of multivariate analysis techniques, such as Boosted Decision Trees or Deep Neural Networks, is being studied and preliminary results suggest that improvements of 25% to 50% are achievable with respect to the current analysis. Furthermore, an advanced usage of the large- $R$  jet substructure is expected to lead to additional improvements. Since the cross-section measurements are still statistically limited, further improvement is expected by increasing the analysed data set. The LHC's Run 3, whose start is imminent, promises an additional  $300 \text{ fb}^{-1}$  of data at a slightly higher collision energy of  $\sqrt{s} = 13.6$  TeV.

The  $VH, H \rightarrow b\bar{b}$  combination will benefit the most from improvements of the individual analyses. In addition to the already mentioned points, the overlap removal between the two analyses can be improved in the future. Instead of a fixed

$p_T^V$  cut, the decision which Higgs boson reconstruction technique will be used could be taken for each event individually. Furthermore, the STXS binning can still be optimised, potentially adding more granularity at high  $p_T^V$ .

Direct searches for  $VH, H \rightarrow c\bar{c}$  can benefit from improvements in the algorithms that are used to perform  $c$ -tagging and, similar to the high- $p_T$   $VH, H \rightarrow b\bar{b}$  measurement, from more complex analysis strategies. Given the similarity of the  $VH, H \rightarrow b\bar{b}$  and  $VH, H \rightarrow c\bar{c}$  processes, a more sophisticated combination procedure of the two analyses is desirable. In order to improve the results, such a combination should allow to constrain e.g. the shapes of similar backgrounds across analyses, where possible.

The SMEFT framework is already being used to connect a multitude of Higgs boson measurements and perform a joint interpretation that benefits from the complementarity of the different measurements. Ultimately, these interpretations need to be extended to as many different areas of the SM as possible, including for example top-quark and diboson measurements but also measurements of electroweak precision observables, both from the LHC and previous precision machines such as LEP.

Ultimately, the  $3\text{ab}^{-1}$  of data that are expected to be recorded at the end of the High-Luminosity LHC phase, will allow to determine the main Higgs boson couplings with a precision of a few percent. Current estimates from conservative scalings suggest [274], that it will be possible to measure the  $ZH, H \rightarrow b\bar{b}$  and  $WH, H \rightarrow b\bar{b}$  cross-sections with uncertainties of 7% and 8%, respectively. Similarly for the  $VH, H \rightarrow c\bar{c}$  signal strength, the upper limit is expected to improve to 6.4 times the SM expectation at the 95% CL. At the same time, this large data set will allow to substantially increase the  $p_T^H$ -reach of the differential measurements. To perform these measurements with the required precision, however, it is vital that also the theory predictions in extreme phase spaces improve hand-in-hand with the analysis improvements. Only then can the full potential of the LHC data be utilised.



# Summary

## It is all about resolution

In the late 19<sup>th</sup> century, the Italian astronomer Schiaparelli points his telescope towards Mars and makes an astonishing observation. On the blurry image of the planet's surface he sees long dark lines which he calls 'canali'. This observation<sup>1</sup> ignites a worldwide controversy about the existence of intelligent life on Mars, an unknown species that is constructing gigantic artificial canals. Today it is known that most of Schiaparelli's 'canali' were optical illusions, caused by trying to interpret substructure on an image with poor resolution. The key to rejecting the canal hypothesis was to increase the resolution of the pictures.

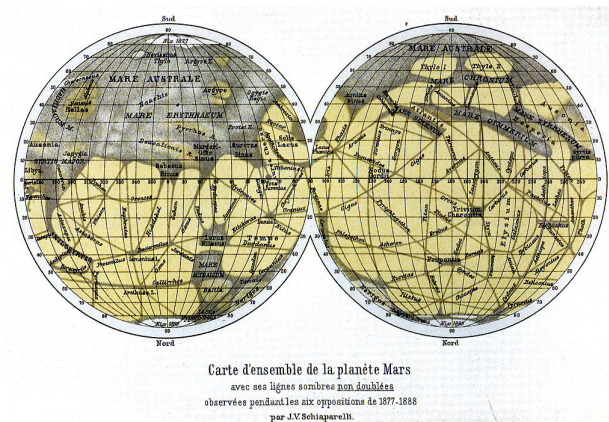


Figure 10.1: Atlas of Mars with canals by Giovanni Schiaparelli (1888).

## Particle physics and the Standard Model

In particle physics, the telescopes that are used to study the universe of the very small are particle colliders, such as the Large Hadron Collider (LHC) at the CERN laboratory in Geneva. The higher the energy of the collider, the better its resolution. The LHC marks the current energy frontier, colliding protons on protons at a record centre-of-mass energy of  $\sqrt{s} = 13$  TeV. The LHC collisions are used to test

<sup>1</sup>Together with a mistranslation of the word 'canali' into English.

the Standard Model (SM) of particle physics, which encapsulates the present-day understanding of Nature's basic building blocks (elementary particles) and their interactions with each other. The SM is an incredibly successful theory, that over time made many predictions that were later experimentally confirmed. The discovery of the Higgs boson by the ATLAS and CMS collaborations in the year 2012 at the LHC is the most recent milestone in the SM's success. Nevertheless, the SM is not a 'theory of everything'. In addition to theoretical issues, there are observed phenomena that the SM cannot explain, like dark matter, neutrino masses or the apparent matter-antimatter asymmetry in the universe. Yet, in the controlled environment of particle colliders, the observations seem to agree with the predictions of the SM.

## Deviations in the tails

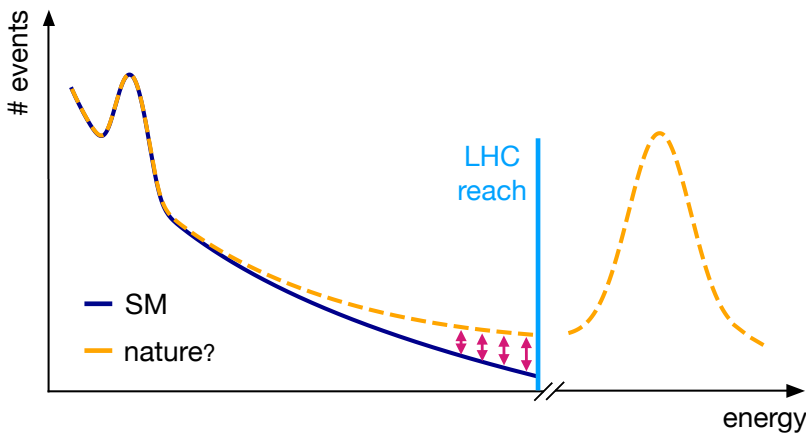


Figure 10.2: Illustration of subtle deviations from the SM prediction as a function of the collision energy. The relative deviation is the largest in the tail of the distribution, towards the limit of the LHC reach.

Many theories exist that change the SM in a way to overcome both the theoretical and the experimental issues that are associated with it. These theories typically predict new forms of matter or new forces, that would manifest themselves as heavy new particles that can be produced in high energy particle collisions. In the absence of a discovery of new matter particles or force carriers, however, the possibility has to be taken seriously that the energy of the LHC is not high enough to directly produce such heavy new particles. Nevertheless, the existence of particles with masses higher than the energy reach of the LHC can alter observables at the LHC indirectly through virtual contributions. Contributions of this kind would manifest themselves as more or less subtle deviations in the distributions of these

observables. Of particular interest are observables that are proportional to the momentum transfer of the collision, where such heavy new particles would lead to differences especially in the tails, as depicted in Figure 10.2. In these cases, the relative deviation from the SM prediction gets larger the higher the momentum transfer of the collision.

## Picturing the Higgs boson

The Higgs boson sits at the heart of the SM: 15 out of the 19 free parameters of the theory are connected to it. As a consequence, many of the proposed modifications of the SM will also significantly alter the Higgs boson's properties. Within the SM, once the Higgs boson mass is known, these properties are uniquely predicted and any measured deviation from the predictions would be a clear sign of new physics. For this reason, a precise determination of the Higgs boson's properties is one of the most important tasks in contemporary particle physics.

Much like Schiaparelli's picture of Mars, however, the present-day picture of the Higgs boson is still blurry in many regions. At the time of writing, the Higgs boson is measured to couple to vector bosons as predicted by the SM within relative uncertainties of  $\mathcal{O}(10\%)$ . The couplings to the fermions of the third generation are observed and agree with the SM predictions within relative uncertainties of  $\mathcal{O}(20\%)$ . Furthermore, there is evidence that the Higgs boson couples to leptons of the second generation. Higgs couplings to the quarks of the second generation or the fermions of the first generations have not been measured. Similarly, current measurements are not sensitive enough to verify if the Higgs boson couples to itself, which is a crucial SM prediction.

## Reconstructing *boosted* Higgs bosons

This thesis increases the resolution of the Higgs boson picture by using the ATLAS detector to measure Higgs bosons that are produced in proton-proton collisions with high momentum transfer. To do so, a novel analysis is designed to measure Higgs bosons  $H$  that are produced in association with a heavy vector boson  $V$  and that decay into a pair of  $b$ -quarks,  $VH, H \rightarrow b\bar{b}$ . The  $VH$  associated production contributes significantly to the total Higgs boson production cross-section at high Higgs boson transverse momentum  $p_T^H$ . At the same time,  $V \rightarrow$  leptons decays create detector signatures that can be triggered on and enhance the signal purity. Using the most abundant Higgs boson decay into a pair of  $b$ -quarks ensures a high enough signal yield to be analysed. The  $b$ -quarks will furthermore hadronise and create collimated sprays of particles, so-called  $b$ -jets. The experimental signature that is targeted therefore consists of two  $b$ -jets that recoil in the transverse plane of the detector against the leptons from the vector-boson decay.

At high  $p_T^H$ , however, the two  $b$ -jets from the Higgs boson decay get geometrically

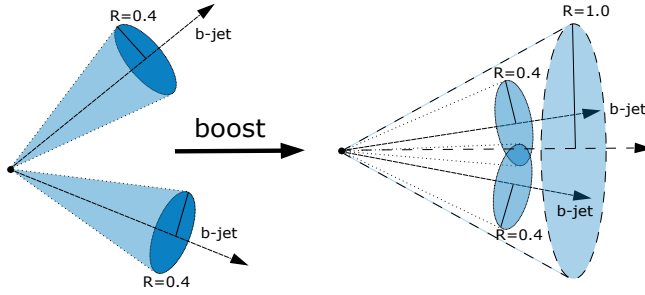


Figure 10.3: Illustration of the reconstruction of a  $H \rightarrow b\bar{b}$  decay using two small- $R$  jets (left) and one large- $R$  jet (right).

close due to the large Lorentz boost of the system, as depicted in Figure 10.3. In contrast to previous measurements of  $VH, H \rightarrow b\bar{b}$  at low and intermediate  $p_T^H$ , the high- $p_T$  analysis presented in this thesis does not reconstruct the Higgs boson candidate using two well separated jets. Instead, the full  $H \rightarrow b\bar{b}$  decay is reconstructed with a single jet of large radius and substructure information is subsequently used to detect the presence of two  $b$ -hadrons inside of the jet. This boosted reconstruction technique yields higher signal acceptance at high  $p_T^H$ .

## Measuring $VH, H \rightarrow b\bar{b}$ at high $p_T^H$

A variety of SM processes that do not involve a Higgs boson can create signatures that look similar to the signal in the ATLAS detector. These processes are referred to as backgrounds, and the goal of the analysis is to suppress the background contribution while at the same time maximising the signal efficiency. This is done by applying a dedicated event selection and furthermore categorising the events according to their kinematic properties into different signal regions.

The observable that is used to extract the signal yield is the invariant mass of the Higgs-candidate jet  $m_J$ , which for the  $VH$  signal is expected to show a peak around 125 GeV. This  $m_J$  distribution is shown in Figure 10.4 for events where the transverse momentum of the reconstructed vector boson  $p_T^V$  is greater than 250 GeV. All signal regions of the analysis are summed in this plot. As can be seen, the analysis faces a variety of backgrounds that are much larger than the signal, which is shown in red. Therefore, good experimental control over all these backgrounds is important for the measurement to succeed.

The measurement is validated with diboson events,  $VZ, Z \rightarrow b\bar{b}$ , that are similar to the  $VH$  signal put show a peak in the  $m_J$  distribution around the  $Z$ -boson mass at  $\sim 91$  GeV. This contribution is indicated in Figure 10.4 in grey. When performing the diboson cross-check, a data excess that corresponds to a significance of 5.4 standard deviations is observed, where 5.7 standard deviations are expected, which validates the analysis strategy. For the  $VH$  signal, a significance of 2.1 standard



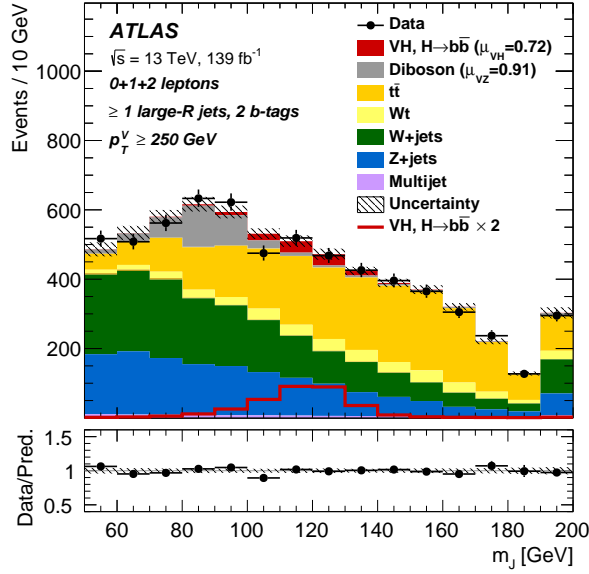


Figure 10.4: The Higgs candidate mass distribution  $m_J$  of the high- $p_T$   $VH, H \rightarrow b\bar{b}$  analysis combining all SRs.

deviations is observed, where 2.7 standard deviations are expected for a SM Higgs boson. The measurement successfully establishes the usage of boosted Higgs boson reconstruction techniques, which allow  $VH$  cross-section measurements at high  $p_T^V$ , for  $250 \text{ GeV} < p_T^V < 400 \text{ GeV}$  and for the first time exclusively for  $p_T^V > 400 \text{ GeV}$ .

## A combination of $VH, H \rightarrow b\bar{b}$ measurements

The dedicated high- $p_T$   $VH, H \rightarrow b\bar{b}$  measurement is subsequently combined with a  $VH, H \rightarrow b\bar{b}$  measurement at low and intermediate  $p_T$  to measure the  $VH$  cross-section differentially as a function of  $p_T^V$  over the largest possible range. This measurement is shown in Figure 10.5 and constitutes the differential  $VH$  cross-section measurement with the widest observable range to date, with relative uncertainties ranging from 30 to 300%.

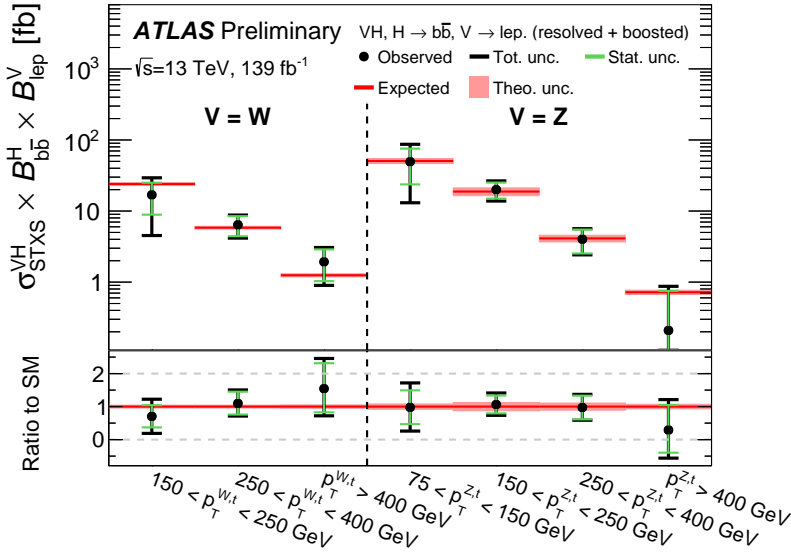


Figure 10.5: Measured  $VH$  simplified template cross-sections times the  $H \rightarrow b\bar{b}$  and  $V \rightarrow \text{leptons}$  branching fractions as a function of  $p_T^V$ . The  $WH$  cross-section is shown on the left part of the plot and the  $ZH$  cross-section on the right part.

## Standard Model Effective Field Theories

The  $VH, H \rightarrow b\bar{b}$  measurements are further used to constrain theories of new physics within the framework of Standard Model Effective Field Theories. This method parameterises the impact of heavy new particles at low energies through effective interactions of the known SM particles. The advantage of this approach is that it allows to consider the observable effect of potential new physics without having to know the actual structure of the underlying theory. Examples of such effective interactions that modify the  $pp \rightarrow VH, H \rightarrow b\bar{b}$  process are shown in Figure 10.6.

With the differential  $VH, H \rightarrow b\bar{b}$  cross-section measurement, the strengths of these effective interactions are constrained. The additional measurements at high  $p_T^V$ , which are possible thanks to the boosted Higgs boson reconstruction techniques developed in this thesis, significantly improve the limits on new physics scenarios that show deviations which grow with the involved momentum transfer. In this way, the Higgs boson measurement is used to constrain generic new physics scenarios up to energy scales of multiple TeV. The measurement consequently also plays a vital role in ATLAS-wide combinations and interpretations of Higgs boson measurements.

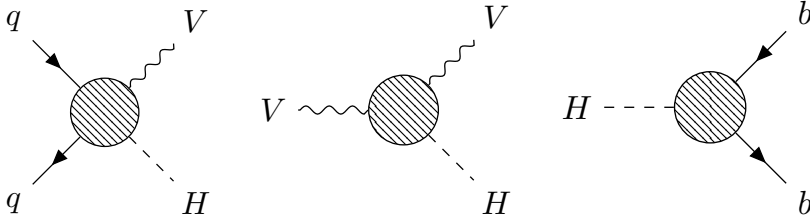


Figure 10.6: Examples of effective interactions that modify the  $pp \rightarrow VH$  production or the  $H \rightarrow b\bar{b}$  decay.

## Reaching for the second generation

Although the precision of the couplings to the fermions of the third generation is steadily increasing, little is experimentally known about the Higgs boson interactions with fermions of the second and first generation. The SM predicts that these interactions should be weaker than for the fermions of the third generation, because the Higgs boson couples to fermions proportional to their mass. Measuring this hierarchy of coupling strengths is therefore an important test of the SM. In the last part of this thesis, the  $VH, H \rightarrow b\bar{b}$  measurement is combined with a direct search for  $VH, H \rightarrow c\bar{c}$ . This combination allows to measure the ratio of the Higgs boson interaction strength between  $b$ -quarks and  $c$ -quarks, therefore probing the hierarchy between the second and third generation. At the 95% confidence level, it is excluded for the first time that the Higgs boson interacts stronger or equal with  $c$ -quarks than it does with  $b$ -quarks.

## Looking ahead

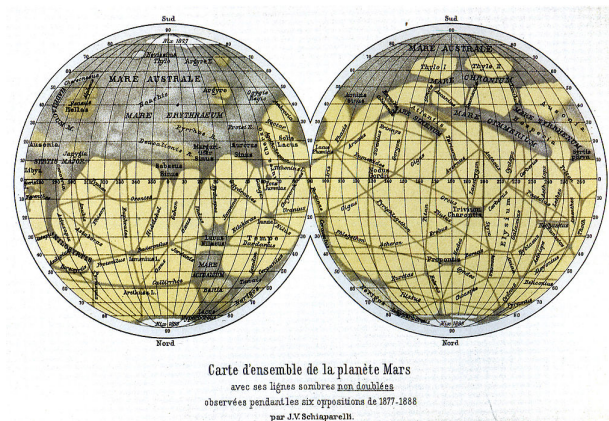
Even though the Higgs boson currently looks like the one predicted by the SM, caution is advised. As the story of Schiaparelli demonstrates, having a high resolution picture is crucial in order to draw the right conclusions. The road towards this high resolution picture of the Higgs boson is already set. In the years to come, the LHC and subsequently its high-luminosity upgrade are expected to increase the proton-proton collision data set further by a factor 20. Together with improvements of analysis techniques, detector upgrades and an increased precision of the theoretical calculations, physicists will ultimately be able to look at the Higgs boson in high definition. These are exciting times for particle physics.



# Samenvatting

## Het draait allemaal om de resolutie

Aan het eind van de 19<sup>e</sup> eeuw richt de Italiaanse astronoom Schiaparelli zijn telescoop op Mars en doet een adembenemende waarneming. Op het griezelige beeld van het oppervlakte van de planeet ziet hij lange, donkere lijnen die hij ‘canali’ noemt. Deze waarneming<sup>2</sup> leidt tot een wereldwijde controverse over het bestaan van een intelligente vorm van leven op Mars: een onbekende soort die gigantische irrigatiekanalen kan uitgraven. Tegenwoordig is het bekend dat de meeste van Schiaparelli’s ‘canali’ optische illusies waren, die verschenen bij pogingen om details te interpreteren op afbeeldingen met een lage resolutie. De sleutel tot het ontkrachten van de kanalenhypothese was de resolutie van de foto’s te verhogen.



Figuur 10.7: Atlas van Mars met kanalen door Giovanni Schiaparelli (1888).

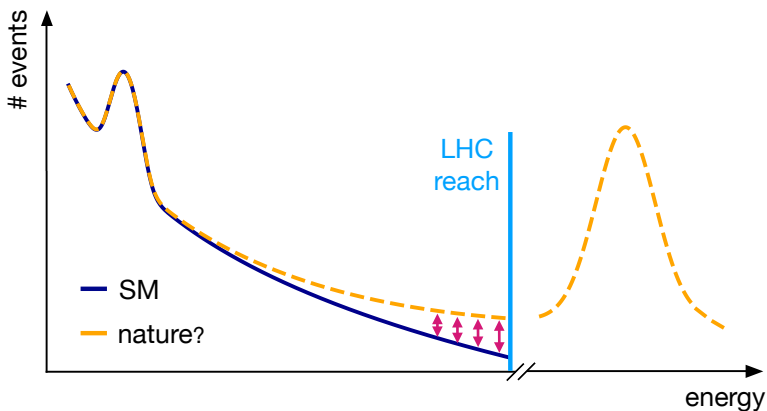
## Deeltjesfysica en het standaardmodel

In de deeltjesfysica zijn deeltjesversnellers zoals de Large Hadron Collider (LHC) op het CERN laboratorium in Genève de telescopen die worden gebruikt om het universum van het allerkleinste te bestuderen. Hoe groter het maximale energiebereik van de versneller, des te beter diens resolutie. De LHC behaalt de allerhoogste

<sup>2</sup>In combinatie met een onjuiste vertaling van het woord ‘canali’ in het Engels.

energieën en stelt onderzoekers in staat om botsingen tussen protonen te bestuderen bij ongeëvenaarde botsingsenergieën van  $\sqrt{s} = 13$  TeV. Deze deeltjesbotsingen worden gebruikt om het standaardmodel (SM) van de deeltjesfysica te testen, dat de hedendaagse kennis over de elementaire bouwsteentjes van de natuur en hun interacties samenvat. Het standaardmodel is een ongelooflijk succesvolle theorie, waaruit over de jaren heen veel voorspellingen zijn afgeleid die later experimenteel zijn bevestigd. De ontdekking van het Higgsboson door de ATLAS- en CMS-experimenten bij het CERN in het jaar 2012 is de meest recente mijlpaal in het succesverhaal van het standaardmodel. Desalniettemin is het standaardmodel geen ‘theorie van alles’. Naast enkele theoretische onvolkomenheden, zijn er bijvoorbeeld ook experimentele waarnemingen die het standaardmodel niet kan verklaren, zoals donkere materie, de massa’s van neutrino’s en de ogenschijnlijke asymmetrie tussen materie en antimaterie in het universum. Toch lijken waarnemingen binnen de streng gecontroleerde meetomgeving van de deeltjesversnellers overeen te komen met de voorspellingen van het standaardmodel.

## Afwijkingen in de staarten



Figuur 10.8: Illustratie van een subtiele afwijking ten opzichte van de voorspelling van het standaardmodel als functie van de totale energie in een deeltjesbotsing. De relatieve afwijking is het grootst in de staart van de verdeling, in de buurt van het maximale energiebereik van de LHC.

Er bestaan veel theorieën die veranderingen aanbrengen in het standaardmodel, met het doel om zowel de theoretische als experimentele tekortkomingen van het model te overwinnen. Deze theorieën voorspellen doorgaans nieuwe vormen van materie of nieuwe krachten, die zich zouden kunnen manifesteren als (tot nog toe) onontdekte massieve deeltjes die kunnen worden geproduceerd bij hoogenergetische

deeltjesbotsingen. Zolang de ontdekking van deze nieuwe deeltjes echter uitblijft, moet de mogelijkheid serieus genomen worden dat het energiebereik van de LHC niet hoog genoeg is om zulke nieuwe massieve deeltjes direct te produceren. Wel is er een kans dat het bestaan van deeltjes met rustmassa's groter dan dit energiebereik bepaalde observabelen in de LHC-data kan veranderen door quantumcorrecties. Bijdragen van dit type zouden kunnen opduiken als subtiele afwijkingen in de waarschijnlijkheidsverdelingen van deze observabelen. Van bijzonder belang zijn observabelen die evenredig schalen met de impulsoverdracht in de deeltjesbotsingen, omdat het bestaan van nieuwe massieve deeltjes in het bijzonder zichtbaar zal zijn in de staart van de bijbehorende waarschijnlijkheidsverdelingen. In zulke gevallen zal de relatieve afwijking van het standaardmodel groeien naarmate de impulsoverdracht in de botsing toeneemt.

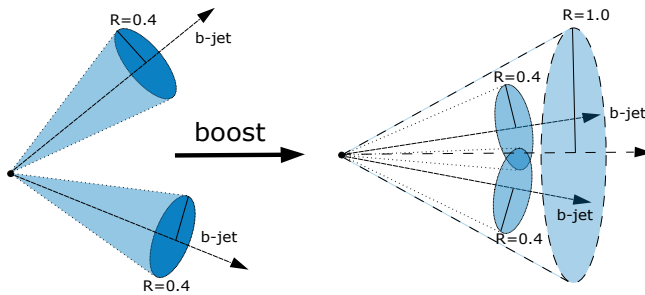
## Het Higgsboson in beeld brengen

Het Higgsboson bevindt zich in het hart van het standaardmodel: 15 van de 19 vrije parameters van het model zijn eraan verbonden. Als gevolg hiervan brengen veel van de voorgestelde aanpassingen van het standaardmodel ook significante veranderingen in de eigenschappen van het Higgsboson met zich mee. Deze eigenschappen worden binnen het standaardmodel op unieke wijze voorspeld zodra de massa van het Higgsboson vastligt, zodat elke afwijking van de voorspelde waarden een duidelijk signaal vormt van nieuwe, onbeschreven natuurwetten. Daarom behoort de precieze meting van de eigenschappen van het Higgsboson tot een van de belangrijkste taken van de hedendaagse deeltjesfysica. Het beeld dat we vandaag de dag van het Higgsboson hebben, is echter net zoals Schiaperelli's foto's van Mars aan het einde van de 19de eeuw, op veel plekken nog onscherp. Zo zijn op het moment van schrijven de koppelingen tussen het Higgsboson en de vectorbosonen van het standaardmodel gemeten met een relatieve meetfout van  $\mathcal{O}(10\%)$ . De koppelingen met de fermionen van de derde generatie zijn waargenomen en stemmen overeen met de verwachting uit het standaardmodel tot op een relatieve meetonauwkeurigheid van  $\mathcal{O}(20\%)$ . Verder zijn er aanwijzingen dat het Higgsboson koppelt met leptonen uit de tweede generatie. Koppelingen tussen het Higgsboson en de quarks van de tweede generatie of de fermionen van de eerste generatie zijn nog niet waargenomen. Ook zijn de huidige metingen niet gevoelig genoeg om te bevestigen dat het Higgsboson koppelt aan zichzelf: een cruciale voorspelling van het standaardmodel.

## Reconstructie van gebooste Higgsbosonen

In dit proefschrift wordt de resolutie van het beeld van het Higgsboson vergroot door middel van metingen aan Higgsbosonen die vrijkomen in proton-proton botsingen in de ATLAS detector met een hoge impulsoverdracht. Dit is bereikt met een nieuwe analysemethode die is ontwikkeld om Higgsbosonen  $H$  te meten die samen

met massieve vectorbosonen  $V$  worden geproduceerd en die vervallen in een paar  $b$ -quarks,  $VH, H \rightarrow b\bar{b}$ . De  $VH$  productie vormt een groot deel van de totale werkzame doorsnede voor de productie van Higgs-bosonen met hoge transversale Higgsboson impuls  $p_T^H$ . Daarnaast leiden de vervalsprocessen  $V \rightarrow$  leptonen tot duidelijke detectorsignalen waarop getriggerd kan worden, waardoor de signaal-ruisverhouding verbetert. Het gebruik van het vervalsproces naar  $b$ -quark paren, dat van alle vervalsprocessen van het Higgsboson het meeste voorkomt, zorgt voor een signaalsterkte die groot genoeg is om een meting te doen. De  $b$ -quarks zelf hadroniseren en vormen een gebundelde sproeier van deeltjes: dit zijn de zogenaamde  $b$ -jets. Het experimentele signaal dat wordt gezocht bestaat dan ook uit twee  $b$ -jets die in het loodrechte vlak van de detector afketsen tegen de leptonen die voortkomen uit het verval van het vector-boson.



Figuur 10.9: Illustratie van de reconstructie van een  $H \rightarrow b\bar{b}$  verval door middel van twee kleine- $R$  jets (links) en een grote- $R$  jet (rechts).

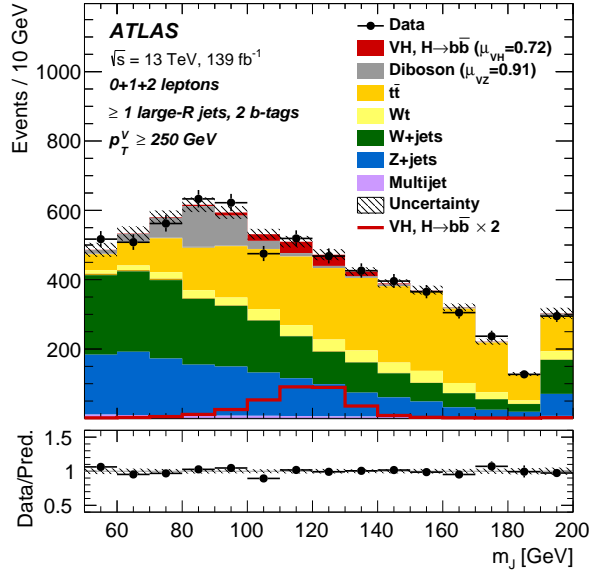
Bij hoge  $p_T^H$  komen de twee  $b$ -jets uit het verval van het Higgsboson geometrisch dicht bij elkaar te liggen door de grote Lorentz *boost* van het systeem, zoals is weergegeven in Figuur 10.9. In tegenstelling tot de vorige metingen aan  $VH, H \rightarrow b\bar{b}$  bij lage en middelgrote  $p_T^H$ , wordt de Higgsboson-kandidaat in de analyse die wordt gepresenteerd in dit proefschrift bij hoge  $p_T^H$  niet gereconstrueerd met twee jets die goed van elkaar onderscheiden worden. In plaats daarvan wordt het volledige  $H \rightarrow b\bar{b}$  verval gereconstrueerd aan de hand van een enkele jet met een grote radius. De informatie in de substructuur van het verval wordt vervolgens gebruikt om de eventuele aanwezigheid van twee  $b$ -hadronen in de jet te herleiden. Deze gebooste reconstructietechniek levert een hogere signaalacceptantie op hoge  $p_T^H$ .

## Meting van $VH, H \rightarrow b\bar{b}$ bij hoge $p_T^H$

Er bestaat een verscheidenheid aan processen binnen het standaardmodel die geen Higgsboson bevatten, maar die signalen opleveren in de ATLAS detector die erg lijken op het beoogde signaal van dit proefschrift. Aan deze processen wordt gerefereerd als achtergronden. Het doel van de gepresenteerde analyse is om de bijdrage van de achtergronden zoveel mogelijk te onderdrukken en tegelijkertijd de signaalefficiëntie te maximaliseren. Dit wordt gerealiseerd door een specifieke



selectie toe te passen en door gemeten gebeurtenissen in verschillende signaalregio's in te delen aan de hand van hun kinematische eigenschappen.



Figuur 10.10: De massadistributie van de Higgskandidaat in de  $VH, H \rightarrow b\bar{b}$  analyse bij hoge  $p_T$ , na de combinatie van alle signaalregio's.

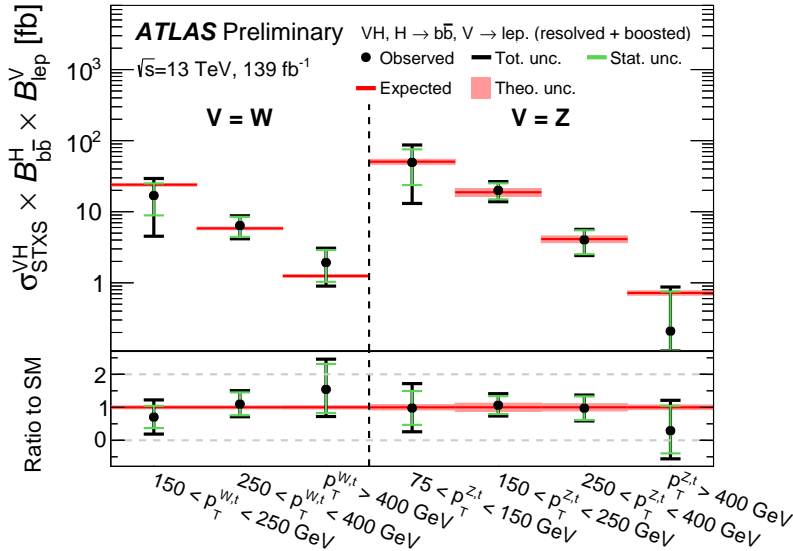
De observabele die wordt gebruikt om het signaal te achterhalen is de invariante massa van de jet van de Higgskandidaat,  $m_J$ , die naar verwachting een piek zou moeten vertonen rond 125 GeV. Deze  $m_J$ -distributie wordt getoond in Figuur 10.10 voor gebeurtenissen waarvan de transversale impuls van het gereconstrueerde vector-boson  $p_T^V$  groter is dan 250 GeV. Alle signaalregio's van de analyse zijn in dit figuur opgeteld. Duidelijk is te zien dat de analyse onderhevig is aan een verscheidenheid aan achtergronden die veel groter zijn dan het signaal, dat in het rood is aangegeven. Daarom is een goede experimentele beheersing van al deze achtergronden van groot belang voor het slagen van de meting.

De meting is gevalideerd aan de hand van gebeurtenissen met twee bosonen (diboson gebeurtenissen),  $VZ, Z \rightarrow b\bar{b}$ , die grotendeels overeenkomstig zijn met het  $VH$  signaal, maar een piek vertonen in de  $m_J$ -distributie rond de massa van het  $Z$ -boson bij  $\sim 91$  GeV. Deze bijdrage is in het grijs weergegeven in Figuur 10.10. Wanneer de diboson-controle wordt uitgevoerd, wordt in de data een overschot aan gebeurtenissen geobserveerd dat correspondeert met een significantie van 5.4 standaardafwijkingen, wat de analysestrategie bekrachtigt. Voor deze meting is een significantie van 5.7 standaardafwijkingen verwacht. Voor het  $VH$  signaal wordt een significantie van 2.1 standaardafwijkingen waargenomen en 2.7 standaardafwijkingen zijn verwacht voor een SM Higgsboson. De meting toont aan dat reconstructietechnieken voor gebooste Higgsbosonen gebruikt kunnen worden

om metingen te verrichten aan de werkzame doorsnede van  $VH$ -processen bij hoge  $p_T$  ( $250 \text{ GeV} < p_T^V < 400 \text{ GeV}$ ) en voor het eerst uitsluitend voor  $p_T^V > 400 \text{ GeV}$ .

## Een combinatie van $VH, H \rightarrow b\bar{b}$ metingen

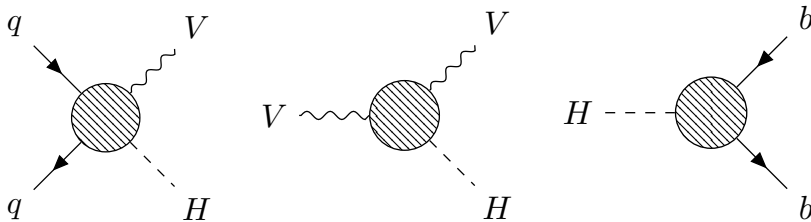
De toegewijde meting van  $VH, H \rightarrow b\bar{b}$  bij hoge  $p_T$  wordt vervolgens gecombineerd met een  $VH, H \rightarrow b\bar{b}$  meting bij lage en middelgrote  $p_T$  om de differentiële werkzame doorsnede van  $VH$  te meten als functie van  $p_T^V$  over een zo groot mogelijk bereik in  $p_T^V$ . Deze meting wordt getoond in Figuur 10.11 en vormt de meting met het grootste waarneembare bereik tot nu toe voor de differentiële werkzame doorsnede van  $VH$ , met relatieve onzekerheden die variëren tussen de 30 en 300%.



Figuur 10.11: De gemeten werkzame doorsnedes voor  $VH$  berekend aan de hand van een gesimplificeerd model, vermenigvuldigd met de vervalskans voor  $H \rightarrow b\bar{b}$  en  $V \rightarrow$  leptonen, als functie van  $p_T^V$ . De werkzame doorsnede voor  $WH$  wordt getoond in het linkerdeel van het figuur en de werkzame doorsnede voor  $ZH$  in het rechterdeel.

## Effectieve veldentheorieën

De metingen van  $VH, H \rightarrow b\bar{b}$  worden verder gebruikt om theorieën over nieuwe fysica te begrenzen binnen het raamwerk van effectieve veldentheorieën. Deze methode parametrizeert de invloed van massieve nieuwe deeltjes bij lage energieën door middel van effectieve interacties tussen de deeltjes die binnen het standaardmodel reeds bekend zijn. Het voordeel van deze methode is dat het de mogelijkheid biedt om waarneembare effecten mee te berekenen, zonder dat de eigenlijke structuur van de onderliggende theorie volledig bekend hoeft te zijn. Voorbeelden van zulke effectieve interacties die de  $pp \rightarrow VH, H \rightarrow b\bar{b}$  processen aanpassen worden getoond in Figuur 10.12.



Figuur 10.12: Voorbeelden van effectieve interacties die het productieproces  $pp \rightarrow VH$  of het vervalproces  $H \rightarrow b\bar{b}$  beïnvloeden.

Met de meting van de differentiële werkzame doorsnede van  $VH, H \rightarrow b\bar{b}$ , wordt de sterkte van deze effectieve interacties begrensd. De extra metingen bij hoge  $p_T^V$ , die mogelijk worden gemaakt door de reconstructietechnieken voor gebooste Higgs-bosonen in dit proefschrift, leiden tot een duidelijke verbetering van de huidige limieten op nieuwe theorieën die afwijkingen van het standaardmodel voorspellen die groeien bij hogere impulsoverdracht. Op deze manier wordt de gepresenteerde meting aan het Higgsboson gebruikt om grenzen te stellen aan mogelijke scenario's van nieuwe fysica tot op een schaal van enkele TeVs. De meting speelt daarom ook een belangrijke rol in de combinaties en interpretaties van Higgsmetingen van de volledige ATLAS-dataset.

## Op weg naar de tweede generatie

Alhoewel de precisie van de koppelingen met fermionen van de derde generatie geleidelijk aan groeit, is er weinig experimenteel bewijs rondom de interacties tussen het Higgsboson en fermionen van de tweede en de eerste generatie. Het standaardmodel voorspelt dat deze interacties zwakker zouden moeten zijn dan voor de fermionen van de derde generatie, omdat de koppeling van het Higgsboson evenredig is met de corresponderende fermion-massa's. Het meten van de hiërarchie van de sterkte van de koppelingen vormt daarom een belangrijke test van het standaardmodel. In het laatste deel van het proefschrift wordt de meting van

$VH, H \rightarrow b\bar{b}$  gecombineerd met een directe zoektocht naar  $VH, H \rightarrow c\bar{c}$ . Deze combinatie biedt de mogelijkheid om de verhouding te meten van de interactiesterkte tussen het Higgsboson en  $b$ -quarks en tussen het Higgsboson en  $c$ -quarks. Daarmee vormt het een toets voor de hiërarchie tussen de tweede en de derde generatie. Dit is de eerste meting die met een betrouwbaarheid van 95% kan uitsluiten dat het Higgsboson sterker of even sterk koppelt aan  $c$ -quarks dan aan  $b$ -quarks.

## Vooruitblik

Alhoewel het Higgsboson zich op dit moment lijkt te gedragen zoals door het standaardmodel wordt voorspeld, is voorzichtigheid geboden. Zoals het verhaal van Schiaparelli aantoont, is het bereiken van een hoge resolutie cruciaal bij het trekken van de juiste conclusies. De weg naar het vervaardigen van een afbeelding van het Higgsboson met een hoog oplossend vermogen is reeds ingezet. In de komende jaren wordt verwacht dat de LHC en zijn upgrade de dataset voor proton-proton botsingen zal vergroten met een factor 20. De bijkomstige detectoruitbreidingen, verbeteringen van analysetechnieken en verhoogde precisies van theoretische berekeningen, zullen deeltjesfysici uiteindelijk in staat stellen om het Higgsboson in HD te observeren. De deeltjesfysica gaat een spannende tijd tegemoet.

# Bibliography

- [1] ATLAS Collaboration, *Observation of a new particle in the search for the Standard Model Higgs boson with the ATLAS detector at the LHC*, Phys. Lett. B **716** (2012) 1, arXiv: 1207.7214 [hep-ex].
- [2] CMS Collaboration, *Observation of a new boson at a mass of 125 GeV with the CMS experiment at the LHC*, Phys. Lett. B **716** (2012) 30, arXiv: 1207.7235 [hep-ex].
- [3] S. D. Bass, A. De Roeck, and M. Kado, *The Higgs boson - its implications and prospects for future discoveries*, 2021, arXiv: 2104.06821 [hep-ph].
- [4] ATLAS Collaboration, *Combined measurements of Higgs boson production and decay using up to 139 fb<sup>-1</sup> of proton-proton collision data at  $\sqrt{s} = 13$  TeV collected with the ATLAS experiment*, ATLAS-CONF-2021-053, 2021, URL: <http://cds.cern.ch/record/2789544>.
- [5] ATLAS Collaboration, *Measurement of the associated production of a Higgs boson decaying into b-quarks with a vector boson at high transverse momentum in pp collisions at  $\sqrt{s} = 13$  TeV with the ATLAS detector*, Physics Letters B **816** (2021) 136204, arXiv: 2008.02508 [hep-ex].
- [6] ATLAS Collaboration, *Measurements of WH and ZH production in the  $H \rightarrow b\bar{b}$  decay channel in pp collisions at 13 TeV with the ATLAS detector*, Eur. Phys. J. C **81** (2021) 178, arXiv: 2007.02873 [hep-ex].
- [7] ATLAS Collaboration, *Combination of measurements of Higgs boson production in association with a W or Z boson in the  $b\bar{b}$  decay channel with the ATLAS experiment at  $\sqrt{s} = 13$  TeV*, ATLAS-CONF-2021-051, 2021, URL: <http://cds.cern.ch/record/2782535>.
- [8] ATLAS Collaboration, *Direct constraint on the Higgs-charm coupling from a search for Higgs boson decays to charm quarks with the ATLAS detector*, ATLAS-CONF-2021-021, 2021, URL: <http://cds.cern.ch/record/2771724>.
- [9] F. Halzen and A. D. Martin, *Quarks & Leptons: An introductory course in modern particle physics*, John Wiley & Sons, 1984, ISBN: 978-0-471-88741-6.
- [10] A. Pich, *The Standard Model of Electroweak Interactions*, 2012, arXiv: 1201.0537 [hep-ph].
- [11] M. Thomson, *Modern particle physics*, Cambridge University Press, 2013, ISBN: 978-1-107-03426-6.

- [12] C. Burgard, *Standard model infographics*,  
URL: <https://texample.net/tikz/examples/model-physics/>.
- [13] Particle Data Group, *Review of Particle Physics*,  
PTEP **2020** (2020) 083C01.
- [14] H. Fritzsch, M. Gell-Mann, and H. Leutwyler,  
*Advantages of the Color Octet Gluon Picture*, Phys. Lett. B **47** (1973) 365.
- [15] D. J. Gross and F. Wilczek, *Asymptotically Free Gauge Theories - I*,  
Phys. Rev. D **8** (1973) 3633.
- [16] H. D. Politzer, *Reliable Perturbative Results for Strong Interactions?*,  
Phys. Rev. Lett. **30** (1973) 1346, ed. by J. C. Taylor.
- [17] S. L. Glashow, *Partial Symmetries of Weak Interactions*,  
Nucl. Phys. **22** (1961) 579.
- [18] A. Salam and J. C. Ward, *Electromagnetic and weak interactions*,  
Phys. Lett. **13** (1964) 168.
- [19] S. Weinberg, *A Model of Leptons*, Phys. Rev. Lett. **19** (1967) 1264.
- [20] P. W. Higgs, *Broken Symmetries and the Masses of Gauge Bosons*,  
Phys. Rev. Lett. **13** (16 1964) 508.
- [21] P. W. Higgs, *Spontaneous symmetry breakdown without massless bosons*,  
Phys. Rev. **145** (1966) 1156.
- [22] F. Englert and R. Brout,  
*Broken Symmetry and the Mass of Gauge Vector Mesons*,  
Phys. Rev. Lett. **13** (9 1964) 321.
- [23] G. S. Guralnik, C. R. Hagen, and T. W. B. Kibble,  
*Global Conservation Laws and Massless Particles*,  
Phys. Rev. Lett. **13** (20 1964) 585.
- [24] T. W. B. Kibble, *Symmetry Breaking in Non-Abelian Gauge Theories*,  
Phys. Rev. **155** (5 1967) 1554.
- [25] N. Cabibbo, *Unitary Symmetry and Leptonic Decays*,  
Phys. Rev. Lett. **10** (1963) 531.
- [26] M. Kobayashi and T. Maskawa,  
*CP Violation in the Renormalizable Theory of Weak Interaction*,  
Prog. Theor. Phys. **49** (1973) 652.
- [27] G. 't Hooft, *Renormalization of Massless Yang-Mills Fields*,  
Nucl. Phys. B **33** (1971) 173.
- [28] G. 't Hooft, *Renormalizable Lagrangians for Massive Yang-Mills Fields*,  
Nucl. Phys. B **35** (1971) 167, ed. by J. C. Taylor.
- [29] C. Bouchiat, J. Iliopoulos, and P. Meyer,  
*An Anomaly Free Version of Weinberg's Model*,  
Phys. Lett. B **38** (1972) 519.

- [30] ALEPH, DELPHI, L3, OPAL, SLD, LEP Electroweak Working Group, SLD Electroweak Group, SLD Heavy Flavour Group, *Precision electroweak measurements on the Z resonance*, Phys. Rept. **427** (2006) 257, arXiv: [hep-ex/0509008](#).
- [31] P. Janot and S. Jadach, *Improved Bhabha cross section at LEP and the number of light neutrino species*, Phys. Lett. B **803** (2020) 135319, arXiv: [1912.02067 \[hep-ph\]](#).
- [32] F. Hasert et al., *Search for elastic muon-neutrino electron scattering*, Physics Letters B **46** (1973) 121, ISSN: 0370-2693.
- [33] D. Denegri, *The discovery of the W and Z*, Phys. Rept. **403-404** (2004) 107.
- [34] CDF Collaboration, *Observation of top quark production in  $\bar{p}p$  collisions*, Phys. Rev. Lett. **74** (1995) 2626, arXiv: [hep-ex/9503002](#).
- [35] D0 Collaboration, *Observation of the top quark*, Phys. Rev. Lett. **74** (1995) 2632, arXiv: [hep-ex/9503003](#).
- [36] DONUT Collaboration, *Observation of tau neutrino interactions*, Phys. Lett. B **504** (2001) 218, arXiv: [hep-ex/0012035](#).
- [37] G. 't Hooft, *Symmetry Breaking through Bell-Jackiw Anomalies*, Phys. Rev. Lett. **37** (1 1976) 8.
- [38] R. D. Peccei and H. R. Quinn, *Constraints Imposed by CP Conservation in the Presence of Instantons*, Phys. Rev. D **16** (1977) 1791.
- [39] Super-Kamiokande Collaboration, *Evidence for oscillation of atmospheric neutrinos*, Phys. Rev. Lett. **81** (1998) 1562, arXiv: [hep-ex/9807003](#).
- [40] SNO Collaboration, *Measurement of the rate of  $\nu_e + d \rightarrow p + p + e^-$  interactions produced by  $^8B$  solar neutrinos at the Sudbury Neutrino Observatory*, Phys. Rev. Lett. **87** (2001) 071301, arXiv: [nucl-ex/0106015](#).
- [41] KamLAND Collaboration, *Precision Measurement of Neutrino Oscillation Parameters with KamLAND*, Phys. Rev. Lett. **100** (2008) 221803, arXiv: [0801.4589 \[hep-ex\]](#).
- [42] KATRIN Collaboration, *Improved Upper Limit on the Neutrino Mass from a Direct Kinematic Method by KATRIN*, Phys. Rev. Lett. **123** (2019) 221802, arXiv: [1909.06048 \[hep-ex\]](#).
- [43] Planck Collaboration, *Planck 2015 results. I. Overview of products and scientific results*, Astron. Astrophys. **594** (2016) A1, arXiv: [1502.01582 \[astro-ph.CO\]](#).
- [44] The Supernova Cosmology Project, *Measurements of  $\Omega$  and  $\Lambda$  from 42 high redshift supernovae*, Astrophys. J. **517** (1999) 565, arXiv: [astro-ph/9812133](#).

- [45] A. G. Riess et al., *Observational evidence from supernovae for an accelerating universe and a cosmological constant*, Astron. J. **116** (1998) 1009, arXiv: astro-ph/9805201.
- [46] J. Martin, *Everything You Always Wanted To Know About The Cosmological Constant Problem (But Were Afraid To Ask)*, Comptes Rendus Physique **13** (2012) 566, arXiv: 1205.3365 [astro-ph.CO].
- [47] M. B. Gavela, P. Hernandez, J. Orloff, and O. Pene, *Standard model CP violation and baryon asymmetry*, Mod. Phys. Lett. A **9** (1994) 795, arXiv: hep-ph/9312215.
- [48] T. Appelquist and J. Carazzone, *Infrared singularities and massive fields*, Phys. Rev. D **11** (10 1975) 2856.
- [49] A. Falkowski et al., *Rosetta: an operator basis translator for Standard Model effective field theory*, Eur. Phys. J. C **75** (2015) 583, arXiv: 1508.05895 [hep-ph].
- [50] B. Henning, X. Lu, T. Melia, and H. Murayama, *2, 84, 30, 993, 560, 15456, 11962, 261485, ...: Higher dimension operators in the SM EFT*, JHEP **08** (2017) 016, [Erratum: JHEP 09, 019 (2019)], arXiv: 1512.03433 [hep-ph].
- [51] S. Weinberg, *Baryon- and Lepton-Nonconserving Processes*, Phys. Rev. Lett. **43** (21 1979) 1566.
- [52] F. Wilczek and A. Zee, *Operator Analysis of Nucleon Decay*, Phys. Rev. Lett. **43** (21 1979) 1571.
- [53] W. Buchmuller and D. Wyler, *Effective Lagrangian Analysis of New Interactions and Flavor Conservation*, Nucl. Phys. B **268** (1986) 621.
- [54] B. Grzadkowski, M. Iskrzynski, M. Misiak, and J. Rosiek, *Dimension-Six Terms in the Standard Model Lagrangian*, JHEP **10** (2010) 085, arXiv: 1008.4884 [hep-ph].
- [55] L. Lehman, *Extending the Standard Model Effective Field Theory with the Complete Set of Dimension-7 Operators*, Phys. Rev. D **90** (2014) 125023, arXiv: 1410.4193 [hep-ph].
- [56] C. W. Murphy, *Dimension-8 operators in the Standard Model Effective Field Theory*, JHEP **10** (2020) 174, arXiv: 2005.00059 [hep-ph].
- [57] I. Brivio, Y. Jiang, and M. Trott, *The SMEFTsim package, theory and tools*, JHEP **12** (2017) 070, arXiv: 1709.06492 [hep-ph].
- [58] J. Ellis, M. Madigan, K. Mimasu, V. Sanz, and T. You, *Top, Higgs, Diboson and Electroweak Fit to the Standard Model Effective Field Theory*, JHEP **04** (2021) 279, arXiv: 2012.02779 [hep-ph].



- [59] R. K. Ellis, W. J. Stirling, and B. R. Webber, *QCD and collider physics*, vol. 8, Cambridge University Press, 2011, ISBN: 978-0-511-82328-2, 978-0-521-54589-1.
- [60] NNPDF Collaboration, *Parton distributions from high-precision collider data*, Eur. Phys. J. C **77** (2017) 663, arXiv: 1706.00428 [hep-ph].
- [61] A. Bhatti and D. Lincoln, *Jet Physics at the Tevatron*, Ann. Rev. Nucl. Part. Sci. **60** (2010) 267, arXiv: 1002.1708 [hep-ex].
- [62] A. V. Bednyakov, B. A. Kniehl, A. F. Pikelner, and O. L. Veretin, *Stability of the Electroweak Vacuum: Gauge Independence and Advanced Precision*, Phys. Rev. Lett. **115** (2015) 201802, arXiv: 1507.08833 [hep-ph].
- [63] M. J. G. Veltman, *Reflections on the Higgs system*, CERN Yellow Reports: Monographs, Lectures given in the Academic Training Program of CERN 1996-1997, URL: <http://cds.cern.ch/record/2654857>.
- [64] J. Fumagalli, *Running in the early Universe: UV sensitivity of single-field inflationary models*, 2018.
- [65] M. Reichert et al., *Probing baryogenesis through the Higgs boson self-coupling*, Phys. Rev. D **97** (2018) 075008, arXiv: 1711.00019.
- [66] B. Patt and F. Wilczek, *Higgs-field portal into hidden sectors*, (2006), arXiv: hep-ph/0605188.
- [67] LHC Higgs Cross Section Working Group, *Handbook of LHC Higgs cross sections: 4. Deciphering the nature of the Higgs sector*, CERN-2017-002 (2017), arXiv: 1610.07922 [hep-ph].
- [68] LHC Higgs Cross Section Working Group, *Handbook of LHC Higgs Cross Sections: 3. Higgs Properties*, CERN-2013-004 (2013), arXiv: 1307.1347 [hep-ph].
- [69] ATLAS Collaboration, *A combination of measurements of Higgs boson production and decay using up to  $139\text{ fb}^{-1}$  of proton-proton collision data at  $\sqrt{s} = 13\text{ TeV}$  collected with the ATLAS experiment*, ATLAS-CONF-2020-027, 2020, URL: <https://cds.cern.ch/record/2725733>.
- [70] CMS Collaboration, *Observation of a new boson with mass near  $125\text{ GeV}$  in  $pp$  collisions at  $\sqrt{s} = 7$  and  $8\text{ TeV}$* , JHEP **06** (2013) 081, arXiv: 1303.4571 [hep-ex].
- [71] ATLAS Collaboration, *Study of the spin and parity of the Higgs boson in diboson decays with the ATLAS detector*, Eur. Phys. J. C **75** (2015) 476, arXiv: 1506.05669 [hep-ex], Erratum: Eur. Phys. J. C **76** (2016) 152.

- [72] ATLAS Collaboration,  
*Study of the CP properties of the interaction of the Higgs boson with top quarks using top quark associated production of the Higgs boson and its decay into two photons with the ATLAS detector at the LHC*,  
Phys. Rev. Lett. **125** (2020) 061802, arXiv: 2004.04545 [hep-ex].
- [73] ATLAS Collaboration, *Test of CP invariance in vector-boson fusion production of the Higgs boson in the  $H \rightarrow \tau\tau$  channel in proton-proton collisions at  $\sqrt{s} = 13$  TeV with the ATLAS detector*,  
Phys. Lett. B **805** (2020) 135426, arXiv: 2002.05315 [hep-ex].
- [74] ATLAS Collaboration,  
*Constraints on Higgs boson properties using  $WW^*(\rightarrow e\nu\mu\nu)jj$  production in  $36.1\text{fb}^{-1}$  of  $\sqrt{s} = 13$  TeV  $pp$  collisions with the ATLAS detector*,  
ATLAS-CONF-2020-055, 2020,  
URL: <http://cds.cern.ch/record/2743624>.
- [75] ATLAS Collaboration, *Measurement of the properties of Higgs boson production at  $\sqrt{s} = 13$  TeV in the  $H \rightarrow \gamma\gamma$  channel using  $139\text{fb}^{-1}$  of  $pp$  collision data with the ATLAS experiment*, ATLAS-CONF-2020-026, 2020,  
URL: <https://cds.cern.ch/record/2725727>.
- [76] ATLAS Collaboration, *Combined measurement of the total and differential cross sections in the  $H \rightarrow \gamma\gamma$  and  $H \rightarrow ZZ^* \rightarrow 4\ell$  decay channels at  $\sqrt{s} = 13$  TeV with the ATLAS detector*, ATLAS-CONF-2019-032, 2019,  
URL: <https://cds.cern.ch/record/2682844>.
- [77] ATLAS Collaboration, *Higgs boson production cross-section measurements and their EFT interpretation in the  $4\ell$  decay channel at  $\sqrt{s} = 13$  TeV with the ATLAS detector*, 2020, arXiv: 2004.03447 [hep-ex].
- [78] ATLAS Collaboration, *Measurements of the Higgs boson inclusive and differential fiducial cross sections in the  $4\ell$  decay channel at  $\sqrt{s} = 13$  TeV*,  
Eur. Phys. J. C **80** (2020) 942, arXiv: 2004.03969 [hep-ex].
- [79] ATLAS Collaboration, *Measurements of gluon fusion and vector-boson-fusion production of the Higgs boson in  $H \rightarrow WW^* \rightarrow e\nu\mu\nu$  decays using  $pp$  collisions at  $\sqrt{s} = 13$  TeV with the ATLAS detector*,  
ATLAS-CONF-2021-014, 2021,  
URL: <http://cds.cern.ch/record/2759651>.
- [80] ATLAS Collaboration,  
*Measurement of the Higgs boson mass in the  $H \rightarrow ZZ^* \rightarrow 4\ell$  decay channel with  $\sqrt{s} = 13$  TeV  $pp$  collisions using the ATLAS detector at the LHC*,  
ATLAS-CONF-2020-005, 2020,  
URL: <https://cds.cern.ch/record/2714883>.
- [81] ATLAS Collaboration,  
*Constraints on off-shell Higgs boson production and the Higgs boson total width in  $ZZ \rightarrow 4\ell$  and  $ZZ \rightarrow 2\ell 2\nu$  final states with the ATLAS detector*,  
Phys. Lett. B **786** (2018) 223, arXiv: 1808.01191 [hep-ex].

- [82] ATLAS Collaboration, *Measurements of Higgs boson production cross-sections in the  $H \rightarrow \tau^+\tau^-$  decay channel in  $pp$  collisions at  $\sqrt{s} = 13$  TeV with the ATLAS detector*, ATLAS-CONF-2021-044, 2021, URL: <http://cds.cern.ch/record/2779179>.
- [83] ATLAS Collaboration, *Observation of Higgs boson production in association with a top quark pair at the LHC with the ATLAS detector*, Phys. Lett. B **784** (2018) 173, arXiv: 1806.00425 [hep-ex].
- [84] ATLAS Collaboration, *A search for the dimuon decay of the Standard Model Higgs boson with the ATLAS detector*, 2020, arXiv: 2007.07830 [hep-ex].
- [85] ATLAS Collaboration, *Search for Higgs boson pair production in the two bottom quarks plus two photons final state in  $pp$  collisions at  $\sqrt{s} = 13$  TeV with the ATLAS detector*, ATLAS-CONF-2021-016, 2021, URL: <http://cds.cern.ch/record/2759683>.
- [86] ATLAS Collaboration, *Search for resonant and non-resonant Higgs boson pair production in the  $b\bar{b}\tau^+\tau^-$  decay channel using 13 TeV  $pp$  collision data from the ATLAS detector*, ATLAS-CONF-2021-030, 2021, URL: <http://cds.cern.ch/record/2777236>.
- [87] ATLAS Collaboration, *Measurements of the Higgs boson production and decay rates and coupling strengths using  $pp$  collision data at  $\sqrt{s} = 7$  and 8 TeV in the ATLAS experiment*, Eur. Phys. J. C **76** (2016) 6, arXiv: 1507.04548 [hep-ex].
- [88] ATLAS Collaboration, *Projections for measurements of Higgs boson cross sections, branching ratios, coupling parameters and mass with the ATLAS detector at the HL-LHC*, ATL-PHYS-PUB-2018-054, 2018, URL: <https://cds.cern.ch/record/2652762>.
- [89] L. Evans and P. Bryant, *LHC Machine*, JINST **3** (2008) S08001.
- [90] *LEP Design Report: Vol.2. The LEP Main Ring*, CERN-LEP-84-01, 1984, URL: <https://cds.cern.ch/record/102083>.
- [91] E. A. Mobs, *The CERN accelerator complex. Complexe des accélérateurs du CERN*, (2016), General Photo, URL: <https://cds.cern.ch/record/2225847>.
- [92] CMS Collaboration, *The CMS experiment at the CERN LHC*, JINST **3** (2008) S08004.
- [93] LHCb Collaboration, *The LHCb Detector at the LHC*, JINST **3** (2008) S08005.
- [94] ALICE Collaboration, *The ALICE experiment at the CERN LHC*, JINST **3** (2008) S08002.
- [95] ATLAS Collaboration, *The ATLAS Experiment at the CERN Large Hadron Collider*, JINST **3** (2008) S08003.

- [96] J. Pequenaio and P. Schaffner, *How ATLAS detects particles: diagram of particle paths in the detector*, 2013, URL: <https://cds.cern.ch/record/1505342>.
- [97] ATLAS Collaboration, *Alignment of the ATLAS Inner Detector in Run-2*, 2020, arXiv: 2007.07624 [hep-ex].
- [98] ATLAS Collaboration, *ATLAS Insertable B-Layer: Technical Design Report*, ATLAS-TDR-19; CERN-LHCC-2010-013, 2010, URL: <https://cds.cern.ch/record/1291633>.
- [99] ATLAS IBL Collaboration, *Production and integration of the ATLAS Insertable B-Layer*, JINST **13** (2018) T05008, arXiv: 1803.00844 [physics.ins-det].
- [100] ATLAS Collaboration, *Performance of the ATLAS Transition Radiation Tracker in Run 1 of the LHC: tracker properties*, JINST **12** (2017) P05002, arXiv: 1702.06473 [hep-ex].
- [101] G. Avoni et al., *The new LUCID-2 detector for luminosity measurement and monitoring in ATLAS*, Journal of Instrumentation **13** (2018) P07017.
- [102] ATLAS Collaboration, *Luminosity determination in pp collisions at  $\sqrt{s} = 13$  TeV using the ATLAS detector at the LHC*, ATLAS-CONF-2019-021, 2019, URL: <https://cds.cern.ch/record/2677054>.
- [103] ATLAS Collaboration, *Approved Plots DAQ*, Accessed on 27.08.2021, URL: <https://twiki.cern.ch/twiki/bin/view/AtlasPublic/ApprovedPlotsDAQ>.
- [104] ATLAS Collaboration, *Performance of the ATLAS trigger system in 2015*, Eur. Phys. J. C **77** (2017) 317, arXiv: 1611.09661 [hep-ex].
- [105] ATLAS Collaboration, *Luminosity Public Results: Run 2*, Accessed on 17.08.2021, URL: <https://twiki.cern.ch/twiki/bin/view/AtlasPublic/LuminosityPublicResultsRun2>.
- [106] ATLAS Collaboration, *ATLAS Computing: Technical Design Report*, ATLAS-TDR-17; CERN-LHCC-2005-022, 2005, URL: <https://cds.cern.ch/record/837738>.
- [107] ATLAS Collaboration, *Performance of the ATLAS track reconstruction algorithms in dense environments in LHC Run 2*, Eur. Phys. J. C **77** (2017) 673, arXiv: 1704.07983 [hep-ex].
- [108] R. Frühwirth, *Application of Kalman filtering to track and vertex fitting*, Nuclear Instruments and Methods in Physics Research Section A: Accelerators, Spectrometers, Detectors and Associated Equipment **262** (1987) 444, ISSN: 0168-9002.
- [109] ATLAS Collaboration, *Reconstruction of primary vertices at the ATLAS experiment in Run 1 proton-proton collisions at the LHC*, Eur. Phys. J. C **77** (2017) 332, arXiv: 1611.10235 [hep-ex].

- [110] ATLAS Collaboration, *Vertex Reconstruction Performance of the ATLAS Detector at  $\sqrt{s} = 13$  TeV*, ATL-PHYS-PUB-2015-026, 2015, URL: <https://cds.cern.ch/record/2037717>.
- [111] ATLAS Collaboration, *Topological cell clustering in the ATLAS calorimeters and its performance in LHC Run 1*, Eur. Phys. J. C **77** (2017) 490, arXiv: 1603.02934 [hep-ex].
- [112] ATLAS Collaboration, *Electron reconstruction and identification in the ATLAS experiment using the 2015 and 2016 LHC proton-proton collision data at  $\sqrt{s} = 13$  TeV*, Eur. Phys. J. C **79** (2019) 639, arXiv: 1902.04655 [hep-ex].
- [113] ATLAS Collaboration, *Electron and photon performance measurements with the ATLAS detector using the 2015–2017 LHC proton-proton collision data*, JINST **14** (2019) P12006, arXiv: 1908.00005 [hep-ex].
- [114] ATLAS Collaboration, *Improved electron reconstruction in ATLAS using the Gaussian Sum Filter-based model for bremsstrahlung*, ATLAS-CONF-2012-047, 2012, URL: <https://cds.cern.ch/record/1449796>.
- [115] ATLAS Collaboration, *Electron and photon reconstruction and performance in ATLAS using a dynamical, topological cell clustering-based approach*, ATL-PHYS-PUB-2017-022, 2017, URL: <https://cds.cern.ch/record/2298955>.
- [116] ATLAS Collaboration, *Muon reconstruction performance of the ATLAS detector in proton-proton collision data at  $\sqrt{s} = 13$  TeV*, Eur. Phys. J. C **76** (2016) 292, arXiv: 1603.05598 [hep-ex].
- [117] ATLAS Collaboration, *Muon reconstruction and identification efficiency in ATLAS using the full Run 2 pp collision data set at  $\sqrt{s} = 13$  TeV*, 2020, arXiv: 2012.00578 [hep-ex].
- [118] G. P. Salam, *Towards Jetography*, Eur. Phys. J. C **67** (2010) 637, arXiv: 0906.1833 [hep-ph].
- [119] M. Cacciari, G. P. Salam, and G. Soyez, *The anti- $k_t$  jet clustering algorithm*, JHEP **04** (2008) 063, arXiv: 0802.1189 [hep-ph].
- [120] M. Cacciari, G. P. Salam, and G. Soyez, *FastJet user manual*, Eur. Phys. J. C **72** (2012) 1896, arXiv: 1111.6097 [hep-ph].
- [121] S. Catani, Y. L. Dokshitzer, M. H. Seymour, and B. R. Webber, *Longitudinally invariant  $K_t$  clustering algorithms for hadron hadron collisions*, Nucl. Phys. B **406** (1993) 187.
- [122] S. D. Ellis and D. E. Soper, *Successive combination jet algorithm for hadron collisions*, Phys. Rev. D **48** (7 1993) 3160.

- [123] ATLAS Collaboration, *Jet energy scale and resolution measured in proton–proton collisions at  $\sqrt{s} = 13$  TeV with the ATLAS detector*, 2020, arXiv: 2007.02645 [hep-ex].
- [124] ATLAS Collaboration, *Performance of pile-up mitigation techniques for jets in pp collisions at  $\sqrt{s} = 8$  TeV using the ATLAS detector*, Eur. Phys. J. C **76** (2016) 581, arXiv: 1510.03823 [hep-ex].
- [125] ATLAS Collaboration, *In situ calibration of large-radius jet energy and mass in 13 TeV proton–proton collisions with the ATLAS detector*, Eur. Phys. J. C **79** (2019) 135, arXiv: 1807.09477 [hep-ex].
- [126] D. Krohn, J. Thaler, and L.-T. Wang, *Jet Trimming*, JHEP **02** (2010) 084, arXiv: 0912.1342 [hep-ph].
- [127] ATLAS Collaboration, *Identification of boosted, hadronically decaying  $W$  bosons and comparisons with ATLAS data taken at  $\sqrt{s} = 8$  TeV*, Eur. Phys. J. C **76** (2016) 154, arXiv: 1510.05821 [hep-ex].
- [128] ATLAS Collaboration, *Performance of jet substructure techniques for large- $R$  jets in proton–proton collisions at  $\sqrt{s} = 7$  TeV using the ATLAS detector*, JHEP **09** (2013) 076, arXiv: 1306.4945 [hep-ex].
- [129] ATLAS Collaboration, *Jet mass reconstruction with the ATLAS Detector in early Run 2 data*, ATLAS-CONF-2016-035, 2016, URL: <https://cds.cern.ch/record/2200211>.
- [130] M. Cacciari, G. P. Salam, and G. Soyez, *The Catchment Area of Jets*, JHEP **04** (2008) 005, arXiv: 0802.1188 [hep-ph].
- [131] M. Cacciari and G. P. Salam, *Pileup subtraction using jet areas*, Phys. Lett. B **659** (2008) 119, arXiv: 0707.1378 [hep-ph].
- [132] D. Krohn, J. Thaler, and L.-T. Wang, *Jets with Variable  $R$* , JHEP **06** (2009) 059, arXiv: 0903.0392 [hep-ph].
- [133] ATLAS Collaboration, *Variable Radius, Exclusive- $k_T$ , and Center-of-Mass Subjet Reconstruction for Higgs( $\rightarrow b\bar{b}$ ) Tagging in ATLAS*, ATL-PHYS-PUB-2017-010, 2017, URL: <https://cds.cern.ch/record/2268678>.
- [134] ATLAS Collaboration, *Measurement of the tau lepton reconstruction and identification performance in the ATLAS experiment using pp collisions at  $\sqrt{s} = 13$  TeV*, ATLAS-CONF-2017-029, 2017, URL: <https://cds.cern.ch/record/2261772>.
- [135] ATLAS Collaboration,  *$E_T^{miss}$  performance in the ATLAS detector using 2015–2016 LHC pp collisions*, ATLAS-CONF-2018-023, 2018, URL: <https://cds.cern.ch/record/2625233>.
- [136] Y. S. Amhis et al., *Averages of  $b$ -hadron,  $c$ -hadron, and  $\tau$ -lepton properties as of 2018*, Eur. Phys. J. C **81** (2021) 226, arXiv: 1909.12524 [hep-ex].

- [137] ATLAS Collaboration, *Monte Carlo to Monte Carlo scale factors for flavour tagging efficiency calibration*, ATL-PHYS-PUB-2020-009, 2020, URL: <https://cds.cern.ch/record/2718610>.
- [138] ATLAS Collaboration, *Comparison of Monte Carlo generator predictions for bottom and charm hadrons in the decays of top quarks and the fragmentation of high  $p_T$  jets*, ATL-PHYS-PUB-2014-008, 2014, URL: <https://cds.cern.ch/record/1709132>.
- [139] ATLAS Collaboration, *Optimisation and performance studies of the ATLAS b-tagging algorithms for the 2017-18 LHC run*, ATL-PHYS-PUB-2017-013, 2017, URL: <https://cds.cern.ch/record/2273281>.
- [140] ATLAS Collaboration, *Secondary vertex finding for jet flavour identification with the ATLAS detector*, ATL-PHYS-PUB-2017-011, 2017, URL: <https://cds.cern.ch/record/2270366>.
- [141] ATLAS Collaboration, *Topological b-hadron decay reconstruction and identification of b-jets with the JetFitter package in the ATLAS experiment at the LHC*, ATL-PHYS-PUB-2018-025, 2018, URL: <https://cds.cern.ch/record/2645405>.
- [142] ATLAS Collaboration, *ATLAS b-jet identification performance and efficiency measurement with  $t\bar{t}$  events in pp collisions at  $\sqrt{s} = 13$  TeV*, Eur. Phys. J. C **79** (2019) 970, arXiv: 1907.05120 [hep-ex].
- [143] ATLAS Collaboration, *Measurement of the c-jet mistagging efficiency in  $t\bar{t}$  events using pp collision data at  $\sqrt{s} = 13$  TeV collected with the ATLAS detector*, 2021, arXiv: 2109.10627 [hep-ex].
- [144] ATLAS Collaboration, *Calibration of light-flavour b-jet mistagging rates using ATLAS proton–proton collision data at  $\sqrt{s} = 13$  TeV*, ATLAS-CONF-2018-006, 2018, URL: <https://cds.cern.ch/record/2314418>.
- [145] ATLAS Collaboration, *Simulation-based extrapolation of b-tagging calibrations towards high transverse momenta in the ATLAS experiment*, ATL-PHYS-PUB-2021-003, 2021, URL: <http://cds.cern.ch/record/2753444>.
- [146] ATLAS Collaboration, *Calibration of ATLAS b-tagging algorithms in dense jet environments*, ATLAS-CONF-2016-001, 2015, URL: <https://cds.cern.ch/record/2127958>.
- [147] ATLAS Collaboration, *Calibration of the ATLAS b-tagging algorithm in  $t\bar{t}$  semileptonic events*, ATLAS-CONF-2018-045, 2018, URL: <https://cds.cern.ch/record/2638455>.

- [148] ATLAS Collaboration, *Jet reconstruction and performance using particle flow with the ATLAS Detector*, Eur. Phys. J. C **77** (2017) 466, arXiv: 1703.10485 [hep-ex].
- [149] D. Duda, *Identification of bottom-quarks in searches for new heavy resonances decaying into boosted top-quarks with the ATLAS detector and a development of an improved b-tagging algorithm*, 2015, URL: <https://cds.cern.ch/record/2069170>.
- [150] K. Becker et al., *Precise predictions for boosted Higgs production*, 2020, URL: <https://cds.cern.ch/record/2718578>.
- [151] ATLAS Collaboration, *Evidence for the  $H \rightarrow b\bar{b}$  decay with the ATLAS detector*, JHEP **12** (2017) 024, arXiv: 1708.03299 [hep-ex].
- [152] ATLAS Collaboration, *Observation of  $H \rightarrow b\bar{b}$  decays and  $VH$  production with the ATLAS detector*, Phys. Lett. B **786** (2018) 59, arXiv: 1808.08238 [hep-ex].
- [153] S. Alioli, P. Nason, C. Oleari, and E. Re, *A general framework for implementing NLO calculations in shower Monte Carlo programs: the POWHEG BOX*, JHEP **06** (2010) 043, arXiv: 1002.2581 [hep-ph].
- [154] NNPDF Collaboration, *Parton distributions for the LHC run II*, JHEP **04** (2015) 040, arXiv: 1410.8849 [hep-ph].
- [155] T. Sjöstrand et al., *An introduction to PYTHIA 8.2*, Comput. Phys. Commun. **191** (2015) 159, arXiv: 1410.3012 [hep-ph].
- [156] ATLAS Collaboration, *Measurement of the  $Z/\gamma^*$  boson transverse momentum distribution in  $pp$  collisions at  $\sqrt{s} = 7$  TeV with the ATLAS detector*, JHEP **09** (2014) 145, arXiv: 1406.3660 [hep-ex].
- [157] G. Cullen et al., *Automated One-Loop Calculations with GoSam*, Eur. Phys. J. C **72** (2012) 1889, arXiv: 1111.2034 [hep-ph].
- [158] K. Hamilton, P. Nason, and G. Zanderighi, *MINLO: Multi-Scale Improved NLO*, JHEP **10** (2012) 155, arXiv: 1206.3572 [hep-ph].
- [159] G. Luisoni, P. Nason, C. Oleari, and F. Tramontano,  *$HW^\pm/HZ + 0$  and 1 jet at NLO with the POWHEG BOX interfaced to GoSam and their merging within MiNLO*, JHEP **10** (2013) 083, arXiv: 1306.2542 [hep-ph].
- [160] M. L. Ciccolini, S. Dittmaier, and M. Krämer, *Electroweak radiative corrections to associated  $WH$  and  $ZH$  production at hadron colliders*, Phys. Rev. D **68** (2003) 073003, arXiv: hep-ph/0306234 [hep-ph].
- [161] O. Brein, A. Djouadi, and R. Harlander, *NNLO QCD corrections to the Higgs-strahlung processes at hadron colliders*, Phys. Lett. B **579** (2004) 149, arXiv: hep-ph/0307206.



- [162] G. Ferrera, M. Grazzini, and F. Tramontano, *Associated Higgs-W-Boson Production at Hadron Colliders: a Fully Exclusive QCD Calculation at NNLO*, Phys. Rev. Lett. **107** (2011) 152003, arXiv: 1107.1164 [hep-ph].
- [163] O. Brein, R. Harlander, M. Wiesemann, and T. Zirke, *Top-Quark Mediated Effects in Hadronic Higgs-Strahlung*, Eur. Phys. J. C **72** (2012) 1868, arXiv: 1111.0761 [hep-ph].
- [164] G. Ferrera, M. Grazzini, and F. Tramontano, *Higher-order QCD effects for associated WH production and decay at the LHC*, JHEP **04** (2014) 039, arXiv: 1312.1669 [hep-ph].
- [165] G. Ferrera, M. Grazzini, and F. Tramontano, *Associated ZH production at hadron colliders: The fully differential NNLO QCD calculation*, Phys. Lett. B **740** (2015) 51, arXiv: 1407.4747 [hep-ph].
- [166] J. M. Campbell, R. K. Ellis, and C. Williams, *Associated production of a Higgs boson at NNLO*, JHEP **06** (2016) 179, arXiv: 1601.00658 [hep-ph].
- [167] L. Altenkamp, S. Dittmaier, R. V. Harlander, H. Rzehak, and T. J. E. Zirke, *Gluon-induced Higgs-strahlung at next-to-leading order QCD*, JHEP **02** (2013) 078, arXiv: 1211.5015 [hep-ph].
- [168] B. Hespel, F. Maltoni, and E. Vryonidou, *Higgs and Z boson associated production via gluon fusion in the SM and the 2HDM*, JHEP **06** (2015) 065, arXiv: 1503.01656 [hep-ph].
- [169] R. V. Harlander, A. Kulesza, V. Theeuwes, and T. Zirke, *Soft gluon resummation for gluon-induced Higgs Strahlung*, JHEP **11** (2014) 082, arXiv: 1410.0217 [hep-ph].
- [170] R. V. Harlander, S. Liebler, and T. Zirke, *Higgs Strahlung at the Large Hadron Collider in the 2-Higgs-doublet model*, Journal of High Energy Physics **2014** (2014), ISSN: 1029-8479, URL: [http://dx.doi.org/10.1007/JHEP02\(2014\)023](http://dx.doi.org/10.1007/JHEP02(2014)023).
- [171] O. Brein, R. V. Harlander, and T. J. E. Zirke, *vh@nnlo – Higgs Strahlung at hadron colliders*, Comput. Phys. Commun. **184** (2013) 998, arXiv: 1210.5347 [hep-ph].
- [172] S. Frixione, P. Nason, and G. Ridolfi, *A positive-weight next-to-leading-order Monte Carlo for heavy flavour hadroproduction*, JHEP **09** (2007) 126, arXiv: 0707.3088 [hep-ph].
- [173] ATLAS Collaboration, *ATLAS Pythia 8 tunes to 7 TeV data*, ATL-PHYS-PUB-2014-021, 2014, URL: <https://cds.cern.ch/record/1966419>.
- [174] M. Czakon and A. Mitov, *Top++: A program for the calculation of the top-pair cross-section at hadron colliders*, Comput. Phys. Commun. **185** (2014) 2930, arXiv: 1112.5675 [hep-ph].

- [175] S. Alioli, P. Nason, C. Oleari, and E. Re, *NLO single-top production matched with shower in POWHEG: s- and t-channel contributions*, JHEP **09** (2009) 111, arXiv: 0907.4076 [hep-ph],  
Erratum: JHEP **02** (2010) 011.
- [176] M. Aliev et al.,  
*HATHOR – HAdronic Top and Heavy quarks crOss section calculator*, Comput. Phys. Commun. **182** (2011) 1034, arXiv: 1007.1327 [hep-ph].
- [177] P. Kant et al.,  
*HatHor for single top-quark production: Updated predictions and uncertainty estimates for single top-quark production in hadronic collisions*, Comput. Phys. Commun. **191** (2015) 74, arXiv: 1406.4403 [hep-ph].
- [178] E. Re, *Single-top Wt-channel production matched with parton showers using the POWHEG method*, Eur. Phys. J. C **71** (2011) 1547, arXiv: 1009.2450 [hep-ph].
- [179] N. Kidonakis, *Two-loop soft anomalous dimensions for single top quark associated production with a  $W^-$  or  $H^-$* , Phys. Rev. D **82** (2010) 054018, arXiv: 1005.4451 [hep-ph].
- [180] T. Gleisberg et al., *Event generation with SHERPA 1.1*, JHEP **02** (2009) 007, arXiv: 0811.4622 [hep-ph].
- [181] E. Bothmann et al., *Event generation with Sherpa 2.2*, SciPost Phys. **7** (2019) 034, arXiv: 1905.09127 [hep-ph].
- [182] F. Cascioli, P. Maierhöfer, and S. Pozzorini,  
*Scattering Amplitudes with Open Loops*, Phys. Rev. Lett. **108** (2012) 111601, arXiv: 1111.5206 [hep-ph].
- [183] T. Gleisberg and S. Höche, *Comix, a new matrix element generator*, JHEP **12** (2008) 039, arXiv: 0808.3674 [hep-ph].
- [184] S. Schumann and F. Krauss,  
*A parton shower algorithm based on Catani–Seymour dipole factorisation*, JHEP **03** (2008) 038, arXiv: 0709.1027 [hep-ph].
- [185] S. Höche, F. Krauss, M. Schönherr, and F. Siegert,  
*QCD matrix elements + parton showers. The NLO case*, JHEP **04** (2013) 027, arXiv: 1207.5030 [hep-ph].
- [186] S. Catani, L. Cieri, G. Ferrera, D. de Florian, and M. Grazzini,  
*Vector Boson Production at Hadron Colliders: A Fully Exclusive QCD Calculation at Next-to-Next-to-Leading Order*, Physical Review Letters **103** (2009), ISSN: 1079-7114.
- [187] F. Caola, K. Melnikov, R. Röntsch, and L. Tancredi,  
*QCD corrections to ZZ production in gluon fusion at the LHC*, Physical Review D **92** (2015), ISSN: 1550-2368.
- [188] J. Butterworth et al., *PDF4LHC recommendations for LHC Run II*, J. Phys. G **43** (2016) 023001, arXiv: 1510.03865 [hep-ph].

- [189] A. Denner, S. Dittmaier, S. Kallweit, and A. Mück, *Electroweak corrections to Higgs-strahlung off W/Z bosons at the Tevatron and the LHC with Hawk*, Journal of High Energy Physics **2012** (2012), ISSN: 1029-8479.
- [190] A. Denner, S. Dittmaier, S. Kallweit, and A. Mück, *HAWK 2.0: A Monte Carlo program for Higgs production in vector-boson fusion and Higgs strahlung at hadron colliders*, Comput. Phys. Commun. **195** (2015) 161, arXiv: 1412.5390 [hep-ph].
- [191] P. Nason and C. Oleari, *NLO Higgs boson production via vector-boson fusion matched with shower in POWHEG*, JHEP **02** (2010) 037, arXiv: 0911.5299 [hep-ph].
- [192] P. Nason, *A new method for combining NLO QCD with shower Monte Carlo algorithms*, JHEP **11** (2004) 040, arXiv: hep-ph/0409146.
- [193] S. Frixione, P. Nason, and C. Oleari, *Matching NLO QCD computations with parton shower simulations: the POWHEG method*, JHEP **11** (2007) 070, arXiv: 0709.2092 [hep-ph].
- [194] D. J. Lange, *The EvtGen particle decay simulation package*, Nucl. Instrum. Meth. A **462** (2001) 152.
- [195] A. Djouadi, J. Kalinowski, and M. Spira, *HDECAY: A program for Higgs boson decays in the Standard Model and its supersymmetric extension*, Comput. Phys. Commun. **108** (1998) 56, arXiv: hep-ph/9704448.
- [196] M. Spira, *QCD Effects in Higgs physics*, Fortsch. Phys. **46** (1998) 203, arXiv: hep-ph/9705337.
- [197] A. Djouadi, M. M. Mühlleitner, and M. Spira, *Decays of supersymmetric particles: The Program SUSY-HIT (SUspect-SdecaY-Hdecay-InTerface)*, Acta Phys. Polon. B **38** (2007) 635, arXiv: hep-ph/0609292.
- [198] A. Bredenstein, A. Denner, S. Dittmaier, and M. M. Weber, *Radiative corrections to the semileptonic and hadronic Higgs-boson decays  $H \rightarrow WW/ZZ \rightarrow 4$  fermions*, JHEP **02** (2007) 080, arXiv: hep-ph/0611234.
- [199] A. Bredenstein, A. Denner, S. Dittmaier, and M. M. Weber, *Precise predictions for the Higgs-boson decay  $H \rightarrow WW/ZZ \rightarrow 4$  leptons*, Phys. Rev. D **74** (2006) 013004, arXiv: hep-ph/0604011 [hep-ph].
- [200] A. Bredenstein, A. Denner, S. Dittmaier, and M. M. Weber, *Precision calculations for the Higgs decays  $H \rightarrow ZZ/WW \rightarrow 4$  leptons*, Nucl. Phys. Proc. Suppl. **160** (2006) 131, [131(2006)], arXiv: hep-ph/0607060 [hep-ph].
- [201] ATLAS Collaboration, *Studies on top-quark Monte Carlo modelling for Top2016*, ATL-PHYS-PUB-2016-020, 2016, URL: <https://cds.cern.ch/record/2216168>.
- [202] R. D. Ball et al., *Parton distributions with LHC data*, Nucl. Phys. B **867** (2013) 244, arXiv: 1207.1303 [hep-ph].

- [203] M. Beneke, P. Falgari, S. Klein, and C. Schwinn, *Hadronic top-quark pair production with NNLL threshold resummation*, Nucl. Phys. B **855** (2012) 695, arXiv: 1109.1536 [hep-ph].
- [204] M. Cacciari, M. Czakon, M. Mangano, A. Mitov, and P. Nason, *Top-pair production at hadron colliders with next-to-next-to-leading logarithmic soft-gluon resummation*, Phys. Lett. B **710** (2012) 612, arXiv: 1111.5869 [hep-ph].
- [205] P. Bärnreuther, M. Czakon, and A. Mitov, *Percent-Level-Precision Physics at the Tevatron: Next-to-Next-to-Leading Order QCD Corrections to  $q\bar{q} \rightarrow t\bar{t} + X$* , Phys. Rev. Lett. **109** (2012) 132001, arXiv: 1204.5201 [hep-ph].
- [206] M. Czakon and A. Mitov, *NNLO corrections to top-pair production at hadron colliders: the all-fermionic scattering channels*, JHEP **12** (2012) 054, arXiv: 1207.0236 [hep-ph].
- [207] M. Czakon and A. Mitov, *NNLO corrections to top pair production at hadron colliders: the quark-gluon reaction*, JHEP **01** (2013) 080, arXiv: 1210.6832 [hep-ph].
- [208] M. Czakon, P. Fiedler, and A. Mitov, *Total Top-Quark Pair-Production Cross Section at Hadron Colliders Through  $O(\alpha_S^4)$* , Phys. Rev. Lett. **110** (2013) 252004, arXiv: 1303.6254 [hep-ph].
- [209] R. Frederix, E. Re, and P. Torrielli, *Single-top  $t$ -channel hadroproduction in the four-flavour scheme with POWHEG and aMC@NLO*, JHEP **09** (2012) 130, arXiv: 1207.5391 [hep-ph].
- [210] S. Frixione, E. Laenen, P. Motylinski, and B. R. Webber, *Angular correlations of lepton pairs from vector boson and top quark decays in Monte Carlo simulations*, JHEP **04** (2007) 081, arXiv: hep-ph/0702198.
- [211] P. Artoisenet, R. Frederix, O. Mattelaer, and R. Rietkerk, *Automatic spin-entangled decays of heavy resonances in Monte Carlo simulations*, JHEP **03** (2013) 015, arXiv: 1212.3460 [hep-ph].
- [212] S. Frixione, E. Laenen, P. Motylinski, C. White, and B. R. Webber, *Single-top hadroproduction in association with a  $W$  boson*, JHEP **07** (2008) 029, arXiv: 0805.3067 [hep-ph].
- [213] N. Kidonakis, *Top Quark Production*, 2014, arXiv: 1311.0283 [hep-ph].
- [214] F. Buccioni et al., *OpenLoops 2*, Eur. Phys. J. C **79** (2019) 866, arXiv: 1907.13071 [hep-ph].
- [215] A. Denner, S. Dittmaier, and L. Hofer, *COLLIER: A fortran-based complex one-loop library in extended regularizations*, Comput. Phys. Commun. **212** (2017) 220, arXiv: 1604.06792 [hep-ph].
- [216] J.-C. Winter, F. Krauss, and G. Soff, *A modified cluster-hadronization model*, Eur. Phys. J. C **36** (2004) 381, arXiv: hep-ph/0311085.

- [217] S. Höche, F. Krauss, M. Schönherr, and F. Siegert,  
*A critical appraisal of NLO+PS matching methods*, JHEP **09** (2012) 049,  
arXiv: 1111.1220 [hep-ph].
- [218] S. Catani, F. Krauss, R. Kuhn, and B. R. Webber,  
*QCD Matrix Elements + Parton Showers*, JHEP **11** (2001) 063,  
arXiv: hep-ph/0109231.
- [219] S. Höche, F. Krauss, S. Schumann, and F. Siegert,  
*QCD matrix elements and truncated showers*, JHEP **05** (2009) 053,  
arXiv: 0903.1219 [hep-ph].
- [220] K. Melnikov and F. Petriello,  
*Electroweak gauge boson production at hadron colliders through  $\mathcal{O}(\alpha_s^2)$* ,  
Phys. Rev. D **74** (2006) 114017, arXiv: hep-ph/0609070.
- [221] A. D. Martin, W. J. Stirling, R. S. Thorne, and G. Watt,  
*Parton distributions for the LHC*, Eur. Phys. J. C **63** (2009) 189,  
arXiv: 0901.0002 [hep-ph].
- [222] ATLAS Collaboration, *Measurement of  $W^\pm$  and Z Boson Production Cross Sections in pp Collisions at  $\sqrt{s} = 13$  TeV with the ATLAS Detector*, ATLAS-CONF-2015-039, 2015,  
URL: <https://cds.cern.ch/record/2045487>.
- [223] S. Agostinelli et al., *GEANT4 – a simulation toolkit*,  
Nucl. Instrum. Meth. A **506** (2003) 250.
- [224] ATLAS Collaboration, *The ATLAS Simulation Infrastructure*,  
Eur. Phys. J. C **70** (2010) 823, arXiv: 1005.4568 [physics.ins-det].
- [225] T. Sjöstrand, S. Mrenna, and P. Skands,  
*A brief introduction to PYTHIA 8.1*,  
Comput. Phys. Commun. **178** (2008) 852, arXiv: 0710.3820 [hep-ph].
- [226] ATLAS Collaboration,  
*The Pythia 8 A3 tune description of ATLAS minimum bias and inelastic measurements incorporating the Donnachie–Landshoff diffractive model*, ATL-PHYS-PUB-2016-017, 2016,  
URL: <https://cds.cern.ch/record/2206965>.
- [227] ATLAS Collaboration, *Measurement of the Inelastic Proton–Proton Cross Section at  $\sqrt{s} = 13$  TeV with the ATLAS Detector at the LHC*,  
Phys. Rev. Lett. **117** (2016) 182002, arXiv: 1606.02625 [hep-ex].
- [228] ATLAS Collaboration, *Reconstruction of hadronic decay products of tau leptons with the ATLAS experiment*, Eur. Phys. J. C **76** (2016) 295,  
arXiv: 1512.05955 [hep-ex].
- [229] R. Costa Batalha Pedro, *Search for the Higgs boson at ATLAS/LHC in WH associated production and decay to b quark pairs*, 2017,  
URL: <https://cds.cern.ch/record/2304102>.

- [230] M. Proissl,  
*Dijet Invariant Mass Studies in the Higgs boson  $H \rightarrow b\bar{b}$  resonance search in association with a  $W/Z$  boson using the ATLAS detector*,  
(2014), Presented 2014, URL: <https://cds.cern.ch/record/1997808>.
- [231] A. D. Bukin, *Fitting function for asymmetric peaks*, 2007,  
arXiv: 0711.4449 [physics.data-an].
- [232] D. Goncalves and J. Nakamura,  
*Role of the  $Z$  polarization in the  $H \rightarrow b\bar{b}$  measurement*,  
Phys. Rev. D **98** (2018) 093005, arXiv: 1805.06385 [hep-ph].
- [233] ATLAS Collaboration,  
*Jet energy scale measurements and their systematic uncertainties in proton–proton collisions at  $\sqrt{s} = 13$  TeV with the ATLAS detector*,  
Phys. Rev. D **96** (2017) 072002, arXiv: 1703.09665 [hep-ex].
- [234] ATLAS Collaboration, *Jet energy resolution in proton–proton collisions at  $\sqrt{s} = 7$  TeV recorded in 2010 with the ATLAS detector*,  
Eur. Phys. J. C **73** (2013) 2306, arXiv: 1210.6210 [hep-ex].
- [235] ATLAS Collaboration, *Jet mass and substructure of inclusive jets in  $\sqrt{s} = 7$  TeV  $pp$  collisions with the ATLAS experiment*,  
JHEP **05** (2012) 128, arXiv: 1203.4606 [hep-ex].
- [236] ATLAS Collaboration, *Measurement of  $b$ -tagging efficiency of  $c$ -jets in  $t\bar{t}$  events using a likelihood approach with the ATLAS detector*,  
ATLAS-CONF-2018-001, 2018,  
URL: <https://cds.cern.ch/record/2306649>.
- [237] ATLAS Collaboration,  
*Performance of missing transverse momentum reconstruction with the ATLAS detector using proton–proton collisions at  $\sqrt{s} = 13$  TeV*,  
Eur. Phys. J. C **78** (2018) 903, arXiv: 1802.08168 [hep-ex].
- [238] J. Bellm et al., *Herwig 7.0/Herwig++ 3.0 release note*,  
Eur. Phys. J. C **76** (2016) 196, arXiv: 1512.01178 [hep-ph].
- [239] J. Bellm et al., *Herwig 7.1 Release Note*, 2017,  
arXiv: 1705.06919 [hep-ph].
- [240] L. Harland-Lang, A. Martin, P. Motylinski, and R. Thorne,  
*Parton distributions in the LHC era: MMHT 2014 PDFs*,  
Eur. Phys. J. C **75** (2015) 204, arXiv: 1412.3989 [hep-ph].
- [241] ATLAS Collaboration,  
*Evaluation of theoretical uncertainties for simplified template cross section measurements of  $V$ -associated production of the Higgs boson*,  
ATL-PHYS-PUB-2018-035, 2018,  
URL: <https://cds.cern.ch/record/2649241>.
- [242] ATLAS Collaboration,  
*Measurement of  $VH$ ,  $H \rightarrow b\bar{b}$  production as a function of the vector-boson transverse momentum in 13 TeV  $pp$  collisions with the ATLAS detector*,  
JHEP **05** (2019) 141, arXiv: 1903.04618 [hep-ex].

- [243] I. W. Stewart and F. J. Tackmann, *Theory Uncertainties for Higgs and Other Searches Using Jet Bins*, Phys. Rev. D **85** (2012) 034011, arXiv: 1107.2117 [hep-ph].
- [244] ATLAS Collaboration, *Improvements in  $t\bar{t}$  modelling using NLO+PS Monte Carlo generators for Run 2*, ATL-PHYS-PUB-2018-009, 2018, URL: <https://cds.cern.ch/record/2630327>.
- [245] ATLAS Collaboration, *Study of top-quark pair modelling and uncertainties using ATLAS measurements at  $\sqrt{s}=13$  TeV*, ATL-PHYS-PUB-2020-023, 2020, URL: <http://cds.cern.ch/record/2730443>.
- [246] M. Bähr et al., *Herwig++ physics and manual*, Eur. Phys. J. C **58** (2008) 639, arXiv: 0803.0883 [hep-ph].
- [247] J. Alwall et al., *The automated computation of tree-level and next-to-leading order differential cross sections, and their matching to parton shower simulations*, JHEP **07** (2014) 079, arXiv: 1405.0301 [hep-ph].
- [248] H.-L. Lai et al., *New parton distributions for collider physics*, Phys. Rev. D **82** (2010) 074024, arXiv: 1007.2241 [hep-ph].
- [249] J. Pumplin et al., *New Generation of Parton Distributions with Uncertainties from Global QCD Analysis*, JHEP **07** (2002) 012, arXiv: hep-ph/0201195.
- [250] K. Cranmer, G. Lewis, L. Moneta, A. Shibata, and W. Verkerke, *HistFactory: A tool for creating statistical models for use with RooFit and RooStats*, 2012, URL: <https://cds.cern.ch/record/1456844>.
- [251] W. Verkerke and D. P. Kirkby, *The RooFit toolkit for data modeling*, eConf **C0303241** (2003) MOLT007, ed. by L. Lyons and M. Karagoz, arXiv: physics/0306116.
- [252] L. Moneta et al., *The RooStats Project*, 2011, arXiv: 1009.1003 [physics.data-an].
- [253] R. J. Barlow and C. Beeston, *Fitting using finite Monte Carlo samples*, Comput. Phys. Commun. **77** (1993) 219.
- [254] F. James and M. Roos, *Minuit: A System for Function Minimization and Analysis of the Parameter Errors and Correlations*, Comput. Phys. Commun. **10** (1975) 343.
- [255] G. Cowan, K. Cranmer, E. Gross, and O. Vitells, *Asymptotic formulae for likelihood-based tests of new physics*, Eur. Phys. J. C **71** (2011) 1554, arXiv: 1007.1727 [physics.data-an], Erratum: Eur. Phys. J. C **73** (2013) 2501.
- [256] I. Asimov and D. Shannon, *Franchise*, Creative Short Stories Series, Creative Education, 1989, ISBN: 978-0-886-82232-3.

- [257] ATLAS Collaboration, *Measurement of  $W^\pm Z$  production cross sections and gauge boson polarisation in  $pp$  collisions at  $\sqrt{s} = 13$  TeV with the ATLAS detector*, Eur. Phys. J. C **79** (2019) 535, arXiv: 1902.05759 [hep-ex].
- [258] C. Hays, A. Martin, V. Sanz, and J. Setford, *On the impact of dimension-eight SMEFT operators on Higgs measurements*, JHEP **02** (2019) 123, arXiv: 1808.00442 [hep-ph].
- [259] C. Degrande, B. Fuks, K. Mawatari, K. Mimasu, and V. Sanz, *Electroweak Higgs boson production in the standard model effective field theory beyond leading order in QCD*, Eur. Phys. J. C **77** (2017) 262, arXiv: 1609.04833 [hep-ph].
- [260] ATLAS Collaboration, *Interpretations of the combined measurement of Higgs boson production and decay*, ATLAS-CONF-2020-053, 2020, URL: <https://cds.cern.ch/record/2743067>.
- [261] J. Brehmer, S. Dawson, S. Homiller, F. Kling, and T. Plehn, *Benchmarking simplified template cross sections in  $WH$  production*, JHEP **11** (2019) 034, arXiv: 1908.06980 [hep-ph].
- [262] ATLAS Collaboration, *Methodology for EFT interpretation of Higgs boson simplified template cross-section results in ATLAS*, ATL-PHYS-PUB-2019-042, 2019, URL: <https://cds.cern.ch/record/2694284>.
- [263] C. Bierlich et al., *Robust Independent Validation of Experiment and Theory: Rivet version 3*, SciPost Phys. **8** (2020) 026, arXiv: 1912.05451 [hep-ph].
- [264] A. Biekötter, A. Knochel, M. Krämer, D. Liu, and F. Riva, *Vices and virtues of Higgs effective field theories at large energy*, Phys. Rev. D **91** (2015) 055029, arXiv: 1406.7320 [hep-ph].
- [265] R. Contino, A. Falkowski, F. Goertz, C. Grojean, and F. Riva, *On the Validity of the Effective Field Theory Approach to SM Precision Tests*, JHEP **07** (2016) 144, arXiv: 1604.06444 [hep-ph].
- [266] M. Farina et al., *Energy helps accuracy: electroweak precision tests at hadron colliders*, Phys. Lett. B **772** (2017) 210, arXiv: 1609.08157 [hep-ph].
- [267] M. Trott, *A methodology for theory uncertainties in the SMEFT*, 2021, arXiv: 2106.13794 [hep-ph].
- [268] A. L. Read, *Presentation of search results: the  $CL_S$  technique*, J. Phys. G **28** (2002) 2693.
- [269] G. Perez, Y. Soreq, E. Stamou, and K. Tobioka, *Constraining the charm Yukawa and Higgs-quark coupling universality*, Phys. Rev. D **92** (2015) 033016, arXiv: 1503.00290 [hep-ph].



- [270] F. J. Botella, G. C. Branco, M. N. Rebelo, and J. I. Silva-Marcos, *What if the masses of the first two quark families are not generated by the standard model Higgs boson?*, Phys. Rev. D **94** (2016) 115031, arXiv: 1602.08011 [hep-ph].
- [271] D. Egana-Ugrinovic, S. Homiller, and P. R. Meade, *Higgs bosons with large couplings to light quarks*, Phys. Rev. D **100** (2019) 115041, arXiv: 1908.11376 [hep-ph].
- [272] S. Bar-Shalom and A. Soni, *Universally enhanced light-quarks Yukawa couplings paradigm*, Phys. Rev. D **98** (2018) 055001, arXiv: 1804.02400 [hep-ph].
- [273] Fermilab Lattice, MILC, and TUMQCD Collaborations, *Up-, down-, strange-, charm-, and bottom-quark masses from four-flavor lattice QCD*, Phys. Rev. D **98** (5 2018) 054517.
- [274] ATLAS Collaboration, *Extrapolation of ATLAS sensitivity to  $H \rightarrow b\bar{b}$  and  $H \rightarrow c\bar{c}$  decays in  $VH$  production at the HL-LHC*, ATL-PHYS-PUB-2021-039, 2021, URL: <http://cds.cern.ch/record/2788490>.



# A Supplementary information to the SMEFT interpretation of the measurement of Higgs boson production at high transverse momentum in the $VH, H \rightarrow b\bar{b}$ channel

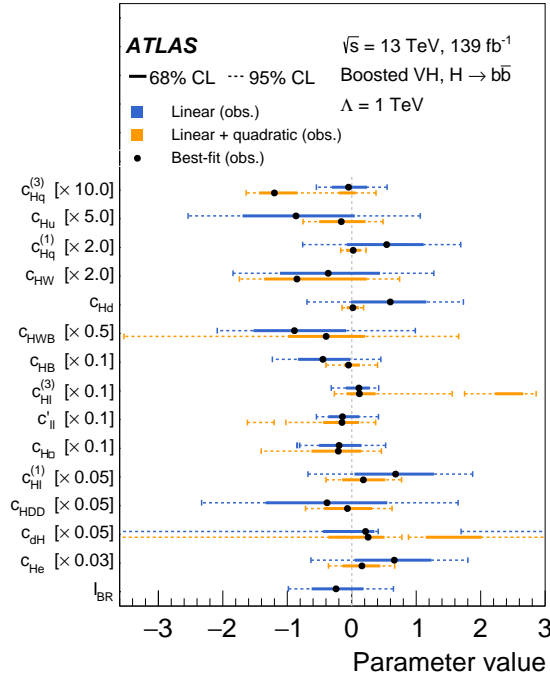


Figure A.1: Summary of observed confidence intervals at 68% and 98% CL from likelihood scans as a function of the 13 + 1 Wilson coefficients and the linearised branching ratio modifier  $I_{BR}$ . Only one Wilson coefficient is varied at a time and the remaining ones are fixed to their SM prediction at zero. The blue lines show the intervals obtained considering only the interference effects and therefore a linear parameterisation. The orange lines indicate the limits when including the terms quadratic in the Wilson coefficients. Published in Ref. [5].

Wilson coefficient	expected	observed
$c_{EA}$	$0.000^{+0.030}_{-0.027}$	$-0.010^{+0.027}_{-0.025}$
$c_{EB}$	$0.00^{+0.20}_{-0.19}$	$-0.21^{+0.19}_{-0.20}$
$c_{EC}$	$0.00^{+0.71}_{-0.67}$	$-0.62^{+0.70}_{-0.66}$
$c_{ED}$	$0.0^{+2.8}_{-2.7}$	$0.4^{+2.8}_{-2.7}$

Table A.1: Expected and observed best-fit values and associated uncertainties (68% CL) from a simultaneous fit of the coefficients of the four leading Eigenoperators. Published in Ref. [5].

Eigenvalue	Eigenoperator
1500.0	$0.988 \cdot c_{Hq}^{(3)} - 0.0629 \cdot c_{Hq}^{(1)} - 0.0317 \cdot c_{Hd} - 0.0008 \cdot c_{He} + 0.0607 \cdot$ $\mathcal{I}_{BR} + 0.107 \cdot c_{Hu} - 0.00145 \cdot c_{Hl}^{(1)} - 0.0143 \cdot c_{Hl}^{(3)} + 0.0108 \cdot c'_{ll} + 0.0114 \cdot$ $c_{HWB} + 0.00416 \cdot c_{HB} - 0.00067 \cdot c_{HD} + 0.0613 \cdot c_{HW} + 0.00716 \cdot c_{H\Box}$
26.9	$-0.129 \cdot c_{Hq}^{(3)} - 0.486 \cdot c_{Hq}^{(1)} - 0.243 \cdot c_{Hd} - 0.00594 \cdot c_{He} + 0.0202 \cdot$ $\mathcal{I}_{BR} + 0.823 \cdot c_{Hu} - 0.011 \cdot c_{Hl}^{(1)} - 0.00348 \cdot c_{Hl}^{(3)} + 0.00215 \cdot c'_{ll} + 0.086 \cdot$ $c_{HWB} + 0.0315 \cdot c_{HB} + 0.00788 \cdot c_{HD} - 0.0329 \cdot c_{HW} + 0.00184 \cdot c_{H\Box}$
2.2	$-0.0859 \cdot c_{Hq}^{(3)} + 0.183 \cdot c_{Hq}^{(1)} - 0.0627 \cdot c_{Hd} - 0.0137 \cdot c_{He} + 0.674 \cdot$ $\mathcal{I}_{BR} + 0.069 \cdot c_{Hu} - 0.0111 \cdot c_{Hl}^{(1)} - 0.158 \cdot c_{Hl}^{(3)} + 0.122 \cdot c'_{ll} + 0.135 \cdot$ $c_{HWB} + 0.0347 \cdot c_{HB} - 0.00407 \cdot c_{HD} + 0.656 \cdot c_{HW} + 0.0817 \cdot c_{H\Box}$
0.1	$0.0223 \cdot c_{Hq}^{(3)} + 0.698 \cdot c_{Hq}^{(1)} - 0.243 \cdot c_{Hd} - 0.0529 \cdot c_{He} - 0.0807 \cdot$ $\mathcal{I}_{BR} + 0.274 \cdot c_{Hu} - 0.0427 \cdot c_{Hl}^{(1)} + 0.00716 \cdot c_{Hl}^{(3)} - 0.0131 \cdot c'_{ll} + 0.52 \cdot$ $c_{HWB} + 0.134 \cdot c_{HB} + 0.0648 \cdot c_{HD} - 0.272 \cdot c_{HW} - 0.00796 \cdot c_{H\Box}$

Table A.2: Eigenoperators that are orthogonal for an unconditional fit to data with systematic uncertainties and their corresponding eigenvalues. Published in Ref. [5].

# Acknowledgements

As this thesis comes to an end, so do my four years as a Ph.D. student at Nikhef and the University of Amsterdam. My field of research, experimental high energy physics, is inherently collaborative and, consequently, I want to use these remaining pages to thank the people that have guided me along my way. Unfortunately, these lines are written under the pressure of having to send the manuscript to the printer, therefore I apologize in advance if I did not mention you personally. Rest assured that you are still dear to me.

First and foremost, I want to thank my promotor Wouter Verkerke and my copromotor Tristan du Pree for giving me the opportunity to conduct my Ph.D. research within the Nikhef ATLAS group. I appreciated all the valuable discussions with Wouter, especially during the review of the thesis manuscript, and the fact that he always manages to free some time despite a completely full agenda. To Tristan I want to express my deep gratitude for taking me on into his research team ‘Higgs from Z to A’ and for being my supervisor in these four years. I thank him for all his support and greatly admire the dedication with which he fights for his students. He always kept an eye on the big picture, continuously encouraged me to broaden my expertise and deepen my knowledge - his door was always open when I was in need of an advice. In addition, his relaxed and informal working style made me feel welcome at Nikhef. He also introduced me (and the rest of the ‘Higgs from Z to A’ group) to Dutch specialties like Jenever or Gourmetten - memories that I will not easily forget.

Furthermore, I am grateful to Jordy de Vries, Marcel Vreeswijk, Marumi Kado, Patrick Decowski and Robert Fleischer for being part of my thesis committee and for taking the time to read my manuscript so carefully. A special thanks goes to Robert for also being my C3 member and for following my PhD journey closely throughout the years.

I want to thank Chris Pollard, Giacinto Piacquadio, Hannah Arnold, Marumi Kado, Tristan du Pree, Valerio Dao and Wouter Verkerke for supporting me in my job applications.

One of the things that I like most about conducting research is the thrill of constantly learning something new. Being a part of the ATLAS collaboration gave me the opportunity to learn from some of the brightest people that I have ever met. I am grateful to *all* the connections and friendships that I have made during my Ph.D. but nevertheless I want to explicitly mention a few below.

The person that heavily influenced me scientifically during this Ph.D. and who taught me how to tackle the daily problems encountered in particle physics research

is Hannah Arnold. It is only thanks to her that I started my Ph.D. at Nikhef and she is largely responsible for me being able to (almost) finish it successfully. Her dedication to the subject and her honesty in approaching problems, paired with her extensive expertise in all steps of an analysis workflow are truly inspiring. Although I cannot put into words how grateful I am, I want to thank her for all her guidance and relentless support, for being an amazing supervisor and a great friend.

Next, I want to thank Valerio Dao who I had the pleasure of working with closely throughout the last four years. His sharp mind and expertise in all topics of high energy physics, paired with his willingness to educate and guide students is incredibly impressive. I am grateful that he always had an open ear for my questions and admire his talent for bringing things to completion, more than once reminding me that 'the best is the enemy of the good'.

This work would not have been possible without the combined effort of many ATLAS physics and performance groups, especially the flavour-tagging group, the Higgs group and more specifically the  $H \rightarrow b\bar{b}$  subgroup. I would like to express my deepest appreciation to all its members who, under the excellent guidance of the group conveners, manage to make the impossible possible on a daily basis. I thank all of them for the friendly and collaborative environment, for their willingness to share their knowledge and for all the interesting discussions that we had during the last four years. Please forgive me that I am not mentioning names here, I fear I would not manage to do this without forgetting people.

When I was not working from home due to ongoing pandemics, I spent most of my time in Amsterdam at Nikhef. Nikhef is an amazing institute and I have greatly benefited both from its research and support infrastructure. Many thanks to the countless people who make Nikhef the exceptional place that it is. I want to furthermore thank the members of the ATLAS group for creating an amazing working environment. I enjoyed our group lunches, coffee breaks, the outings, the after-work borrels on Friday and all the other activities that we did throughout the years. Many thanks to Anamika, Andrea A., Andrea V., Alice, Alessio, Ann-Kathrin, Ash, Birgit, Broos, Bryan, Clara, Carlo G., Carlo P., Carsten, Denys, Dylan, Edwin, Emma, Federica, Flavia, Florian, Frank, Geoffrey, Hannah, Hella, Ivo, JJ., Jordy, Kees, Lucrezia, Lydia, Marc, Marcus, Marcel, Marion, Marko, Marten, Mat, Matteo, Michiel, Nicolo, Oliver, Osama, Pamela, Peter, Pepijn, Rahul, Stefano, Terry, Tim, Tristan, Wouter, Zef, Zhuoran, and all the people that I unfortunately forgot to mention. Within Tristan's research team, I am especially happy to have worked closely together with Cecile, Geoffrey, Giovanni, Hannah, Marion, Marko, Osama, Pepijn and Zhuoran. I want to thank them for all the nice collaborations during busy times.

I am especially grateful to Marko Stamenkovic, who started his Ph.D. together with me in the 'Higgs from Z to A' group and who was my 'brother in arms' both in Amsterdam and at CERN. I value his close friendship a lot and will never forget the good times we had, from physics workshops and Indie festivals to holidays on Texel. He made the occasional late nights in the office enjoyable and always has

two or three crazy new ideas up his sleeve to discuss. I am sorry that his attempt to train my taste in music was without success, but I hope we will have many more occasions in the future to try.

A special thanks goes to Ash McDougall and Rahul Balasubramanian, not least for having to deal with me during the time we shared an apartment in Amsterdam. Ash and Rahul are both incredibly kind people and I happily look back to all the nice times we had, be it living on the floor while waiting for the furniture to arrive, exploring the canals by boat or the traditional Friday evening Saag Paneer.

Furthermore, I want to also thank Manuel Guth, Benjamin Jäger and Christopher Böhm who studied with me during my time in Freiburg. I greatly appreciate that we managed to stay in contact beyond our studies and even though we don't see each other that often I always value their advice and look forward to the next time we can share a drink.

Outside the world of physics, I am grateful to have a circle of friends from my home town Elzach, most of which I know already since I was a little child. Even though we are more and more scattered around the world, I greatly appreciate the few times a year that we see each other and get together like no time has passed.

I cannot begin to express my thanks to Bouke, whose kindness, love and support is beyond anything imaginable. Without the understanding for all the long nights, the early mornings and everything in between this thesis would not have been possible. I consider myself extremely lucky to have found such a special person. I owe you everything.

Last but not least I want to thank my family, especially my parents Anita and Arne and my brothers Gabriel and Niklas, for always being there for me. Even though I did not visit them nearly as much as they deserve, I am extremely happy to have a place that I can always come back home to.

*To all of you who were part of my Ph.D. journey - thank you very much! I hope we will be able to see each other at the defence and celebrate together afterwards.*

Brian Moser,  
Amsterdam, January 2022







